Crystal engineering and sorption studies of cyclotriveratrylene and *C*-methylcalix[4]resorcinarene solvates

Richard Michael Payne

Thesis presented for the degree of

Doctor of Philosophy

Department of Chemistry

University of Cape Town

South Africa

November 2019

Supervisor:

Dr. Clive L. Oliver

Dedication

To my loving parents, Ian and Desireé, I would not be where I am today without your sacrifices and your constant love and support. My only regret is that you are no longer here to share this moment with me.

This is for you.

Thank you for everything. I miss you every day.

Love always,

Richard

Acknowledgements

I would like to thank my supervisor, Dr. Clive Oliver, for his advice, constant support and never-ending patience.

There are many others whom I would like to thank:

Professors Susan Bourne, Mino Caira and Luigi Nassimbeni for always making time to help me whenever requested and to Professor Nassimbeni for our conversations on politics, history, religion, science and the future of the universe.

Dr. Hong Su for the single crystal data collection and processing.

Pieter de Kock and Yaasien Ely for all equipment maintenance requirements.

Karin Badenhorst, Deirdre Brooks, Crystal Losper, Joanne Polzin, Martina Mayiya, Saroja Naicker and Leeta Lalbahadur for helping me to navigate the minefield of paperwork and forms.

Monique Muller, for always maintaining a safe workplace environment with an iron fist, a smile and colourful hairstyles.

Nicole Sykes for her friendship, sense of humour and putting up with me in the neighbouring cubicle.

The rest of the Centre for Supramolecular Chemistry and Research team, thank you for your support and assistance when required. My PhD years have been better because of you.

The entire Department of Chemistry, thank you for always making me feel welcome and supporting me during dark times.

My friends and family for their love and support.

I am grateful to the NRF for providing a scholarship in the form of the NRF Innovation Doctoral Scholarship. Any conclusions reached in this work are those of the author and the NRF does not accept liability in this regard.

I would like to acknowledge the University of Cape Town for providing the equipment and facilities required to complete this work as well as financial assistance.

Publications

Parts of this thesis have been published in international peer-reviewed journals:

‘Single-crystal-to-single-crystal transformation of the desolvation of a cyclotriveratrylene-acetonitrile inclusion complex *via* a gating mechanism with subsequent polymorphism’ Payne, R.M.; Oliver, C.L. *CrystEngComm*, **2016**, *18*, (41), 7965-7971.

‘A propanol-seamed *C*-methylcalix[4]resorcinarene hexamer accessible *via* solution crystallization, liquid-assisted grinding and vapour sorption’ Payne, R.M.; Oliver, C.L. *CrystEngComm*, **2018**, *20*, (14), 1919-1922.

Plagiarism Declaration

I, Richard Michael Payne, hereby declare that this thesis represents my own work, both in concept and execution, unless otherwise stated/referenced/quoted.

Signed by candidate

Richard Michael Payne

Date: 14 November 2019

Abstract

Cyclotriveratrylene compounds crystallised from acetonitrile (**1**) and 2-butanone (**4**) are shown to be nearly isostructural, resulting in the formation of dimeric capsules, while the compound which crystallised from chloroform (**3**) results in the formation of layers of cyclotriveratrylene molecules separated by layers of chloroform molecules. **1** is found to undergo a single-crystal-to-single-crystal transformation following desolvation. Consecutive single-crystal X-ray diffraction experiments on **1** at 50 °C reveal that the rotation of a unique, single methoxy group of the host molecule may permit the escape of the solvent molecules from the apparently nonporous crystal.

C-methylcalix[4]resorcinarene has been shown previously to form either channel-type structures or hexameric, spherical assemblies when crystallised from various alcohol molecules. The effect of the length of the alkyl chain of the solvent alcohol was studied. It was established that the short-chain alcohols favour the formation of channel-type structures while the longer-chain alcohols favour the formation of the hexameric, spherical assemblies. A hexameric assembly structure crystallised from 1-propanol (**8**) displays a ~25% increased interior volume over known assemblies and is found to be the first of these types of assemblies to form by vapour sorption. A hexameric assembly structure crystallised from 1-butanol (**9**) has already been published in the literature. However, SCXRD studies for this work revealed additional structural information not apparent in the literature structure. Another hexameric assembly structure, this time crystallised from 1-pentanol (**10**), was shown to be similar to the structure of **9**, with certain differences.

Characterization of these structures was performed by single-crystal X-ray diffraction, powder X-ray diffraction, hot stage microscopy and thermal analysis. All compounds were shown to maintain crystallinity upon heating and desolvation – however, several transitioned through an amorphous phase.

Gas and vapour sorption analysis was performed on all activated compounds. Some of these compounds were found to resolvate to their original solvated structures merely upon exposure of the desolvated powders to the solvent vapours.

Table of Contents

Chapter 1 – Introduction

Supramolecular chemistry is defined by molecular structures held together by noncovalent interactions and plays significant parts in biochemistry, chemistry, nanoscience and numerous other areas.[1] Within supramolecular chemistry, host molecules are generally larger molecules which encapsulate or trap smaller guest molecules within their own molecular cavities or cavities which are formed by the supramolecular association of these host molecules into larger host systems.

Crystal engineering is the preparation of functional molecular crystals.[2] During the 1990s, numerous considerations drove the development of crystal engineering.[3] There was a requirement for more applied objectives for basic research. At the same time, small molecule crystallography was becoming more accessible to non-specialists, but perhaps, the most significant consideration was the cultural consideration in the growth of crystal engineering. The supramolecular insight into chemistry produced a significant 'conceptual shift': from emphasis on atoms and bonds between atoms to emphasis on molecules and bonds between molecules.[3] These intermolecular interactions include Coulombic interactions, van der Waals' forces and hydrogen bonds, among others.[3] The official definition of supramolecular chemistry excludes coordination bonds due to them being short and strong as opposed to weak and long.[4] Supramolecular chemistry has blurred all the customary lines between the various chemical disciplines (biological, organometallic, inorganic, organic). Instead, the focus has centred on the *collective* characteristics of the assembly of molecules and how those characteristics are related to those of the individual molecules.[3] Since the early 1990s, crystal engineering has grown from analysis of crystal structures with regard to intermolecular interactions, to the preparation of crystals with predicted topologies, to design and manipulation of crystal properties.[5-13] At the outset of crystal engineering, a particular characteristic was linked to a molecular structure, which therefore became linked with a particular intermolecular interaction.[2] Thereafter, interactions were associated with certain structural motifs within crystal structures, leading to 'supramolecular synthons'.[10] Currently, though, crystal engineering has reached the point where it is possible to target a certain desirable characteristic and determine the crystal structure likely to confer this desirable characteristic.[14]

The supramolecular chemistry of host-guest systems is currently of immense and growing significance and interest.[15-17] Host-guest systems containing powerful intermolecular interactions are also seen in polymer science, allowing the creation of polyrotaxanes (mechanically interlocked molecular structures consisting of linear polymers encircled by macrocyclic hosts which are prevented from dissociating by bulky end groups) and polypseudorotaxanes (polyrotaxanes without the bulky end groups),[18-20] catenanes[21] and polycatenanes (molecules which consist of two (catenanes) or more (polycatenanes) interlocked rings like links in a chain),[22,23] pseudorotaxane-type supramolecular polymers[24-26] and star, dendritic, graft and block polymer self-assembly from appropriately functionalized macromolecules.[27-29] The search for binding host-guest pairs of increasing strength is an ongoing endeavour in laboratories all over the world.[30-32]

Since the cation-complexing properties of the crown ethers were first discovered in 1967,[33,34] the growth of novel categories of macrocyclic hosts has been one of the most significant subjects in supramolecular chemistry.[35-37] Macrocycles such as cyclodextrins,[38,39] crown ethers,[40] cucurbiturils[41,42] and calixarenes[43,44] have been widely investigated to study their self-assembly features and host-guest interaction arrangement because of their different selectivity characteristics. It has been shown, for example, that calix[4]arene crown ether can selectively bind amino groups with great specificity *via* the macrocyclic cavity-mediated host-guest interactions.[45,46] Some commonly used host molecules are displayed below (Figure 1.1).

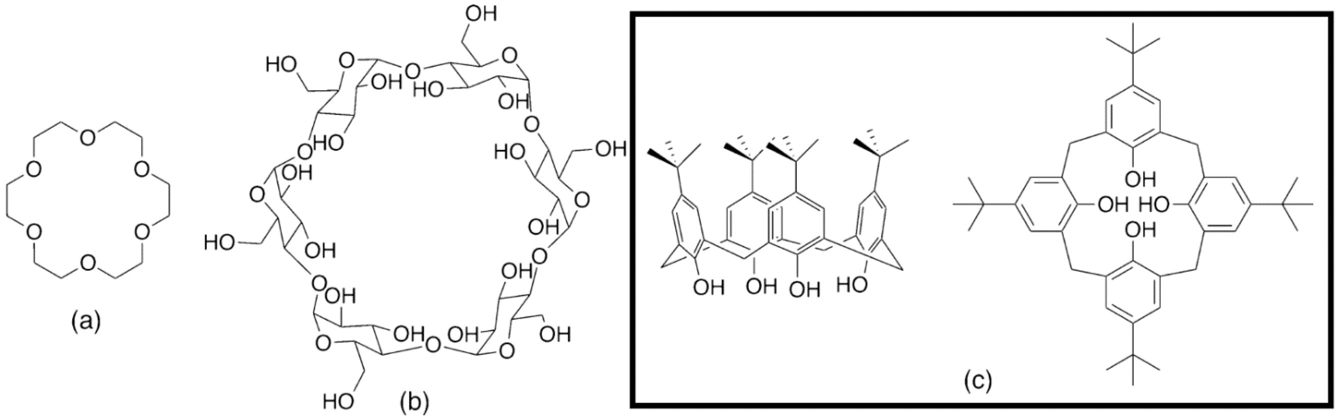

Figure 1.1: Organic host macrocycles in host-guest chemistry: (a) 18-crown-6 (b) α-cyclodextrin (c) *tert*-butylcalix[4]arene (side and top views). Figure adapted from reference number 47 and reproduced with the permission of American Chemical Society (ACS) Publications.

The definition of porosity is an important consideration in the discussion of sorption capabilities of materials. Barbour defined three types of porosity: conventional porosity, porosity ‘without pores’ and virtual porosity.[48] Conventional porosity refers to compounds such as metal-organic frameworks (MOFs) or zeolites, which maintain structural integrity after guest evacuation creating open, unobstructed channels. Permeability is therefore maintained, and the structure remains porous. Porosity ‘without pores’ describes apparently non-porous compounds, for example compounds that either have no voids or have isolated voids, which have been shown to have the ability to adsorb guest molecules. Virtual porosity describes the inappropriate practice of relying only on creating packing diagrams in the stick or ball-and-stick style or on the deletion of guest molecule coordinates and claiming porosity without further experiments.

An important emerging phenomenon in solid-state chemistry is the ability of some molecules to undergo a single-crystal-to-single-crystal (SC-SC) transformation.[49] This refers to a crystal maintaining monocrystallinity after a physical event (for example, a polymorphic transition or desolvation) which causes a change in crystal structure. The single crystal X-ray structure of this different form can therefore be determined by single-crystal X-ray diffraction, yielding possible insight into the mechanism of the transformation. SC-SC transformations are still relatively rare. However, the phenomenon has been increasingly reported in recent times, especially for MOFs. As an example, a thermally-triggered SC-SC transformation has been reported in the complex $[\{bpbp\}Co_2(O_2)\}_2(NH_2bdc)](NO_3)_4 \cdot 7H_2O$ (bpbp = 2,6-bis(*N,N*-bis(2-pyridylmethyl)aminomethyl)-4-*tert*-butylphenolato; NH_2bdc = 2-amino-1,4-benzenedicarboxylato) (Figure 1.2).[50] The oxy form converted into the deoxy form $[\{bpbp\}Co_2(NO_3)\}_2(NH_2bdc)](NO_3)_2 \cdot 2H_2O$ upon heating at 80 °C for about 5 minutes. The deoxy form subsequently reverted to the oxy form upon uptake of a stoichiometric quantity of oxygen. A unique two-step SC-SC transformation has been displayed by a cobalt complex $[Co(hep\text{-}H)(H_2O)_4] \cdot SO_4$ (hep-H = 2-(2-hydroxyethyl)pyridine) (Figure 1.3).[51] Fluorochromism is a change in observed colour of a particular solid or solution. Mechanofluorochromism (MFC) of molecular solids is usually caused by external mechanical forces inducing a change in intermolecular interactions.[52] A unichromophoric anthracene-pentiptycene derivative exhibiting both photomechanofluorochromism (PMFC) and MFC, resulting in different fluorescence colours comprising red-green-blue and near-pure white-light emission, has been reported.[52] This derivative crystallises in two polymorphs, the green and yellow emissive forms. The pairwise stacked anthracene groups within these polymorphs experience [4 + 4] photodimerization to yield a UV black emissive photodimer. This photodimer is generated by a SC-SC transformation (Figure 1.4). This dimer then exerts local photomechanical forces on neighbouring molecules, therefore known as PMFC.

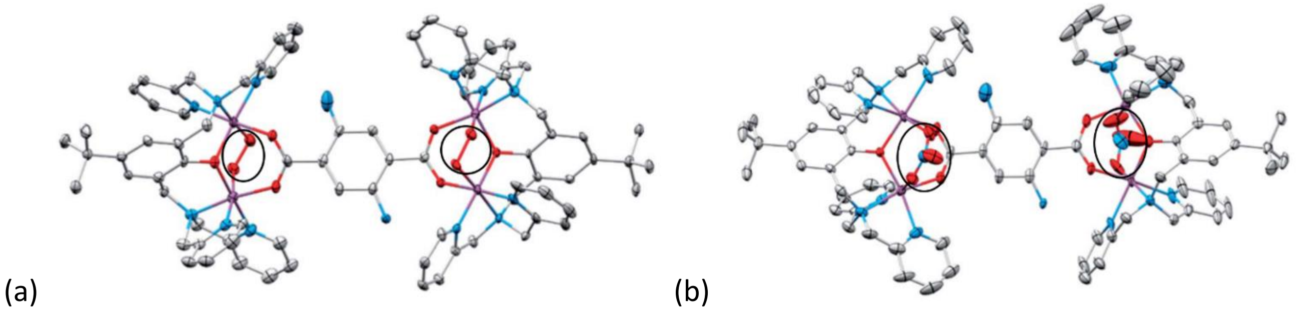

Figure 1.2: Molecular structure of the cations in (a) $[\{bpbp\}Co_2(O_2)\}_2(NH_2bdc)](NO_3)_4{\cdot}7H_2O$ and (b) deoxy $[\{bpbp\}Co_2(NO_3)\}_2(NH_2bdc)](NO_3)_2{\cdot}2H_2O$ complexes. A pair of amine nitrogen atoms are displayed on the 2-aminoterephthalato linker due to disorder over two positions at 50 % occupancy each. Hydrogen atoms are omitted for clarity.[50] Figure reproduced with the permission of the Royal Society of Chemistry (RSC).

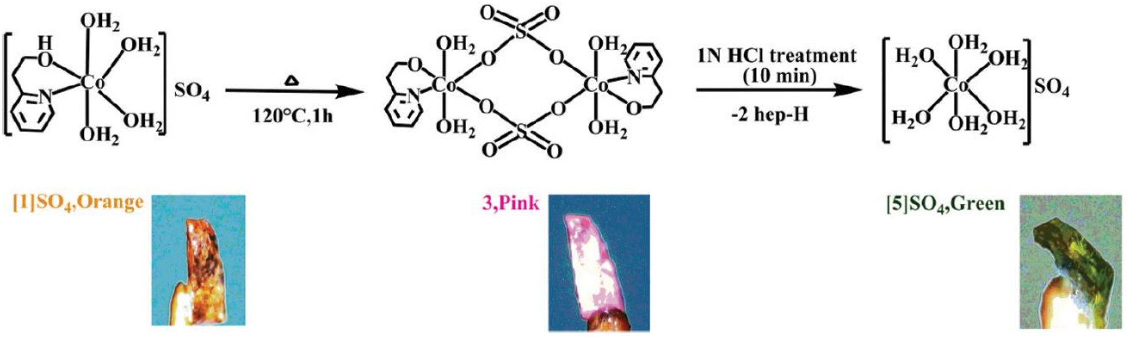

Figure 1.3: Stepwise SC-SC transformations from an ionic monomer to a neutral dimer to another ionic monomer by displacement of the sulfate ion.[51] Figure reproduced with the permission of the RSC.

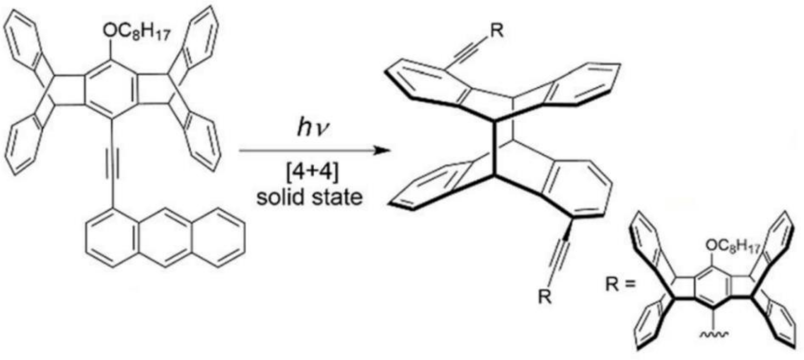

Figure 1.4: Structural formulae of the anthracene-pentiptycene derivative and its photodimer generated by solid-state [4 + 4] photodimerization.[52] Figure reproduced with the permission of the RSC.

A novel inclusion compound, a guanidinium 1,3,5-tri(4-sulfophenyl)benzene (G_3TSPHB) encompassing isophorone guests which enclose apparently inaccessible and isolated voids, has been reported (Figure 1.5).[53] This compound was found to be susceptible to guest exchange with hexafluorobenzene through a SC-SC transformation after exposure to hexafluorobenzene vapour for 1 h. Single-crystal X-ray diffraction of transformation intermediates revealed a crystal system transition from monoclinic to hexagonal before complete guest exchange.

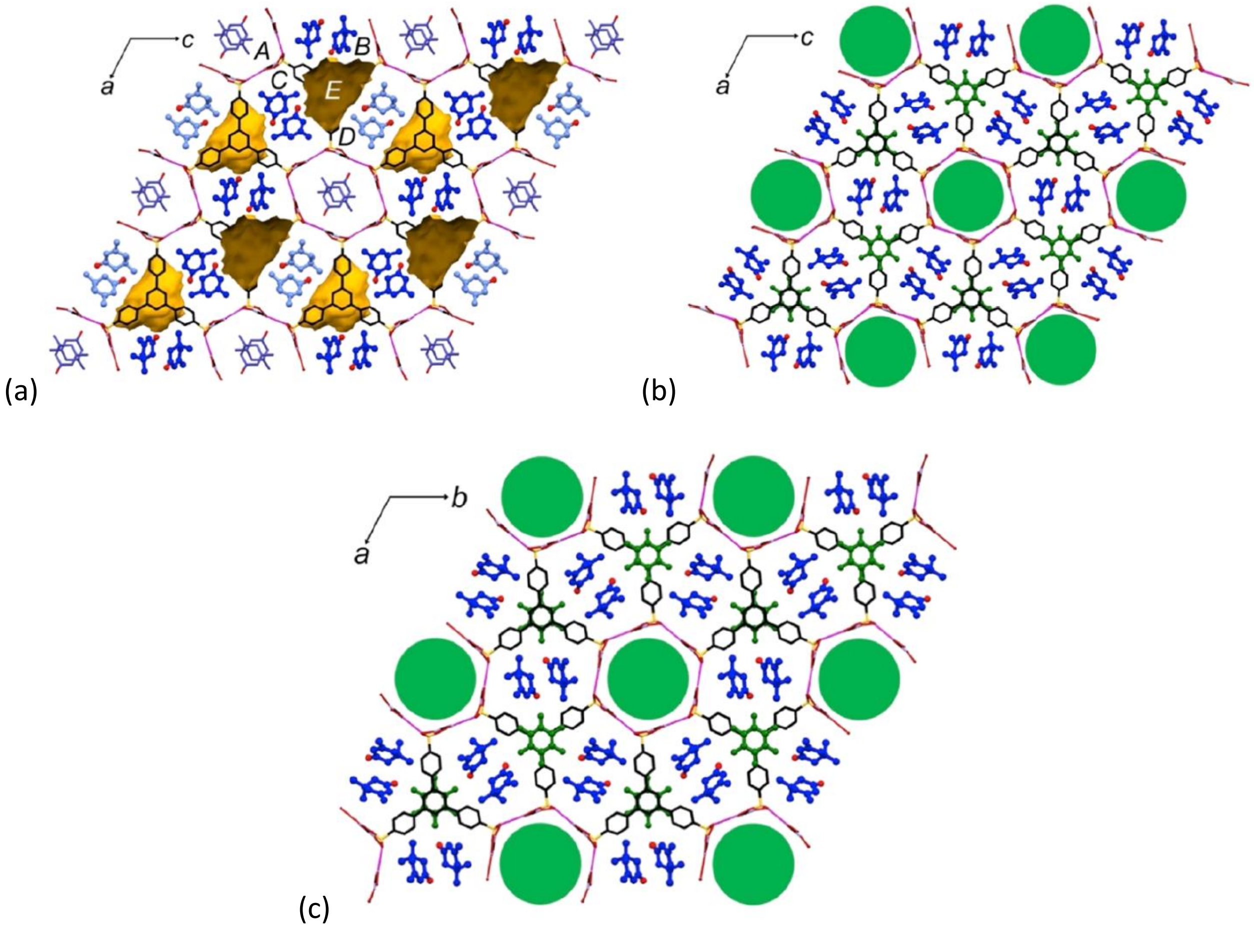

(a) (b)

(c)

Figure 1.5: (a) Crystal structure of the initial G_3TSPHB-isophorone compound, viewed along the irregular guanidinium-sulfonate cylinders (void A), running parallel to the *b*-axis in the $P2_1$ space group, while void E contains severely disordered isophorone molecules which could not be refined (b) Crystal structure of intermediate state, after 8 min. exposure to the vapour of 25 % v/v hexafluorobenzene/hexane solution, viewed along the *b*-axis. The structure still refined optimally as $P2_1$, and the guanidium-sulfonate cylinders are almost hexagonal (c) Crystal structure of the transformed G_3TSPHB-hexafluorobenzene compound, viewed along the hexagonal guanidinium-sulfonate cylinders which run parallel to the *c*-axis. The green circles in (b) and (c) represent completely disordered hexafluorobenzene guest molecules.[53] Figures reproduced with the permission of ACS Publications.

A few other examples of SC-SC transformations in the literature are reported to be those that are solvent exchange-induced,[54] ion exchange-induced[55,56] and light-induced.[57,58]

1.1. Host Compounds

1.1.1. Calixarenes

Calixarene is a general name given to a class of macrocyclic molecules comprising phenolic units linked by methylene bridges. The name 'calixarene' originated from the Greek word 'calix' meaning 'chalice' and 'arene' due to the arene rings which are components of the molecule.[59] They were first discovered in 1872 when Adolph von Baeyer presented the preparation of calixarenes as products of the reaction of aldehydes with phenols in the presence of strong acid.[60] Baekeland then patented a procedure in which a minor quantity of base was utilized to produce resinous compounds he called Bakelite at the start of the twentieth century.[61] However, the structural features of the Bakelite were uncertain until the mid-1940s to early 1950s, when a tetrameric cyclic structure was suggested for the product of the base-catalyzed condensation of formaldehyde and *p-tert*-butylphenol.[62,63] In the late 1970s, these formaldehyde phenol products were given the name 'calixarenes'.[64] The present IUPAC nomenclature for calixarenes is as follows: a number in brackets, *n*, situated between calix and arene shows how many phenolic units are connected by methylene bridges to constitute the macrocycle of the molecule. Appropriate prefixes describe substitution on the aromatic rings, e.g. *p-tert*-butylcalix[4]arene, which has tertiary butyl groups in the *para*-position on each phenolic ring. Calixarenes consisting of four, six or eight phenolic units can be easily synthesized in high yields with exceptional purity. The calixarene frame has a distinct hollow with potentially different polarities on the lower edge and the upper edge, depending on the functionalization of these edges. They can also be tailored with respect to functional group and cavity size to produce selective hosts. Calixarene chemistry has grown into a crucial branch of supramolecular chemistry since the 1970s.[65-67] They comprise a category of molecules with different and rare characteristics that are the subjects of widespread research. This is due to their adaptable molecular recognition characteristics, exceptional void and conformational structures, and wide availability.[68-70] Calixarenes and their substituted analogues have been utilized for the recognition of organic molecules, neutral compounds, anions and cations.[71-73] Calixarenes are also extremely prevalent in chromatography as stationary phases or in sorption applications as sorbent because of their reversible interactions with various types of guest molecules.[74] Several examples of calixarenes are displayed below (Figure 1.6).

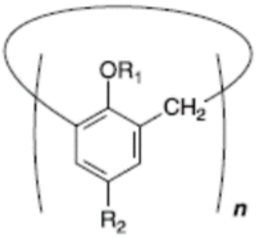

1 n=4; R_1 = H; R_2 = *t*-Bu
2 n=8; R_1 = $(CH_2)_3SO_3Na$; R_2 = H
3 n=8; R_1 = H; *t*-Bu

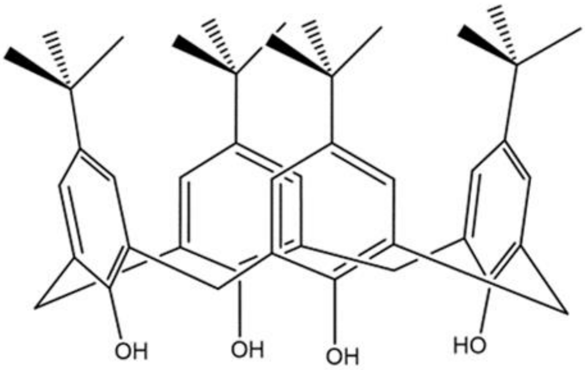

1

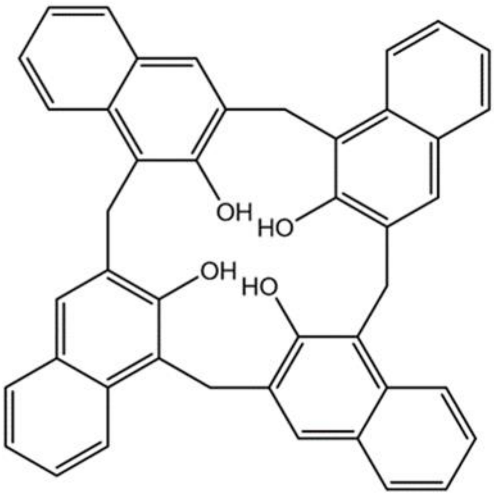

4

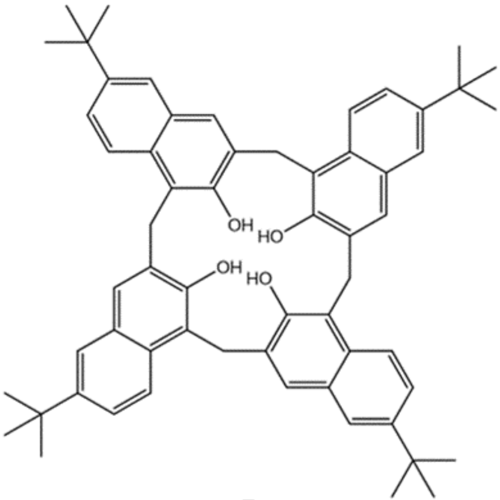

5

Figure 1.6: Structures of several calixarenes (**1** – *p*-*tert*-butylcalix[4]arene, **2** – octasodium *p*-3-sulfonatopropylcalix[8]arene, **3** – *p*-*tert*-butylcalix[8]arene, **4** – calix[4]naphthalene, **5** – *tert*-butylcalix[4]naphthalene).

In 1992, it was shown that the water-soluble calix[8]arene derivative **2** (Figure 1.6) was able to extract C_{60} into an aqueous phase.[75] In addition, it was then found that *p*-*tert*-butylcalix[8]arene (**3** – Figure 1.6) could preferentially isolate C_{60} from a solution containing C_{60} and C_{70} in toluene.[76,77] This was achieved by forming a 1:1 complex with C_{60}. Efforts to crystallise this complex from chloroform led to de-complexation, yielding pure C_{60}. This and several other discoveries resulted in widespread research of the interactions between numerous other calixarenes and calixarene derivatives with fullerenes.[78]

1.1.2. Calix[n]resorcinarenes

Resorcinarenes (Figure 1.7), a subgroup of calixarenes formed from the condensation of 1,3-dihydroxybenzene and an aldehyde, have also attracted much attention over the last twenty years, playing a vital role in supramolecular chemistry owing to their structural characteristics, making them versatile host molecules for the encapsulation of different guest molecules. They have been shown to encapsulate sugars[79-81] and alcohols,[82,83] methylammonium compounds[84-86] (especially acetylcholine[87-89]) and alkali metal cations.[90,91] They have also been used as ion tunnels[92] and as surfactants on gold[93-95] and thin films.[96-98]

Distinct spherical molecular structures formed by spontaneous self-assembly routes are prevalent in nature. Spherical fullerenes[99] and viruses[100] are examples in which covalent and non-covalent forces, respectively, guide the formation of smaller subunits into larger assemblies. Nature employs the concepts of supramolecular chemistry, enabling biological processes to utilize noncovalent interactions, for example hydrogen bonds which hold together the DNA double helix. The assembly of intricate synthetic structures in both the solid state and solution is becoming increasingly possible. This generally means that known structures must be studied, modelled and honed to create further structures of greater intricacy. These include the preparation of spherical, self-assembled molecular capsules. A shared characteristic of these molecular cages is their capability to trap charged and/or neutral guests whose chemical properties, shape and size match those of the inner surface of the host.[101-103] These assemblies have possible uses as mimics of biological systems, nanoreactors, van der Waals catalysts and drug delivery agents. These characteristics have led to the new appearance of monomolecular[104-106] and dimeric capsules,[107,108] most

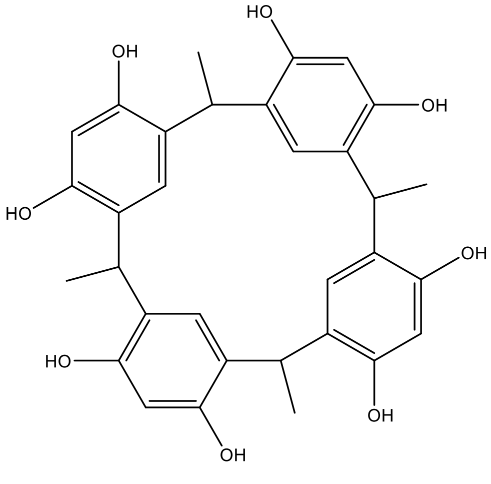

Figure 1.7: An example of a resorcinarene – in this case, *C*-methylcalix[4]resorcinarene.

of which are formed because of the head-to-head arrangement of multi-aromatic, bowl-shaped host molecules such as calix[4]arenes.[104,106,108] However, genuine structural imitation of naturally-occurring assemblies, based on the self-assembly of more than three host molecules, continues to be elusive. These spherical assemblies are usually highly symmetrical and regularly take the form of Archimedean or Platonic solids. As an example of a large supramolecular assembly in nature, 180 indistinguishable protein subunits amassed into an icosahedron forms the cowpea chlorotic mottle virus (Figure 1.8). The general conformation of the viron changes with pH, resulting in holes in the outer shell, therefore permitting the migration of molecular matter between the exterior and interior of the viron.[109] While obtaining similar manipulation over the composition, conformation and size of synthetic supramolecular structures is a difficult task, developments have occurred in manipulating both the composition and volume of interior chemical space within the hydrogen bonding-assembled hexameric spheres from pyrogallol[4]arenes[110-112] or resorcin[4]arenes.[113-114] These molecular assemblies are positioned so that the centroids of the six host molecules can be imagined to be located on the faces of a cube, but can also be described as positioned on the vertices of an octahedron, with the pattern of the hydrogen bonding symbolizing the small rhombicuboctahedron and the snub cube, respectively.[115]

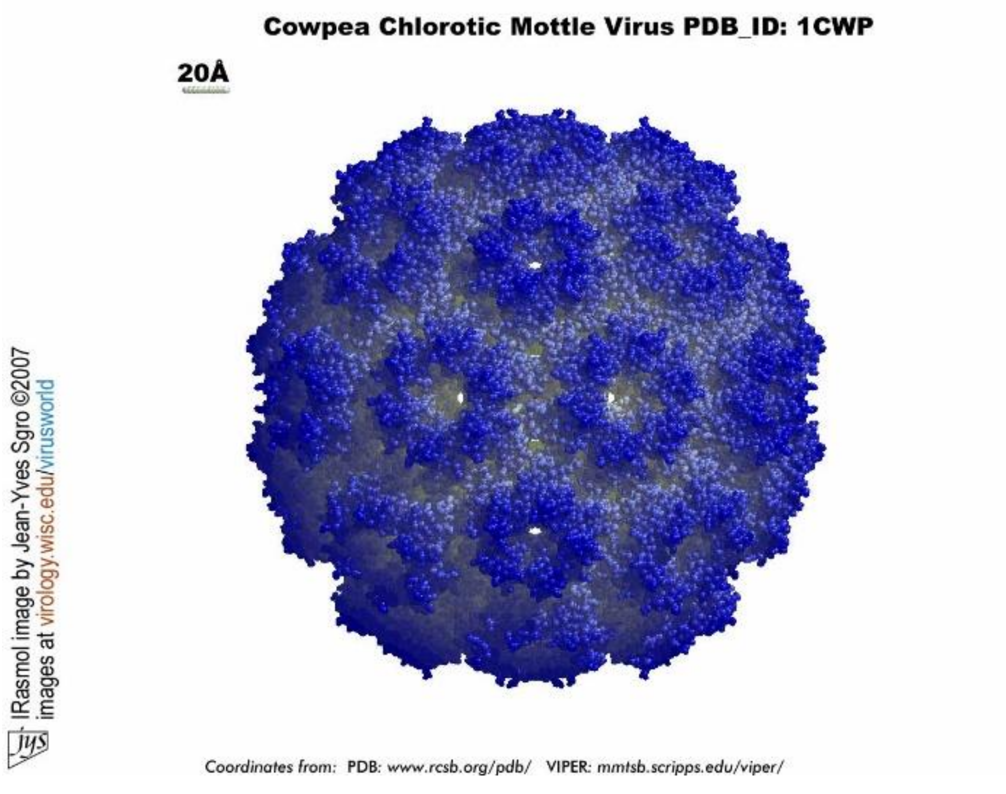

Figure 1.8: The cowpea chlorotic mottle virus. (http://www.virology.wisc.edu/virusworld/images/ccmv-ictv9style-blue.jpg)

1.1.3. Heterocalixaromatics

Fascination with heterocalixaromatics has developed quickly in recent times.[116] Heterocalixaromatics consist of aromatic rings linked by heteroatoms (Figure 1.9), as opposed to regular calixarenes in which the aromatic rings are linked by methylene bridges. The first amine-bridged and oxygen-bridged calix[4]arenes date back to the 1960s.[117,118] However, in the subsequent five decades, they have not drawn interest from the organic chemistry community, probably due to the difficulties of their preparation.[117,118] Yet in recent times, significant advancements in the synthesis of these compounds have been made,[119-121] opening the way for the study of the supramolecular chemistry of these hosts.

The different steric and electronic properties of the heteroatoms result in essentially novel types of macrocyclic hosts. Increasing efforts are being made to derivatize simple calixarene frames.[122-124] One of the relatively new advancements in this area is the synthesis of novel calixarenes by substituting their phenol moieties with other heteroarene units such as pyridine, enabling the adjustment of their voids to improve their selectivities towards different molecular guests.[116] The different characteristics of varied heterocalixaromatics include the molecular recognition features and exciting structures that are controlled by the bridging heteroatoms. This has led to several fascinating macrocycles, for example calixpyridines,[68,125,126] calixpyrroles,[69,127,128] and other calixheteroaromatics (Figure 1.10).[68-70] Calixpyrroles have been demonstrated to be strong anion receptors.

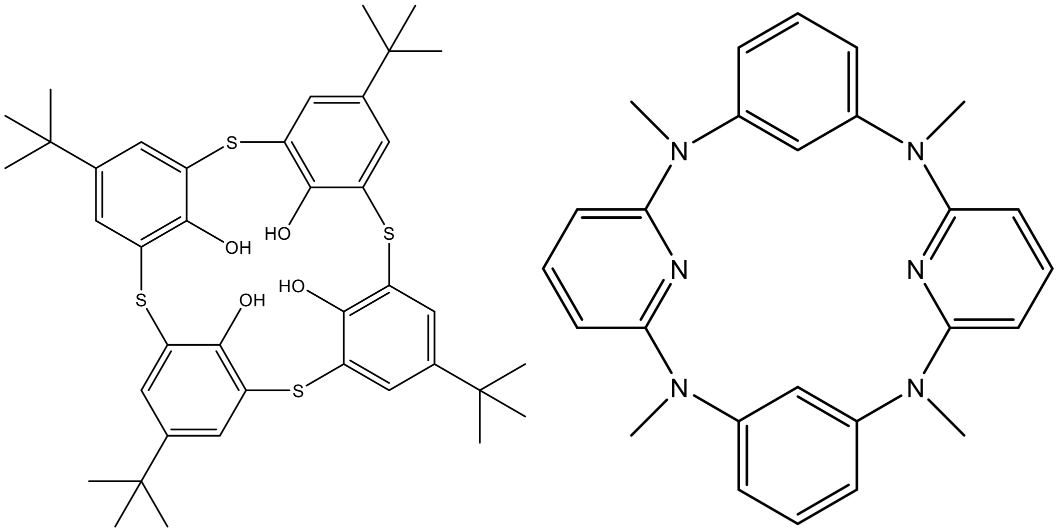

Figure 1.9: Two examples of heterocalixaromatics synthesized in (a) 1997 (*p-tert*-butylthiacalix[4]arene) and (b) 2004 (an azacalix[2]arene[2]pyridine).[119,121]

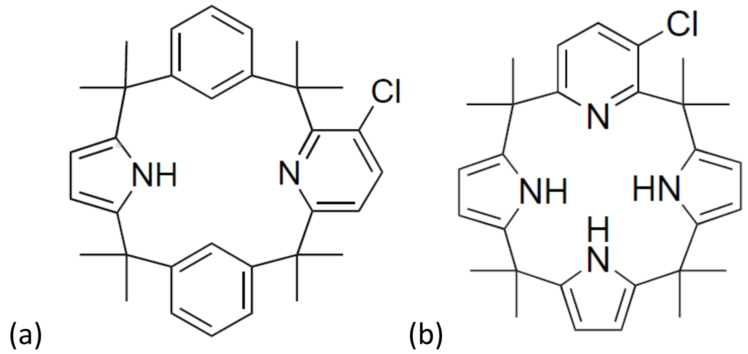

Figure 1.10: Structural formulae of (a) a chloro-substituted calix[2]benzene[1]pyridine[1]pyrrole and (b) a chloro-substituted calix[1]pyridine[3]pyrrole.[68] Figures reproduced with the permission of John Wiley & Sons.

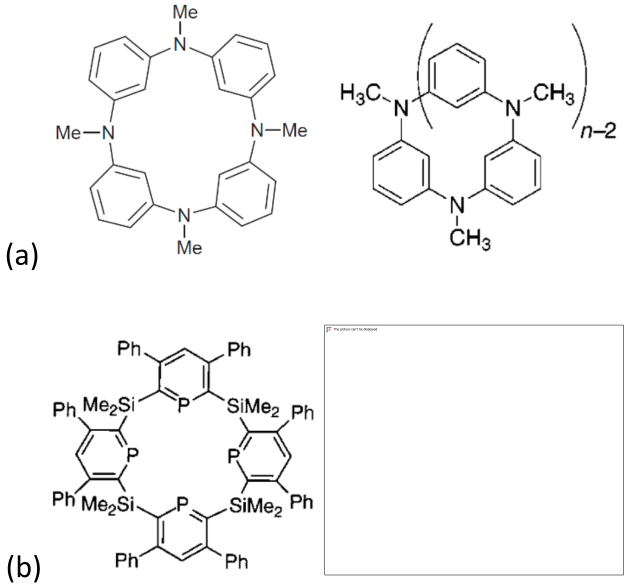

Figure 1.11: (a) The molecular structures of various azacalix[*n*]arenes (where 3 ≤ *n* ≤ 8).[130,131] (b) The structures of the silicon-bridged calix[*n*]phosphaarenes.[134] Figures reproduced with permissions of the RSC, ACS Publications and the American Association for the Advancement of Science.

Reaction of 1,3-dihydroxybenzene with 1,3-difluoro-4,6-dinitrobenzene formed a tetranitro-substituted tetraoxocalix[4]arene in a low yield,[129] while both the Pd^0-catalyzed condensation of benzene-1,3-diamine and 1,3-dibromobenzene derivatives and the Pd^{II}-catalyzed cyclic oligomerization of 3-bromo-*N*-methylaniline resulted in extremely low yields of combinations of azacalix[*n*]arenes (*n* = 3-8) (Figure 1.11).[120,130,131] The coupling of 1,3-dibromobenzene or phenol with dichlorodimethylsilane has resulted in silicon-bridged calixarenes in low yields,[132,133] and several heteroatom-bridged calixheteroaromatics have been synthesized by including new heteroatoms into heteroaromatics.[116] An example is the silicon-bridged calix[*n*]phosphaarenes, which behave as ligands with powerful π-acceptor characteristics (Figure 1.11).[134,135] However, extremely poor, and hence non-viable, yields were obtained in nearly all cases for heteroatom-bridged macrocyclic hosts.[132-134]

Meticulous manipulation over intricate chemical structures by the use of an external stimulus warrants attention because of possible uses in adaptive and useful smart materials, such as self-healing materials[136-138] and drug-delivery systems.[139-141] Supramolecular methods manipulate the reversible character of noncovalent forces and have been particularly valuable in the preparation of responsive and self-assembled compounds. Structures that react to ions or guest molecules,[142-144] heat[145,146] or light[147,148] have been discovered. Especially exciting are compounds that rely on highly-ordered, predictable forces,[149] as these generally deliver superior consistency in terms of self-assembly in addition to a greater quantity of stimuli that can be employed to manipulate the structure. Several instances of self-assembled compounds made *via* these highly-ordered, predictable noncovalent forces have been reported.[150,151] However, oligomeric structures formed from heteroditopic monomers which show stimuli-responsive molecular switching action have not yet been discovered. These structures may permit a degree of stimulus-based manipulation that is hitherto unseen. Recently, it was discovered that anion-bound tetrathiafulvalene-annulated calix[4]pyrroles are capable of forming 1:1 complexes with $Li@C_{60}$, C_{60} or C_{70}, where the fullerene is fixed *via* charge-transfer interactions in the bowl-like pouches of the calix[4]pyrroles in both the solid state and in solution.[152,153] These complexes do not form without the anions, and are unstable in the presence of competitive guests. Typically, calix[4]pyrroles assume the thermodynamically more stable 1,3-alternate conformation in noncompeting solvents, without a coordinating anion. However, addition of a coordinating anion causes a change to the cone-like anion-bound conformers.[154] The fullerene-calix[4]pyrrole complexes are therefore the result of a precise molecular switching procedure, where an anion salt with a noncompetitive countercation is employed to generate the structure appropriate for C_{60} binding. Therefore, if these calix[4]pyrroles are combined with an appropriately anion-functionalized fullerene, they could be utilized to generate a novel division of stimulus-responsive compounds whose purpose might be manipulated *via* conformational switching at the monomer level.

1.1.4. Spherical Assemblies

In 1997, a significant advance was made in small-molecule supramolecular chemistry by increasing the number of chemical entities which enclose chemical space, i.e. where guest is completely surrounded by host molecules, when MacGillivray and Atwood discovered a spherical molecular assembly made up of 6 *C*-methylcalix[4]resorcinarene (CMCR) molecules and 8 water molecules held together by sixty O–H···O hydrogen bonds (Figure 1.12).[113] It self-assembles and maintains its arrangement in nonpolar solvents and encapsulates guest molecules inside a distinct void. The electron density maxima suggested that guest molecules are located inside the cavity, although their identity could not be determined due to the high degree of disorder imposed by the high symmetry of the assembly. The interior void volume was determined to be approximately 1 400 Å^3, which represented a four-fold increase in interior volume over the previous largest assemblies.[107] The structure displays 432 (*O*) point group symmetry and is chiral.

CMCR has been subsequently shown to assemble in a similar fashion with 6 (±)-2-ethylhexanol molecules and 2 water molecules as an assembly made up of 58 O–H···O hydrogen bonds which traps three 2-ethylhexanol molecules within the cavity, as indicated by NMR, TGA and elemental analysis data (Figure 1.13).[155] The size of the cavity of this assembly is approximately 1 290 Å^3. This assembly has S_6 point group symmetry and is achiral, as dictated by the point group symmetry. A major structural difference between the Atwood and Holman assemblies is that opposing CMCR molecules are staggered in the former and eclipsed in the latter.

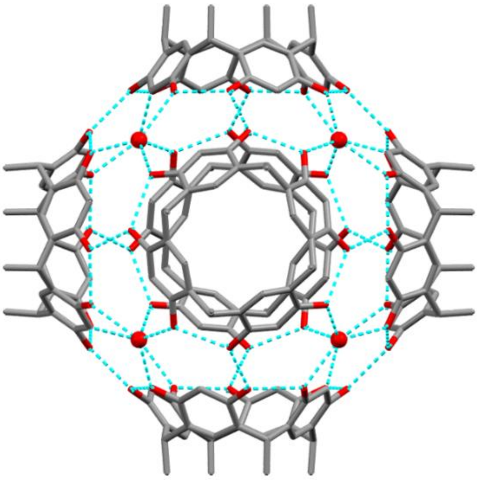

Figure 1.12: The spherical assembly consisting of CMCR and water molecules (shown as red spheres). Hydrogen bonds are shown in blue and hydrogen atoms have been omitted for clarity.[113]

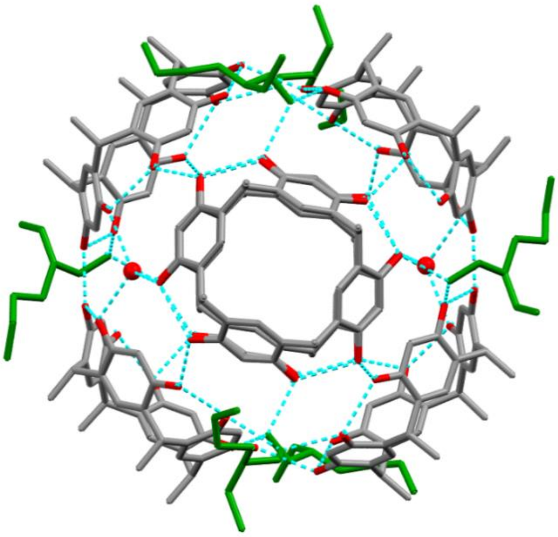

Figure 1.13: The CMCR-2-ethylhexanol-water assembly as observed in the single crystal X-ray structure. The water molecules are displayed as red spheres and the 2-ethylhexanol molecules are shown in green. Hydrogen atoms and minor components of disordered 2-ethylhexanol guests are omitted for clarity.[155]

It has also been found that it is feasible to manipulate the characteristic symmetry of the spherical assembly made up of *p*-sulfonatocalix[4]arene host molecules.[115] These host molecules usually favour the infinite bilayer arrangement, where neighbouring calixarenes are positioned 'up-down' relative to each other.[156] A search of the Cambridge Structural Database (5 August 2019) reveals 120 structures containing *p*-sulfonatocalix[4]arene, of which 9 have no 3D coordinates. Of the remaining 111, the vast majority contain the 'up-down' bilayer motif. However, under controlled conditions in a ternary system using pyridine *N*-oxide, a lanthanide(III) nitrate salt and pentasodium *p*-sulfonatocalix[4]arene, it was possible to cause 'up-up' packing of the calixarenes, imparting considerable curvature to the overall packing, leading to the generation of either tubular or spherical assemblies.[157,158] The spherical assembly is made up of twelve calixarenes positioned at the vertices of an icosahedron (Figure 1.14). These assemblies do not form a close-packed arrangement in the broader structure as icosahedra cannot pack densely in three dimensions by sharing faces, edges or vertices. However, the replacement of pyridine *N*-oxide with 18-crown-6 in the above system leads to the formation of a significantly different spherical assembly and therefore a much more closely-packed overall structure.

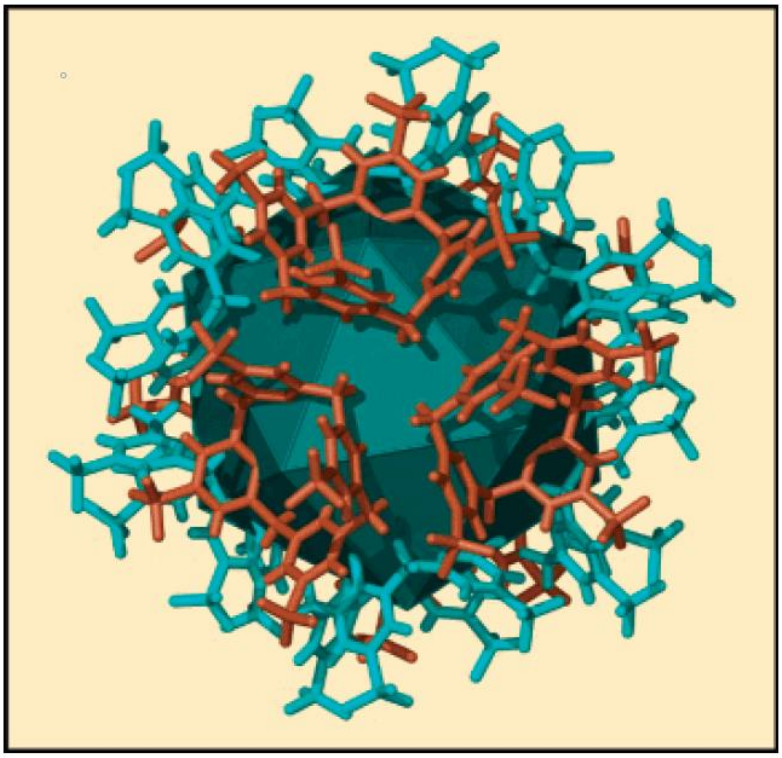

Figure 1.14: Spherical assembly generated by the aggregation of twelve *p*-sulfonatocalix[4]arene molecules. The twelve *p*-sulfonatocalix[4]arene molecules are situated at the vertices of an icosahedron. The crystallographically equivalent calixarenes are shown in blue (six around the middle of the sphere) and orange (three in the front and three at the back).[115] Figure reproduced with the permission of ACS Publications.

This spherical assembly is made up of twelve calixarenes positioned at the vertices of a cuboctahedron (Figure 1.15). This assembly can appear as either a Platonic icosahedral or an Archimedean cuboctahedron arrangement. This difference is attributed to the restraint on adjacent calixarenes of neighbouring assemblies by their shared 18-crown-6 guest molecules. A discrete spherical assembly made up of twelve *p*-sulfonatocalix[4]arene molecules would favour positioning of the calixarenes at the vertices of an icosahedron. However, when the assemblies are positioned to generate a three-dimensional crystal, either hexagonal or cubic close-packed arrangements of the assemblies should be favoured. Therefore, the long-range structure packs such that the assemblies are positioned along vectors symbolizing the vertices of an Archimedean cuboctahedron. The Archimedean solid results in a substantial 30 % increase in the volume of the cavity (975 Å^3 to 1 258 Å^3).

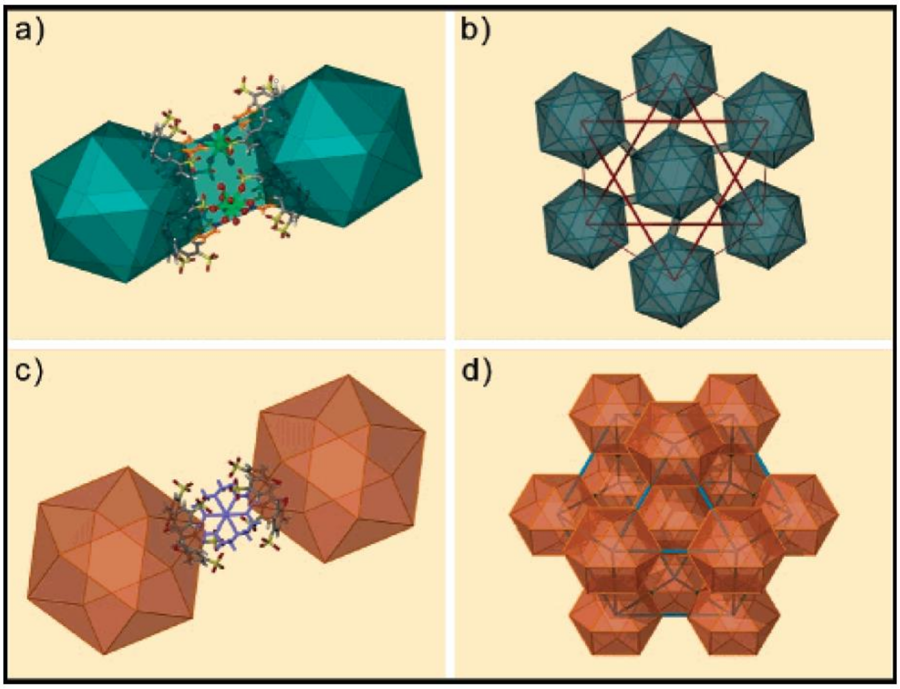

Figure 1.15: Contrast between the icosahedral (a & b) and cuboctahedral (c & d) arrangements of *p*-sulfonatocalix[4]arene molecules.[115] Figure reproduced with the permission of ACS Publications.

Twelve molecules of β-carbonyl-*para*-octyl-calix[4]arene have been shown to form aggregates which pack in a cubic structure and which have two types of cavities occupied by water molecules (Figure 1.16).[159] The packing and the aggregates both resemble inverse micelles. This was the first occasion that a structure of an assembly resembling an inverse micelle has been observed at the atomic level. The C–H···O intermolecular forces of the β-carbonyl in addition to the rigid calix[4]arene frame appear to be the main contributors to the overall structure.

Several metal analogues of hexameric assemblies have also been prepared. One of these is a discrete, neutral, large pseudo-spherical coordination assembly formed from 24 Cu(II) ions and 6 pyrogallol[4]arene ligands (Figure 1.17),[160] which is similar to its hydrogen-bonded pyrogallol[4]arene analogue, and has a void space of approximately 1 200 Å^3, which is a very similar volume to that enclosed by its hydrogen-bonded analogue.

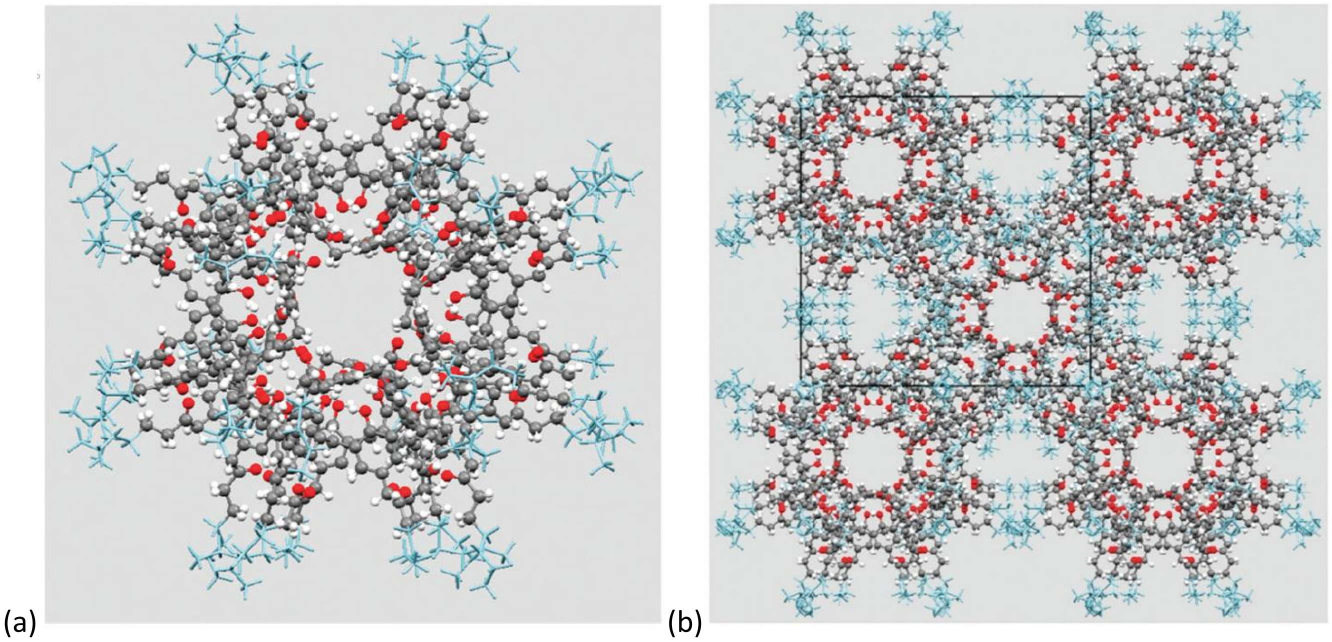

Figure 1.16: (a) The twelve-molecule assembly of β-carbonyl-*para*-octyl-calix[4]arene in the ball-and-stick style, with the disordered components of the hydrocarbon chains displayed in the stick style in light blue (b) Packing of the aggregates of β-carbonyl-*para*-octyl-calix[4]arene in the cubic crystal, shown in the ball-and-stick style, with disordered components of the hydrocarbon chains shown in the stick style in light blue with one set of unit cell axes also displayed. The large voids seemingly apparent in the disordered areas are in reality much smaller as they are partially occupied by disordered chains from the layers below and above.[159] Figure reproduced with the permission of the RSC.

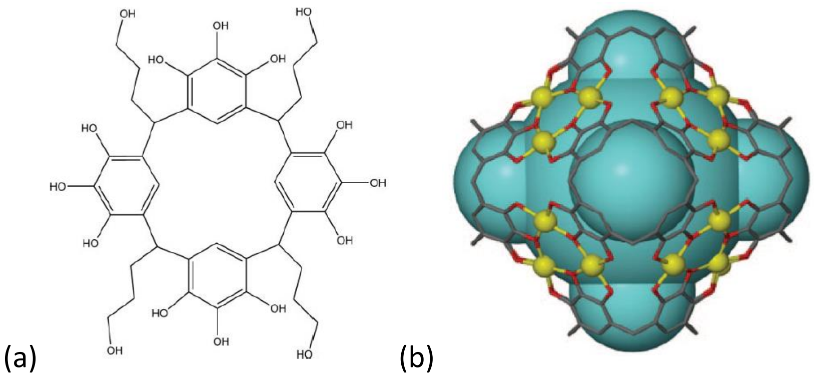

Figure 1.17: (a) Structural formula of *C*-propan-3-ol pyrogallol[4]arene ligand (b) Stick bond depiction of the hexameric coordination capsule displaying the metal-mediated self-assembly of 24 Cu(II) ions and 6 pyrogallol[4]arenes. Axial copper-coordinated water molecules, hydrogen atoms and alkyl tails have been removed for clarity. Copper ions are depicted as yellow spheres.[160] Figures reproduced with the permission of the Proceeding of the National Academy of Sciences, U.S.A. Copyright (2005) National Academy of Sciences, U.S.A.

In another study, both Cu(II) and Ni(II) ions were employed with *C*-methylpyrogallol[4]arene to produce dimeric and hexameric structures (Figure 1.18).[161] The pyrogallol[4]arene macrocycles act as chelates for

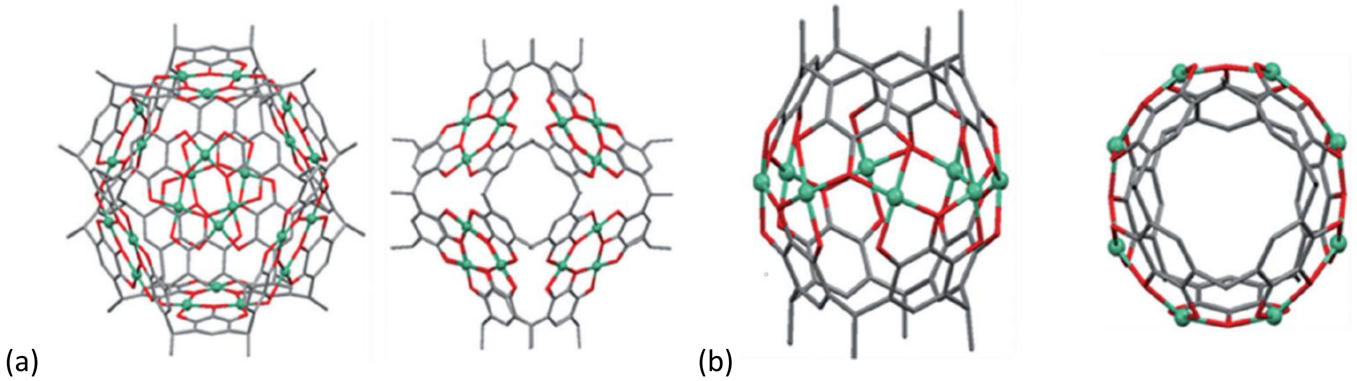

Figure 1.18: (a) The pyrogallol[4]arene nickel hexamer viewed from two different angles (b) Side (left) and top (right) views of the pyrogallol[4]arene nickel dimeric capsule. Green spheres represent nickel ions.[161] Figure reproduced with the permission of John Wiley & Sons.

eight, twelve or twenty-four metal ions. It was concluded that the dimeric structures are formed preferentially in solution at high temperatures in methanol as opposed to acetonitrile and with nickel as the metal ion.

The fluorescent probe molecule pyrene butyric acid (PBA) has been used as a guest molecule in *C*-hexylpyrogallol[4]arene assemblies held together by O–H···O hydrogen bonds in order to examine the environment within the cavity of the assemblies (Figure 1.19).[162] It was established that in both the solid state and solution, the assemblies trap two PBA guest molecules. Furthermore, it has been shown that a small structural change in the host molecules can have significant effects on the interactions between assemblies and the broader crystal packing.[103] These interactions between assemblies are then translated through the assembly walls to the cavity within.

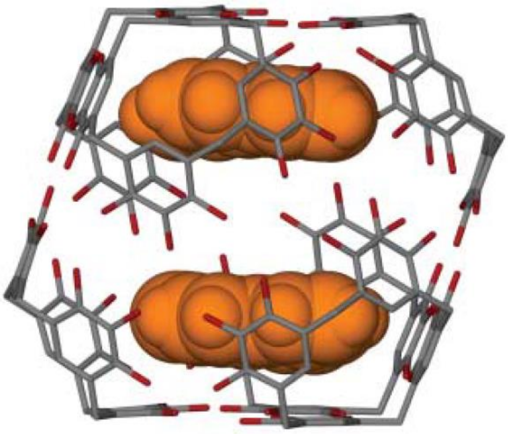

Figure 1.19: Diagram of the crystal structure of the *C*-hexylpyrogallol[4]arene assembly displaying the orange space-filling representations of the resolved pyrene moieties within the assembly. The butyric acid side chains of the PBA guest (not displayed), and possibly acetonitrile solvent molecules, take up the remaining void space.[162] Figure reproduced with the permission of the American Association for the Advancement of Science.

1.1.5. Cyclotriveratrylene

Cyclotriveratrylene (CTV), cyclic trimers of veratrole, are supramolecular, bowl-shaped, molecular hosts able to bind organometallic and organic guest molecules within a molecular hollow.[163-166] CTV (Figure 1.20) is a macrocyclic molecule which exhibits a crown-like structure with a shallow molecular cavity and a pyramidal shape with the aromatic rings forming the three faces of the pyramid and the methylene groups positioned at the apices of the pyramid.[167-169]

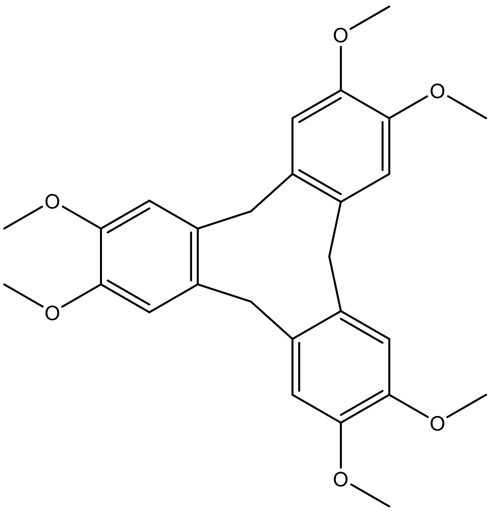

Figure 1.20: The structural formula of CTV.

Interest in modified CTVs has developed since their discovery by Collet *et al.* in the early 1980s.[170] Molecules based on CTV have served a wide range of purposes in both supramolecular chemistry and soft materials.[163] CTV and related molecules have been used as precursors for cryptophanes and cavitands, and as components in coordination and self-assembled supramolecular systems.[163,171,172] For example, CTV and its analogues have been widely examined for their binding with smaller organic and organometallic guests.[173-175] Their ability to host guests such as C_{60} and anionic C_{70} dimers, lanthanides and xenon has led to the growth of functionalized CTV derivatives for biomedical applications like MRI-based diagnostic techniques and the distribution of fullerenes as cytotoxic anti-tumour agents.[176-178] Molecules based on CTV have also been utilized as components of cage-type, discrete, metallo-supramolecular assemblies, such as assemblies of triply interlocking cage-catenane species,[179,180] a self-entangled Solomon's cube[181] and coordination polymers.

One of the triply-interlocking cage-catenane species that has been reported consists of a CTV-related host molecule, (±)-2,7,12-trimethoxy-3,8,13-tris(4-[4'-methyl-2,2'-bipyridyl]benzyloxy)-10,15-dihydro-5*H*-tribenzo[*a,d,g*]cyclononane (TTDT) in the compounds $[M_3(TTDT)_2(NO_3)_3]_2^{6+}$ where M = Co(II) or Zn(II) (Figure 1.21).[179] The self-assembly of these [2]catenanes showed that these motifs could be obtained by 3D symmetrical metallo-supramolecular assemblies in which strong π-π stacking interactions between ligands are not necessarily required.

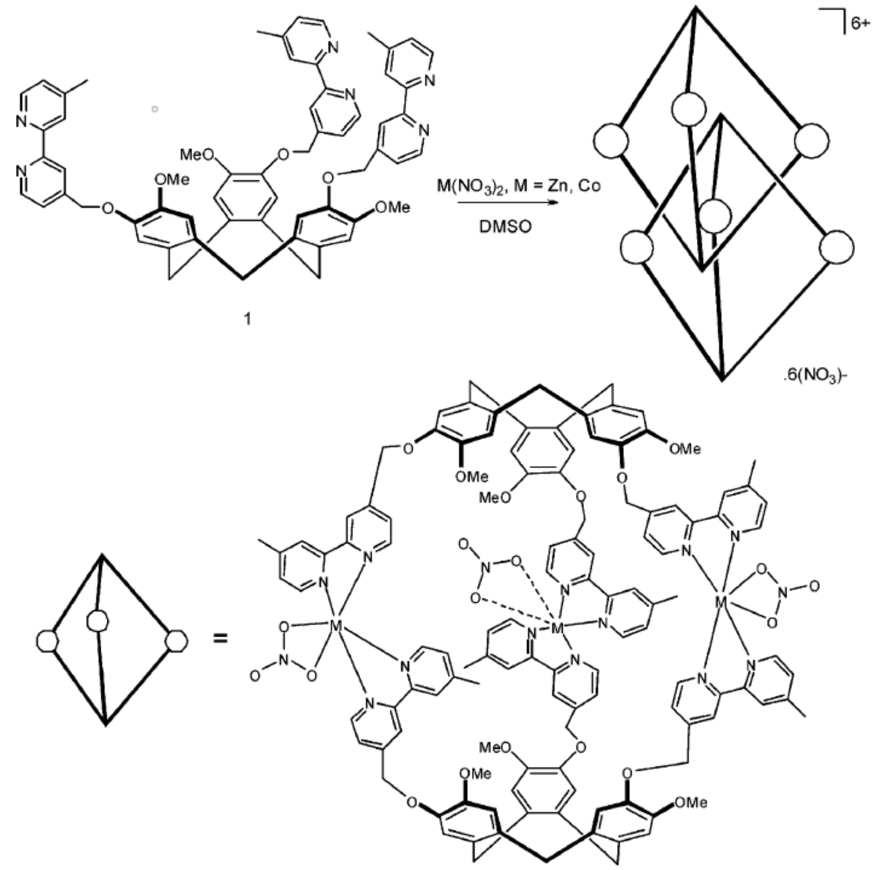

Figure 1.21: Self-assembly of the [2]catenane species.[179] Figure reproduced with the permission of ACS Publications.

The self-assembly of a $[Pd_6(\text{tris(isonicotinoyl)cyclotriguaiacylene})_8]^{12+}$ stella octangula complex has also been shown (Figure 1.22).[182]

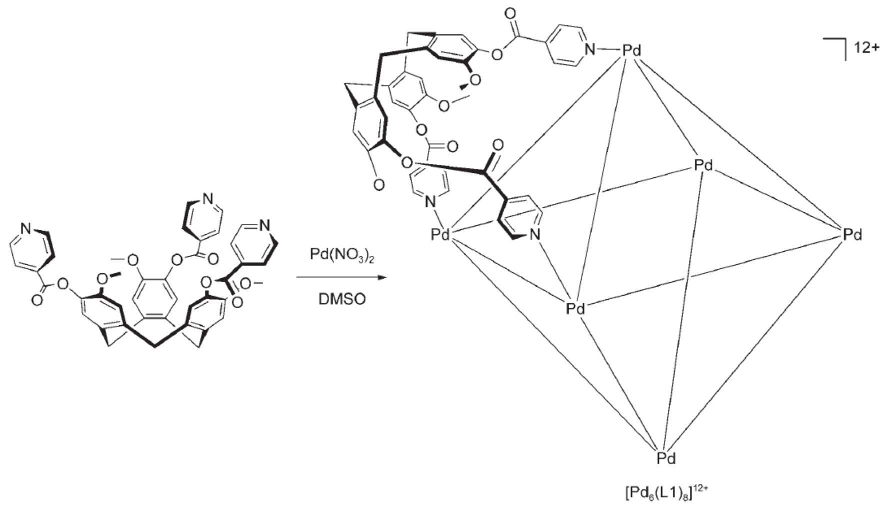

Figure 1.22: Self-assembly of the $[Pd_6(\text{tris(isonicotinoyl)cyclotriguaiacylene})_8]^{12+}$ cage.[182] Figure reproduced with the permission of John Wiley & Sons.

CTV and 1,2-dicarbadodecaborane(12) (*o*-carborane) have been shown to self-assemble into infinite arrays with helical chain or 2D hexagonal grid topologies through bifurcated $\mathrm{C–H_{carborane}\cdots(O)_2}$ hydrogen bonding (Figure 1.23).[183] The built-in receptor sites display shape-specific recognition for fullerene C_{70} or *o*-carborane. A helical hydrogen-bonded carborane···CTV chain is formed in the structure (1,2-dichlorobenzene)(CTV)(*o*-carborane)(C_{70}) along with CTV···C_{70} host-guest interactions, while (CTV)(*o*-carborane)$_2$ displays hydrogen-bonded carborane···CTV hexagonal grids along with CTV···carborane host-guest interactions.

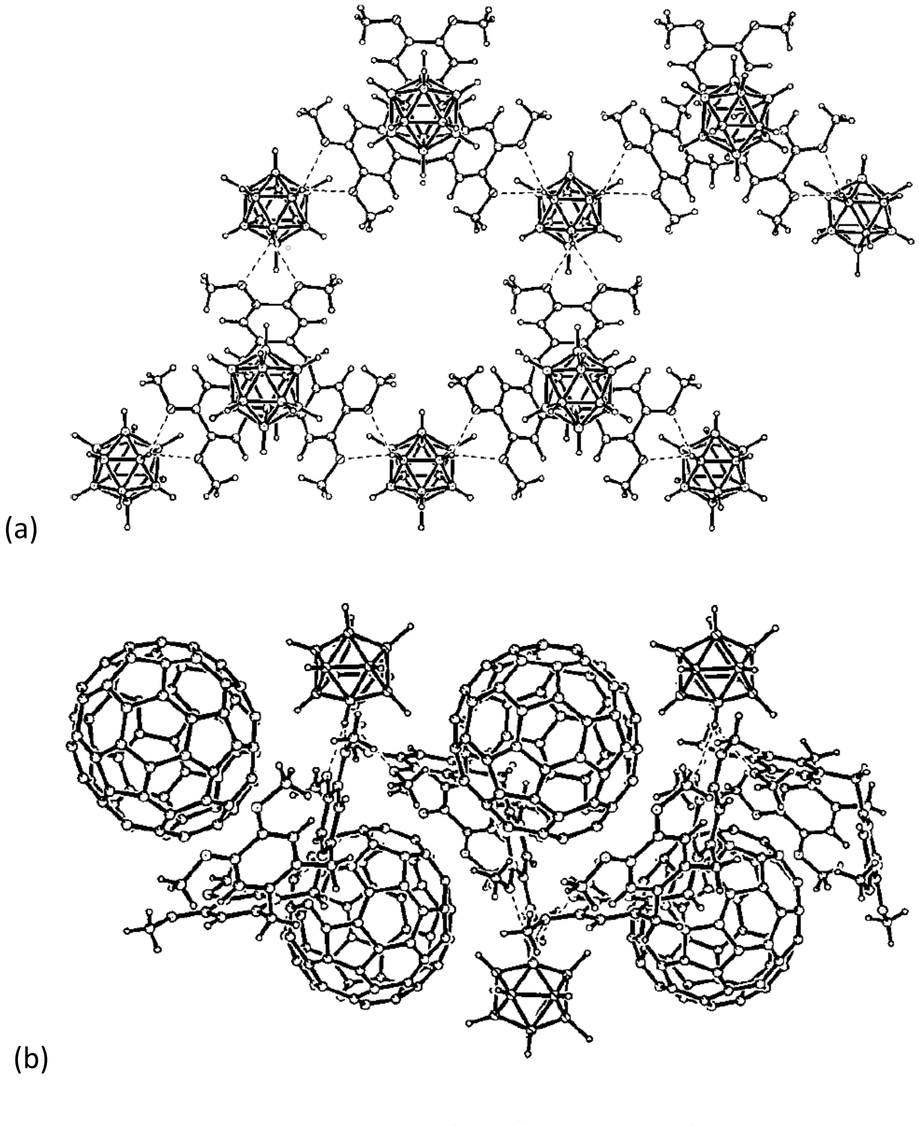

Figure 1.23: (a) Section of the crystal structure of (CTV)(*o*-carborane)$_2$ displaying the 2D hexagonal grid formed by B/C–H···O hydrogen bonding and the inclusion of an *o*-carborane guest in the CTV bowl. The *o*-carborane is disordered and every icosahedral vertice involved in the hydrogen-bonding interaction has ⅔ carbon and ⅓ boron occupancy (b) Section of the crystal structure of (1,2-dichlorobenzene)(CTV)(*o*-carborane)(C_{70}) displaying a side-on view of an infinite helical chain formed by hydrogen-bonding interactions between CTV and *o*-carborane. Ball-and-socket type host-guest complexes are formed between the CTV hosts and the C_{70} guests.[183] Figures reproduced with the permission of John Wiley & Sons.

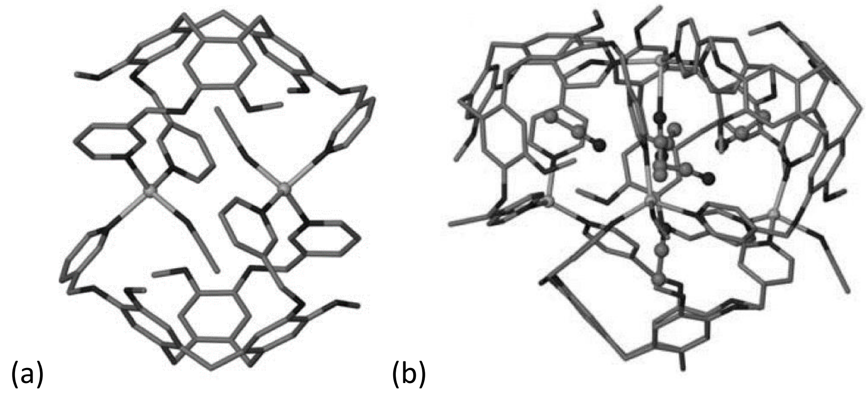

Figure 1.24: (a) Stick depiction of the capsule structure of $[Ag_2(\text{tris(3-pyridylmethylamino)cyclotriguaiacylene})_2(CH_3CN)_2]^{2+}$ (b) Host-guest interactions within the tetrahedron $[Ag_4(\text{tris(4-pyridylmethylamino)cyclotriguaiacylene})_4(CH_3CN)_4]^{4+}$ with the tetrahedron displayed in the ball-and-stick format with guest acetonitrile molecules inside, while silver centres are represented as spheres.[184] Figures reproduced with the permission of John Wiley & Sons.

The first structural characterizations of metallosupramolecular cages consisting of CTV-derived ligands were reported in 2005 (Figure 1.24).[184] The geometrically-accommodating silver centres along with the additional flexibility of the prepared host molecules, tris(pyridylmethylamino)cyclotriguaiacylenes, yielded a $[Ag_2(\text{tris(3-pyridylmethylamino)cyclotriguaiacylene})_2(CH_3CN)_2]\cdot 2PF_6\cdot 4CH_3CN$ dimeric capsule which encapsulates two coordinated CH_3CN guest molecules. The use of the 4-pyridyl cyclotriguaiacylene analogue resulted in the formation of an enlarged stellated tetrahedron also consisting of four silver centres with five CH_3CN guest molecules encapsulated within the internal cavity.

The solid-state and gas-phase supramolecular behaviours of CTV and $Na[Co(C_2B_9H_{11})_2]$ have been studied (Figure 1.25).[185] In the solid state, $[Na(CTV)][Co(C_2B_9H_{11})_2](CF_3CH_2OH)_{0.25}$ forms a crystalline complex featuring a 2D $[Na(CTV)]_\infty$ coordination polymer with novel topology and layers templated around the cobalt counterion. This coordination polymer disintegrates in solution and $[Na_n(CTV)_m]^{n+}$ fragments are found in the gas phase and can complex either one or two cobalt counterions.

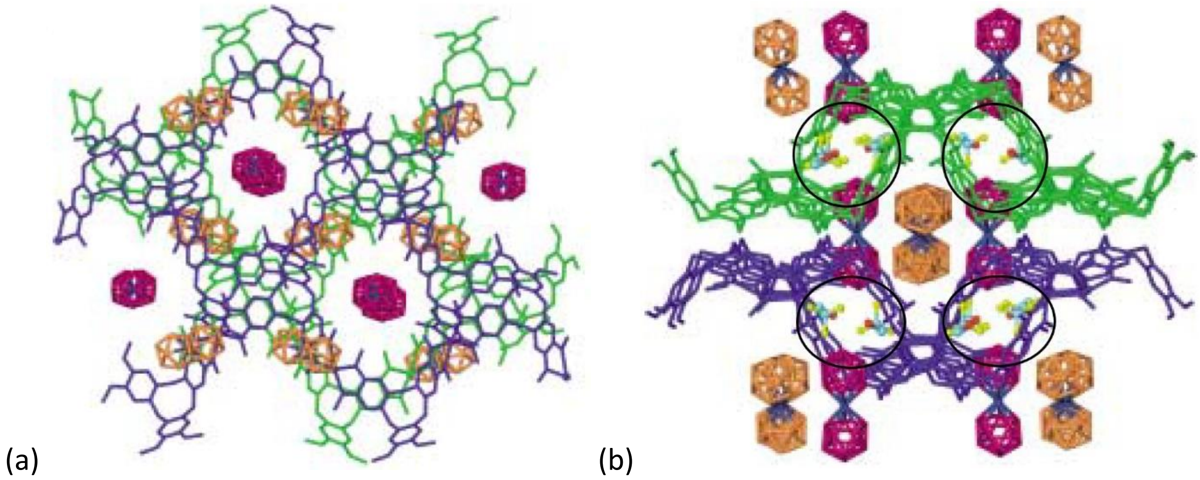

Figure 1.25: Crystal packing in $[Na(CTV)][Co(C_2B_9H_{11})_2](CF_3CH_2OH)_{0.25}$ (a) Packing of two $[Na(CTV)]_\infty$ networks displayed in green and blue. Two crystallographically unique types of $[Co(C_2B_9H_{11})_2]^-$ anions are in orange and purple. The C/B positions are not differentiated. The 2,2,2-trifluoroethanol guest molecules are omitted for clarity (b) Crystal packing displaying a side-on view of the $[Na(CTV)]_\infty$ networks, highlighting the cavities containing 2,2,2-trifluoroethanol within each network and the diamond-shaped channels generated by the network packing and inhabited by the $[Co(C_2B_9H_{11})_2]^-$ anions displayed in orange.[185] Figures reproduced with the permission of John Wiley & Sons.

The complex $\{(Na[2.2.2]cryptate)[CTV][Co(C_2B_9H_{11})_2]\}_2(CH_3CN)$ features two CTV-encapsulated $(Na[2.2.2]cryptate)^+$ supermolecules, each with a different arrangement of the cryptate cation within the cavity of the CTV (Figure 1.26).[186] This complex also features a densely-packed chain of $[Co(C_2B_9H_{11})_2]^-$ counter-anions displaying dihydrogen-bonding. An analogous CTV-cation structure is observed in $\{(Na[2.2.2]cryptate)(CTV)(CHCl_3)_3[CB_{11}H_{12}]\}$ (Figure 1.26).

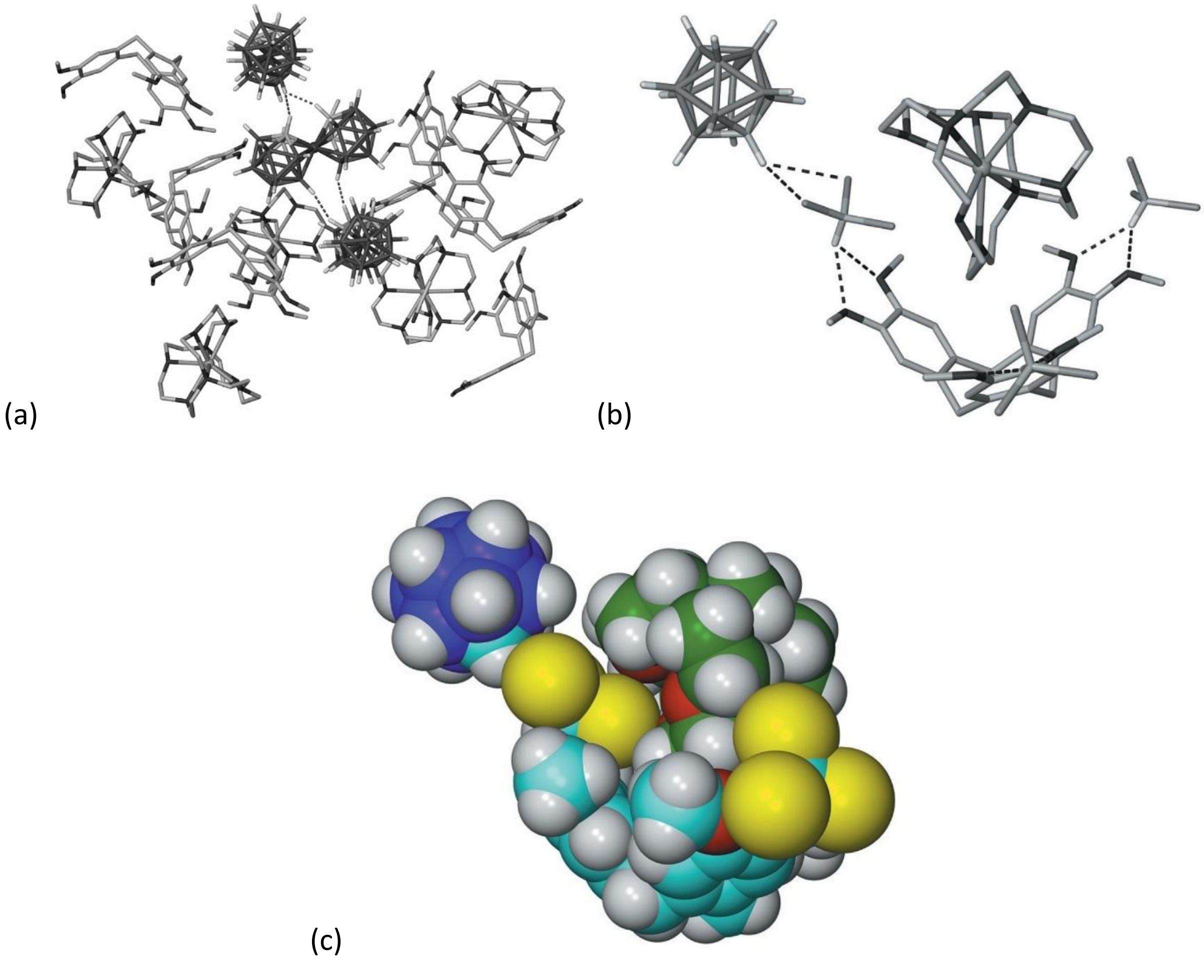

Figure 1.26: (a) Partial crystal packing diagram of $\{(Na[2.2.2]cryptate)[CTV][Co(C_2B_9H_{11})_2]\}_2(CH_3CN)$. Dashed lines represent dihydrogen bond C–H···B–H contacts < 2.3 Å between $[Co(C_2B_9H_{11})_2]^-$ anions (b) Hydrogen-bonding interactions in the crystal structure of $\{(Na[2.2.2]cryptate)(CTV)(CHCl_3)_3[CB_{11}H_{12}]\}$ between the CTV, $CHCl_3$ and $[CB_{11}H_{12}]^-$ anions are shown. Only hydrogen atoms on the $[CB_{11}H_{12}]^-$ anions and the $CHCl_3$ molecules are displayed for clarity (c) Space-filling depiction, showing how a Cl atom from one $CHCl_3$ molecule is positioned in the fissure of the $(Na[2.2.2]cryptate)^+$. Carbon atoms are displayed in blue, except in the [2.2.2]cryptate, where they are displayed in green.[186] Figures reproduced with the permission of the RSC.

To date, very little work has been done on porous structures incorporating CTV or functionalized CTV. Pd_3L_2 metallo-cryptophane assemblies with CTV-type L ligands (Figure 1.27) have been shown to be stabilized by a bis-N-heterocyclic carbene as an auxiliary *cis*-protecting ligand.[187] However, the usage of protecting chelating ligands like ethylenediamine led to a Pd_3L_2-to-Pd_6L_8 rearrangement in solution. The stabilized crystalline Pd_3L_2 compounds were shown to take up iodine or 1,2-dichlorobenzene in a SC-SC transformation, in spite of not displaying conventional porosity. Once absorbed, the iodine could not be effortlessly removed, showing that these structures could possibly be useful as separation and storage

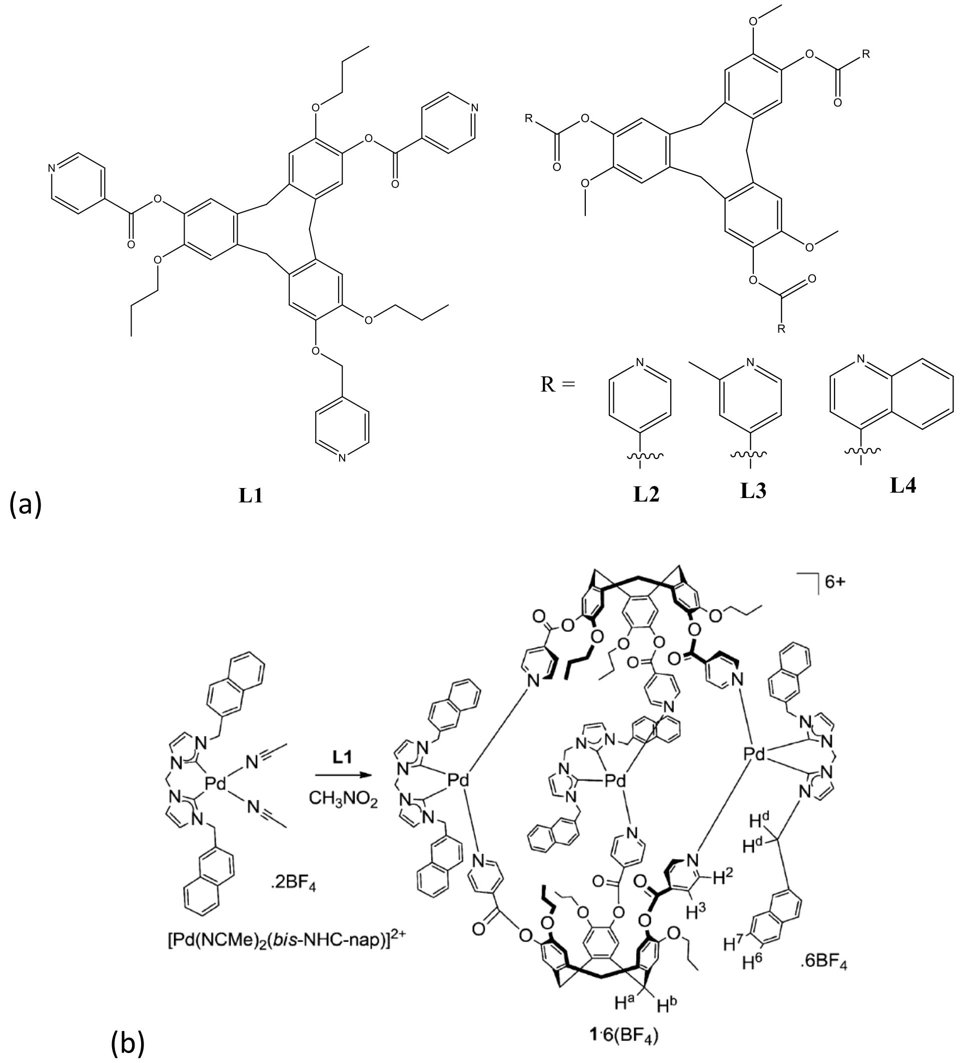

Figure 1.27: (a) Ligands **L1**-**L4** used to construct metallo-cryptophane cages (b) Self-assembly of the metallo-cryptophane cage *syn*-$[Pd_3(\text{bis-NHC-nap})_3(\mathbf{L1})_2]^{6+}$ from **L1** (bis-NHC-nap = bis-N-heterocyclic carbene).[187] Figure reproduced with the permission of ACS Publications.

agents for radioactive I_2. Early results also indicated preferential binding of Xe over Kr, indicating potential for separating these noble gases.

The porous, rigid materials **CTV-CMP-1** and **CTV-CMP-2** (Figure 1.28) (where CMP = conjugated microporous polymer) were produced by Suzuki and Sonogashira-Hagihara coupling reactions and displayed good chemical and thermal stabilities.[188] These compounds were subjected to gas sorption studies. **CTV-CMP-1** displayed reasonable hydrogen sorption at 77 K of approximately 0.81 wt. % at 1.13 bar and **CTV-CMP-2** displayed less hydrogen sorption of approximately 0.51 wt. % at 77 K. These compounds are analogous to activated carbons and could potentially be useful in organic compound separation and gas separation.

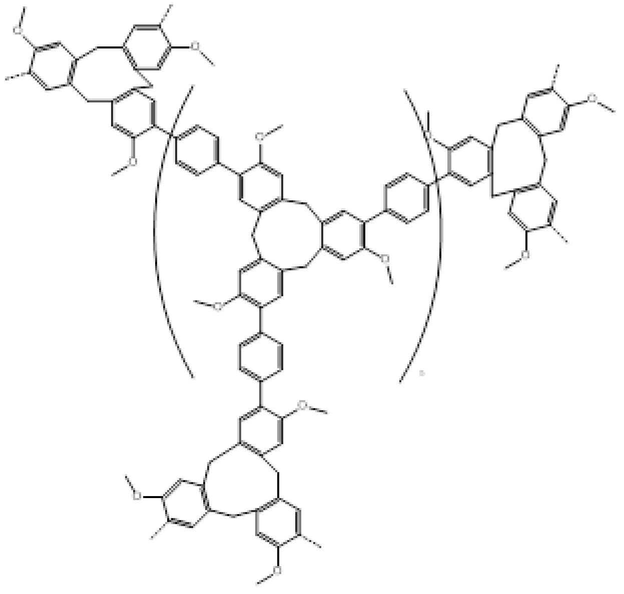

CTV-CMP-1

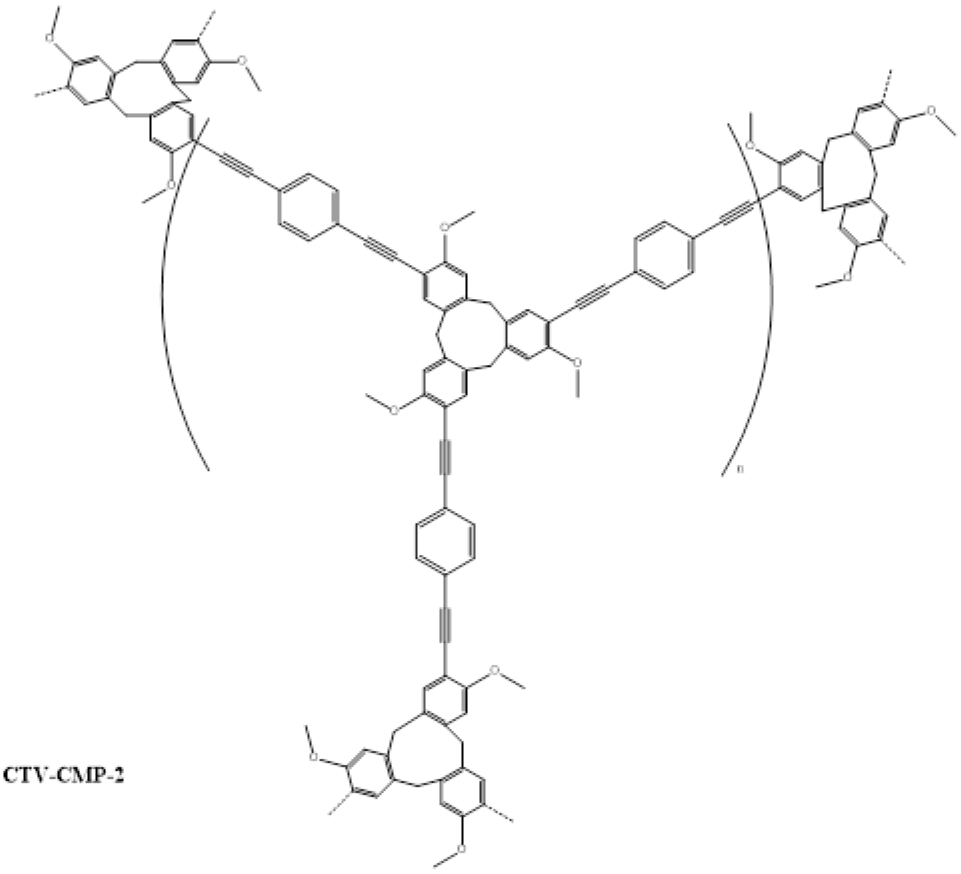

CTV-CMP-2

Figure 1.28: The structural formulae of **CTV-CMP-1** and **CTV-CMP-2**.[188]

Lastly, two rigid porous macrocyclic CTV-based polymers, **Click-POP-1** and **Click-POP-2**, (where POP = porous organic polymer) were prepared (Figure 1.29).[189] Both exhibit high thermal stability and reasonable hydrogen storage capabilities with 0.46 wt. % at 77 K. Their nitrogen adsorption displayed type-I isotherm with BET surface areas of 342 and 317 m^2 g^{-1}.

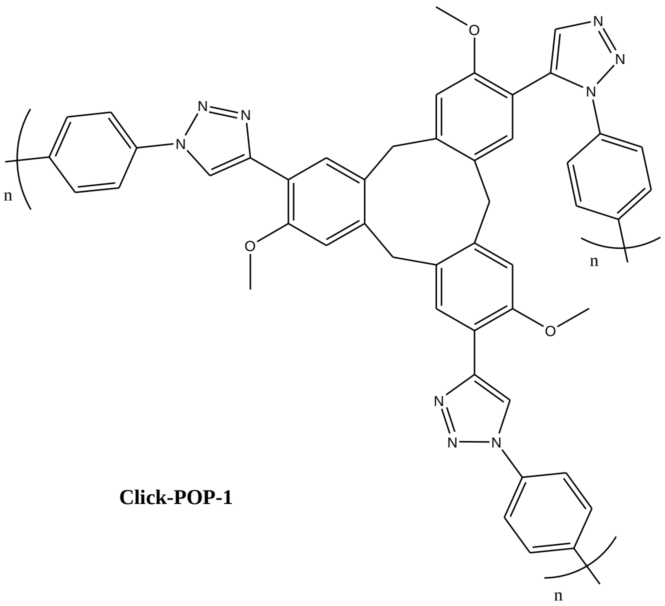

Click-POP-1

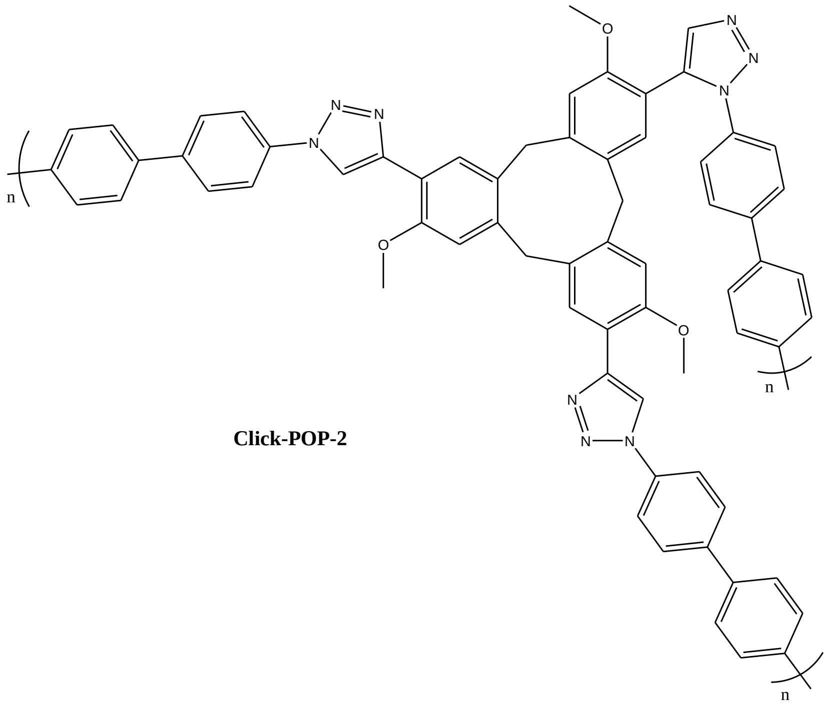

Click-POP-2

Figure 1.29: The structural formulae of **Click-POP-1** and **Click-POP-2**.[189]

1.2. Gas Sorption

The phenomenon of adsorption of molecules onto a surface was realized by Michael Faraday as far back as 1834.[190] Irving Langmuir derived a mathematical expression for the adsorption of gas onto a surface 84 years later, in 1918.[191] There are five different, idealized types of isotherms in adsorption onto a surface (Figure 1.30).[192] Type I is the well-known Langmuir adsorption isotherm appropriate for describing rigid microporous materials,[193] Type II is the sigmoid or S-shaped isotherm, usually observed for a macroporous material, while the three other types do not currently have names.[192] Types II and III are similar to Types IV and V. The only difference between them is that for Types II and III, as the vapour pressure p_0 of the adsorbed gas is approached, the adsorption increases, while for Types IV and V, maximum adsorption is reached at a lower pressure than the vapour pressure P_0 of the gas. In fact, the Type IV isotherm appears to correspond well with a flexible porous material characterized by a gentle enlargement of the pores,[194] while the Type V isotherm appears to correspond well with a flexible porous material which slowly becomes porous after starting as a seemingly nonporous material.[195,196] Langmuir described the Type I isotherm in 1915,[197] deriving his famous isotherm equation for adsorption in a unimolecular layer, shown below (**Eqn. 1**).[191]

$$\boldsymbol{\theta_A = V/V_m = K_{eq}{}^{A}P_A/(1+K_{eq}{}^{A}P_A)}$$

where $\boldsymbol{\theta_A}$ is the fractional occupancy of the adsorption sites, **V** is the volume of gas A adsorbed, $\mathbf{V_m}$ is the volume of the monolayer of gas molecules A on the solid surface, $\mathbf{K_{eq}{}^{A}}$ is the equilibrium constant for the adsorption of gas A and $\mathbf{P_A}$ is the partial pressure of the gas.

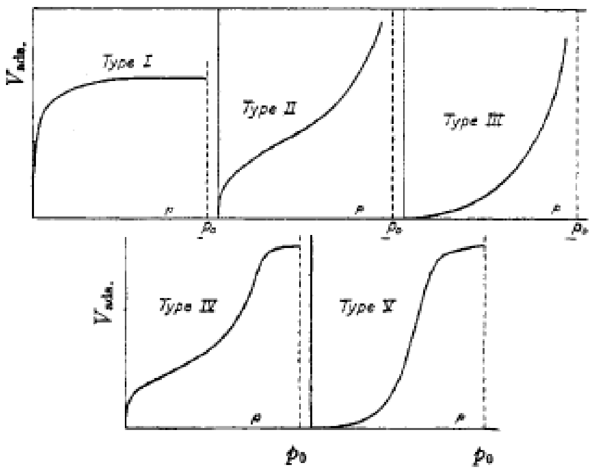

Figure 1.30: The five types of van der Waals adsorption isotherms.[192] Figure reproduced with the permission of ACS Publications.

Thereafter, Brunauer, Emmett and Teller (BET) derived an isotherm equation for the multimolecular adsorption of gases that explains both the sigmoid isotherm and Langmuir isotherm as special cases, shown below (**Eqn. 2**).[198]

$$\mathbf{1/V[(P_0/P) - 1] = [(c - 1)/V_m c](P/P_0) + 1/V_m c}$$

where **V** is the volume of gas adsorbed, **P** and $\mathbf{P_0}$ are the equilibrium and the saturation pressure of the gas at a given temperature, **c** is the BET constant relating constants such as heats of desorption and vapourisation, and $\mathbf{V_m}$ is the monolayer adsorbed gas volume. In a later article, this equation was extended to cover all five types of adsorption isotherms described in the literature.[192]

More recently, newer isotherms have been discovered and these are generally caused by flexible compounds exposed to gas pressure (Figure 1.31). Type I is the well-known Langmuir adsorption isotherm appropriate for describing rigid microporous materials,[193] Type F-I is the sigmoid or S-shaped isotherm, usually observed for a microporous flexible compound exhibiting a slow increase in pore size,[194] while the other types do not currently have names.[192] Type F-III represents a microporous flexible compound displaying a slow change from nonporous to porous.[195,196] Types F-II and F-IV are similar to Types F-I and F-III, respectively. The only difference between them is that for Types F-II and F-IV, the change in the structure is sudden, while for Types F-I and F-III, the change is more gradual.

The early days of gas sorption mainly focused on adsorbents such as charcoal, metal surfaces and zeolites. However, in recent times, attention has shifted to MOFs[199-201] and covalent organic frameworks (COFs). MOFs can be prepared by linking the inorganic structural building components (nodes) with organic ligands (linkers). The organic linkers can be tuned with various functional groups *via* organic synthesis, such as sulfonate ($R - SO_3^-$),[202-204] phosphonate ($R - PO_3^{2-}$),[205-207] carboxylate ($R - COO^-$)[208-210] and other organic halo ligands ($R - X$).[211] MOFs are documented as encouraging compounds for drug delivery,[212,213] catalysis[214,215] and separation[216,217] because of their variety in both chemistry and structure, high flexibility,[218,219] organized pore structure[220,221] and large surface area.[222,223] With the crucial necessity of

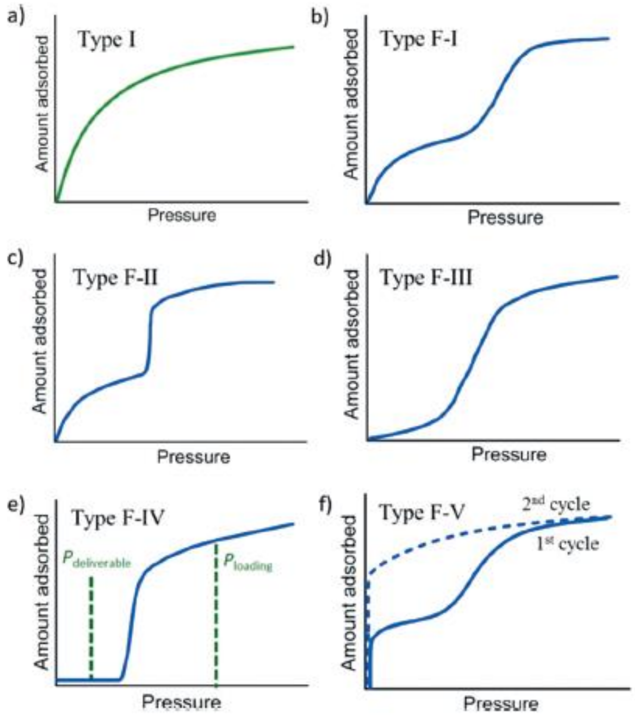

Figure 1.31: Classification of isotherm profiles for microporous, flexible compounds. Type F-V, not discussed in the text, displays a shape memory effect.[193] Figure reproduced with the permission of John Wiley & Sons.

controlling CO_2 emissions in recent times,[224] a major research focus has been on CO_2 separation and capture.[225-227] Established separation techniques require high energy consumption and large-scale phase change. Hence the great potential for the use of original porous compounds for energy-efficient CO_2 separation.[217,228]

Recently, gas sorption studies on purely organic, non-polymeric host systems have emerged. The crystal structures of *p*-*tert*-butylcalix[4]arene, *p*-*tert*-pentylcalic[4]arene and *p*-*tert*-octylcalix[4]arene contain pores appropriate to adsorb hydrogen molecules.[229] It was found that it is feasible to use purely organic materials for hydrogen sorption, although the hydrogen sorption abilities of these structures are low compared to many MOFs in the literature (Figure 1.32).

A novel porous organic solid has been reported, 1,2-dimethoxy-*p*-*tert*-butylcalix[4]dihydroquinone.[230] The nanoporous structure is self-assembled from supramolecular units consisting of six calix[4]dihydroquinone molecules and two water molecules. Each unit is octahedrally connected to six surrounding ones by inclusion of their

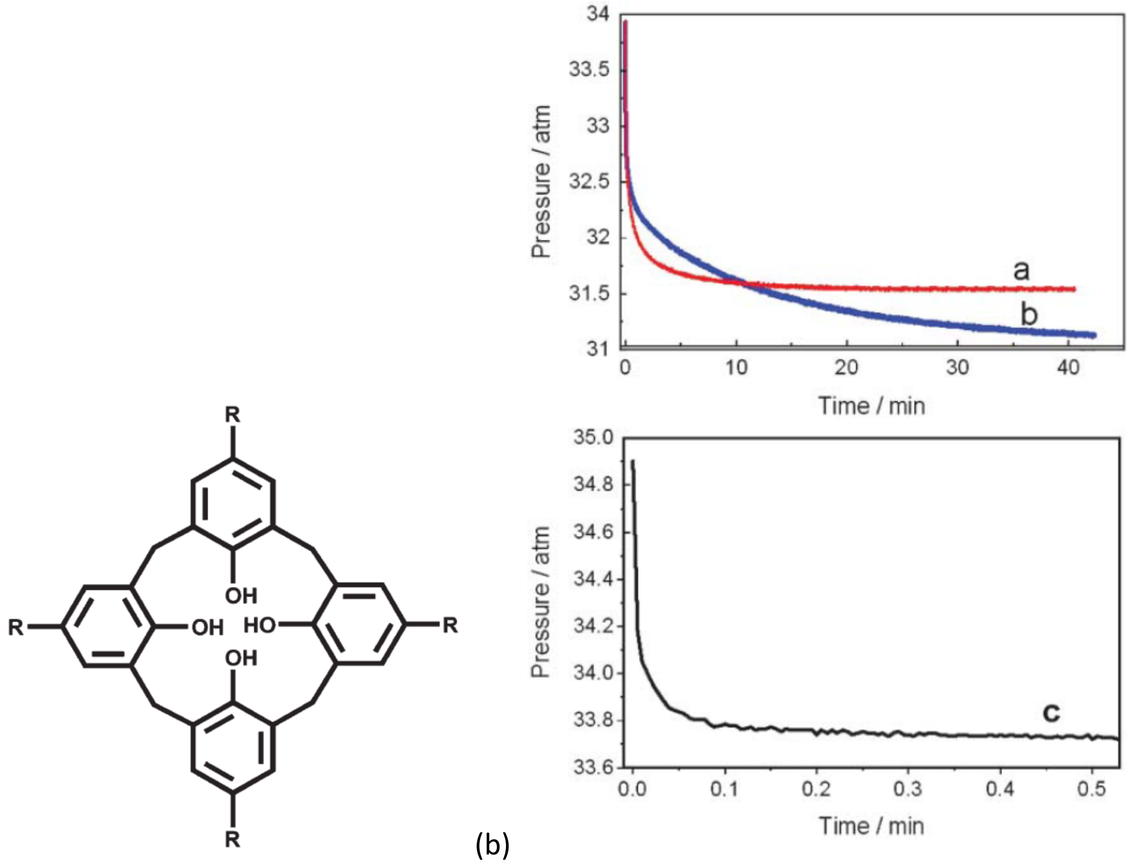

(a) (b)

Figure 1.32: (a) Structural formula of the host molecules *p*-*tert*-butylcalix[4]arene (R = *tert*-butyl), *p*-*tert*-pentylcalix[4]arene (R = *tert*-pentyl) and *p*-*tert*-octylcalix[4]arene (R = *tert*-octyl) (b) Isotherms for hydrogen sorption at room temperature by a – *p*-*tert*-butylcalix[4]arene, b – *p*-*tert*-pentylcalix[4]arene and c – *p*-*tert*-octylcalix[4]arene.[229] Figures reproduced with the permission of the RSC.

tert-butyl groups, resulting in the formation of cavities and channels (Figure 1.33). There are two hydrophobic cavities per unit cell, each bordered by eight supramolecular units with the *tert*-butyl groups as the interior walls of the cavity. CO_2 uptake of the activated sample was measured. Equilibrium was reached at 640 torr after 30 minutes, with the calculated mass weight of CO_2 determined to be 0.5 %. The absorption isotherm of CO_2 at high pressures suggests a Type 1 relationship, with the calculated CO_2 weight percentage in the lattice voids

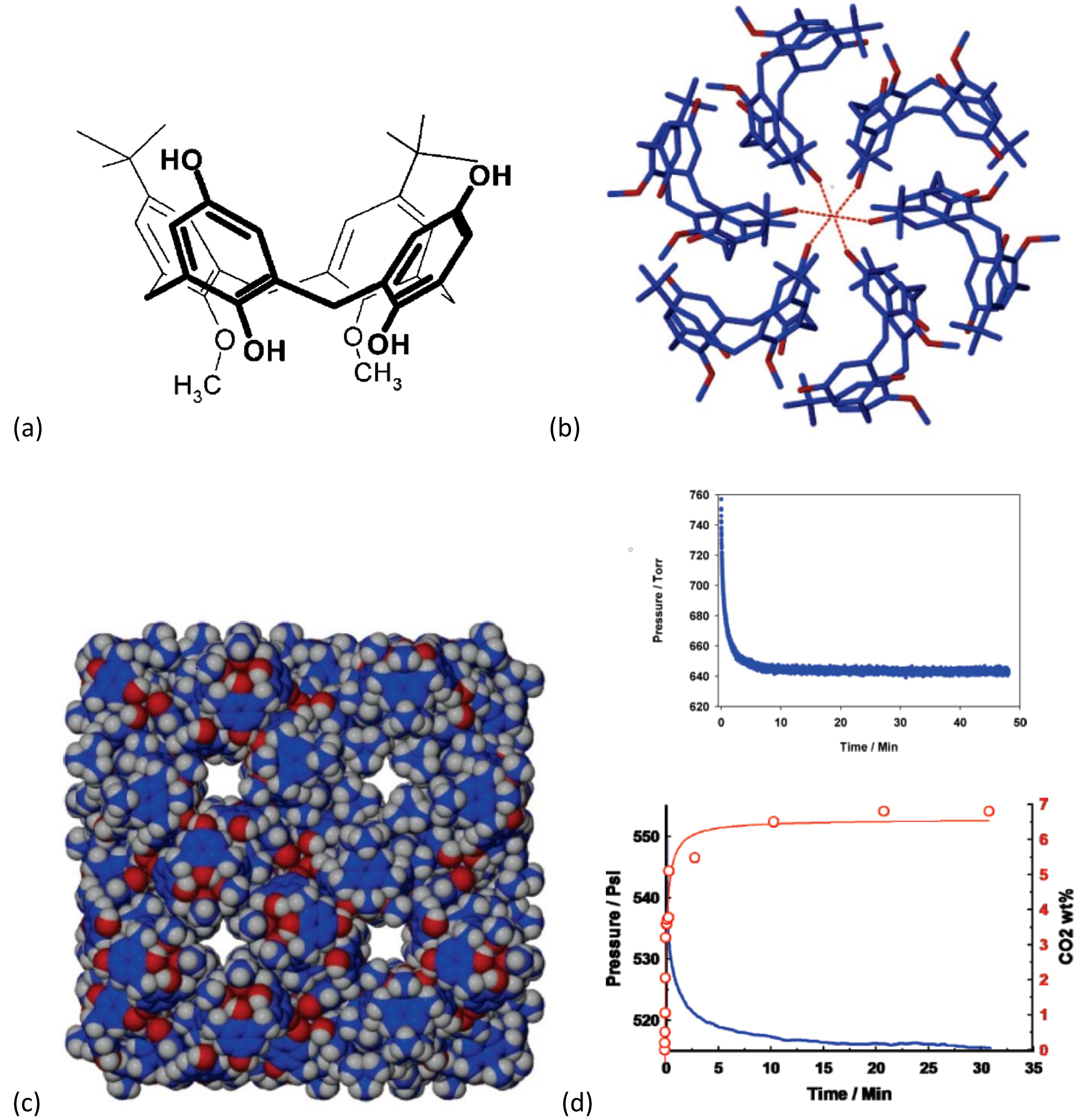

Figure 1.33: (a) The structural formula of 1,2-dimethoxy-*p*-*tert*-butylcalix[4]dihydroquinone (b) Supramolecular network made up of two water molecules and six calix[4]dihydroquinones. Hydrogen bonding between calix[4]dihydroquinones and water is displayed as dotted lines (c) Space-filling model of the nanoporous structure displaying two hydrophobic cavities (upper right and lower left) and polar open channels. Water molecules have been omitted for clarity (d) Isothermal sorption of CO_2 of the nanoporous structure at 298 K (top). CO_2 weight percentage in the nanoporous structure as a function of time and pressure (bottom).[230] Figures reproduced with the permission of ACS Publications.

established as 6.9 %. Sorption cycles could be repeated numerous times, as the nanoporous structure did not collapse to a close-packed structure after desorption of CO_2. Exposure to H_2 gas at 20 atm did not yield observable adsorption. This material is therefore highly selective for CO_2 over H_2.

1.3. Aims & Objectives

A cyclic trimer of veratrole, 2,3,7,8,12,13-hexamethoxy-10,15-dihydro-5*H*-tribenzo[a,d,g][9]annulene, known as cyclotriveratrylene (CTV) (Figure 1.34), acts as a bowl-shaped molecular host, capable of binding small molecules or ions.[163-165] CTV consists of three 4,5-dimethoxybenzene rings linked in a 1-2 fashion by methylene bridges. CTV is related to calix[*n*]arenes (where *n* is usually 4, 6 or 8) but is less common in terms of the diversity of inclusion complexes prepared and their variety of applications.[163,167] Molecules based on a CTV scaffold have been used in various applications, including as coordination polymers and as constituents of cage-like, discrete, metallo-supramolecular assemblies.[179-181] CTV and related structures have also been utilized as precursors for cryptophanes and cavitands,[163,171-173,185,231-233] where they bind smaller guest molecules.[174,175,234] Their ability to bind guests such as C_{60} and anionic C_{70} dimers, lanthanides and xenon has led to functionalized CTV derivatives being used for biomedical applications such as magnetic resonance imaging (MRI)-based diagnostic techniques and the distribution of fullerenes as cytotoxic antitumour agents.[176-178,235-237] However, very little investigation has been done on porous structures containing CTV or its analogues.

Sizeable supramolecular assemblies of macromolecules are found in nature, such as ribosomes, cellular membranes and viruses.[238-240] These complex structures are bound by non-covalent interactions which are important in the functioning of these biological mechanisms. However, large multi-component supramolecular assemblies ($n > 3$) which encapsulate chemical space are rarely found in supramolecular chemistry. The first example of such an assembly was formed using a bowl-shaped host molecule *C*-methylcalix[4]resorcinarene (CMCR) (Fig. 1.35), which spontaneously assembles in a nitrobenzene solution to form a large, chiral assembly made up of 6 CMCR and 8 water molecules, with the latter 'stitching' the CMCR molecules into the spherical assembly by O-H···O hydrogen bonds.[113] Since this discovery, a similar hexameric assembly of CMCR was reported, with 6 of the 8 water molecules replaced by 2-ethylhexanol molecules.[155] Large hexameric assemblies have also been reported for the structurally similar pyrogallolarenes, which have three hydroxyl groups per aromatic ring and longer hydrocarbon chains replacing the methyl groups.[103,111,241-244] CMCR has also been shown to crystallize in two unique hexameric arrangements within the same crystal from 1-butanol.[245] These two hexameric assemblies were bound by a water molecule into a supra-heterodimer. Although CMCR is the original molecule that formed these hexameric assemblies, and many hexameric assemblies have been formed with related host molecules, very few assemblies have been formed with this molecule, despite CMCR being co-crystallized with many solvents and/or guests.[246]

Thus, the aims and objectives of this project were to:

- Produce novel solvates of cyclotriveratrylene
- Investigate the thermal behaviours of these materials
- Investigate whether these materials maintain their crystallinity
- Investigate whether these materials are porous
- Activate these materials and subject them to gas sorption analysis to determine their uptake of and affinity towards various gases
- Crystallise *C*-methylcalix[4]resorcinarene from various alcohols in order to examine the effect of the length of the alkyl chain on the structure
- Examine the thermal behaviour of these materials and assess their suitability for porosity studies
- Examine these materials for maintenance of crystallinity after solvent removal
- Activate these materials and subject them to gas sorption analysis to determine their affinity towards various gases

1.4. References

1. Supramolecular Chemistry: Concepts and Perspectives; A Personal Account; Lehn, J.-M.; VCH: Weinheim, Germany, **1995**.
2. Desiraju, G.R. *IUCrJ*, **2017**, *4*, 710-711.
3. Braga, D. *Chem. Commun.*, **2003**, 2751-2754.
4. Molecule-Based Materials: The Structural Network Approach; Öhrström, L.; Larsson, K.; Elsevier: Amsterdam, The Netherlands, **2005**.
5. Aakeröy, C.B. *Acta Cryst.*, **1997**, *B53*, 569-586.
6. Almarsson, Ö.; Zaworotko, M.J. *Chem. Commun.*, **2004**, 1889-1896.
7. Bolla, G.; Nangia, A. *Chem. Commun.*, **2016**, *52*, 8342-8360.
8. Braga, D.; Grepioni, F.; Maini, L.; d'Agostino, S. *IUCrJ*, **2017**, *4*, 369-379.
9. Crystal Engineering. The Design of Organic Solids; Desiraju, G.R.; Elsevier: Amsterdam, The Netherlands, **1989**.
10. Desiraju, G.R. *Angew. Chem. Int. Ed. Eng.*, **1995**, *34*, 2311-2327.
11. Desiraju, G.R. *Nature*, **2001**, *412*, 397-400.
12. Desiraju, G.R. *Angew. Chem. Int. Ed.*, **2007**, *46*, 8342-8356.
13. Desiraju, G.R. *J. Am. Chem. Soc.*, **2013**, *135*, 9952-9967.
14. Saha, S.; Desiraju, G.R. *J. Am. Chem. Soc.*, **2017**, *139*, 1975-1983.
15. Zhong, D.-C.; Lu, T.-B. *Chem. Commun.*, **2016**, *52*, 10322−10337.
16. Teyssandier, J.; De Feyter, S.; Mali, K. S. *Chem. Commun.*, **2016**, *52*, 11465−11487.
17. Zheng, Y.; Wyman, I. W. *Polymers*, **2016**, *8*, 198/1−198/18.
18. Harada, A.; Takashima, Y.; Nakahata, M. *Acc. Chem. Res.*, **2014**, *4*, 2128−2140.
19. Arunachalam, M.; Gibson, H. W. *Prog. Polym. Sci.*, **2014**, *39*, 1043−1073.
20. Tamura, A.; Yui, N. *Chem. Commun.*, **2014**, *50*, 13433−13446.
21. Synergy in Supramolecular Chemistry; Charbonniere, L. J.; Trabolsi, A.; CRC Press: Boca Raton, USA, **2015**.
22. Niu, Z.; Gibson, H. W. *Chem. Rev.* **2009**, *109*, 6024−6046.
23. Synthesis of Polymers; Niu, Z.; Gibson, H. W.; Wiley: New York, USA, **2012**.

24. Gibson, H. W.; Yamaguchi, N.; Niu, Z.; Jones, J. W.; Rheingold, A. L.; Zakharov, L. N. *J. Polym. Sci., Part A: Polym. Chem.*, **2010**, *48*, 975− 985.
25. Zhang, M.; Yan, X.; Huang, F.; Niu, Z.; Gibson, H. W. *Acc. Chem. Res.*, **2014**, *47*, 1995−2005.
26. Wei, P.; Yan, X.; Huang, F. *Chem. Soc. Rev.*, **2015**, *44*, 815−832.
27. Jones, J. W.; Bryant, W. S.; Bosman, A. W.; Janssen, R. A. J.; Meijer, E. W.; Gibson, H. W. *J. Org. Chem.*, **2003**, *68*, 2385−2389.
28. Lee, M.; Schoonover, D.; Gies, A.; Hercules, D. M.; Gibson, H. W. *Macromolecules*, **2009**, *42*, 6483−6494.
29. Lee, M.; Moore, R. B.; Gibson, H. W. *Macromolecules*, **2011**, *44*, 5987−5993.
30. Xue, M.; Yang, Y.; Chi, X.; Zhang, Z.; Huang, F. *Acc. Chem. Res.*, **2012**, *45*, 1294−1308.
31. Ogoshi, T.; Yamagishi, T. *Eur. J. Org. Chem.*, **2013**, *2013*, 2961−2975.
32. Sato, S.; Yamasaki, T.; Isobe, H. *Proc. Natl. Acad. Sci. U. S. A.*, **2014**, *111*, 8374−8379.
33. Pedersen, C.J. *J. Am. Chem. Soc.*, **1967**, *89*, 2495-2496.
34. Pedersen, C.J. *J. Am. Chem. Soc.*, **1967**, *89*, 7017-7036.
35. Comprehensive Supramolecular Chemistry; Atwood, J.L.; Davies, J.E.D.; MacNicol, D.D.; Vogtle, F.; Lehn, J.-M.; Elsevier: Netherlands, **1996**.
36. Functional Synthetic Receptors; Schrader, T.; Hamilton, A.D.; Wiley-VCH: Weinheim, Germany, **2005**.
37. Macrocyclic Chemistry Current Trends and Future Perspectives; Gloe, K.; Springer: Dordrecht, Netherlands, **2005**.
38. Chen, G.; Jiang, M. *Chem. Soc. Rev.*, **2011**, *40*, 2254-2266.
39. Mellet, C.O.; Fernandez, J.M.G.; Benito, J.M. *Chem. Soc. Rev.*, **2011**, *40*, 1586-1608.
40. Gokel, G.W.; Leevy, W.M.; Weber, M.E. *Chem. Rev.*, **2004**, *104*, 2723-2750.
41. Kim, K.; Selvapalam, N.; Ko, Y.H.; Park, K.M.; Kim, D.; Kim, J. *Chem. Soc. Rev.*, **2007**, *36*, 267-279.
42. Masson, E.; Ling, X.; Joseph, R.; Kyeremeh-Mensah, L.; Lu, X. *RSC Adv.*, **2012**, *2*, 1213-1247.
43. Acharya, A.; Samanta, K.; Rao, C.P. *Coordin. Chem. Rev.*, **2012**, *256*, 2096-2125.
44. Kim, H.J.; Lee, M.H.; Mutihac, L.; Vicens, J.; Kim, J.S. *Chem. Soc. Rev.*, **2012**, *41*, 1173-1190.
45. Chen, H.; Gu, L.; Yin, Y.; Koh, K.; Lee, J. *Int. J. Mol. Sci.*, **2011**, *12*, 2315-2324.

46. Oh, S.W.; Moon, J.D.; Lim, H.J.; Park, S.Y.; Kim, T.; Park, J.; Han, M.H.; Snyder, M.; Choi, E.Y. *FASEB J.*, **2005**, *19*, 1335-1337.
47. Debbert, S.L.; Hoh, B.D.; Dulak, D.J. *J. Chem. Educ.*, **2016**, *93*, 372-375.
48. Barbour, L.J. *Chem. Commun.*, **2006**, 1163-1168.
49. Barbour, L.J. *Aust. J. Chem.*, **2006**, *59*, 595-596.
50. Sundberg, J.; Cameron, L.J.; Southon, P.D.; Kepert, C.J.; McKenzie, C.J. *Chem. Sci.*, **2014**, *5*, 4017-4025.
51. Mobin, S.M.; Mohammad, A. *Dalton Trans.*, **2014**, *43*, 13032-13040.
52. Hsu, L.-Y.; Maity, S.; Matsunaga, Y.; Hsu, Y.-F.; Liu, Y.-H.; Peng, S.-M.; Shinmyozu, T.; Yang, J.-S. *Chem. Sci.*, **2018**, *9*, 8990-9001.
53. Li, Y.; Handke, M.; Chen, Y.-S.; Shtukenberg, A.G.; Hu, C.T.; Ward, M.D. *J. Am. Chem. Soc.*, **2018**, *140*, 12915-12921.
54. Supriya, S.; Das, S.K. *J. Am. Chem. Soc.*, **2007**, *129*, 3464-3465.
55. Li, N.; Jiang, F.; Chen, L.; Li, X.; Chen, Q.; Hong, M. *Chem. Commun.*, **2011**, *47*, 2327-2329.
56. Huang, C.; Wang, Y.; Wei, C.; Li, N.; Ji, F.; Wu, J.; Hou, H. *Inorg. Chem. Commun.*, **2013**, *32*, 68-73.
57. Papaefstathiou, G.S.; Zhong, Z.; Geng, L.; MacGillivray, L.R. *J. Am. Chem. Soc.*, **2004**, *126*, 9158-9159.
58. Medishetty, R.; Bai, Z.; Yang, H.; Wong, M.W.; Vittal, J.J. *Cryst. Growth Des.*, **2015**, *15*, 4055-4061.
59. https://en.wikipedia.org/wiki/Calixarene
60. Baeyer, A. *Berlin*, **1872**, *5*, 25.
61. Baekeland, L.H. *US Patent Numbers 942, 699*, **1908**.
62. Zinke, A.; Ziegler, E. *X. Mitteilung Ber. Dtsch. Chem. Ges.*, **1944**, *77B*, 264-272.
63. Zinke, A.; Kretz, R.; Leggewie, E.; Hössinger, K. *Monatsch. Chem.*, **1952**, *83*, 1213-1227.
64. Gutsche, C.D.; Dhawan, B.; No, K.H.; Muthukrishnan, R. *J. Am. Chem. Soc.*, **1981**, *103*, 3782-3792.
65. Gutsche, C. D. in Calixarenes Revisited; Stoddard, J. F., Ed.; Monographs in Supramolecular Chemistry; Royal Society of Chemistry: Cambridge, **1998**.

66. Calixarenes in Action; Mandolini, L., Ungaro, R., Eds.; Imperial College: London, England, **2000**.
67. Calixarenes 2001; Asfari, Z., Böhmer, V., Harrowfield, J., Eds.; Kluwer Academic: Dordrecht, **2001**.
68. Sessler, J.L.; Cho, W.-S.; Lynch, V.; Král, V. *Chem. Eur. J.*, **2002**, *8*, 1134-1143.
69. Cafeo, G.; Kohnke, F.H.; La Torre, G.L.; Parisi, M.F.; Nascone, R.P.; White, A.J.P.; Williams, D.J. *Chem. Eur. J.*, **2002**, *8*, 3148-3156.
70. Guillard, J.; Meth-Cohn, O.; Rees, C.W.; White, A.J.P.; Williams, D.J. *Chem. Commun.*, **2002**, 232-233.
71. Shinkai, S. *Tetrahedron*, **1993**, *49*, 8933-8968.
72. Gutsche, C.D.; Nam, K.C. *J. Am. Chem. Soc.*, **1988**, *110*, 6153-6162.
73. Bayrakci, M.; Ertul, Ş.; Yilmaz, M. *Tetrahedron*, **2009**, *65*, 7963-7968.
74. Sokoliess, T.; Menyes, U.; Roth, U.; Jira, T. *J. Chromatogr.*, **2000**, *898*, 35-52.
75. Williams, R.M.; Verhoeven, J.W. *Recl. Trav. Chim. Pays-Bas*, **1992**, *111*, 531-532.
76. Atwood, J.L.; Koutsoantonis, G.A.; Raston, C.L. *Nature*, **1994**, *368*, 229-231.
77. Suzuki, T.; Nakashima, K.; Shinkai, S. *Chem. Lett.*, **1994**, 699-702.
78. Zhong, Z.-L.; Ikeda, A.; Shinkai, S. in *Calixarenes 2001*; Asfari, Z.; Böhmer, V.; Harrowfield, J.; Vicens, J., Eds.; Kluwer Academic: Dordrecht, **2001**, Chapter 26, 476-495.
79. Aoyama, Y.; Tanaka, Y.; Sugahara, S. *J. Am. Chem. Soc.*, **1989**, *111*, 5397-5404.
80. Kurihara, K.; Ohto, K.; Tanaka, Y.; Aoyama, Y.; Kunitake, T. *J. Am. Chem. Soc.*, **1991**, *113*, 444-450.
81. Kikuchi, Y.; Tanaka, Y.; Sutarto, S.; Kobayashi, K.; Toi, H.; Aoyama, Y. *J. Am. Chem. Soc.*, **1992**, *114*, 10302-10306.
82. Kobayashi, K.; Asakawa, Y.; Kikuchi, Y.; Toi, H.; Aoyama, Y. *J. Am. Chem. Soc.*, **1993**; *115*, 2648-2654.
83. Kikuchi, Y.; Kato, Y.; Tanaka, Y.; Toi, H.; Aoyama, Y. *J. Am. Chem. Soc.*, **1991**, *113*, 1349-1354.
84. Schneider, H.-J.; Güttes, D.; Schneider, U. *Angew. Chem. Int. Edn. Engl.*, **1986**, *25*, 647-649.

85. Lippmann, T.; Wilde, H.; Pink, M.; Schäfer, A.; Hesse, M.; Mann, G. *Angew. Chem. Int. Edn. Engl.*, **1993**, *32*, 1195-1197.
86. Schneider, H.-J.; Güttes, D.; Schneider, U. *J. Am. Chem. Soc.*, **1988**, *110*, 6449-6454.
87. Schneider, H.-J.; Schneider, U. *J. Org. Chem.*, **1987**, *52*, 1613-1615.
88. Murayama, K.; Aoki, K. *Chem. Commun.*, **1997**, 119-120.
89. Inouye, M.; Hashimoto, K.; Isagawa, K. *J. Am. Chem. Soc.*, **1994**, *116*, 5517-5518.
90. Koide, Y.; Oka, T.; Imamura, A.; Shosenji, H.; Yamada, K. *Bull. Chem. Soc. Jpn.*, **1993**, *66*, 2137-2142.
91. Letzel, M.C.; Agena, C.; Mattay, J. *J. Mass Spectrom.*, **2002**, *37*, 63-68.
92. Tanaka, Y.; Kobuke, Y.; Sokabe, M. *Angew. Chem. Int. Ed. Engl.*, **1995**, *34*, 693-694.
93. Davis, F.; Stirling, C.J.M. *Langmuir*, **1996**, *12*, 5365-5374.
94. Schönherr, H.; Vancso, G.J.; Huisman, B.-H.; van Veggel, F.C.J.M.; Reinhoudt, D.N. *Langmuir*, **1997**, *13*, 1567-1570.
95. Adams, H.; Davis, F.; Stirling, C.J.M. *Chem. Commun.*, **1994**, 2527-2529.
96. Moreira, W.C.; Dutton, P.J.; Aroca, R. *Langmuir*, **1994**, *10*, 4148-4152.
97. Moreira, W.C.; Dutton, P.J.; Aroca, R. *Langmuir*, **1995**, *11*, 3137-3144.
98. Dutton, P.J.; Conte, L. *Langmuir*, **1999**, *15*, 613-617.
99. Kroto, H.W.; Heath, J.R.; O'Brien, S.C.; Curl, R.F.; Smalley, R.E. *Nature*, **1985**, *318*, 162-163.
100. Caspar, D.; Klug, A. *Cold Spring Harb. Symp. Quant. Biol.*, **1962**, *27*, 1-24.
101. Casjens, S. in Virus Structure and Assembly; Casjens, S., Ed.; Jones and Bartlett, Boston, **1995**, 75-147.
102. Schwarz, H.; Weiske, T.; Böhme, D.K.; Hrušák, J. in Buckminsterfullerenes; Billups, W.E.; Ciufolini, M.A., Eds.; VCH, New York, **1993**, 257-283.
103. Cave, G.W.V.; Antesberger, J.; Barbour, L.J.; McKinlay, R.M.; Atwood, J.L. *Angew. Chem. Int. Ed.*, **2004**, *43*, 5263-5266.
104. Sherman, J.C.; Cram, D.J. *J. Am. Chem. Soc.*, **1989**, *111*, 4527-4528.
105. Garel, L.; Dutata, J.-P.; Collet, A. *Angew. Chem. Int. Ed Engl.*, **1993**, *32*, 1169-1171.
106. Timmerman, P.; Verboom, W.; van Veggel, F.C.; van Duynhoven, J.P.; Reinhoudt, D.N. *Angew. Chem. Int. Ed. Engl.*, **1994**, *33*, 2345-2348.

107. Kang, J.; Rebek, Jr., J. *Nature*, **1997**, *385*, 50-52.

108. Shimizu, K.D.; Rebek, Jr., J. *Proc. Natl. Acad. Sci. USA*, **1995**, *92*, 12403-12407.

109. Douglas, T.; Young, M. *Nature*, **1998**, *393*, 152-155.

110. Atwood, J.L.; Barbour, L.J.; Jerga, A. *J. Supramol. Chem.*, **2001**, *1*, 131-134.

111. Atwood, J.L.; Barbour, L.J.; Jerga, A. *Chem. Commun.*, **2001**, *22*, 2376-2377.

112. Atwood, J.L.; Barbour, L.J.; Jerga, A. *Proc. Natl. Acad. Sci. U.S.A.*, **2002**, *99*, 4837-4841.

113. MacGillivray, L.R.; Atwood, J.L. *Nature*, **1997**, *389*, 469-472.

114. Shivanyuk, A.; Rebek, J. *Chem. Commun.*, **2001**, 2424-2425.

115. Atwood, J.L.; Barbour, L.J.; Dalgarno, S.J.; Hardie, M.J.; Raston, C.L.; Webb, H.R. *J. Am. Chem. Soc.*, **2004**, *126*, 13170-13171.

116. König, B.; Fonseca, M.H. *Eur. J. Inorg. Chem.*, **2000**, 2303-2310.

117. Smith, G.W. *Nature*, **1963**, *198*, 879.

118. Sommer, N.; Staab, H.A. *Tetrahedron Lett.*, **1966**, 2837-2841.

119. (a) Kumagai, H.; Hasegawa, M.; Miyanari, S.; Sugawa, Y.; Sato, Y.; Hori, T.; Ueda, S.; Kamiyama, H.; Miyano, S. *Tetrahedron Lett.*, **1997**, *38*, 3971-3972. (b) Akdas, H.; Bringel, L.; Graf, E.; Hosseini, M.W.; Mislin, G.; Pansanel, J.; De Cian, A.; Fischer, J. *Tetrahedron Lett.*, **1998**, *39*, 2311-2314.

120. Fukushima, W.; Kanbara, T.; Yamamoto, T. *Synlett.*, **2005**, 2931-2934.

121. Wang, M.-X.; Zhang, X.-H.; Zheng, Q.-Y. *Angew. Chem. Int. Ed.*, **2004**, *43*, 838-842.

122. Zadmard, R.; Schrader, T. *J. Am. Chem. Soc.*, **2005**, *127*, 904-915.

123. Darbost, U.; Rager, M.-N.; Petit, S.; Jabin, I.; Reinaud, O. *J. Am. Chem. Soc.*, **2005**, *127*, 8517-8525.

124. Seneque, O.; Rager, M.-N.; Giorgi, M.; Prange, T.; Tomas, A.; Reinaud, O. *J. Am. Chem. Soc.*, **2005**, *127*, 14833-14840.

125. Král, V.; Gale, P.A.; Anzenbacher, P.; Jursiková, K.; Lynch, V.; Sessler, J.L. *Chem. Commun.*, **1998**, 9-10.

126. Newkome, G.R.; Joo, Y.J.; Fronczek, F.R. *J. Chem. Soc. Chem. Commum.*, **1987**, 854-856.

127. Gale, P.A.; Sessler, J.L.; Král, V. *Chem. Commun.*, **1998**, 1-8.

128. Depraetere, S.; Smet, M.; Dehaen, W. *Angew. Chem. Int. Ed.*, **1999**, *38*, 3359-3361.

129. Lehmann, F.P.A. *Tetrahedron*, **1974**, *30*, 727-733.

130. Ito, A.; Ono, Y.; Tanaka, K. *New J. Chem.*, **1998**, *22*, 779-781.

131. Ito, A.; Ono, Y.; Tanaka, K. *J. Org. Chem.*, **1999**, *64*, 8236-8241.

132. König, B.; Rödel, M.; Bubenitschek, P.; Jones, P.G.; Thondorf, I. *J. Org. Chem.*, **1995**, *60*, 7406-7410.

133. Yoshida, M.; Goto, M.; Nakanishi, F. *Organometallics*, **1999**, *18*, 1465-1470.

134. Avarvari, N.; Mezailles, N.; Richard, L.; Le Floch, P.; Mathey, F. *Science*, **1998**, *280*, 1587-1589.

135. Avarvari, N.; Maigrot, N.; Richard, L.; Mathey, F.; Le Floch, P. *Chem. Eur. J.*, **1999**, *5*, 2109-2118.

136. Burattini, S.; Greenland, B.W.; Chappell, D.; Colquhoun, H.M.; Hayes, W. *Chem. Soc. Rev.*, **2010**, *39*, 1973-1985.

137. Burnworth, M.; Tang, L.; Kumpfer, J.R.; Duncan, A.J.; Beyer, F.L.; Fiore, G.L.; Rowan, S.J.; Weder, C. *Nature*, **2011**, *472*, 334-337.

138. Ge, Z.; Hu, J.; Huang, F.; Liu, S. *Angew. Chem. Int. Ed. Engl.*, **2009**, *48*, 1798-1802.

139. Lewis, J.E.M.; Gavey, E.L.; Cameron, S.A.; Crowley, J.D. *Chem. Sci.*, **2012**, *3*, 778-784.

140. Xuan, W.; Zhu, C.; Liu, Y.; Cui, Y. *Chem. Soc. Rev.*, **2012**, *41*, 1677-1695.

141. Li, X.; Li, J.; Gao, Y.; Kuang, Y.; Shi, J.; Xu, B. *J. Am. Chem. Soc.*, **2010**, *132*, 17707-17709.

142. Verdejo, B.; Rodríguez-Llansola, F.; Escuder, B.; Miravet, J.F.; Ballester, P. *Chem. Commun.*, **2011**, *47*, 2017-2019.

143. Rodríguez-Hernández, J.; Lecommandoux, S. *J. Am. Chem. Soc.*, **2005**, *127*, 2026-2027.

144. Kim, D.S.; Lynch, V.M.; Park, J.S.; Sessler, J.S. *J. Am. Chem. Soc.*, **2013**, *135*, 14889-14894.

145. Arotçaréna, M.; Heise, B.; Ishaya, S.; Laschewsky, A. *J. Am. Chem. Soc.*, **2002**, *124*, 3787-3793.

146. Jones, D.M.; Smith, J.R.; Huck, W.T.; Alexander, C. *Adv. Mater.*, **2002**, *14*, 1130-1133.

147. Xu, J.-F.; Chen, Y.-Z.; Wu, D.; Wu, L.-Z.; Tung, C.-H.; Yang, Q.-Z. *Angew. Chem. Int. Ed. Engl.*, **2013**, *52*, 9738-9742.

148. Dong, S.; Gao, L.; Li, J.; Xu, D.; Zhou, Q. *Polym. Chem.*, **2013**, *4*, 3968-3973.

149. Wong, C.-H.; Zimmerman, S.C. *Chem. Commun.*, **2013**, *49*, 1679-1695.

150. Hu, X.-Y.; Xiao, T.; Lin, C.; Huang, F.; Wang, L. *Acc. Chem. Res.*, **2014**, *47*, 2041-2051.

151. Elacqua, E.; Lye, D.S.; Weck, M. *Acc. Chem. Res.*, **2014**, *47*, 2405-2416.

152. Fukuzumi, S.; Ohkubo, K.; Kawashima, Y.; Kim, D.S.; Park, J.S.; Jana, A.; Lynch, V.M.; Kim, D.; Sessler, J.L. *J. Am. Chem. Soc.*, **2011**, *133*, 15938-15941.

153. Davis, C.M.; Lim, J.M.; Larsen, K.R.; Kim, D.S.; Sung, Y.M.; Lyons, D.M.; Lynch, V.M.; Nielsen, K.A.; Jeppesen, J.O.; Kim, D.; Park, J.S.; Sessler, J.L. *J. Am. Chem. Soc.*, **2014**, *136*, 10410-10417.

154. Gale, P.A.; Sessler, J.L.; Král, V.; Lynch, V.M. *J. Am. Chem. Soc.*, **1996**, *118*, 5140-5141.

155. Ugono, O.; Holman, K.T. *Chem. Commun.*, **2006**, 2144-2146.

156. Coleman, A.W.; Bott, S.G.; Morley, S.D.; Means, C.M.; Robinson, K.D.; Zang, H.; Atwood, J.L. *Angew. Chem., Int. Ed., Eng.*, **1988**, *27*, 1361-1362.

157. Orr, G.W.; Barbour, L.J.; Atwood, J.L. *Science*, **1999**, *285*, 1049-1052.

158. Atwood, J.L.; Barbour, L.J.; Hardie, M.J.; Raston, C.L. *Coord. Chem. Rev.*, **2001**, *222*, 3-32.

159. Suwinska, K.; Leśniewska, B.; Wszelaka-Rylik, M.; Straver, L.; Jebors, S.; Coleman, A.W. *Chem. Commun.*, **2011**, 8766-8768.

160. McKinlay, R.M.; Cave, G.W.V.; Atwood, J.L. *Proc. Natl. Acad. Sci.*, **2005**, *102*, 5944-5948.

161. Kumari, H.; Mossine, A.V.; Kline, S.R.; Dennis, C.L.; Fowler, D.A.; Teat, S.J.; Barnes, C.L.; Deakyne, C.A.; Atwood, J.L. *Angew. Chem. Int. Ed.*, **2012**, *51*, 1452-1454.

162. Dalgarno, S.J.; Tucker, S.A.; Bassil, D.B.; Atwood, J.L. *Science*, **2005**, *309*, 2037-2039.

163. Hardie, M.J. *Chem. Soc Rev.*, **2010**, *39*, 516-527.

164. Collet, A.; Dutasta, J.-P.; Lozach, B.; Canciell, J. In *Supramolecular Chemistry I – Directed Synthesis and Molecular Recognition*; Weber, E., Ed.; Springer, Berlin, 1993; Vol. 165, Chapter 3, pp 103-129.

165. Brotin, T.; Dutasta, J.-P. *Chem. Rev.*, **2009**, *109*, 88-130.

166. Henkelis, J.J.; Hardie, M.J. *Chem. Commun.*, **2015**, *51*, 11929-11943.

167. Lindsey, A.S. *Chem. Ind.*, **1963**, 823-824.

168. Erdtman, H.; Ryhage, R.; Haglid, F. *Acta Chem. Scand.*, **1964**, *18*, 1249-1254.

169. Lindsey, A.S. *J. Chem. Soc.*, **1965**, 1685-1692.

170. Gabard, J.; Collet, A. *J. Chem. Soc., Chem. Commun.*, **1981**, 1137-1139.

171. Collet, A. *Tetrahedron*, **1987**, *43*, 5725-5759.

172. Hardie, M.J.; Ahmad, R.; Sumby, C.J. *New J. Chem.*, **2005**, *29*, 1231-1240.

173. Wytko, J.A.; Boudon, C.; Weiss, J.; Gross, M. *Inorg. Chem.*, **1996**, *35*, 4469-4477.

174. Holman, K.T.; Orr, G.W.; Atwood, J.L.; Steed, J.W. *Chem. Commun.*, **1998**, 2109-2110.

175. Staffilani, M.; Bonvicini, G.; Steed, J.W.; Holman, K.T.; Atwood, J.L.; Elsegood, M.R.J. *Organometallics*, **1998**, *17*, 1732-1740.

176. Steed, J.W.; Junk, P.C.; Atwood, J.L.; Barnes, M.J.; Raston, C.L.; Burkhalter, R.S. *J. Am. Chem. Soc.*, **1994**, *116*, 10346-10347.

177. Konarev, D.V.; Khasanov, S.S.; Vorontsov, I.I.; Saito, G.; Antipin, M.Y.; Otsuka, A.; Lyubovskaya, R.N. *Chem. Commun.*, **2002**, 2548-2549.

178. Rio, Y.; Nierengarten, J.F.; *Tetrahedron Lett.*, **2002**, *43*, 4321-4324.

179. Westcott, A.; Fisher, J.; Harding, L.P.; Rizkallah, P.; Hardie, M.J. *J. Am. Chem. Soc.*, **2008**, *130*, 2950-2951.

180. Henkelis, J.J.; Ronson, T.K.; Harding, L.P.; Hardie, M.J. *Chem. Commun.*, **2011**, *47*, 6560-6562.

181. Ronson, T.K.; Fisher, J.; Harding, L.P.; Rizkallah, P.J.; Warren, J.E.; Hardie, M.J. *Nature Chem.*, **2009**, *1*, 212-216.

182. Ronson, T.K.; Fisher, J.; Harding, L.P.; Hardie, M.J. *Angew. Chem. Int. Ed.*, **2007**, *46*, 9086-9088.

183. Hardie, M.J.; Godfrey, P.D.; Raston, C.L. *Chem. Eur. J.*, **1999**, *5*, 1828-1833.

184. Sumby, C.L.; Hardie, M.J. *Angew. Chem. Int. Ed.*, **2005**, *44*, 6395-6399.

185. Hardie, M.J.; Raston, C.L. *Angew. Chem. Int. Ed.*, **2000**, *39*, 3835-3839.

186. Hardie, M.J.; Raston, C.L. *Chem. Commun.*, **2001**, 905-906.

187. Henkelis, J.J.; Carruthers, C.J.; Chambers, S.E.; Clowes, R.; Cooper, A.I.; Fisher, J.; Hardie, M.J. *J. Am. Chem. Soc.*, **2014**, *136*, 14393-14396.

188. Han, X.; Li, L.; Huang, Z.; Liu, J.; Zheng, Q. *Chin. J. Chem.*, **2013**, *31*, 617-623.

189. Song, J.; Huang, Z.; Zheng, Q. *Chin. J. Chem.*, **2013**, *31*, 577-581.

190. Thomas, J.M. *Chem. Commun.*, **2017**, 9179-9184.

191. Langmuir, I. *J. Am. Chem. Soc.*, **1918**, *40*, 1361-1402.

192. Brunauer, S.; Deming, L.S.; Deming, W.E.; Teller, E. *J. Am. Chem. Soc.*, **1940**, *62*, 1723-1732.

193. Yang, Q.-Y.; Lama, P.; Sen, S.; Lusi, M.; Chen, K.-J.; Gao, W.-Y.; Shivanna, M.; Pham, T.; Hosono, N.; Kusaka, S.; Perry IV, J.J.; Ma, S.; Space, B.; Barbour, L.J.; Kitagawa, S.; Zaworotko, M.J. *Angew. Chem. Int. Ed.*, **2018**, *57*, 5684-5689.

194. Serre, C.; Millange, F.; Thouvenot, C.; Noguès, M.; Marsolier, G.; Louër, D.; Férey, G. *J. Am. Chem. Soc.*, **2002**, *124*, 13519-13526.

195. Kitaura, R.; Seki, K.; Akiyama, G.; Kitagawa, S. *Angew Chem. Int. Ed.*, **2003**, *42*, 428-431.

196. Bon, V.; Klein, N.; Senkovska, I.; Heerwig, A.; Getzschmann, J.; Wallacher, D.; Zizak, I.; Brzhezinskaya, M.; Mueller, U.; Kaskel, S. *Phys. Chem. Chem. Phys.*, **2015**, *17*, 17471-17479.

197. Langmuir, I. *J. Am. Chem. Soc.*, **1915**, *37*, 1139-1167.

198. Brunauer, S.; Emmett, P.H.; Teller, E. *J. Am. Chem. Soc.*, **1938**, *60*, 309-319.

199. Yaghi, O.M.; Li, H. *J. Am. Chem. Soc.*, **1995**, *117*, 10401-10402.

200. Li, J.-R.; Kuppler, R.J.; Zhou, H.-C. *Chem. Soc. Rev.*, **2009**, *38*, 1477-1504.

201. Li, J.-R.; Sculley, J.; Zhou, H.-C. *Chem. Rev.*, **2012**, *112*, 869-932.

202. Shimizu, G.K.H.; Ramanathan, V.; Taylor, J.M. *Chem. Soc. Rev.*, **2009**, *38*, 1430-1449.

203. Chandler, B.D.; Enright, G.D.; Pawsey, S.; Ripmeester, J.A.; Cramb, D.T.; Shimizu, G.K.H. *Nat. Mater.*, **2008**, *7*, 229-235.

204. Ribas, X.; Maspoch, D.; Wurst, K.; Veciana, J.; Rovira, C. *Inorg. Chem.*, **2006**, *45*, 5383-5392.

205. Finn, R.C.; Zubieta, J. and Haushalter, R.C. In *Progress in Inorganic Chemistry*; Karlin, K.D., Ed.; Wiley, New York, 2002; Volume 51, Chapter 5, pp 421.

206. Clearfield, A. In *Progress in Inorganic Chemistry*; Karlin, K.D., Ed.; Wiley, New York, 1997; Volume 47, pp 371-510.

207. Bao, S.S.; Zheng, L.M.; Liu, Y.J.; Xu, W.; Feng, S. *Inorg. Chem.*, **2003**, *42*, 5037-5039.

208. Kitagawa, S.; Kitaura, R.; Noro, S. *Angew. Chem. Int. Ed.*, **2004**, *43*, 2334-2375.

209. Yaghi, O.M.; O'Keeffe, M.; Ockwig, N.W.; Chae, H. K.; Eddaoudi, M.; Kim, J. *Nature*, **2003**, *423*, 705-714.

210. Long, J.R.; Yaghi, O.M. *Chem. Soc. Rev.*, **2009**, *38*, 1213-1214.

211. Phan, A.; Doonan, C.J.; Uribe-Romo, F.J.; Knobler, C.B.; O'Keeffe, M.; Yaghi, O.M. *Acc. Chem. Res.*, **2010**, *43*, 58-67.

212. Cai, W.; Chu, C.C.; Liu, G.; Wang, Y.X.J. *Small*, **2015**, *11*, 4806-4822.

213. Giménez-Marqués, M.; Hidalgo, T.; Serre, C.; Horcajada, P. *Coord. Chem. Rev.*, **2015**, *307*, 342-360.

214. Kathalikkattil, A.C.; Babu, R.; Tharun, J.; Roshan, R.; Park, D.W. *Catal. Surv. Asia*, **2015**, *19*, 223-235.

215. Bhattacharjee, S.; Lee, Y.-R.; Puthiaraj, P.; Cho, S.-M.; Ahn, W.-S. *Catal. Surv. Asia*, **2015**, *19*, 203-222.

216. Adatoz, E.; Avci, A.K.; Keskin, S. *Sep. Purif. Technol.*, **2015**, *152*, 207-237.

217. Li, J.R.; Ma, Y.; McCarthy, M.C.; Sculley, J.; Yu, J.; Jeong, H.-K.; Balbuena, P.B.; Zhou, H.-C. *Coord. Chem. Rev.*, **2011**, *255*, 1791-1823.

218. Cheetham, A.K.; Rao, C.N.R.; Feller, R.K. *Chem. Commun.*, **2006**, 4780-4795.

219. Wang, Z.Q.; Cohen, S.M. *Chem. Soc. Rev.* **2009**, *38*, 1315-1329.

220. Tranchemontagne, D.J.; Mendoza-Cortes, J.L.; O'Keeffe, M.; Yaghi, O.M. *Chem. Soc. Rev.*, **2009**, *38*, 1257-1283.

221. Ockwig, N.W.; Delgado-Friedrichs, O.; O'Keeffe, M.; Yaghi, O.M. *Acc. Chem. Res.*, **2005**, *38*, 176-182.

222. Farha, O.K.; Eryazici, I.; Jeong, N.C.; Hauser, B.G.; Wilmer, C.E.; Sarjeant, A.A.; Snurr, R.Q.; Nguyen, S.S.; Yazaydin, A.O.; Hupp, J.T. *J. Am. Chem. Soc.*, **2012**, *134*, 15016-15021.

223. Wang, T.C.; Bury, W.; Gómez-Gualdrón, D.A.; Vermeulen, N.A.; Mondloch, J.E.; Deria, P.; Zhang, K.; Moghadam, P.Z.; Sarjeant, A.A.; Snurr, R.Q.; Stoddart, J.F.; Hupp, J.T.; Farha, O.K. *J. Am. Chem. Soc.*, **2015**, *137*, 3585-3591.

224. Matthews, H.D.; Gillett, N.P.; Stott, P.A.; Zickfeld, K. *Nature*, **2009**, *459*, 829-832.

225. Mu, B.; Walton, K.S. *J. Chem. Eng. Data*, **2011**, *56*, 390-397.

226. Wang, T.; Ge, K.; Chen, K.; Hou, C.; Fang, M. *Phys. Chem. Chem. Phys.*, **2016**, *18*, 13084-13091.

227. Wang, T.; Lackner, K.S.; Wright, A. *Environ. Sci. Technol.*, **2011**, *45*, 6670-6675.

228. D'Alessandro, D.M.; Smit, B.; Long, J.R. *Angew. Chem. Int. Ed.*, **2010**, *49*, 6058-6082.

229. Thallapally, P.K.; Lloyd, G.O.; Wirsig, T.B.; Bredenkamp, M.W.; Atwood, J.L.; Barbour, L.J. *Chem. Commun.*, **2005**, 5272-5274.

230. Thallapally, P.K.; McGrail, B.P.; Atwood, J.L.; Gaeta, C.; Tedesco, C.; Neri, P. *Chem. Mat.*, **2007**, *19*, 3355-3357.

Chapter 2 – Experimental

2.1. Materials

Formaldehyde solution (>34.5 wt. %) and veratrole (>99 %) were purchased from Sigma Aldrich (Germany) and used as received. Cyclotriveratrylene (CTV) was synthesized *via* a literature method.[1] 5 mL of veratrole was mixed with 11 mL of 70 % sulfuric acid in a round-bottomed flask. The formaldehyde solution was added dropwise with stirring. The product was purified by refluxing in 37.5 mL ethanol and collecting the precipitate by hot filtration, followed by recrystallization of the precipitate from benzene.

C-methylcalix[4]resorcinarene was purchased from Sigma Aldrich (Germany) and used as received.

2.2. Methods of Preparation

2.2.1. Crystallization Procedures

Generally, crystals were obtained by slow evaporation. However, crystallization procedures will be discussed in more detail at the beginning of the respective results chapters.

2.2.2. Liquid-Assisted Grinding (LAG)

Liquid-assisted grinding (LAG) is a method in which one or more solids are ground together with the addition of a few drops of liquid using a mortar and pestle for a certain period of time, resulting in a powder which can then be used for powder X-ray diffraction. The PXRD pattern obtained can then be compared to the calculated pattern obtained from a single crystal X-ray diffraction experiment, in order to confirm the identity of the powder. Materials which can be produced by LAG in addition to crystallization therefore have the advantage that LAG is generally a much faster preparation method than waiting for crystallization to occur.

2.3. Thermal analysis

Three thermal analysis techniques were employed, namely hot stage microscopy (HSM), thermogravimetric analysis (TGA) and differential scanning calorimetry (DSC).

2.3.1. Hot Stage Microscopy (HSM)

Hot Stage Microscopy (HSM) allows visual observation of thermal events indicated in the TGA and DSC thermograms, as well as those not detected by TGA or DSC. These changes can include loss of monocrystallinity, indicated by opacification of the crystals, and colour changes. In order to observe solvent loss, single crystals were covered by silicone oil and placed on a glass slide. The solvent loss can then be seen as bubbles evolving from the crystals. The temperatures at which events were observed in the HSM analyses generally showed a lag, (i.e. at observed higher temperatures) compared to those observed with DSC or TGA. This is probably due to the difference in particle size, as well as the fact that the HSM needs to heat up the oil as well as the sample, hence heating a greater volume of material.

HSM was performed on a Nikon SMZ-10 stereoscopic microscope fitted with a Linkam THMS600 hot stage and a Linkam TP92 control unit. Samples were placed under silicone oil on a cover slip and heated at 10 °C min^{-1}. Thermal events were monitored with a Sony Digital Hyper HAD colour video camera and captured using the Soft Imaging System program, analySIS.[2]

2.3.2. Thermogravimetric Analysis (TGA)

Thermogravimetric analysis (TGA) studies were employed to confirm the number and type of guest molecules, if discrete, non-overlapping thermal events occurred, and to determine the temperature of melting/decomposition. Before TG experiments were performed, samples were removed from the vials with a spatula and thoroughly surface dried on filter paper.

TG analysis was performed using a TA-Q500 Thermogravimetric Analyser from TA Instruments with the TA Universal Analysis program and a 60 mL min^{-1} dry nitrogen purge gas flow rate. The samples (1–3.5 mg) were weighed directly into an open aluminium oxide crucible. During the experiments the sample holder was continuously purged with a dry nitrogen flow of 60 mL min^{-1}. Measurements were performed using a heating rate of 10 °C min^{-1}.

2.3.3. Differential Scanning Calorimetry (DSC)

Differential Scanning Calorimetry (DSC) measures the difference in heat flow between the sample and a reference pan in order to change their temperatures at the same rate and thus requiring differential heating rates when thermal events occur. The enthalpies of different thermal events as well as the melting point temperature of the sample can be determined in this manner. Crystals were removed from the vials and carefully surface dried before DSC studies. The sample was then transferred to a closed, vented aluminium pan. For all runs, samples weighed approximately 1–2 mg. Endothermic and exothermic events are shown in the DSC traces by troughs and peaks, respectively.

DSC was performed using a TA Instruments Discovery 25 instrument which was calibrated using standard materials. The sample was weighed directly into an aluminium pan with a lid, on an analytical balance. Two small holes were created in the lid to allow for venting. During the experiment, the sample holder was continuously purged with a dry nitrogen flow of 40 mL min^{-1}.

Measurements in the DSC were done using a heating rate of 10 °C min^{-1}. Data were analysed using the TRIOS Software program from TA Instruments.

2.4. X-Ray Diffraction

2.4.1. Single crystal X-ray diffraction (SCXRD) analysis and structure determination

Suitable single crystals were selected and mounted on a cryoloop in paratone N oil.[3] In a few cases, crystallization yielded large, single crystals or clusters of crystals necessitating crystal cutting to obtain an appropriately sized crystal or to isolate a monocrystalline fragment. Data collection, in most cases, was carried out on a Bruker KAPPA APEX II DUO single crystal X-ray diffractometer using graphite monochromated Mo Kα (λ = 0.71073 Å) radiation, produced at 50 kV and 30 mA using a Bruker K780 generator.[4] Cooling was obtained with a constant stream of nitrogen gas produced by an Oxford Cryostream–700 (Oxford Cryosystems, UK) at a flow rate of 20 mL min^{-1}. A new single crystal X-ray diffractometer was obtained towards the end of this project and this was used for data collection of compounds **9** and **10**. This diffractometer is a Bruker D8 VENTURE single crystal X-ray diffractometer using Mo Kα (λ = 0.71073 Å) or Cu Kα (λ = 1.54178 Å) radiation, produced at 50 kV and 1.4 mA using a Bruker K430 generator.[4] Cooling was obtained with a constant stream of nitrogen gas produced by an Oxford Cryostream–800 (Oxford Cryosystems, UK) at a flow rate of 6 mL min^{-1}. Data reduction and cell refinement were performed using SAINT-Plus.[5] The X-ray diffraction data were scaled and corrected for absorption using SADABS.[6]

The X-ray data was then analysed and the space group was suggested by the XPREP[7] program which also prepared the input files for structure solution. The structure was solved by direct methods, implemented in SHELXS-97.[8] Refinement proceeded by the full-matrix least-squares method, based on F^2 values against all reflections as implemented in SHELXL-2014/7 or SHELXL-2018/1 or, in the case of the literature structure **5**, SHELXL-97, with anisotropic displacement parameters for all non-H atoms.[8] When all non-hydrogen atoms refined satisfactorily with isotropic temperature factors, they were refined anisotropically. Reflections at low angles and with observed intensities significantly lower than the calculated value were omitted due to potential truncation of these reflections by the beam-stop. The hydrogen atoms were placed in idealized positions in a riding model. All hydrogen atoms were refined isotropically and assigned temperature factors that relate to the atom they are attached to. The hydrogen atoms on the water molecules were not modelled. SHELXS-97, SHELXL-2014/7 and SHELXL-2018/1 were accessed via either the X-SEED[9] or OLEX2[10] interfaces. The data file extensions for each program and this data can be found in the Appendix.

2.4.2. Powder X-ray diffraction (PXRD)

For each compound, the single crystal X-ray data (unit cell parameters, space group symmetry, and atomic coordinates) were input in the program MERCURY.[11] This program then produces idealized Powder X-Ray Diffraction (PXRD) patterns using the same wavelength as that used experimentally (λ = 1.5406 Å) and the formula $I(hkl) = mLp|F(hkl)|^2$. $I(hkl)$ is the intensity of the reflections with diffraction indices hkl, m is the reflection multiplicity, L is the Lorentz factor, p is the polarization factor and $F(hkl)$ is the structure factor. This predicted pattern is compared to the experimentally obtained pattern to determine whether or not the single crystal is representative of the bulk sample. PXRD is also used to determine whether the desired compound has been obtained in subsequent experiments, either through crystallization or by liquid-assisted grinding (LAG) with a mortar and pestle.

For both PXRD and variable-temperature powder X-ray diffraction (VT-PXRD), powders were mounted on a flat (zero-background for regular PXRD) sample holder. X-ray powder data were collected in a Bruker D8 Advance X-ray diffractometer with copper radiation (Cu Kα, λ = 1.5406 Å) generated at 30 kV and 40 mA. Each sample was scanned between 4 and 40° 2θ with a scan rate step size of 0.02° s^{-1}.

VT-PXRD experiments were performed to reveal whether structural changes occurred as a result of solvent removal (due to a temperature increase) and whether the compound maintained crystallinity with an increase in temperature. This is desirable since it is preferable for porous compounds to maintain long-range order after solvent removal. The patterns obtained from VT-PXRD also reveal any structural changes with temperature.

The regular PXRD stage was rotated during each data collection to correct for preferred orientation effects, while this was not possible for the VT-PXRD data collections due to the way the sample stage is set up.

2.5. Gas Sorption Studies

2.5.1. Gas Sorption Analyser

Gas and vapour sorption studies were performed to investigate the ability of the compounds to adsorb gases, for example carbon dioxide and nitrogen. These experiments were carried out using a Micromeritics 3Flex Surface Area Analyser. Sample sizes in the range 50–150 mg were treated in a Micromeritics Flowprep with a constant flow of nitrogen gas over the sample for at least 12 hours and heating at 60 °C in order to evacuate the compound of as much solvent as possible before further *in situ* evacuation occurred on the 3Flex analyser, which involved heating of the sample between 60–125 °C under vacuum. Great care was taken to ensure that the preparation methods succeeded by carefully monitoring increase in pressures at vacuum/low pressures, as well as weighing of samples after treatment to make sure that masses were close to expected values as suggested by TGA analysis. This ensured the removal of any solvent still present in the compound as an empty framework was required for the analysis. A Micromeritics water bath was used for experiments performed at 273 K or 298 K, while liquid nitrogen was used for experiments performed at 77 K.

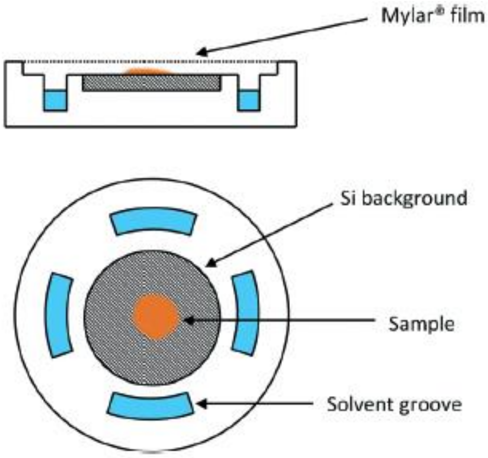

Figure 2.1: Side-on and top views of the sample holder.[12]

For *in* situ PXRD 1-propanol vapour sorption, powders were mounted on a specially-constructed zero-background sample holder (Fig. 2.1).[12] X-ray powder data were collected in a Bruker D8 Advance X-ray diffractometer with copper radiation (Cu Kα, λ = 1.5406 Å) at 30 kV and 40 mA. Each sample was scanned between 4 and 40° 2θ with a scan rate step size of 0.02° s^{-1}. The PXRD patterns were recorded at ambient temperature at intervals of 46.5 min.

2.6. Additional Computer Packages

The Cambridge Structural Database[13] (CSD) was used to assess the novelty of the reported structures. The CSD was also employed to obtain literature structures for certain compounds. MERCURY[11] was used as a graphical interface for POV-RAY.[14] The molecular structures and crystal packing diagrams were drawn using POV-RAY accessed through MERCURY,[11] which was also used to generate calculated powder patterns. MERCURY was also used to assist in studying the three-dimensional shapes of cavities or channels. The analysis of molecular parameter and geometrical data were calculated using PLATON.[15-16] Specifically, hydrogen bonds D–H···A (where D is the donor atom, H is the hydrogen atom and A is the acceptor atom) were assigned using the default PLATON definition of the distance D···A (Å) < radius of D (Å) + radius of A (Å) + 0.50 Å and the distance H···A (Å) < radius of H (Å) + radius of A (Å) – 0.12 Å and the angle D–H···A > 100.0°. D–H···π interactions were assigned using the default PLATON definition of the distance H···centroid < 3.0 Å and the angle between H···centroid vector and the line perpendicular to the centroid < 30°.

2.7. References

1. Zhang, H.; Atwood, J.L. *J. Crystallogr. and Spec. Res.*, **1990**, *20*, 465-470.
2. Soft Imaging System GmbH: Digital Solutions for Imaging and Microscopy, Version 3.1 for Windows, © **1987-2000**.
3. Paratone N oil, (Exxon Chemical Co., Tx, USA).
4. APEX2, Version 1.0-27, Bruker AXS Inc., Madison, Wisconsin, USA.
5. *Bruker (2007)*, Bruker AXS Inc., Madison, Wisconsin USA, **2007**.
6. Sheldrick, G.M. *SADABS*, Bruker AXS Inc., Madison, Wisconsin USA, **2001**.
7. XPREP, *Data Preparation and Reciprocal Space Exploration*, Version 5.1, © Bruker Analytical X-ray Systems, **1997**.
8. Lubben, J.; Wandtke, C.M.; Sheldrick, G.M.; Hubschle, C.B.; Ruf, M.; Dittrich, B. *Acta Crystallogr., Sect. A: Found. And Adv.*, **2019**, *75 (Pt 1)*, 50-62.
9. Barbour, L.J. *J. Supramol. Chem.*, **2001**, *1*, 189.
10. Dolomanov, O.V.; Bourhis, L.J.; Gildea, R.J.; Howard, J.A.K.; Puschmann, H. *J. Appl. Cryst.*, **2009**, *42*, 339-341.
11. Macrae, C.F.; Bruno, I.J.; Chisholm, J.A.; Edgington, P.R.; McCabe, P.; Pidcock, E.; Rodriguez-Monge, L.; Taylor, R.; van de Streek, J.; Wood, P.A. *J. Appl. Cryst.*, **2008**, *41*, 466-470.
12. Sykes, N.M.; Su, H.; Weber, E.; Bourne, S.A.; Nassimbeni, L.R. *CrystEngComm*, **2017**, *19*, 5892-5896.
13. The Cambridge Structural Database, Groom, C.R.; Bruno, I.J.; Lightfoot, M.P.; Ward, S.C. *Acta Cryst.*, **2016**, *B72*, 171-179.

14. POV-Ray for Windows, Version 3.6, The Persistence of Vision Development Team, © **1991** – **2003**.
15. Spek, A.L. Program PLATON, A Multipurpose Crystallographic Tool, Version 10500, © **1980** – **2000**, Utrecht University, The Netherlands.
16. Spek, A.L. *J. Appl. Cryst.*, **2003**, *36*, 7.

Chapter 3 – Preparation and Analysis of Cyclotriveratrylene Solvates

3.1. Introduction

2,3,7,8,12,13-hexamethoxy-10,15-dihydro-5*H*-tribenzo[a,d,g][9]annulene, known as cyclotriveratrylene (CTV), is a cyclic trimer of veratrole (Fig. 3.1) and acts as a bowl-shaped molecular receptor, able to bind small ions or molecules.[1-3] Methylene bridges link three 4,5-dimethoxybenzene rings in a 1-2 fashion to form the CTV molecule. CTV is related to calix[*n*]arenes (where *n* is usually 4, 6 or 8) but is less common in terms of the diversity of inclusion complexes prepared and their variety of applications.[1,4] Molecules with CTV as a foundation have been used in various applications, including as coordination polymers and as constituents of cage-like, discrete, metallo-supramolecular assemblies.[5-7] Their ability to bind guests such as C_{60} and anionic C_{70} dimers, lanthanides and xenon has led to functionalized CTV derivatives being used for biomedical applications such as magnetic resonance imaging (MRI)-based diagnostic techniques and the distribution of fullerenes as cytotoxic anti-tumour agents.[8-14] CTV and related structures have also been utilized as precursors for cryptophanes and cavitands,[1,15-21] where they bind smaller guest molecules.[22-24] However, very little investigation has been done on porous structures containing CTV or its analogues.

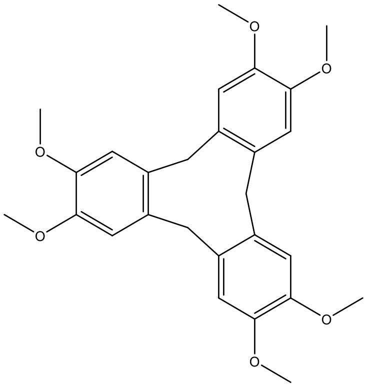

Figure 3.1: The structural formula of cyclotriveratrylene (CTV).

Presented in this chapter are the syntheses of several novel CTV inclusion compounds containing various solvents, chosen based on their polarity and their ability to solubilize CTV. These compounds have been characterized by X-ray diffraction and thermal analysis. One of the compounds has also shown a SC–SC transformation upon desolvation. After desolvation, all of the compounds were subjected to gas and/or vapour sorption studies.

3.2. Experimental Procedures

3.2.1. Materials

A formaldehyde solution (> 34.5 wt%) and veratrole (> 99 %) were purchased from Sigma Aldrich and used as received. CTV was synthesized *via* a literature method.[25] Veratrole (5 mL, 39.23 mmol) was mixed with 70 % sulfuric acid (11 mL) in a round-bottomed flask. A two-fold excess of 34.5 % formaldehyde (6.25 mL, 78.27 mmol) was added dropwise with stirring. The solution was allowed to stir for 24 h. The purple mixture was then vacuum-filtered, washing three times with water. The purple solid obtained was then dissolved in ethanol (37.5 mL) and refluxed for 2 h. The precipitate was collected by vacuum filtration and recrystallised from benzene. The solution was once again vacuum-filtered, yielding the pure CTV as a grey powder.

3.2.2. Preparation of crystal forms

3.2.2.1. CTV-acetonitrile solvate 1 ($(C_{27}H_{30}O_6)_2 \cdot CH_3CN$) (**1**)

CTV (60 mg) was dissolved in 1:1 v/v acetonitrile:chloroform (5 mL total volume) with stirring. The vial containing the resulting solution was then covered with perforated parafilm. Slow evaporation of the solvents led to the appearance of rectangular brown crystals after 7 – 10 days.

3.2.2.2. CTV-acetonitrile solvate 1 post-desolvation ($(C_{27}H_{30}O_6)_2$) (**1a**)

Crystals of **1** were heated under vacuum at 90 °C for 24 h, yielding the desolvated form **1a**, a process which occurred *via* a SC–SC transformation.

3.2.2.3. CTV-acetonitrile solvate 2 ($(C_{27}H_{30}O_6)_2 \cdot (CH_3CN)_3$) (**2**)

A saturated solution of CTV in acetonitrile was prepared by dissolving CTV (100 mg) in a minimum volume (2 mL) of acetonitrile with heating (60 °C) and stirring to form a saturated solution. The remaining undissolved solid was removed using a needle, a syringe and a 0.45 µm syringe filter. The uncapped vial was allowed to stand at room temperature in order for the solvent to evaporate, resulting in crystals appearing within a few hours.

3.2.2.4. CTV-chloroform ($C_{27}H_{30}O_6 \cdot (CHCl_3)_2$) (**3**)

CTV (60 mg) was dissolved in chloroform (5 mL) with stirring. The vial was covered with perforated parafilm and allowed to stand at room temperature in order for the solvent to evaporate, leading to the appearance of crystals after a few days.

3.2.2.5. CTV-2-butanone ($(C_{27}H_{30}O_6)_4 \cdot C_4H_8O$) (**4**)

CTV (100 mg) was dissolved in 2 mL of 2-butanone with stirring and mild heating (50 °C). The vial was allowed to stand uncapped and covered with perforated parafilm. Slow evaporation of the solvent leads to the appearance of crystals after a few days.

3.2.3. Liquid-Assisted Grinding

Compounds **1** and **4** could also be prepared by liquid-assisted grinding in the presence of acetonitrile and 2-butanone, respectively. The CTV host was placed in a mortar and ground with a pestle after the addition of several drops of acetonitrile to make a paste. Grinding proceeded for 10 minutes.

3.3. Characterization Results & Discussion

3.3.1. CTV-acetonitrile solvate 1 ($(C_{27}H_{30}O_6)_2 \cdot CH_3CN$) (**1**) and CTV-acetonitrile solvate 1 post-desolvation ($(C_{27}H_{30}O_6)_2$) (**1a**)

3.3.1.1. Single Crystal X-ray Diffraction Analysis

1 crystallised from acetonitrile in the monoclinic space group $P2_1/c$, with single crystal X-ray structure analysis revealing that the asymmetric unit (ASU) of **1** contains two unique CTV molecules and one acetonitrile molecule (Table 3.1 and Fig. 3.2).

Table 3.1: Crystal data and refinement parameters for **1** and **1a**.

	1	**1a**
Empirical formula	$(C_{27}H_{30}O_6)_2 \cdot CH_3CN$	$(C_{27}H_{30}O_6)_2$
Formula weight	942.07	901.02
Temperature (K)	173.15	153.15
Crystal system	Monoclinic	Monoclinic
Space group	$P2_1/c$	$P2_1/c$
a (Å)	18.7531(8)	18.606(2)
b (Å)	25.0061(11)	24.551(3)
c (Å)	10.5276(5)	10.4027(13)
α (°)	90	90
β (°)	91.2590(10)	90.819(3)
γ (°)	90	90
Volume (Å^3)	4 935.6(4)	4 751.5(10)
Z	4	4
ρ_{calc} (g.cm^{-3})	1.268	1.260
μ (mm^{-1})	0.089	0.088
F(000)	2 008	1 920
Crystal size (mm^3)	0.30 x 0.20 x 0.10	0.60 x 0.33 x 0.24
Radiation	MoKα (λ = 0.71073 Å)	MoKα (λ = 0.71073 Å)
2ϑ range for data collection (°)	2.714 – 59.034	2.746 – 52.944
Index ranges	$-25 \leq h \leq 25, -34 \leq k \leq 32, -14 \leq l \leq 14$	$-23 \leq h \leq 22, -30 \leq k \leq 30, -12 \leq l \leq 13$
Reflections collected	112 892	48 505
Independent reflections	13 782 [R_{int} = 0.0792, R_{sigma} = 0.0468]	9 790 [R_{int} = 0.0362, R_{sigma} = 0.0310]
Data/restraints/parameters	13 782/0/635	9 790/0/607
Goodness-of-fit on F^2	1.023	1.027
Final R indexes [$I \geq 2\sigma(I)$]	R_1 = 0.0476, wR_2 = 0.1117	R_1 = 0.0444, wR_2 = 0.1005
Final R indexes [all data]	R_1 = 0.0925, wR_2 = 0.1322	R_1 = 0.0696, wR_2 = 0.1122
Largest diff. peak/hole (e.Å^{-3})	0.36/-0.25	0.68/-0.38

One of the unique CTV molecules forms dimeric, centrosymmetric capsules which encapsulate two acetonitrile molecules per capsule (Fig. 3.2a), while the second unique CTV molecule stacks to form columns of partially self-included CTV molecules (Fig. 3.2b). The stacked columns and dimers are arranged in alternating 2D layers in the *bc* plane which stack along the *a*-axis (Fig. 3.2c). No classic hydrogen bonds are present, but five unique C–H···O hydrogen bonds and two unique C–H···π interactions are involved in host-host and host-solvent interactions (Table 3.2).

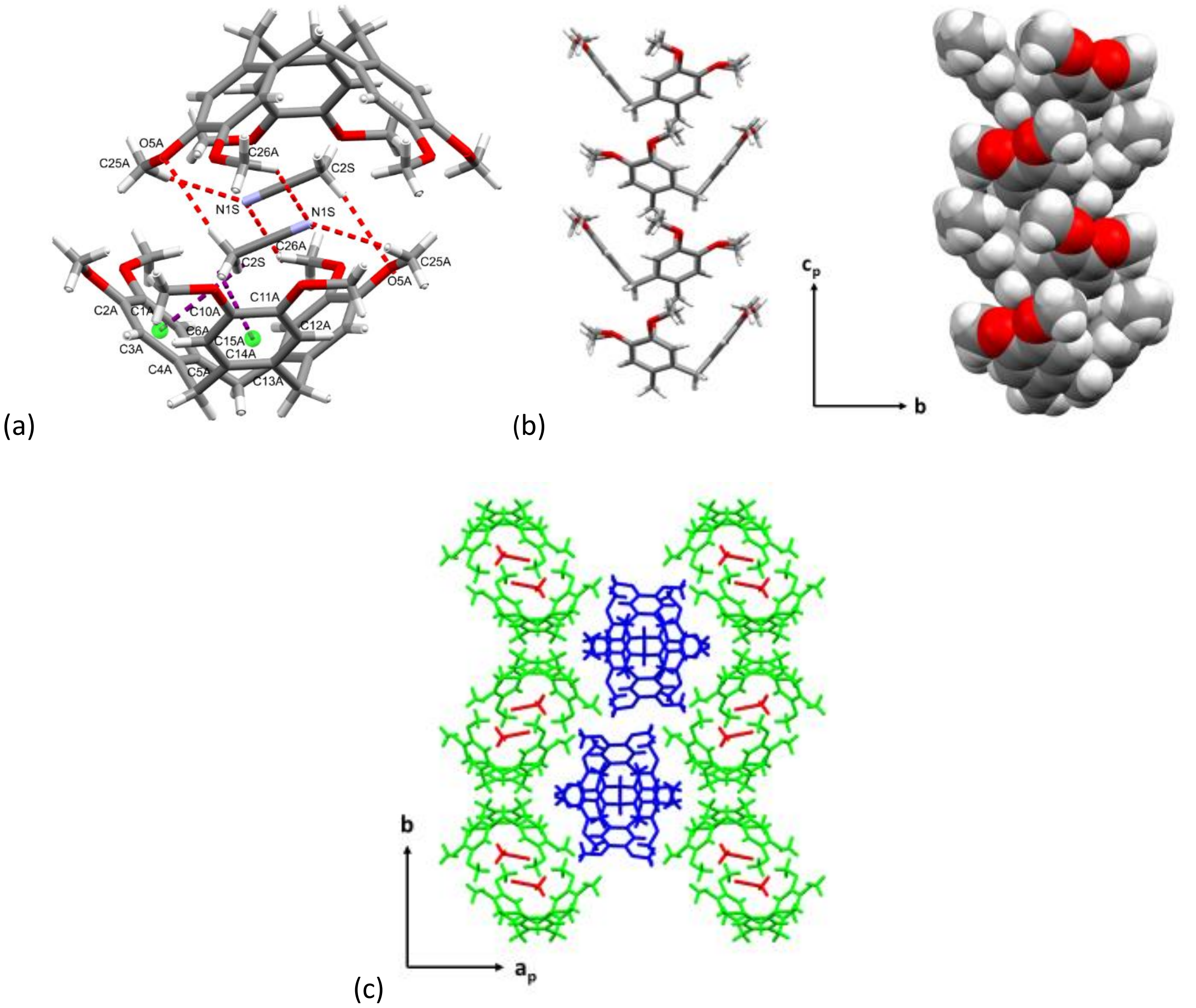

Figure 3.2: (a) Centrosymmetric dimer formed by one of the ASU CTV molecules. Hydrogen bonds are displayed in red and C–H···π interactions in purple. Green spheres represent centroids of aromatic rings involved in C–H···π interactions (shown only for one molecule of the dimer) (b) stacked columns of the second ASU CTV molecule in capped stick and space-fill styles (c) crystal packing in **1** along the *c*-axis. Crystallographically unique host and solvent molecules are colour-coded.

The CTV molecules of the centrosymmetric dimer are indirectly linked through six host-solvent C–H···O/C–H···N hydrogen bonds, four of which (the unique C25A–H25A···N1S and C26A–H26A···N1S interactions) involve the acetonitrile nitrogen atom acting as a bifurcated hydrogen bond acceptor for CTV methyl hydrogen atoms, and the remaining two (the unique C2S–H2SC···O5A interaction) which involve the CTV methoxy oxygen atom acting as a hydrogen bond acceptor for an acetonitrile methyl hydrogen atom. The acetonitrile molecules also form two unique C–H···π interactions with the dimer CTV molecule (indicated on only one side of the dimer in Figure 3.2(a)).

Table 3.2: Hydrogen bonding parameters for **1** and **1a**.

Bonding atoms	D–H (Å)	H···A (Å)	D···A (Å)	D–H···A (°)	Symmetry operators
1					
C16B–H16D···O1A	0.98	2.48	3.209(2)	131	x, y, -1+z
C2S–H2SC···O5A	0.98	2.57	3.547(2)	172	x, y, z
C25A–H25A···N1S	0.98	2.53	3.458(2)	158	-x, 1-y, 2-z
C25B–H25E···O5A	0.98	2.54	3.390(2)	145	-x, ½+y, 3/2-z
C26A–H26A···N1S	0.98	2.56	3.312(2)	134	x, y, z
C9B–H9BB···Cg14[n]	0.99	2.88	3.8281(16)	162	x, 3/2-y, ½+z
C7B–H7BB···Cg1[a]	0.98	2.99	3.904(2)	156	1-x, ½+y, 3/2-z
C7B–H7BC···Cg12[l]	0.98	2.87	3.5220(19)	125	x, 3/2-y, -½+z
C2S–H2SA···Cg1[a]	0.98	2.97	3.425(2)	110	-x, 1-y, 2-z
C2S–H2SB···Cg2[b]	0.98	2.71	3.5148(19)	140	-x, 1-y, 2-z
C27A–H27A···Cg2[b]	0.99	2.75	3.6197(16)	148	x, ½-y, ½+z
1a					
C7B–H7BB···O6A	0.98	2.47	3.104(2)	122	x, ½-y, -½+z
C8A–H8AB···O5A	0.98	2.49	3.452(3)	167	-x, -y, 3-z
C8B–H8BA···Cg1[a]	0.98	2.98	3.900(2)	157	-x, -y, 2-z
C8B–H8BC···Cg12[l]	0.98	2.90	3.587(2)	128	x, ½-y, ½+z
C25B–H25A···Cg14[n]	0.98	2.91	3.549(2)	124	x, ½-y, ½+z
C27B–H27A···Cg13[m]	0.99	2.87	3.8449(19)	167	x, ½-y, -½+z
C27A–H27D···Cg2[b]	0.99	2.73	3.6115(19)	148	x, -½-y, -½+z

[a] Cg1 (C1A/C2A/C3A/C4A/C5A/C6A), [b] Cg2 (C10A/C11A/C12A/C13A/C14A/C15A), [l] Cg12 (C1B/C2B/C3B/C4B/C5B/C6B), [m] Cg13 (C10B/C11B/C12B/C13B/C14B/C15B), [n] Cg14 (C19B/C20B/C21B/C22B/C23B/C24B)

The unit cell parameters of **1a** are similar to **1** with the retention of the space group symmetry (Table 3.1). The reduction in unit cell volume (~180 Å^3) is probably not only due to the 20 K temperature difference of the respective data collections. The ASU of **1a** contains two CTV molecules with similar packing as observed in **1**, however, the solvent is absent. This was confirmed by thermogravimetric analysis on the bulk sample, which indicated negligible mass loss before decomposition, while the SQUEEZE routine in PLATON[26] revealed a residual electron density of only 6 electrons per unit cell for **1a**.

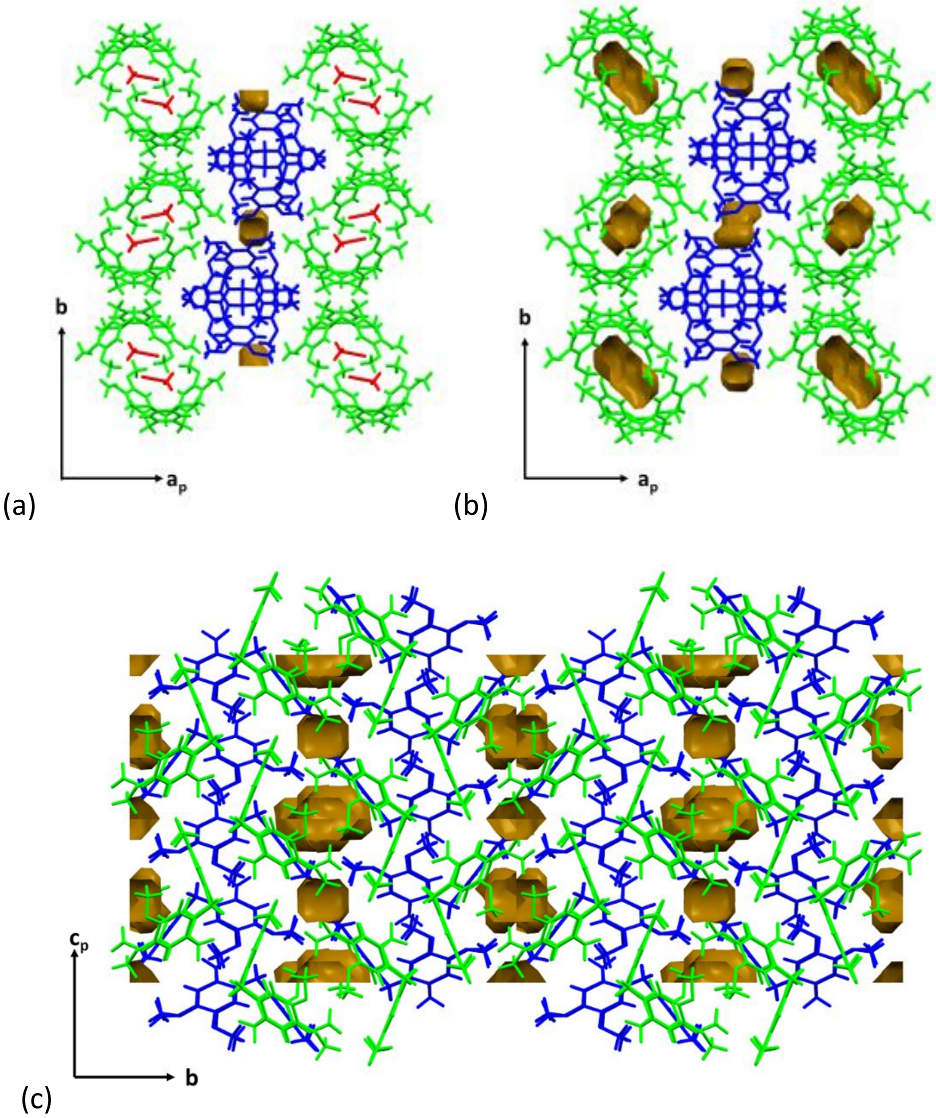

(a) (b)

(c)

Figure 3.3: (a) Crystal packing in **1** displaying isolated voids viewed along the *c*-axis (b) Showing the similar packing and voids in **1a** when viewed along the *c*-axis and (c) Crystal packing in **1a** displaying isolated voids viewed along the *a*-axis.

The total void space for **1a** (Fig. 3.3) calculated by MERCURY,[27] using a probe radius of 1.2 Å, is 158 Å^3 or 3.3 % per unit cell, mainly because of the dimeric capsule cavity. A much smaller part of this unit cell void space, 0.8 % per unit cell, is from the space between the columns of stacked CTV molecules, determined by artificially placing atoms within the dimeric cavities in **1a**. This total void space is smaller than the 289 Å^3 or 5.9 % per unit cell potential total void space calculated for **1**, if the acetonitrile solvent molecule coordinates are deleted, suggesting that the relative host arrangement is slightly different after solvent removal. The potential voids in **1** are discrete, therefore the solvent removal process likely involves cooperative movement of either whole molecules, or their functional groups, in order to retain monocrystallinity as revealed by the SC-SC transformation. It seems that the latter is plausible with the evacuation of the solvent molecules likely occurring along the ~10 Å *c*-axis with at least one unique rotatable methoxy group acting as a 'gate' (Fig. 3.4). This is shown to be a plausible explanation by simply taking one methoxy group of a CTV dimer molecule in **1**, such as O6A-C26A and artificially rotating it by 75° around the O6A-C20A bond so that C26A points away from the dimer cavity. This leads to the cavities of two neighbouring dimers being linked where they were formerly disconnected (Fig. 3.4). This is supported by the fact that two corresponding methoxy groups in **1** and **1a** are found in considerably different orientations as indicated by the corresponding C26A-O6A-C20A-C19A and C7A-O1A-C1A-C2A torsion angles of -170.0(1)° and -80.4(1)° for **1** and **1a**, respectively. In **1a**, the corresponding methoxy group O1A-C7A points towards the interior of the dimeric capsule (Fig. 3.5), which is permitted by the absence of the acetonitrile molecule and supports that a rotatable methoxy group may act as a 'gate' for desolvation.

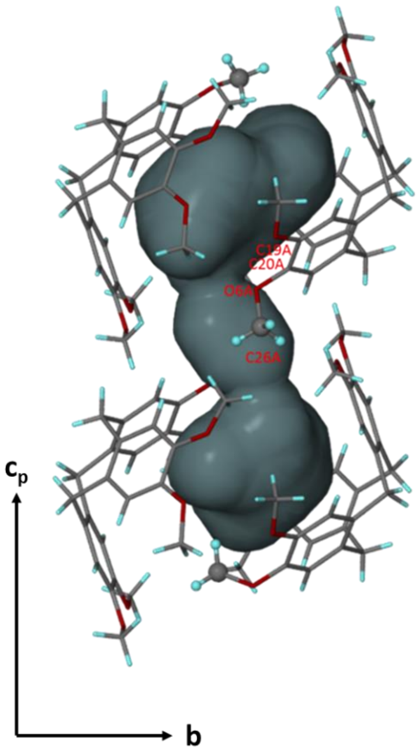

Figure 3.4: Two neighbouring dimers in the structure of **1** viewed along the *a*-axis. Artificial rotation by 75° of the O6 methyl group (displayed in ball-and-stick style) around the O6A-C20A bond away from the dimeric void results in the connection of two neighbouring voids. A probe radius of 1.5 Å was used in the program MSROLL. As MSROLL requires a closed cavity, only the labelled methyl group was manipulated. However, rotation of the centrosymmetrically-related methyl will result in a channel being formed.

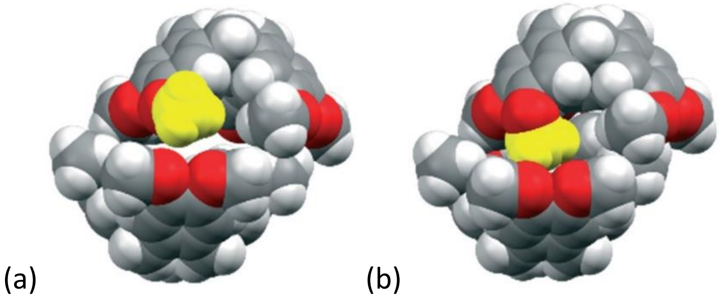
(a) (b)

Figure 3.5: (a) Dimer in **1** with the methyl group coloured in yellow corresponding to methyl group in (b) **1a** that is rotated towards the interior of the cavity.

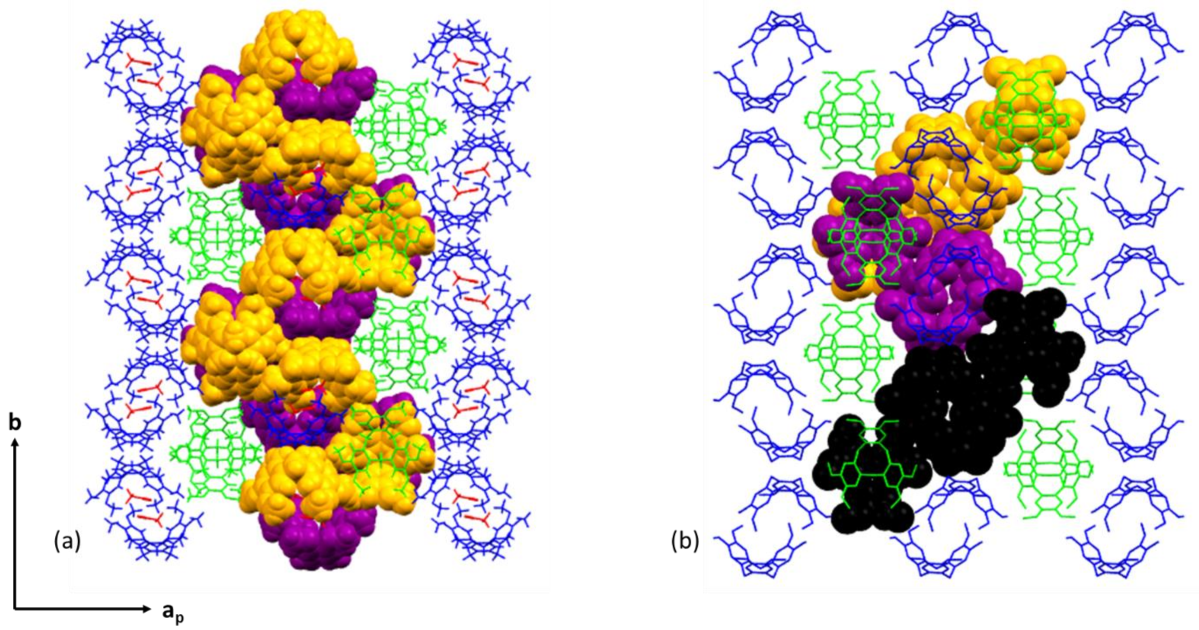

Figure 3.6: CTV molecules shown in space-filling mode and in the same colour are connected *via* C–H···O hydrogen bonds, resulting in 1D zig-zag chains in (a) **1** and isolated tetramers in (b) **1a**. Only selected chains and tetramers are shown for clarity.

In **1**, the remaining two unique C–H···O hydrogen bonds (C16B–H16D···O1A and C25B–H25E···O5A) connect the two asymmetric CTV molecules so that 1D zigzag strands of linked CTV molecules, which consist of dimer and column CTV molecules, are formed along the ~25 Å axis (Fig. 3.6a). In **1a**, the shift of the dimeric CTV molecules closer to each other results in these molecules directly linking to one another by a unique C–H···O hydrogen bond (C8A–H8AB···O5A). A second unique C–H···O hydrogen bond (C7B–H7BB···O6A) links the dimeric capsule to a column CTV molecule on each side of the capsule. As opposed to **1**, these column CTV molecules are not linked to a second dimeric capsule, yielding hydrogen-bonded tetramers (Fig. 3.6b). These tetramers are related to one another by the crystallographic 2_1 axis along the *b*-direction (Fig. 3.6b).

3.3.1.2. Variable-Temperature Powder X-ray Diffraction

Variable-temperature PXRD experiments were performed on **1**, as prepared by LAG, over the temperature range 30-210 °C (Fig. 3.7). The sample was found to be crystalline over the entire temperature range. Note that all VT-PXRDs traces performed have three artefact peaks at 4.6°, 6.9° and 36.1° 2θ – these are caused by the variable-temperature sample holder and will not be referred to hereafter. The 30 °C PXRD pattern matches closely with the calculated PXRD pattern from the single crystal structure of **1**, showing that the preparation was successful and that the single crystal structure is representative of the bulk sample. At 100 °C, the three peaks at 8.4°, 8.9° and 9.2° 2θ are decreasing and the pattern agrees more closely with the calculated PXRD pattern of **1a**. From 130-200 °C, the appearance of peaks of increasing intensities at 8.2° and 9.1° 2θ suggests that **1a** transforms to another polymorph, **1b**, a second desolvated form of **1**.

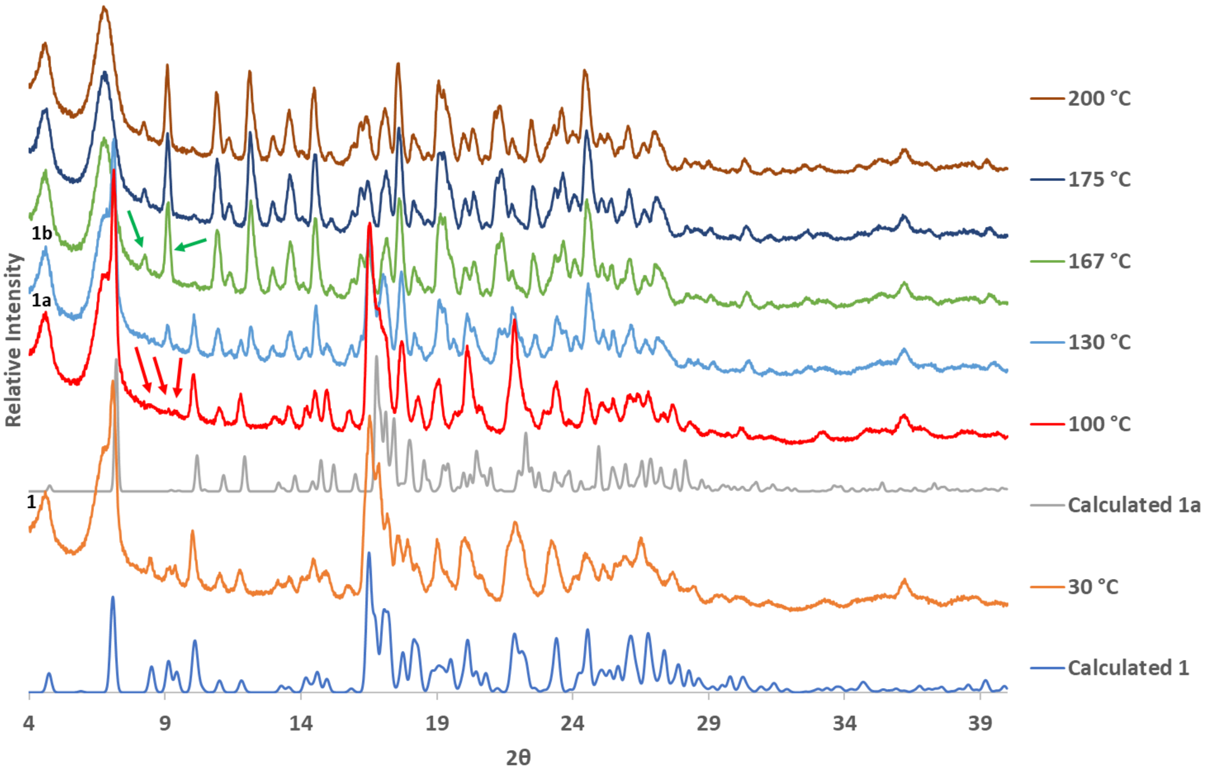

Figure 3.7: VT-PXRD patterns in the range 30-200 °C compared with the calculated patterns of **1** and **1a**. Arrows indicate peaks referred to in the text (red – decreasing relative intensity, green – increasing relative intensity).

3.3.1.3. Hot Stage Microscopy, Differential Scanning Calorimetry and Thermogravimetric Analysis

HSM photographs (Fig. 3.8) of crystals of **1**, covered with silicone oil, give a visual indication of their desolvation as bubbles are formed in the silicone oil with heating. The first bubble appears at 60 °C, with more rapid evolution of bubbles occurring at 110 °C, accompanied by the concomitant opacification of the crystals, indicating loss of monocrystallinity. This is followed by melting and decomposition, observed at 240-250 °C. The first thermal event, as indicated by DSC and TG analyses (Fig. 3.9), seems to be a complex combination of desolvation of **1** with subsequent rearrangement of the host molecules into **1b**, suggested by the broad endotherm with a shoulder observed in the DSC thermogram at a similar temperature to desolvation in the TGA thermogram.

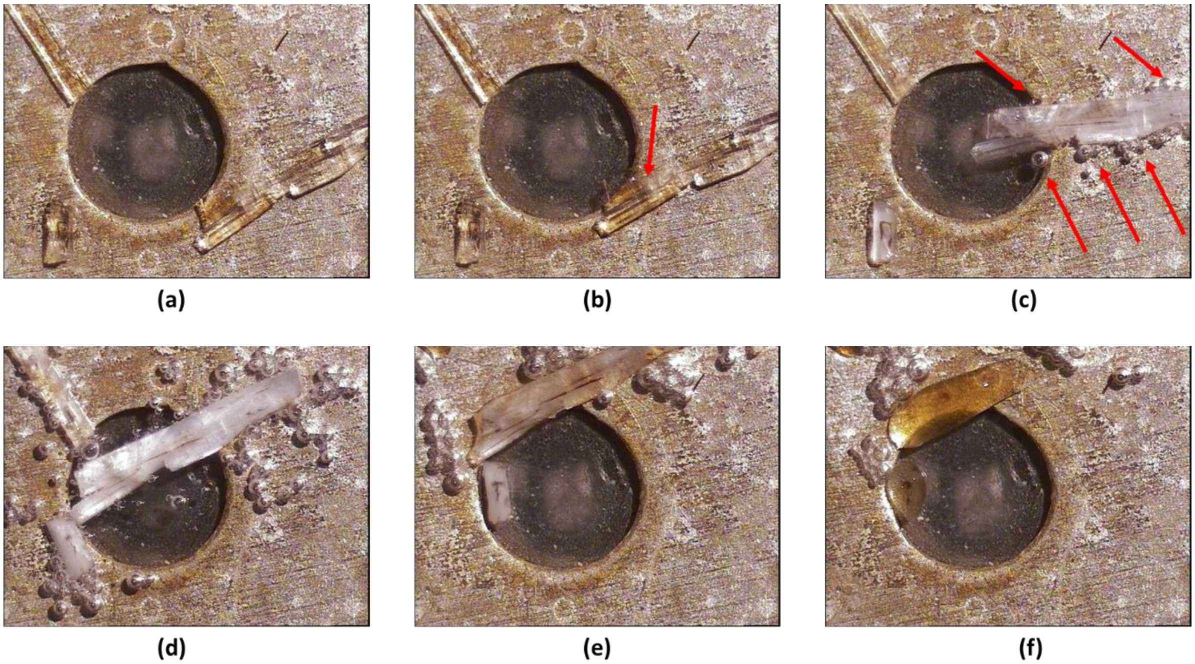

Figure 3.8: HSM photographs of compound **1** under silicone oil at different temperatures. (a) 21 °C, (b) 60 °C, (c) 110 °C, (d) 120 °C, (e) 240 °C and (f) 250 °C (bubbles indicate the release of solvent as pointed out by the red arrows in (b) and (c)).

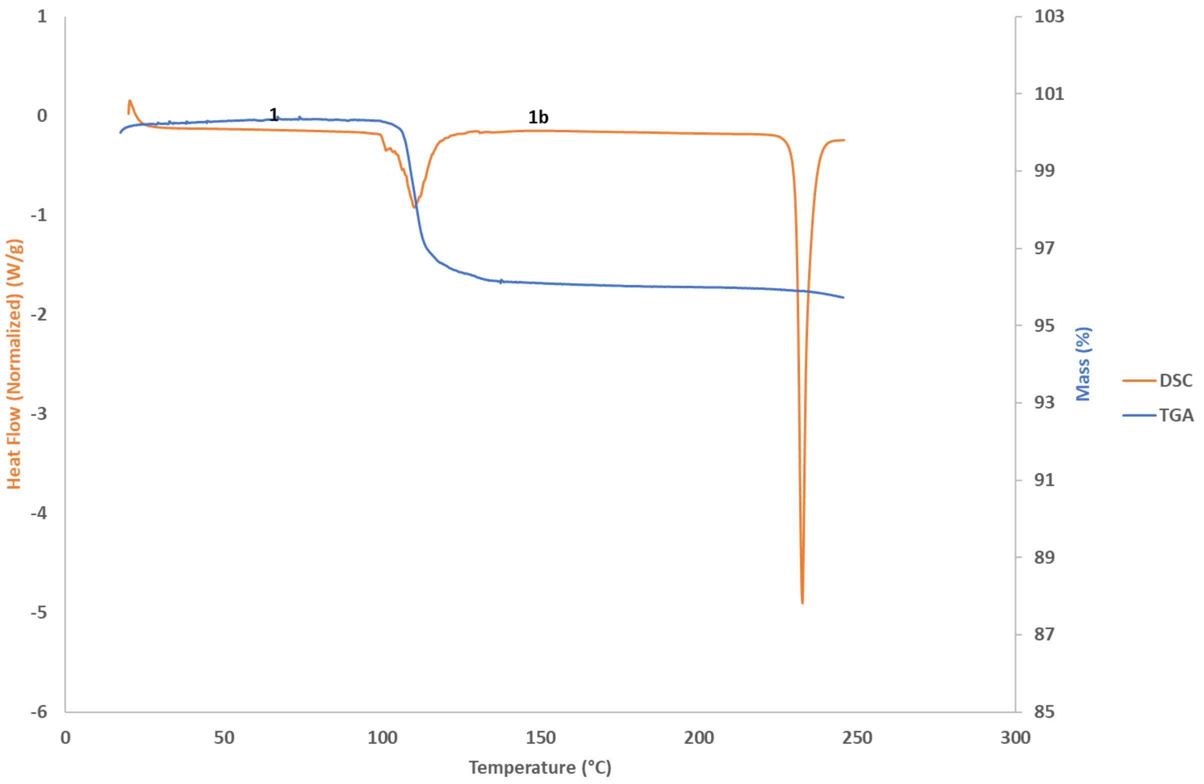

Figure 3.9: DSC and TGA thermograms of **1**.

Table 3.3: TG analysis table for compound **1**.

Thermal Event	Temperature Range (°C)	Mass Loss (%)
Mass loss	96.1–135.2	4.12 (calc. 4.36)
Melting & decomposition	234.7–250.0*	-

*not taken to full decomposition

Table 3.4: DSC analysis table for compound **1**.

Thermal Event	Onset Temperature (°C)	Temperature Range (°C)	Peak Temperature (°C)	Enthalpy (J g^{-1})
Desolvation & phase change	103.4	103.4–123.9	109.7	40.20
Melting & decomposition	230.3	230.3–241.2	232.4	93.31

The rearrangement to **1b** was separately confirmed by heating crystals on the DSC apparatus to 130 °C and subjecting them to subsequent PXRD analysis. The characteristic peaks of **1b** at 8.2° and 9.1° 2θ (as indicated by the green arrows in Fig. 3.7) are also present in the PXRD pattern of this thermally treated sample, confirming that it has transformed into **1b** (Fig. 3.10). The VT-PXRD experimental conditions were different, as the heating of **1** was slower because patterns were recorded at 20-25 °C intervals from room temperature, permitting **1a** to be observed. The TGA thermogram of **1** (Fig. 3.9) reveals a single-step mass loss of 4.12 % (calculated 4.39 %) between 100-115 °C, corresponding to 1 acetonitrile molecule per asymmetric unit, which is consistent with complete desolvation as per the single crystal structure of **1**.

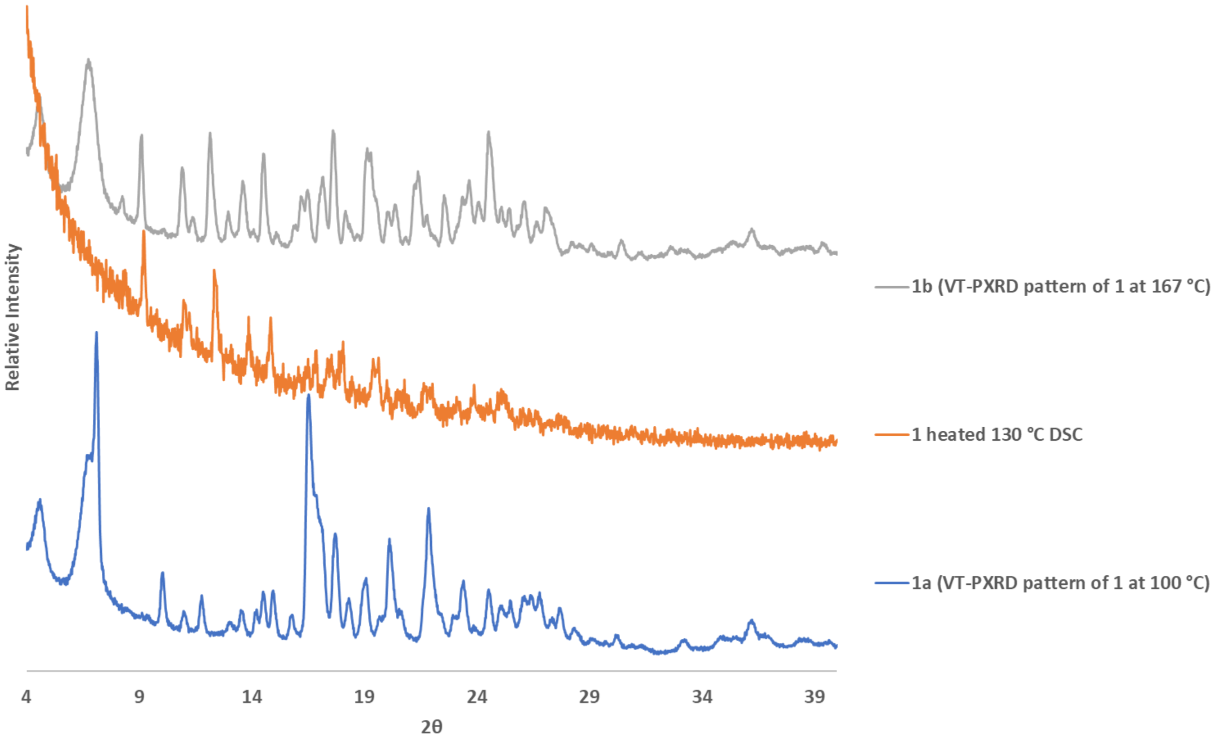

Figure 3.10: PXRD patterns showing **1** heated on DSC apparatus to 130 °C (in orange) compared with **1a** (in blue) and **1b** (in grey). Note that the low signal-to-noise ratio of the PXRD pattern at 130 °C is due to the small sample mass required for the DSC analysis.

3.3.1.4 Variable-Temperature Single Crystal X-ray Diffraction (VT-SCXRD)

In situ VT-SCXRD experiments were performed on **1** to attempt to follow the SC-SC transformation of **1** to **1a** and subsequently possibly to **1b**. Heating was performed by the flow of hot, dry air over the crystal using the cryostream nozzle of the diffractometer. Initially, unit cell parameters were collected at temperatures ranging from 25-110 °C. After 100 °C, the crystal was no longer single as revealed by the severe loss of intensity of the diffraction spots. However, these conditions are very different from how **1a** was originally produced (90 °C under vacuum *vs.* the continuous flow of dry air over the crystal). So, the method was adjusted to performing consecutive data collections at 50 °C on the same crystal (2 hours were needed for a complete data set). The structure was then solved and refined and subjected to a SQUEEZE analysis to determine the residual electron count per unit cell for each data collection.

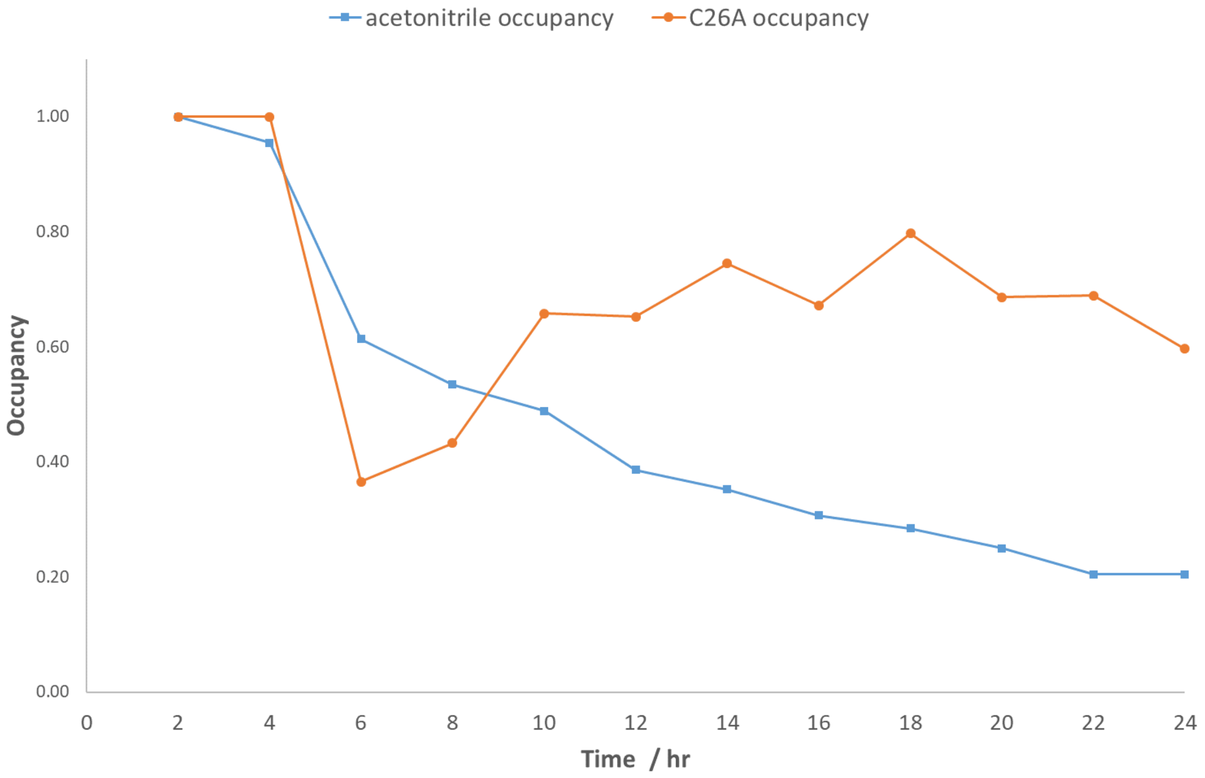

Figure 3.11: Occupancies of acetonitrile and C26A position after consecutive *in situ* 2-hour SCXRD data collections at 50 °C. Acetonitrile occupancy was calculated from a SQUEEZE electron count per unit cell analysis and the C26A occupancy was refined in SHELX-2014.

Consecutive data collections reveal a continuous decrease in the residual electron count per unit cell, indicating the acetonitrile loss from the crystal (Fig. 3.11). The electron count after 24 hours was 18 electrons per unit cell, slightly more than the 6 electrons per unit cell calculated for the structure of the crystal subjected to 90 °C under vacuum for 24 hours. Moreover, after 6 hours the position of C26A had to be modelled over two positions (second position labelled C27A), indicating dynamic rotation of this methyl group (Fig. 3.12). The second disordered position (C27A) shows the methyl group pointing towards the interior of the dimer cavity as space becomes available, allowed by the desolvation. Rotation of the methyl group away from the dimer cavity is not observed, suggesting that this rotation is short-lived in comparison to the rotation towards the interior of the cavity. However, the observed disorder supports a 'gating' hypothesis for solvent movement out of the structure. The *in situ* SCXRD experiments prove that the SC-SC transformation from **1** to **1a** can occur during a VT-SCXRD experiment under the appropriate conditions. However, the conversion from **1a** to **1b** was not observed whilst the crystal remained monocrystalline.

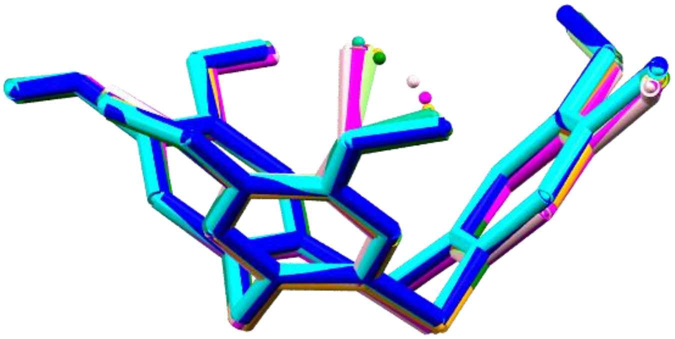

Figure 3.12: Overlay of twelve CTV dimer molecules from the twelve consecutive *in situ* 2-hour SCXRD data collections of **1** at 50 °C. After six hours, the C26A methyl group is disordered over two positions (second position C27A), suggesting dynamic rotation of the methyl group.

3.3.2. CTV-acetonitrile solvate 2 ($(C_{27}H_{30}O_6)_2 \cdot (CH_3CN)_3$) (**2**)

3.3.2.1. Single Crystal X-ray Diffraction Analysis

Crystallization of CTV from minimal solvent (100 mg in 2 mL solvent used, compared with 60 mg in 5 mL solvent used for **1**) resulted in crystals with different unit cell parameters to those of **1**, as well as a different formula, $(C_{27}H_{30}O_6)_2 \cdot (CH_3CN)_3$ (**2**) (Table 3.5).

Table 3.5: Crystal data and refinement parameters for **2**.

	2
Empirical formula	$(C_{27}H_{30}O_6)_2 \cdot (CH_3CN)_3$
Formula weight	1 024.18
Temperature (K)	173.11
Crystal system	Monoclinic
Space group	$P2_1/n$
***a* (Å)**	8.4028(11)
***b* (Å)**	32.484(5)
***c* (Å)**	20.633(3)
***α* (°)**	90
***β* (°)**	91.651(3)
***γ* (°)**	90
Volume (Å^3)	5 629.5(13)
Z	4
ρ_{calc} (g.cm^{-3})	1.208
μ (mm^{-1})	0.084
***F*(000)**	2 184.0
Radiation	MoKα (λ = 0.71073 Å)
2ϑ range for data collection (°)	2.508 – 56.722
Index ranges	$-9 \leq h \leq 11$, $-43 \leq k \leq 43$, $-27 \leq l \leq 27$
Reflections collected	54 275
Independent reflections	14 049 [R_{int} = 0.1209, R_{sigma} = 0.1328]
Data/restraints/parameters	14 049/0/691
Goodness-of-fit on F^2	0.980
Final *R* indices [$I \geq 2\sigma(I)$]	R_1 = 0.0655, wR_2 = 0.1386
Final *R* indices (all data)	R_1 = 0.1764, wR_2 = 0.1853
Largest diff. peak/hole (e.Å^{-3})	0.73/-0.46

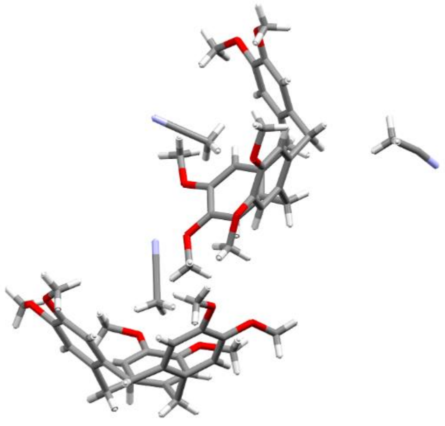

Figure 3.13: The ASU of **2**.

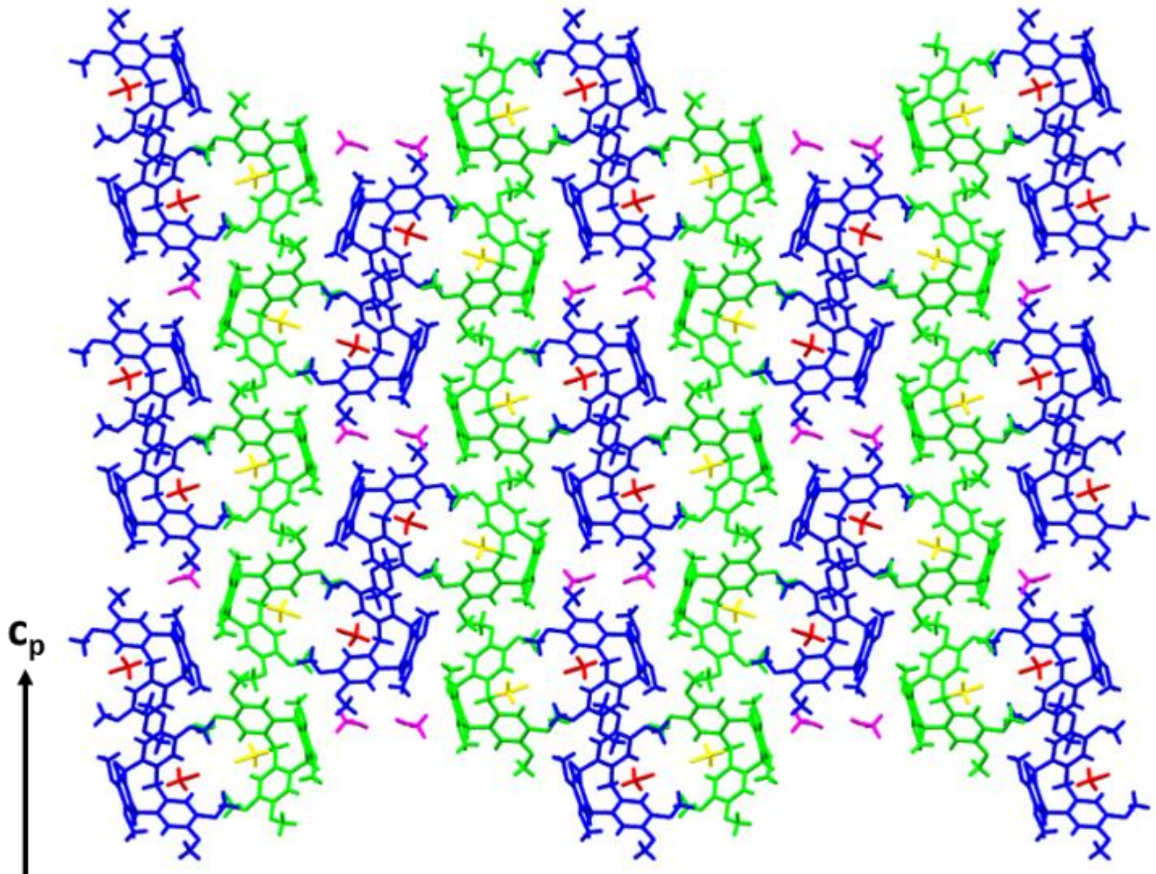

Figure 3.14: Packing diagram of **2** viewed along the *a*-axis. Crystallographically unique molecules are colour-coded.

Single crystal X-ray analysis reveals that the ASU of **2** contains two unique CTV molecules and three acetonitrile molecules (Fig. 3.13). There are two different channels within the structure of **2** – one formed by the internal cavities of the CTV molecules, which contain two of the three ASU acetonitrile molecules (red and yellow acetonitrile molecules in Fig. 3.14), and one formed by the packing of the interlocking chains, which contains the other ASU acetonitrile molecule (purple acetonitrile molecules in Fig. 3.14). The two crystallographically-independent CTV molecules form a 'zipper' motif (interlocking chain), with the intercalated CTV molecules partially included within the cavities of adjacent host molecules (Fig. 3.15). The acetonitrile molecules occupy the channels formed by these 'zippers' (Fig. 3.14 and 3.16).

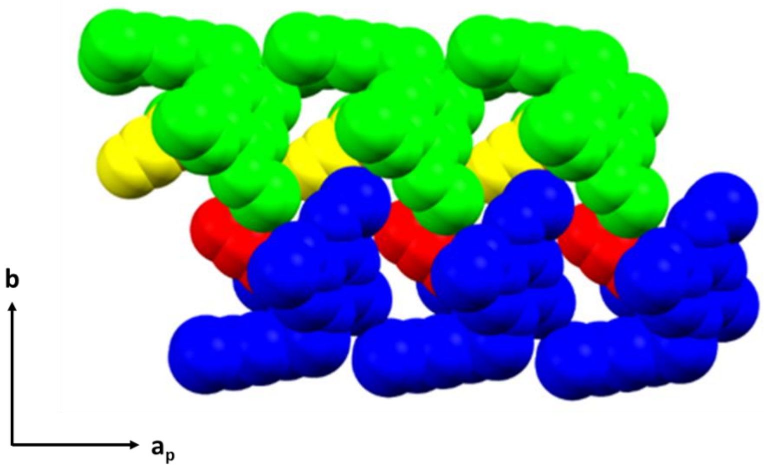

Figure 3.15: Diagram showing the 'zipper' motif formed by the packing of the unique CTV molecules in the ASU with molecules displayed in the space-filling mode.

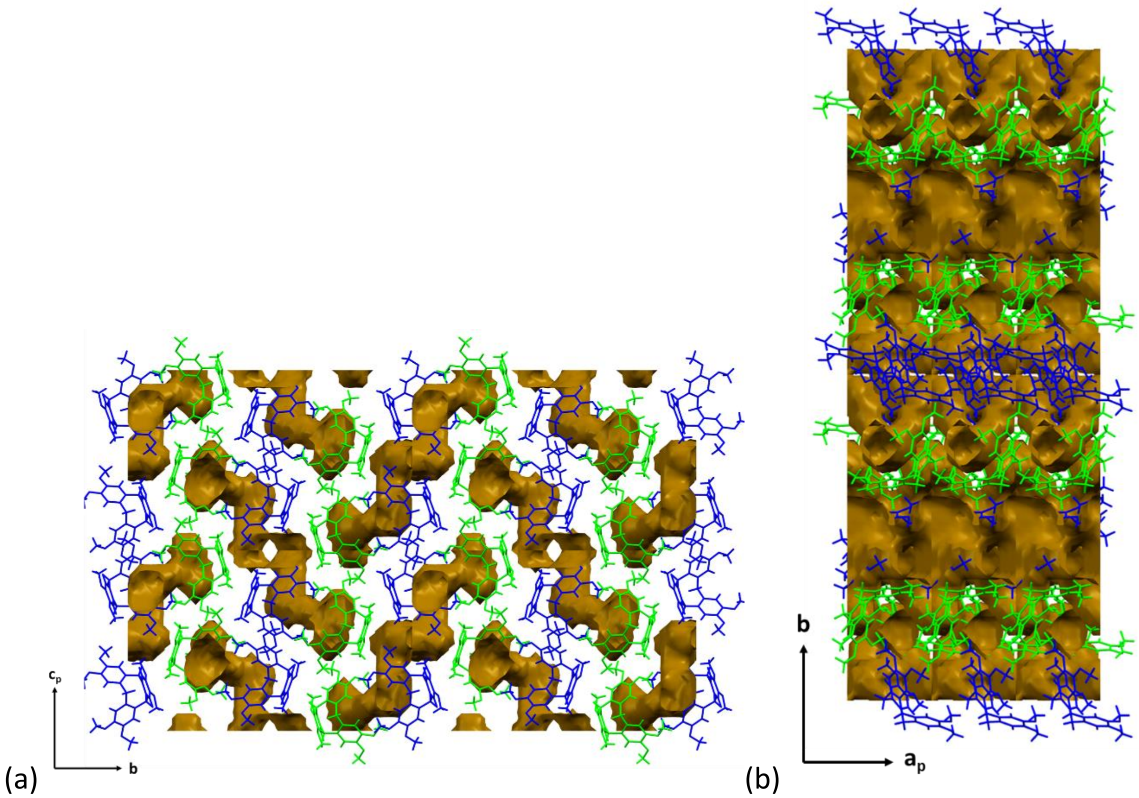

(a) (b)

Figure 3.16: (a) The solvent occupied voids displayed after artificial removal of the acetonitrile molecule coordinates viewed along the *a*-axis and (b) the solvent-occupied voids in the structure of **2** following deletion of the acetonitrile molecule coordinates viewed along the *c*-axis. Note the continuous 'zig-zag' channels.

No classic hydrogen bonds are present, but three unique C–H···O hydrogen bonds seem to be involved in host-host interactions (Fig. 3.17). All the host-host C–H···O hydrogen bonds are between symmetrically equivalent CTV molecules, one of which is intrachain (C18A–H18A···O1A) with the other two being interchain (C7A–H7AB···O3A and C17B–H17F···O5B) (Table 3.6). Of the two interchain hydrogen bonds, the C7A–H7AB···O3A interaction propagates a continuous interchain network, while the C17B–H17F···O5B interaction forms a dimeric motif between pairs of symmetrically-equivalent CTV molecules. There are also nine unique C–H···π interactions (Fig. 3.17) within the structure. Six of these interactions are between the methyl groups of the two ASU acetonitrile molecules positioned within the cavities of the CTV molecules (Table 3.6). The other three are C–H···π host-host interactions which are interchain (C8A–H8AB···Cg13^{e}, C8B–H8BB···Cg1^{a} and C16A–H16B···Cg3^{c}) and all of which form a continuous network.

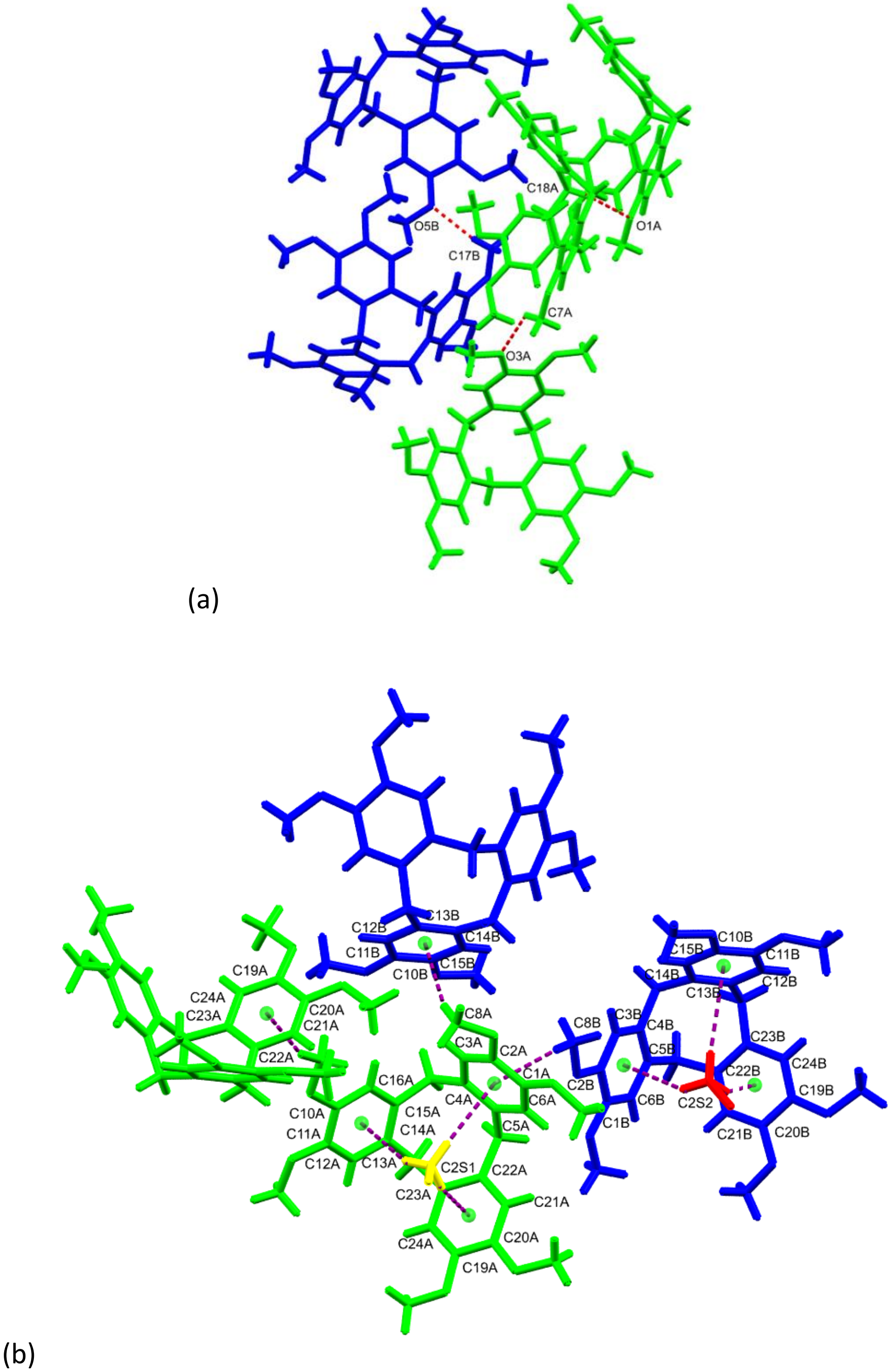

Figure 3.17: (a) C–H···O hydrogen bonding network, shown as red dashed lines, in the crystal structure of **2** (b) C–H···π bonding network, shown as purple dashed lines, in the crystal structure of **2**. The green spheres represent the centroids of the aromatic rings. Note that these are not isolated clusters but continuous networks. Only unique interactions are shown for clarity.

Table 3.6: Hydrogen bonding parameters for **2**.

Bonding atoms	D–H (Å)	H···A (Å)	D···A (Å)	D–H···A (°)	Symmetry operators
C7A–H7AB···O3A	0.98	2.49	3.140(5)	123	-½+x, ½-y, -½+z
C17B–H17F···O5B	0.98	2.35	3.323(3)	170	1-x, 1-y, 1-z
C18A–H18A···O1A	0.99	2.50	3.291(3)	137	1+x, y, z
C8A–H8AB···Cg13[e]	0.98	2.72	3.666(3)	162	½-x, -½+y, 3/2-z
C8B–H8BB···Cg1[a]	0.98	2.91	3.862(4)	164	½+x, ½-y, ½+z
C16A–H16B···Cg3[c]	0.98	2.71	3.620(4)	155	-½+x, ½-y, ½+z
C2S2–H2SA···Cg14[f]	0.98	2.74	3.599(4)	146	x, y, z
C2S2–H2SC···Cg13[e]	0.98	3.07	4.036	167	x, y, z
C2S2–H2SB···Cg12[d]	0.98	2.64	3.423(4)	136	x, y, z
C2S1–H2SD···Cg1[a]	0.98	2.79	3.745(4)	167	x, y, z
C2S1–H2SE···Cg2[b]	0.98	2.76	3.601(4)	144	x, y, z
C2S1–H2SF···Cg3[c]	0.98	2.73	3.585(4)	146	x, y, z

[a]Cg1 (C1A/C2A/C3A/C4A/C5A/C6A), [b]Cg2 (C10A/C11A/C12A/C13A/C14A/C15A), [c]Cg3 (C19A/C20A/C21A/C22A/C23A/C24A), [d]Cg12 (C1B/C2B/C3B/C4B/C5B/C6B), [e]Cg13 (C10B/C11B/C12B/C13B/C14B/C15B), [f]Cg14 (C19B/C20B/C21B/C22B/C23B/C24B)

3.3.2.2. Powder X-ray Diffraction and Variable-Temperature Powder X-ray Diffraction

VT-PXRD over the temperature range 30-215 °C shows that the sample remains crystalline over the whole temperature range of analysis (Fig. 3.18). The 30 °C PXRD pattern matches closely with the calculated PXRD pattern from the single crystal structure of **2**, indicating that the single crystal is representative of the bulk sample. At 50 °C, a peak appears at around 8.4° 2θ, while the peak at around 10.1° 2θ has decreased. There are also some significant changes in the PXRD pattern between 18-21° 2θ at the same temperature, suggesting desolvation to **2b** has occurred (as suggested by TGA in Section 3.3.2.3). However, after 50 °C, there do not seem to be any further changes observed.

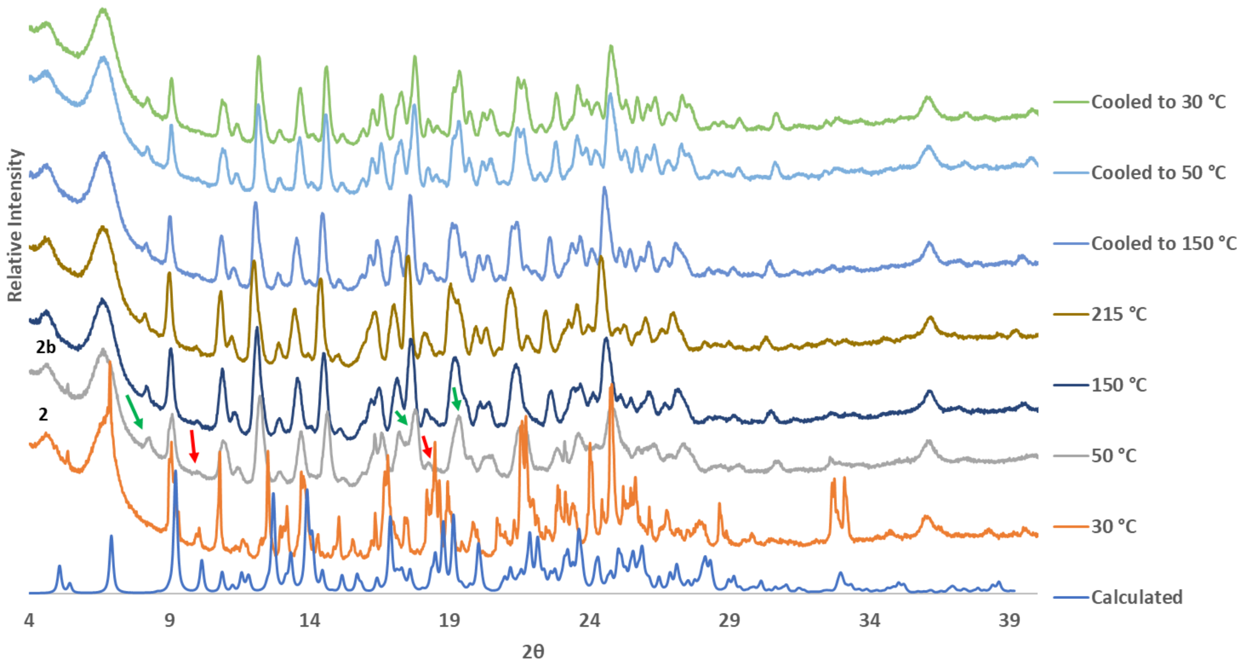

Figure 3.18: VT-PXRD patterns in the range 30-215 °C of **2**. Arrows indicate peaks referred to in the text (red – decreasing relative intensity, green – increasing relative intensity).

3.3.2.3. Hot Stage Microscopy, Differential Scanning Calorimetry and Thermogravimetric Analysis

HSM photographs (Fig. 3.19) of crystals of **2** show crystals beginning to turn opaque at 50 °C, revealing the loss of monocrystallinity, with slight bubbling starting at around 90 °C. Upon reaching 150 °C, all bubbling has ceased, and the crystal is completely opaque. No further changes are observed until the onset of melting at around 237 °C. DSC analysis (Fig. 3.20) displays a broad endotherm in the temperature range 54.0-79.7 °C, representing desolvation to form **2b**, followed by a second endotherm in the temperature range 231.4-236.9 °C, representing melting. These temperatures are slightly higher than those observed in the VT-PXRD experiments, because the VT-PXRD experimental conditions were different, as the heating of **2** was slower because patterns were recorded at 25 °C intervals from room temperature, with each VT-PXRD pattern being recorded over 45 minutes. The TGA thermogram of **2** (Fig. 3.20) shows a single-step mass loss of 11.64 % (calculated 12.02 %) in the temperature range 55.2-80.0 °C corresponding to three acetonitrile molecules per asymmetric unit.

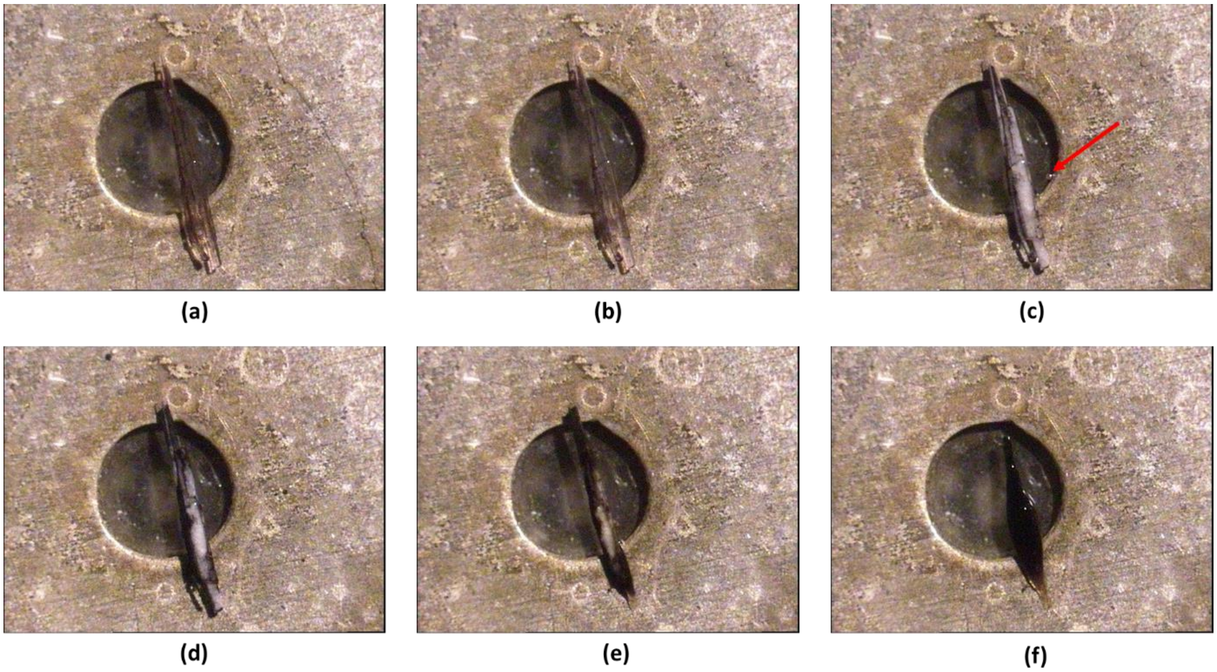

Figure 3.19: Hot stage microscope photographs of compound **2** under silicone oil at different temperatures: (a) 21 °C, (b) 50 °C, (c) 90 °C, (d) 150 °C, (e) 237 °C and (f) 247 °C (bubbles show the release of solvent – the red arrow in (c) indicates the first bubble).

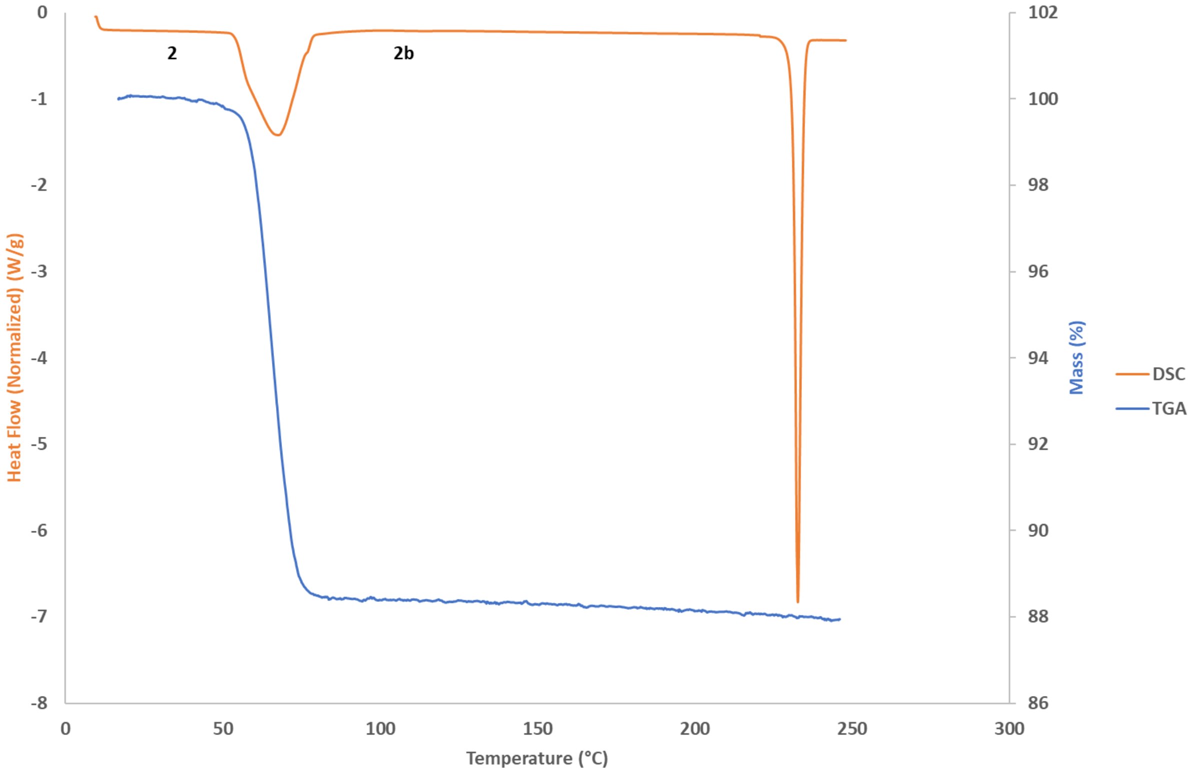

Figure 3.20: DSC and TGA thermograms of **2**.

Table 3.7: TG analysis table for compound **2**.

Thermal Event	Temperature Range (°C)	Mass Loss (%)
Mass loss	55.2–80.0	11.64 (calc. 12.03)

Table 3.8: DSC analysis table for compound **2**.

Thermal Event	Onset Temperature (°C)	Temperature Range (°C)	Peak Temperature (°C)	Enthalpy (J g^{-1})
Mass loss	54.0	54.0–79.7	67.6	107.79
Melting	231.4	231.4–236.9	232.8	88.29

3.3.3. CTV-chloroform ($C_{27}H_{30}O_6 \cdot (CHCl_3)_2$) (**3**)

3.3.3.1. Single Crystal X-ray Diffraction Analysis

3 crystallised from a solution of chloroform in the monoclinic space group $P2_1/n$, with single crystal X-ray analysis showing that the ASU consists of one CTV molecule and two unique chloroform molecules (Table 3.9).

Table 3.9: Crystal data and refinement parameters for **3**.

	3
Empirical formula	$C_{27}H_{30}O_6 \cdot (CHCl_3)_2$
Formula weight	689.24
Temperature (K)	173.10
Crystal system	Monoclinic
Space group	$P2_1/n$
***a* (Å)**	16.5727(9)
***b* (Å)**	9.6650(5)
***c* (Å)**	20.3442(10)
α (°)	90
β (°)	92.5150(10)
γ (°)	90
Volume (Å^3)	3 255.5(3)
Z	4
ρ_{calc} (g.cm^{-3})	1.406
μ (mm^{-1})	0.567
***F*(000)**	1 424.0
Crystal size (mm^3)	0.407 x 0.185 x 0.106
Radiation	MoKα (λ = 0.71073)
2ϑ range for data collection (°)	3.104 – 56.830
Index ranges	$-22 \leq h \leq 22$, $-12 \leq k \leq 12$, $-26 \leq l \leq 27$
Reflections collected	42 071
Independent reflections	8 151 [R_{int} = 0.0460, R_{sigma} = 0.0372]
Data/restraints/parameters	8 151/0/376
Goodness-of-fit on F^2	1.041
Final *R* indices [$I \geq 2\sigma(I)$]	R_1 = 0.0658, wR_2 = 0.1636
Final *R* indices (all data)	R_1 = 0.0983, wR_2 = 0.1856
Largest diff. peak/hole (e.Å^{-3})	1.47/-1.39

The CTV molecules form columns which propagate along the *b*-axis and stack in an antiparallel fashion along the *c*-axis (Fig. 3.21). The chloroform molecules are found in channels between the layers of CTV columns (Fig. 3.22).

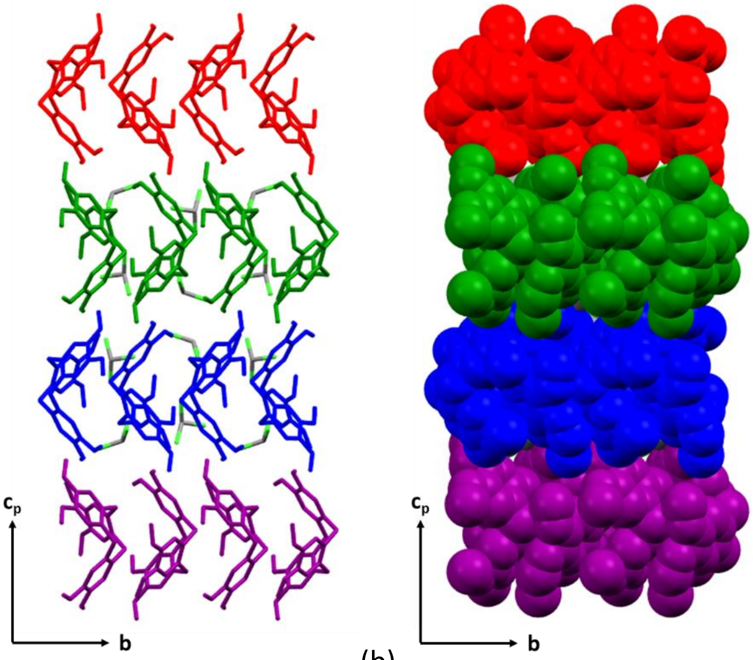

(a) (b)

Figure 3.21: The anti-parallel columns of CTV molecules in the crystal packing of **3** viewed along the *a*-axis shown in (a) capped stick and (b) space-filling mode. Different columns are colour-coded. Hydrogen atoms have been omitted for clarity.

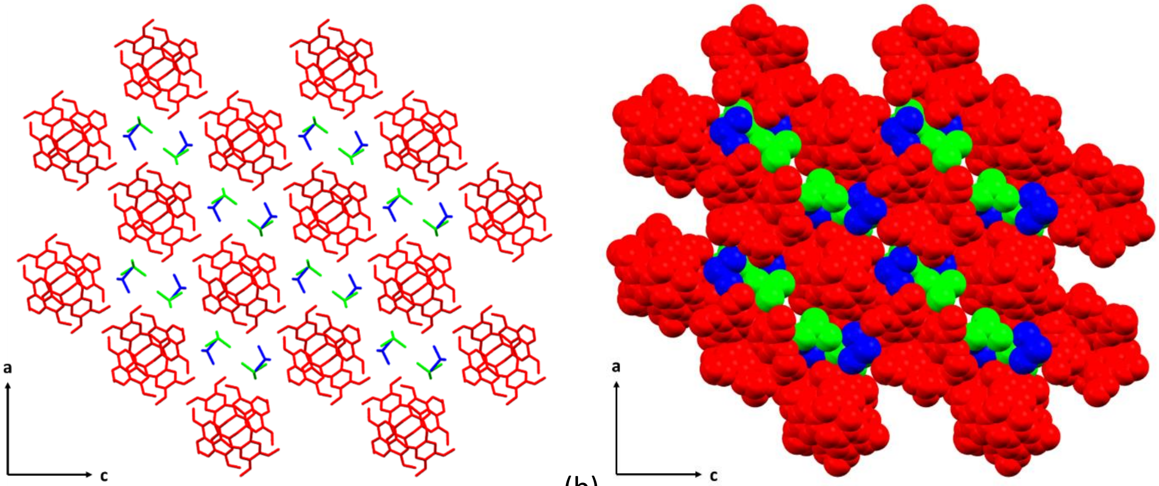

(a) (b)

Figure 3.22: The layers of CTV columns and chloroform molecules in the crystal packing of **3** viewed along the *b*-axis displayed in (a) capped stick and (b) space-filling mode. Crystallographically unique molecules are colour-coded. Hydrogen atoms have been omitted for clarity.

As for **1** and **2**, which contain acetonitrile, no classic hydrogen bonds are present in the structure of **3**. However, there are one unique C–H···O host–host hydrogen bond and four unique C–H···O host–solvent hydrogen bonds present in the structure (Fig. 3.23). The C–H···O host-host hydrogen bond is intercolumnar (C17–H17A···O3), linking two adjacent columns together through two centrosymmetrically-related hydrogen bonds (Fig. 3.23 and Table 3.10). The S1- (C1S1–H1S1···O1 and C1S1–H1S1···O2) and S2-labelled (C1S2–H1S2···O5 and C1S2–H1S2···O6) chloroform molecules act as bifurcated hydrogen bond donors (Fig. 3.23). There are also three unique intracolumnar C–H···π interactions, two between the methoxy groups of one CTV molecule and the aromatic rings of the CTV molecule which it partially includes, and one between the methylene bridge of one CTV molecule and an aromatic ring of the CTV into which it is partially included (Fig. 3.24).

Table 3.10: Hydrogen bonding parameters for **3**.

Bonding atoms	D – H (Å)	H ··· A (Å)	D ··· A (Å)	D – H ··· A (°)	Symmetry operators
C1S1–H1S1···O1	1.00	2.40	3.247(4)	141	½+x, 3/2-y, -½+z
C1S1–H1S1···O2	1.00	2.29	3.188(4)	149	½+x, 3/2-y, -½+z
C1S2–H1S2···O5	1.00	2.34	3.219(4)	147	-1+x, y, z
C1S2–H1S2···O6	1.00	2.48	3.312(4)	140	-1+x, y, z
C17–H17A···O3	0.98	2.54	3.505(4)	169	1-x, 1-y, -z
C1S2-Cl1S···O1	1.75	3.22	4.892	159	-½+x, 3/2-y, -½+z
C8–H8A···Cg3[c]	0.98	2.95	3.741(4)	139	3/2-x, -½+y, ½-z
C25–H25B···Cg1[a]	0.98	2.97	3.760(3)	138	3/2-x, -½+y, ½-z
C27–H27A···Cg2[b]	0.99	2.51	3.478(3)	166	3/2-x, ½+y, ½-z

[a]Cg1 (C1/C2/C3/C4/C5/C6), [b]Cg2 (C10/C11/C12/C13/C14/C15), [c]Cg3 (C19/C20/C21/C22/C23/C24)

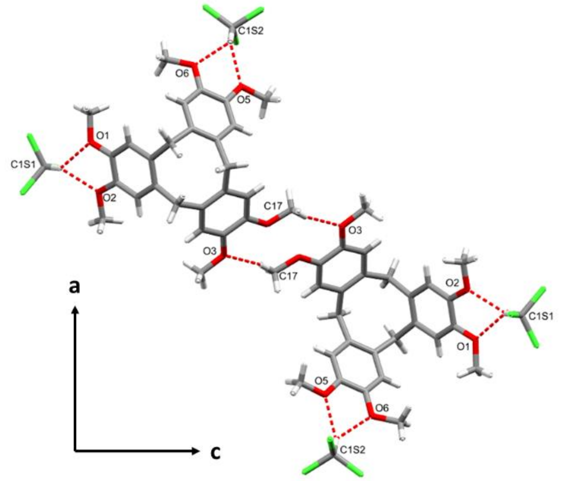

Figure 3.23: The C-H···O hydrogen bonding network of **3** viewed along the *b*-axis. The antiparallel nature of the dimer formed by the C17–H17A···O3 hydrogen bonds is shown.

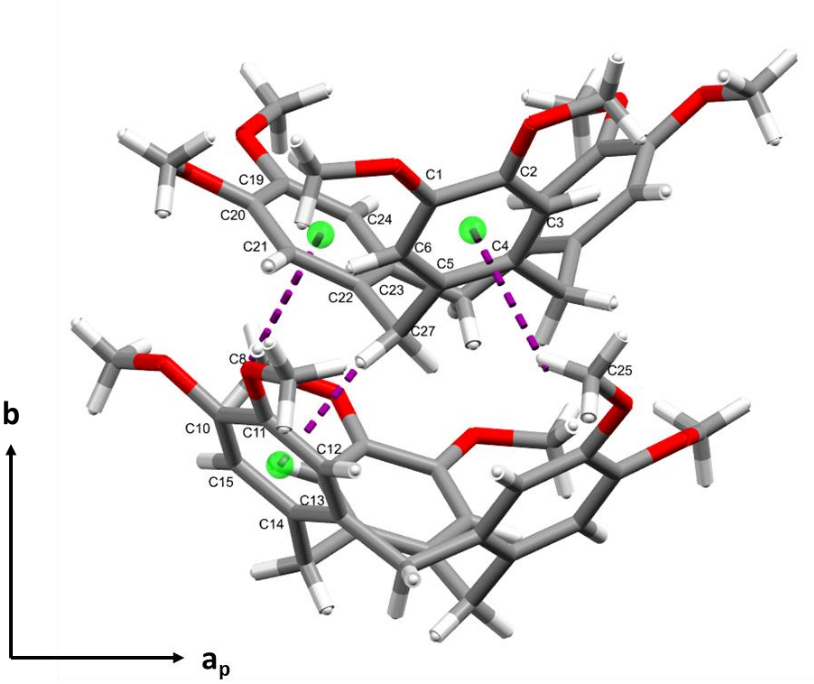

Figure 3.24: The C–H···π interactions of **3** viewed along the *c*-axis. Green spheres represent the centroids of the aromatic rings involved in C-H···π interactions.

Halogen bonding is also observed within the structure of **3**. There is one unique halogen bond – C1S2-Cl1S···O1. Along with the hydrogen bonds involving the solvent, these appear to play a

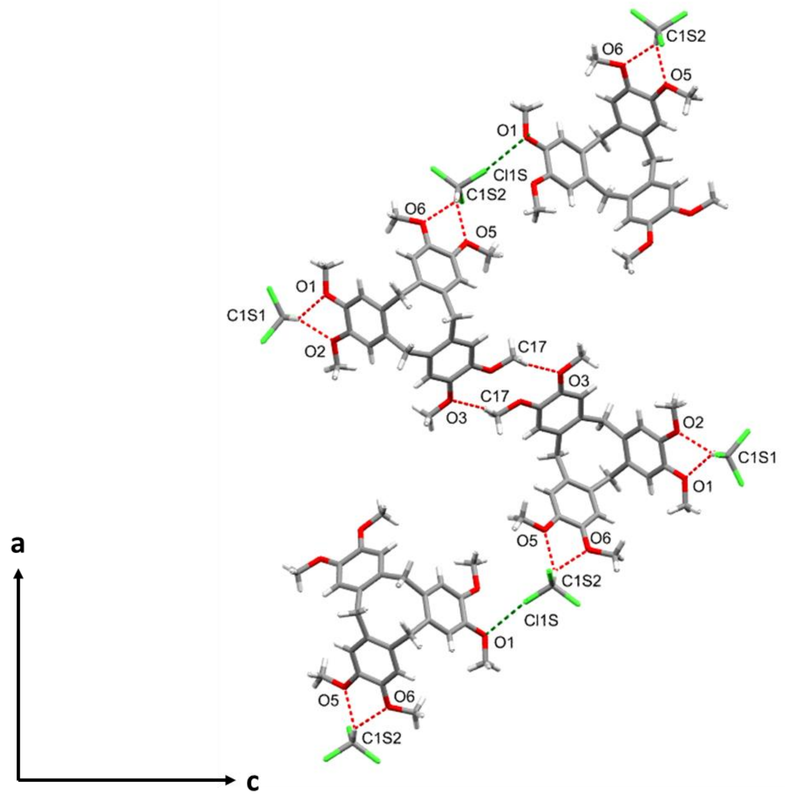

Figure 3.25: The halogen and hydrogen bonding network linking two layers of CTV columns viewed along the *b*-axis. The hydrogen bonds are displayed as red dashed lines and the halogen bonds as green dashed lines.

significant role in linking the different columns of host molecules, with the S2-labelled chloroform molecules acting as bridges (Fig. 3.25).

3.3.3.2. Variable-Temperature Powder X-ray Diffraction

VT-PXRD over the temperature range 25–210 °C reveals that the sample remains crystalline over the entire temperature range of analysis (Fig. 3.26). A room-temperature preliminary run was performed to confirm the identity of the sample before beginning the VT-PXRD experiment. This PXRD pattern agrees closely with the calculated PXRD pattern from the single crystal structure of **3**, except that the latter is shifted to higher 2θ values due to smaller d-spacings resulting from a SCXRD analysis at -100 °C. The only profile difference is the appearance of a double peak at 8.2°

and 8.5° 2θ instead of a single peak – this is attributed to rapid loss of solvent, even at ambient temperature, supported by TG analysis (see section 3.3.3.3. – Thermal Analysis). The pattern begins to display changes almost immediately, indicating that exposure to the atmosphere at room temperature for about 45 minutes (the duration of each PXRD experiment) can result in the start of desolvation. The first VT-PXRD run at 25 °C shows more changes when compared with the room-temperature preliminary run as more time has elapsed. The peak at 10.5° 2θ has decreased dramatically, while the peaks between 13.9° and 15.4° 2θ are less resolved. The peak at 16.5° 2θ has also decreased substantially, while there is a general broadening of peaks at higher 2θ. Further changes start appearing in the pattern at 130 °C. The two peaks at 8.0° and 8.4° 2θ have reduced, with a new peak appearing at 8.6° 2θ. There is a marked increase in the peak at 12.5° 2θ, while the peaks at 14.6° and 15.1° 2θ have decreased and increased intensities, respectively. There is also a new peak at 15.9° 2θ. In the pattern at 160 °C, the three peaks at 8.2°, 8.5° and 8.9° 2θ have decreased, while a new peak appears at 9.2° 2θ.

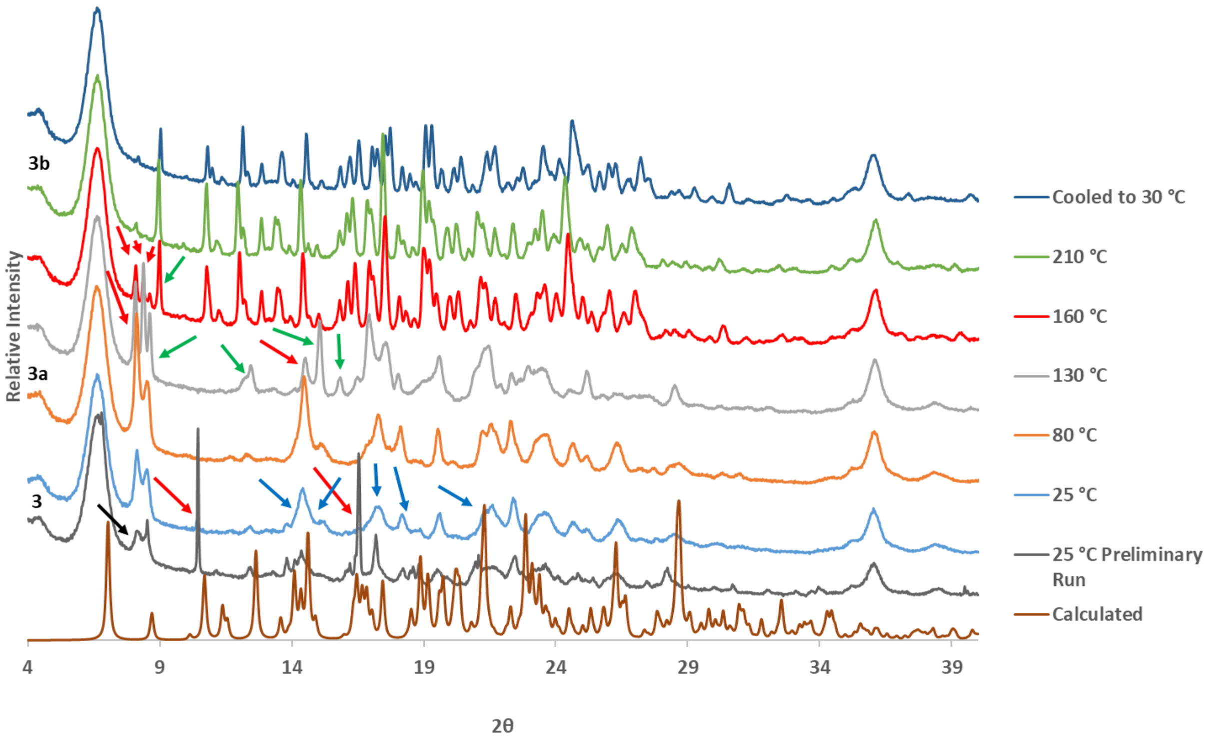

Figure 3.26: VT-PXRD patterns of ground crystals of **3** in the range 25–210 °C, compared with the calculated pattern obtained from the crystal structure of **3**. Arrows indicate peaks referred to in the text (red – decreasing relative intensity, green – increasing relative intensity, black – double peak below 10° 2θ, blue – change in peak resolution).

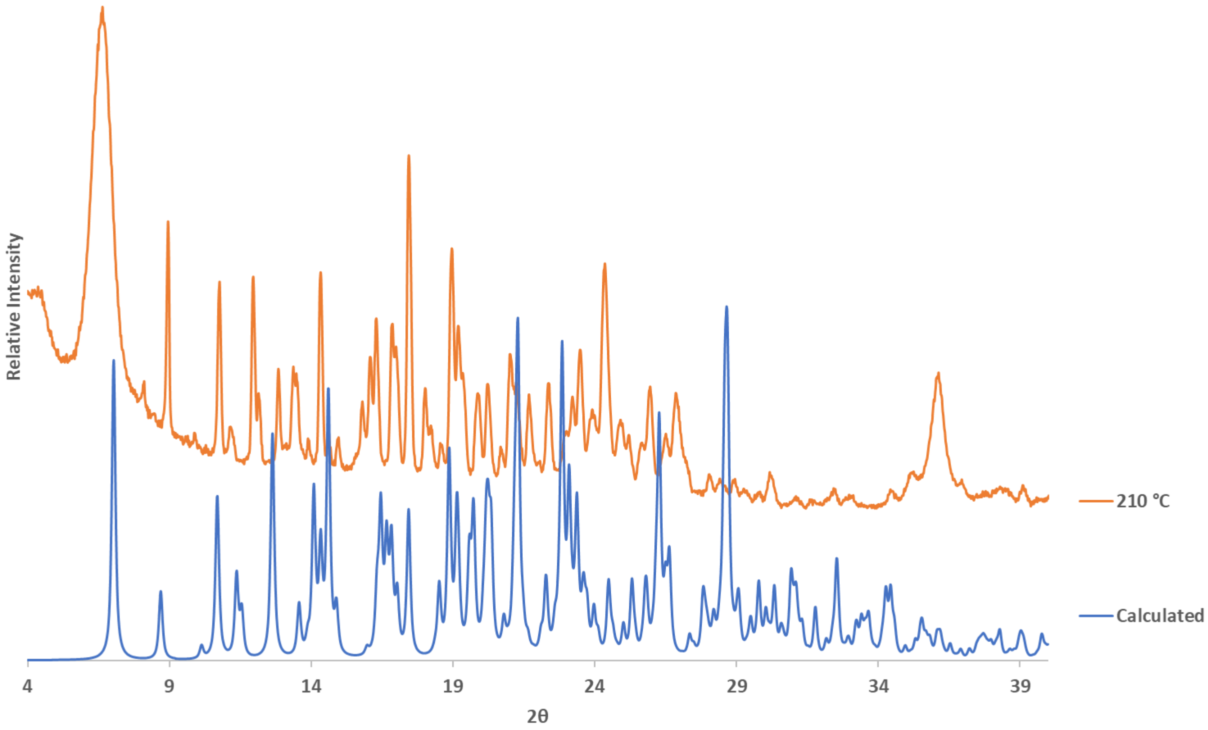

Figure 3.27: Comparison between calculated PXRD pattern obtained from single crystal structure of **3** (in blue) and the VT-PXRD powder pattern of **3b** at 210 °C (in orange).

A comparison between the calculated PXRD pattern from the single crystal structure of **3** and the VT-PXRD powder pattern of **3b** at 210 °C (Fig. 3.27) reveals that these two patterns are not the same but are very similar. Therefore, it is plausible that the structure of **3b** is very similar to the structure of **3**, just without the presence of the chloroform molecules, and that the layers of host molecules (shown in Fig. 3.22) are simply closer together.

3.3.3.3. Hot Stage Microscopy, Differential Scanning Calorimetry and Thermogravimetric Analysis

HSM photographs (Fig. 3.28) of crystals of **3** show visual indication of their desolvation as bubbles are formed in the silicone oil upon heating. The first bubble appears at 60 °C, with more vigorous bubbling occurring at 90 °C along with the crystals going opaque which is a sign of the loss of monocrystallinity.

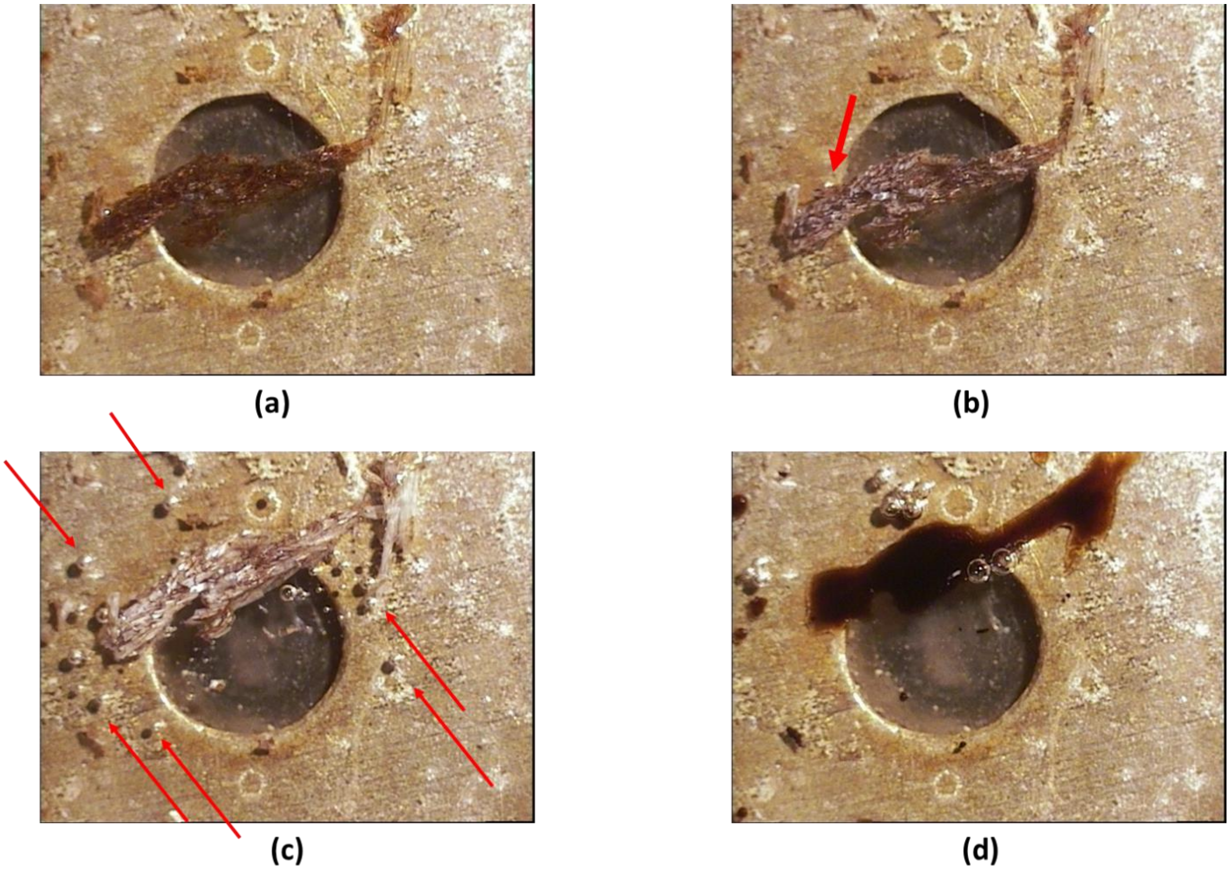

Figure 3.28: Hot stage microscope photographs of compound **3** under silicone oil at various temperatures: (a) 22 °C, (b) 60 °C, (c) 90 °C and (d) 240 °C (bubbles indicate the release of solvent – the red arrows indicate the bubbles).

DSC analysis (Fig. 3.29) shows a broad endotherm in the temperature range 20–100 °C (onset at 62.8 °C), indicating desolvation which starts at room temperature, as indicated by immediate mass loss in the TGA thermogram upon the start of the analysis at 20 °C. This corresponds with the change in structure from **3** to **3a** observed in the VT-PXRD experiments. There is subsequently a second endotherm observed in the DSC thermogram in the range 108 – 154 °C, corresponding to the transition from **3a** to **3b**. As previously observed, the VT-PXRD powder patterns display changes which seem to take place at lower temperatures than those observed in the DSC experiments (see section 3.3.3.2. – Powder X-ray Diffraction and Variable-Temperature Powder X-ray Diffraction). The TGA thermogram of **3** (Fig. 3.29) shows a single-step mass loss of 32.12 % (calculated 34.64 %) in the temperature range 18.9–150 °C corresponding to two chloroform molecules per asymmetric unit. This mass loss is slightly lower than expected, probably due to solvent loss from the crystals immediately upon removal from the mother liquor at room temperature. Despite fast sample preparation, this mass loss could not be recorded in time.

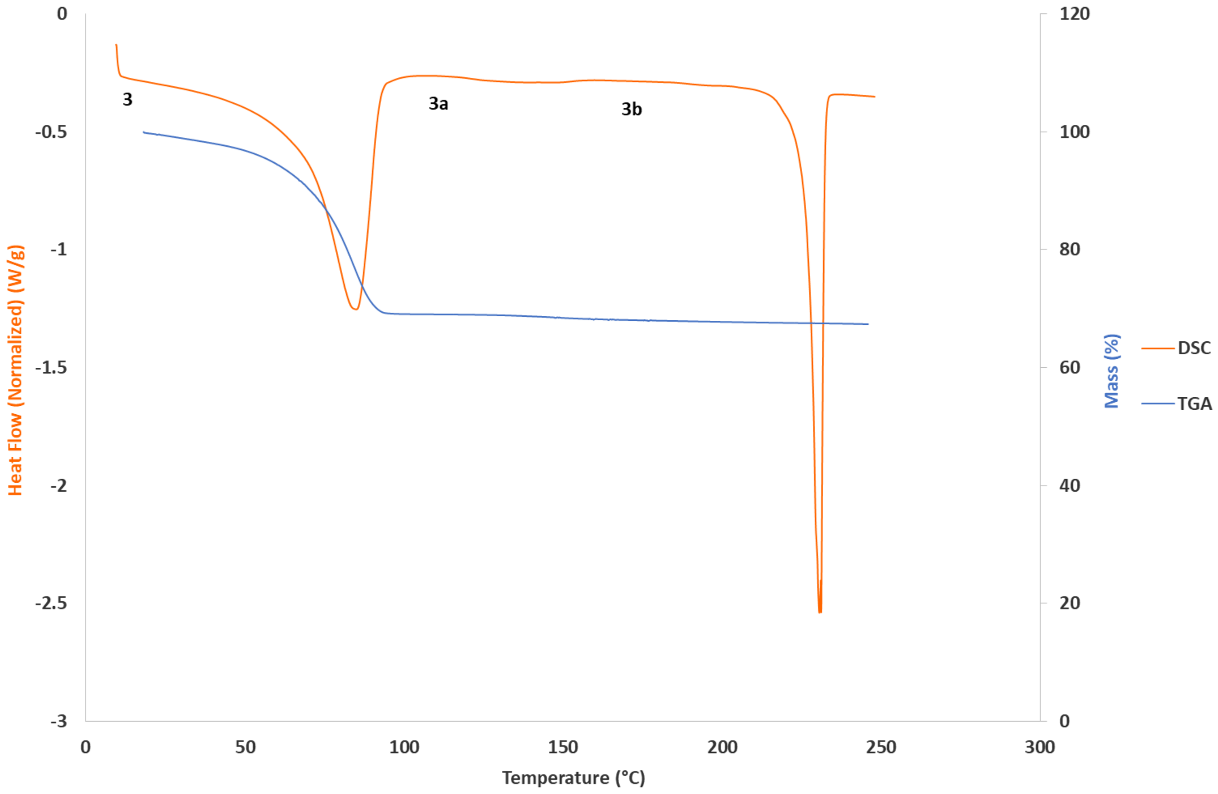

Figure 3.29: DSC and TGA thermograms of **3**.

Table 3.11: TG analysis table for compound **3**.

Thermal Event	Temperature Range (°C)	Mass Loss (%)
Mass loss	18.9–95.3	32.12 (calc. 34.64)

Table 3.12: DSC analysis table for compound **3**.

Thermal Event	Onset Temperature (°C)	Temperature Range (°C)	Peak Temperature (°C)	Enthalpy (J g^{-1})
Mass loss and desolvation to form **3a**	62.8	62.8–99.9	84.4	128.92
Transition from **3a** to **3b**	108.5	108.5–154.5	123.5	2.48
Melting	226.4	226.4–234.3	230.6	58.94

3.3.4. CTV-2-butanone ($(C_{27}H_{30}O_6)_4 \cdot C_4H_8O$) (**4**)

3.3.4.1. Single Crystal X-ray Diffraction Analysis

4 crystallised from a solution of 2-butanone in the monoclinic space group *P*2$_1$/*c* (Table 3.13). Single-crystal X-ray analysis shows that the ASU of **4** contains two unique CTV molecules and a 2-butanone molecule modelled with 50 % occupancy.

Table 3.13: Crystal data and refinement parameters for **4**.

	4
Empirical formula	$(C_{27}H_{30}O_6)_4 \cdot C_4H_8O$
Formula weight	1 874.14
Temperature (K)	105.34
Crystal system	Monoclinic
Space group	$P2_1/c$
***a* (Å)**	18.684(4)
***b* (Å)**	24.580(5)
***c* (Å)**	10.466(2)
***α* (°)**	90
***β* (°)**	91.316(5)
***γ* (°)**	90
Volume ($Å^3$)	4 805.3(17)
Z	2
ρ_{calc} ($g.cm^{-3}$)	1.295
μ (mm^{-1})	0.091
***F*(000)**	2 000.0
Crystal size (mm^3)	0.420 x 0.150 x 0.070
Radiation	MoKα (λ = 0.71073)
2ϑ range for data collection (°)	2.738 – 56.654
Index ranges	$-22 \leq h \leq 24$, $-32 \leq k \leq 32$, $-13 \leq l \leq 10$
Reflections collected	62 892
Independent reflections	11 929 [R_{int} = 0.0557, R_{sigma} = 0.0454]
Data/restraints/parameters	11 929/0/629
Goodness-of-fit on F^2	1.022
Final *R* indices [$I \geq 2\sigma(I)$]	R_1 = 0.0458, wR_2 = 0.1008
Final *R* indices (all data)	R_1 = 0.0731, wR_2 = 0.1137
Largest diff. peak/hole (e.$Å^{-3}$)	0.46/-0.30

The crystal packing is very similar to that seen in **1**, with one of the CTV molecules in the ASU forming centrosymmetric, dimeric capsules which encapsulate one disordered 2-butanone molecule (located about an inversion centre, disordered over two positions, each with 50 % occupancy) per dimer (Fig. 3.30a), while the second CTV molecule in the ASU 'stacks' to form columns of CTV molecules (Fig. 3.30b). The dimers and stacked columns are arranged in 2D layers in the *bc* plane which stack along the *a*-axis (Fig. 3.30c).

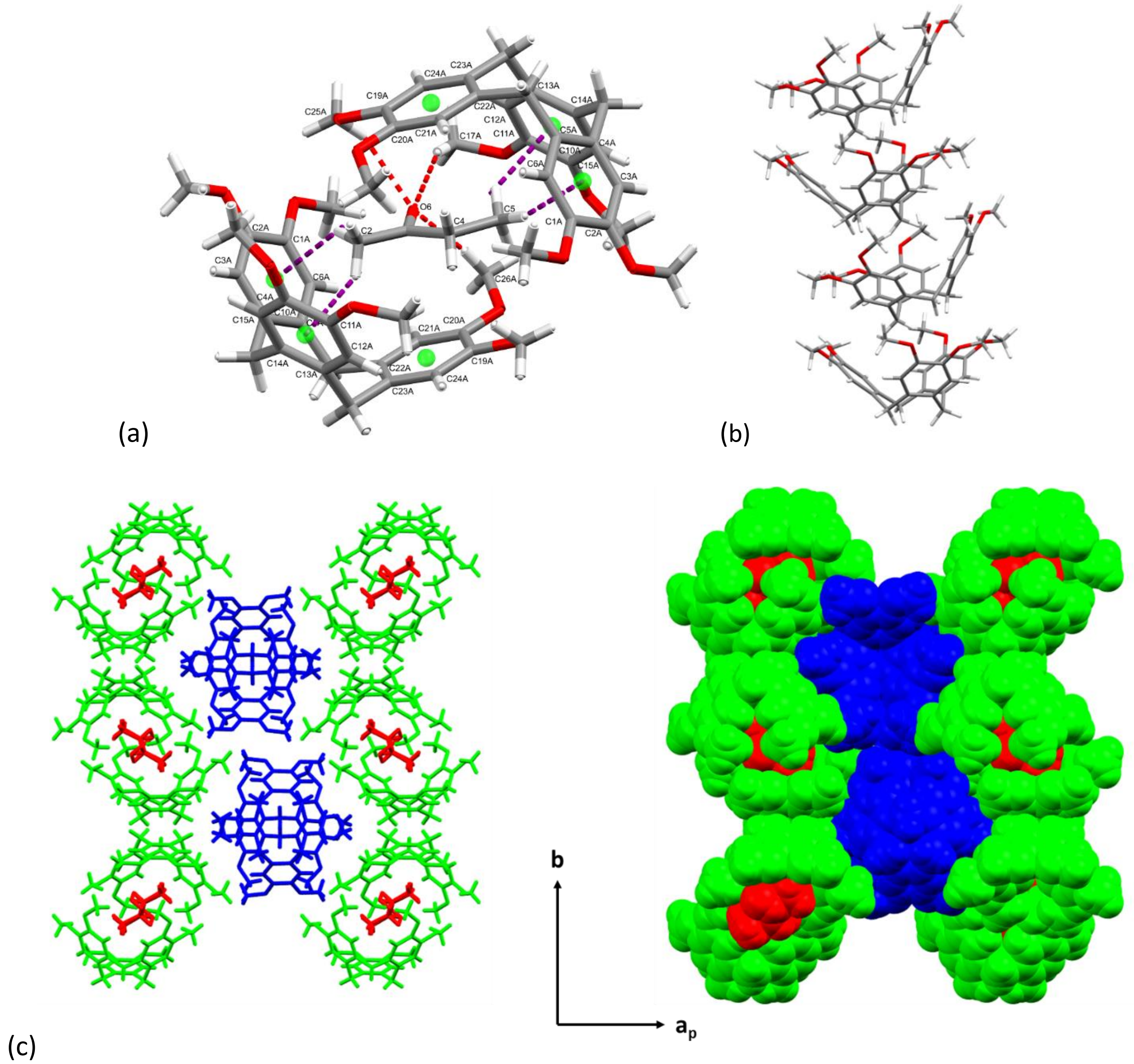

Figure 3.30: (a) Centrosymmetric dimer formed by ASU CTV molecule 1 in **4** (hydrogen bonds shown in red and C–H···π interactions shown in purple). Only one of the disordered 2-butanone molecules is displayed for clarity. The green spheres represent the centroids of the aromatic rings (b) stacking of ASU CTV molecule 2 in **4** (c) crystal packing in **4** viewed along the *c*-axis.

Table 3.14: Hydrogen bonding parameters for **4**.

Bonding atoms	D–H (Å)	H···A (Å)	D···A (Å)	D–H···A (°)	Symmetry operators
C8B–H8BC···O6A	0.98	2.56	3.358(2)	138	x, y, z
C17A–H17A···O6	0.98	2.57	3.484(3)	156	-x, 1-y, 1-z
C17B–H17D···O4A	0.98	2.43	3.125(2)	128	-x, ½+y, 3/2-z
C24A–H24A···O1A	0.95	2.59	3.2734(19)	129	x, y, 1+z
C25A–H25A···O6	0.98	2.46	3.340(3)	149	-x, 1-y, 1-z
C26A–H26A···O6	0.98	2.41	3.359(3)	162	x, y, z
C2–H2A···Cg2[b]	0.98	2.82	3.572(7)	134	x, y, z
C2–H2B···Cg1[a]	0.98	2.74	3.472(7)	132	x, y, z
C5–H5A···Cg2[b]	0.98	2.67	3.459(6)	137	-x, 1-y, 1-z
C5–H5C···Cg1[a]	0.98	2.66	3.609(7)	163	-x, 1-y, 1-z
C16B–H16F···Cg5[e]	0.98	2.99	3.6755(19)	128	x, 3/2-y, ½+z
C18A–H18B···Cg1[a]	0.99	2.70	3.5690(18)	147	x, 3/2-y, ½+z
C18B–H18D···Cg4[d]	0.99	2.85	3.8113(18)	165	x, 3/2-y, -½+z
C26B–H26E···Cg6[f]	0.98	2.85	3.4828(19)	123	x, 3/2-y, ½+z
C26B–H26F···Cg2[b]	0.98	2.98	3.904(2)	158	-1+x, y, z

[a]Cg1 (C1A/C2A/C3A/C4A/C5A/C6A), [b]Cg2 (C10A/C11A/C12A/C13A/C14A/C15A), [d]Cg4 (C1B/C2B/C3B/C4B/C5B/C6B), [e]Cg5 (C10B/C11B/C12B/C13B/C14B/C15B), [f]Cg6 (C19B/C20B/C21B/C22B/C23B/C24B)

No classical hydrogen bonds are present in the structure of **4**. However, six unique C–H···O hydrogen bonds are involved in host–host and host–solvent interactions (Fig. 3.31). Three of these are unique host–solvent C–H···O hydrogen bonds (C17A–H17A···O6, C25A–H25A···O6 and C26A–H26A···O6), with the O6 atom of the 2-butanone molecule acting as a trifurcated hydrogen bond acceptor (Fig. 3.30a). Two of these interactions are from the same dimer CTV molecule (C17A–H17A···O6 and C25A–H25A···O6) and the remaining one is from the adjacent symmetry-related CTV molecule making up the dimeric capsule. Therefore, the 2-butanone is acting as a bridge between the dimeric capsule CTV molecules, with the oxygen atom playing a crucial role. The other three unique C–H···O interactions are all host-host interactions (Fig. 3.31), with two between a dimer CTV molecule and two adjacent CTV column molecules (one on each side when viewed along the *c*-axis) and one between a CTV dimer molecule to a CTV molecule in an adjacent dimer down the *c*-axis. There are also nine unique C–H···π interactions within the structure of **4**. Four of these are between the 2-butanone solvent molecule and the dimer CTV molecule, stabilizing the 2-butanone molecule within the dimeric cavity (Fig. 3.30a and Table 3.14). The other five are unique host-host C–H···π interactions, three of which are between adjacent CTV molecules in the same column, while one is between CTV molecules of neighbouring dimers along the *b*-axis (C18A–H18B···Cg1[a]) and the remaining one is between a dimer CTV molecule and a column CTV molecule (C26B–H26F···Cg2[b]) (Fig. 3.32). It should also be noted that both the C–H···O hydrogen bonding interactions and the C–H···π interactions are continuous networks of interactions and not discrete moieties.

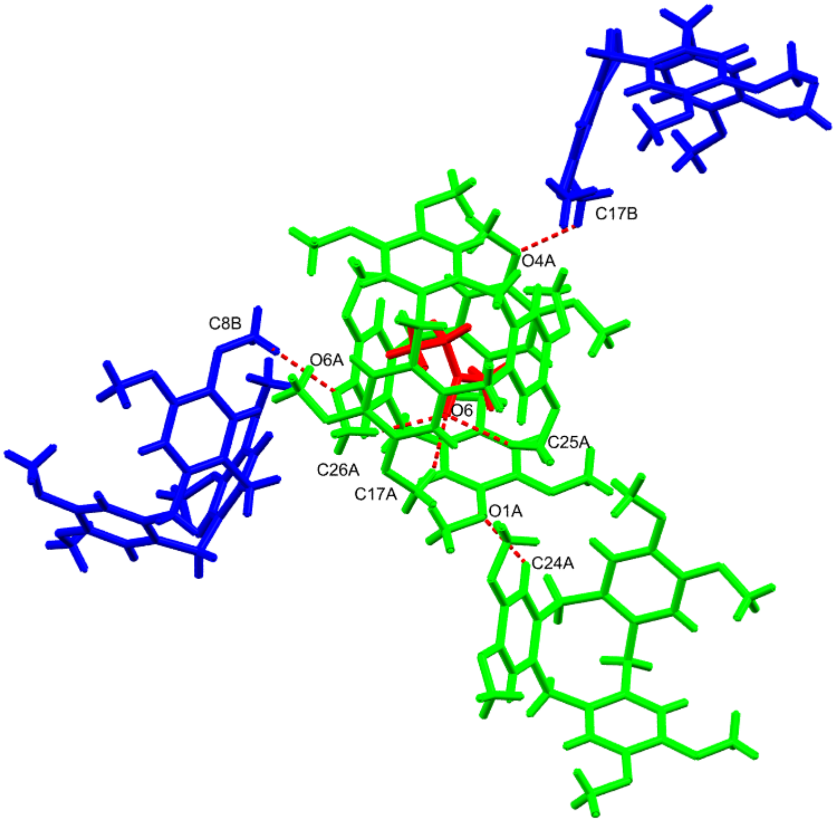

Figure 3.31: All unique hydrogen bonds within the structure of **4**, displayed as dashed red lines. Note that this is a continuous network – only unique interactions are displayed for clarity.

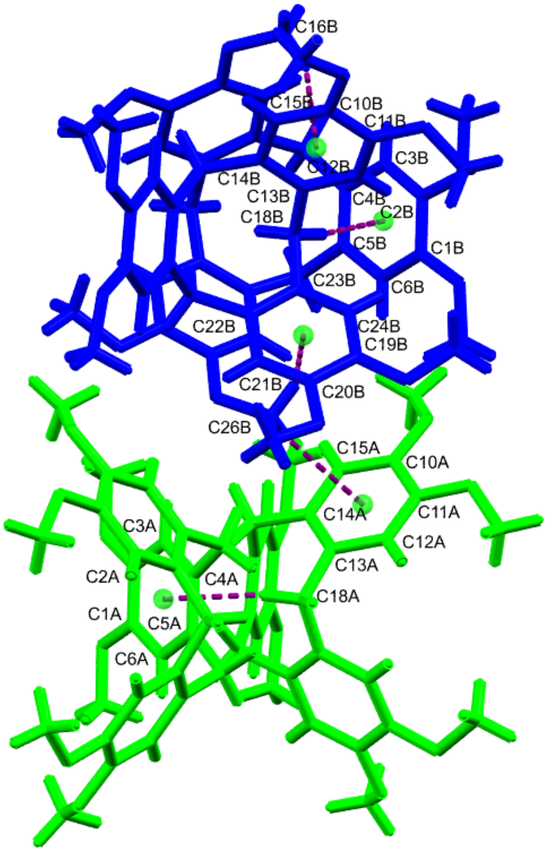

Figure 3.32: The five unique host-host C–H···π interactions within the structure of **4**, displayed as dashed purple lines. The centroids are displayed in green. Note that this is a continuous network – only unique interactions are displayed for clarity.

The structure packs in a very similar manner to **1** (Fig. 3.33), with one of the major differences being that the dimeric capsules formed in **1** each contain two acetonitrile molecules, while the dimeric capsules formed in **4** each contain one 2-butanone molecule. When the 2-butanone molecules are artificially removed, the void space for **4** calculated by MERCURY[27] (using a probe radius of 1.2 Å) is 5.6 % per unit cell, which is very similar to the 5.9 % void volume per unit cell for **1** upon artificial solvent removal. Like **1**, this void volume is a combination of dimer cavities and spaces between the stacked columns of CTV molecules.

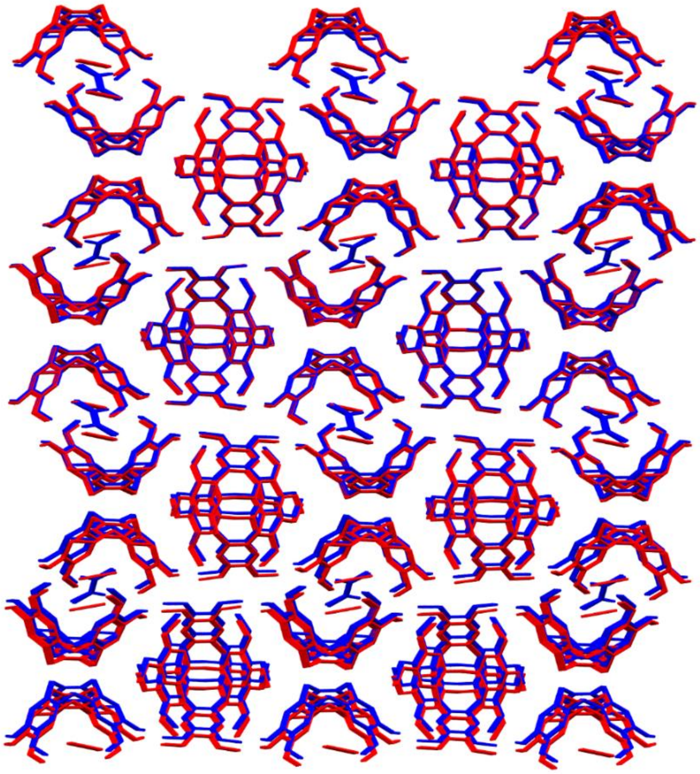

Figure 3.33: Overlay of crystal packing in **1** (red) and **4** (blue). Hydrogen atoms have been omitted for clarity.

3.3.4.2. Powder X-ray Diffraction and Variable-Temperature Powder X-ray Diffraction

As was the case for **1**, **4** could also be prepared by liquid-assisted grinding of CTV in the presence of 2-butanone for approximately 10 minutes (Fig. 3.34). Due to the similarities in the packing between **1** and **4**, a comparison of their respective calculated PXRD patterns from their single crystal structures show close agreement (Fig. 3.35).

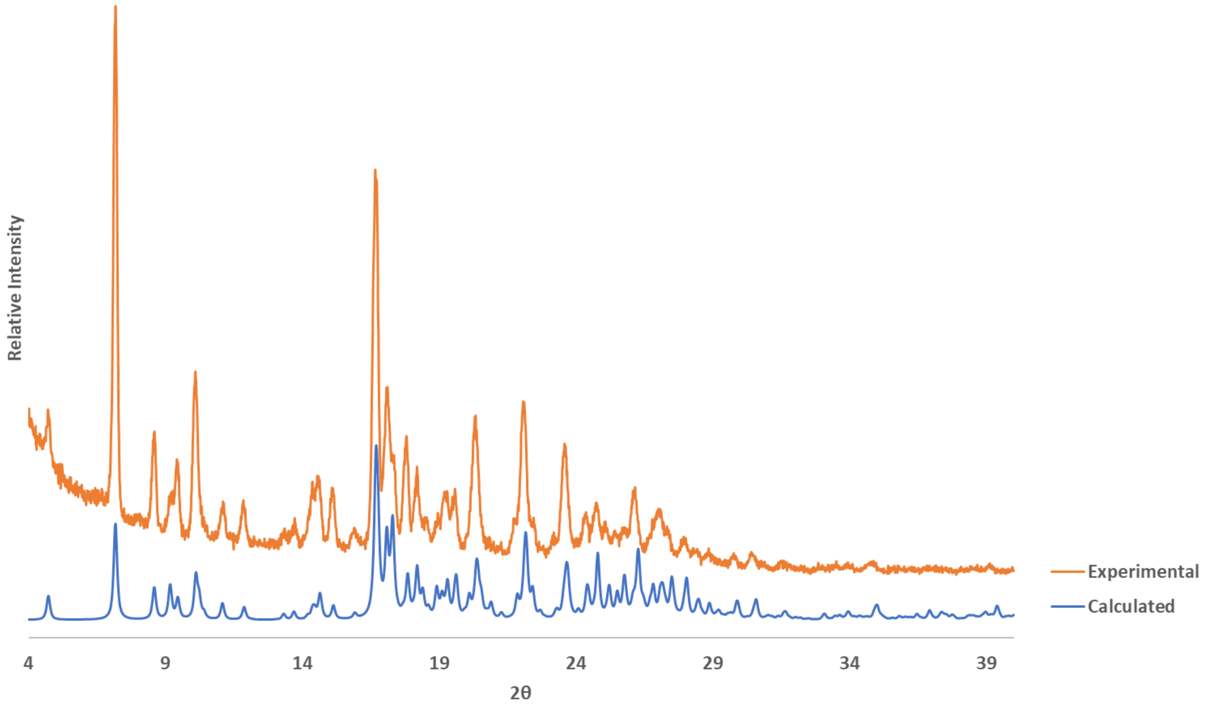

Figure 3.34: Comparison between calculated PXRD pattern of **4** (in blue) and the experimentally obtained pattern *via* liquid-assisted grinding of CTV with 2-butanone (in orange).

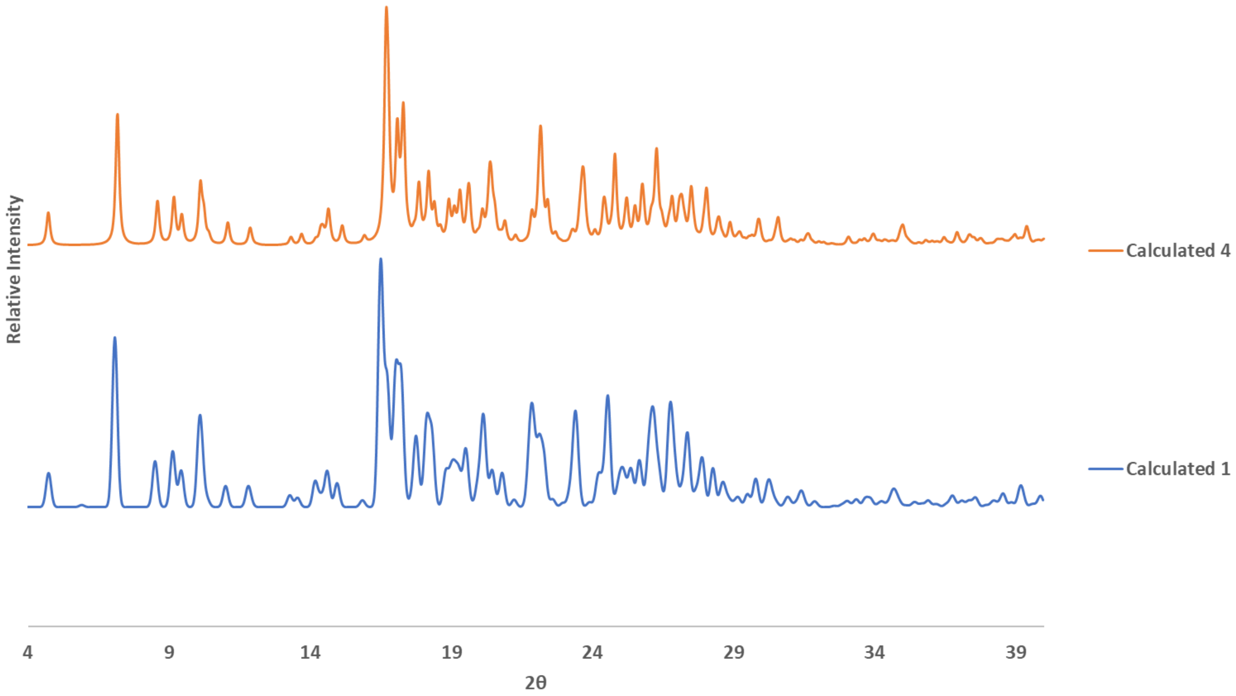

Figure 3.35: Comparison between calculated powder patterns of **1** (in blue) and **4** (in orange).

VT-PXRD experiments performed on **4** over the temperature range 30–210 °C revealed that the sample remains crystalline over the entire temperature range of analysis (Fig. 3.36). The 30 °C PXRD pattern matches closely with the calculated PXRD pattern from the single crystal structure of **4**. At 125 °C, however, the PXRD pattern has changed and closely matches that of **1b**, the final desolvated form of **1** (Fig. 3.37). This is also expected due to the similarity in the structures of **1** and **4**. The difference in the behaviour between **1** and **4** upon heating is that **1** went through a clearly–visible transition phase, **1a**, at around 100 °C before going to the final desolvated form, **1b**. This transition phase is not observed for **4**, which seems to go straight from the solvated form **4** to the desolvated form **4b** at 125 °C with no phase transition in between (the PXRD pattern of **4** at 100 °C still closely matches the pattern at 30 °C).

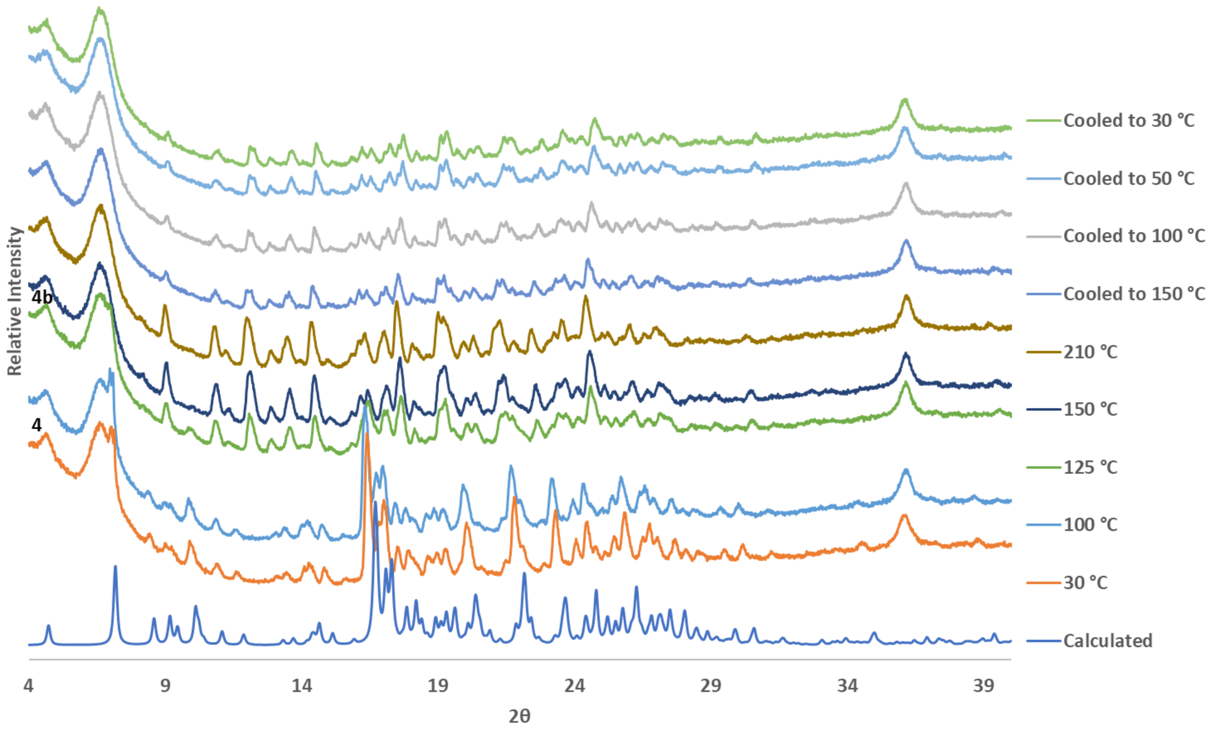

Figure 3.36: VT-PXRD patterns of **4** in the range 30–210 °C compared with the calculated pattern of **4**.

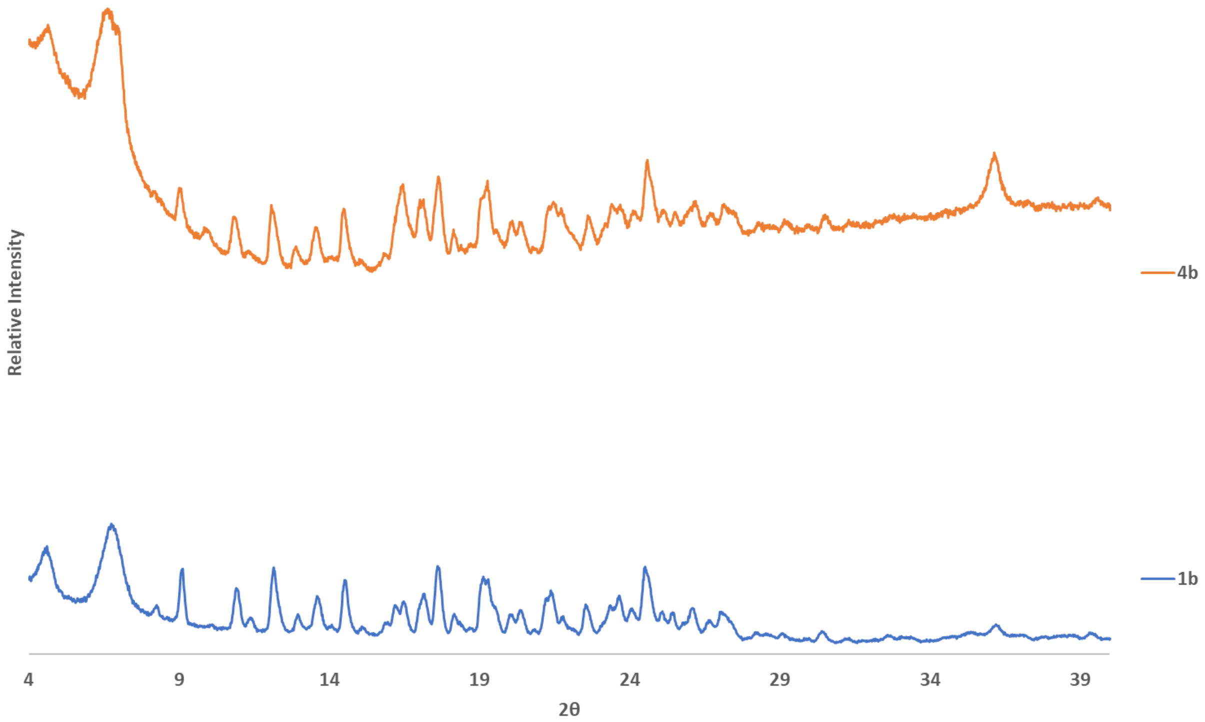

Figure 3.37: VT-PXRD patterns of the final desolvated form **1b** (in blue) and the desolvated **4b** (in orange).

3.3.4.3. Hot Stage Microscopy, Differential Scanning Calorimetry and Thermogravimetric Analysis

HSM photographs (Fig. 3.38) of crystals of **4** give visual indication of their desolvation as bubbles are formed in the silicone oil upon heating. The initial bubbling begins at 110 °C, with more vigorous bubbling occurring at 130 °C accompanied by the crystals becoming opaque, suggesting the loss of monocrystallinity. The bubbling continues until melting at ~250 °C, suggesting continuous solvent loss until melting.

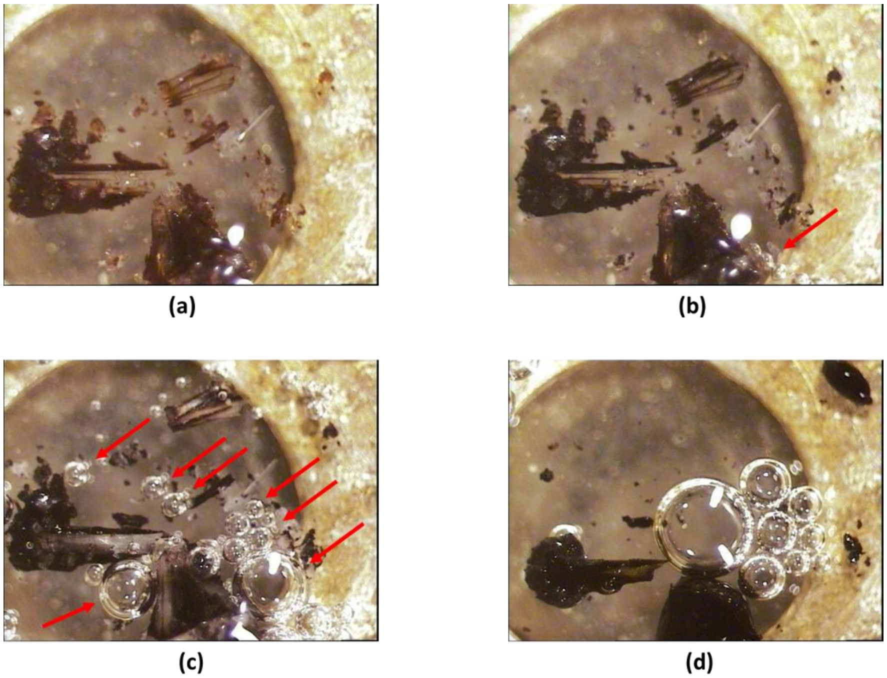
(a) (b) (c) (d)

Figure 3.38: Hot stage microscope photographs of compound **4** under silicone oil at various temperatures: (a) 25 °C, (b) 110 °C, (c) 130 °C and (d) 250 °C (bubbles indicate the release of solvent – the red arrows indicate bubbling).

This is supported by the TGA thermogram of **4**, which never plateaus after solvent loss begins (Fig. 3.39). DSC and TG analyses (Fig. 3.39) indicate the first thermal event in the temperature range 111–152 °C, representing desolvation and simultaneous rearrangement of the host molecules to form **4b**. This is suggested by the broad endotherm with a shoulder observed in the DSC thermogram at a similar temperature to desolvation in the TGA thermogram. This is a similar profile to the first DSC endotherm of **1**, except that shoulder is on the opposite side of the peak. The TGA thermogram of **4** displays a continuous mass loss, initially steep and then becoming more gradual, of 3.49 % (calculated 3.85 %) in the temperature range 123–250 °C, with most of the mass lost between 111–152 °C.

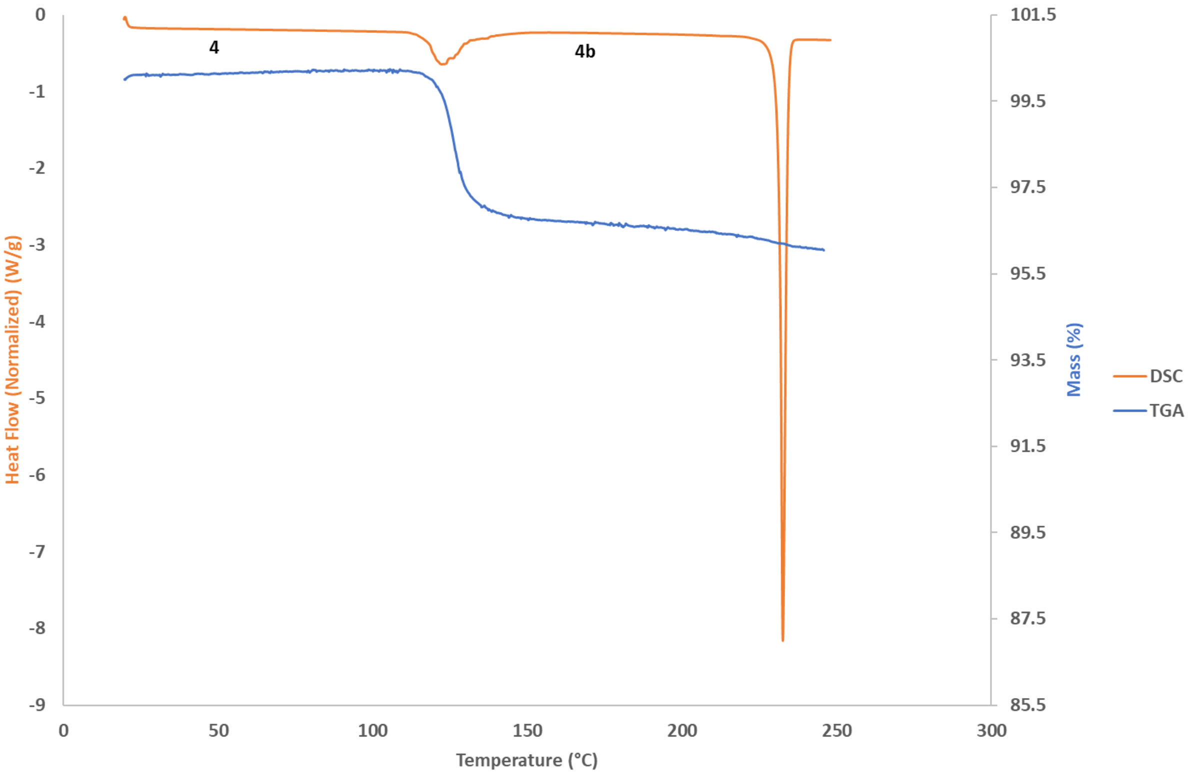

Figure 3.39: DSC and TGA thermograms of **4**.

Table 3.15: TG analysis table for compound **4**.

Thermal Event	Temperature Range (°C)	Mass Loss (%)
Mass loss	111.3–152.0	3.49 (calc. 3.85)
Decomposition	224.1–*	-

*not taken to full decomposition

Table 3.16: DSC analysis table for compound **4**.

Thermal Event	Onset Temperature (°C)	Temperature Range (°C)	Peak Temperature (°C)	Enthalpy (J g^{-1})
Mass loss	117.8	117.8–141.8	123.9	31.27
Decomposition	231.4	231.4–236.34	232.6	98.58

3.3.5. Structural Analysis

The desolvated compounds **1b**, **2b**, **3b** and **4b** all display the same PXRD pattern and are therefore concluded to be the same desolvated phase (Fig. 3.40). This is confirmed by the onset temperatures of melting of **1b**, **2b** and **4b**, which are all in the range 230.3–231.4 °C (Table 3.17). The melting onset temperature of **3b** is slightly lower at 226.4 °C, but this could be due to trace impurities within the sample. The melting endotherm of **3b** is also broader than those of **1b**, **2b** and **4b**.

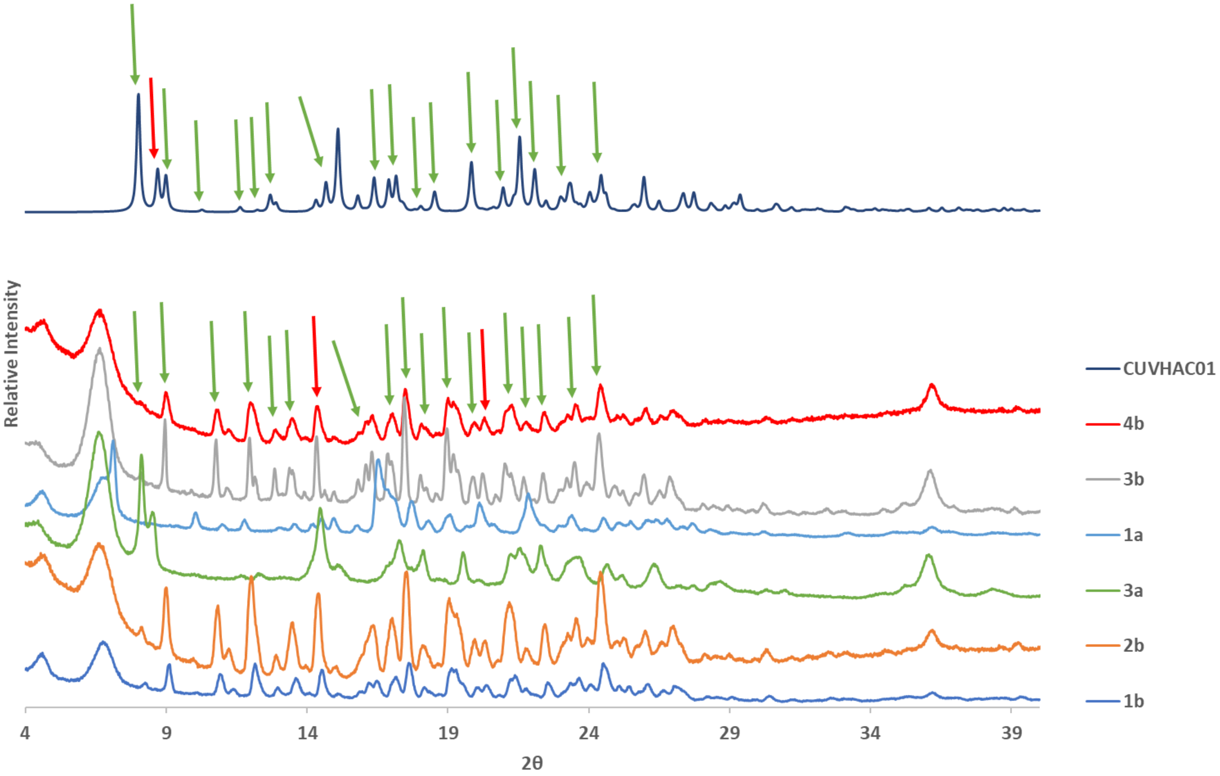

Figure 3.40: The PXRD patterns of all desolvated compounds **1**–**4**. Green arrows indicate similarities and red arrows indicate differences.

Table 3.17: Onset temperatures of melting of CTV host compounds.

Compound	Onset Temperature of Melting (°C)
1b	230.3
2b	231.4
3b	226.4
4b	231.4

Unfortunately, the structure of this final phase before melting could not be determined, but the questions remain as to what the structure is and how two dimer-and-column structures (**1** and **4**), a semi-stacked structure (**2**) and a layers-of columns structure (**3**) all reduce to the same structure upon heating and desolvation. The first clue to the answer to the first of these questions is found when comparing the PXRD patterns of this final phase to a PXRD pattern obtained from a structure already in the CSD (refcode: CUVHAC01).[25] There are definite similarities, although the PXRD patterns are not identical. Specifically, the peak indicated by the red arrow at 8.7° 2θ in the CUVHAC01 PXRD pattern does not appear in the **4b**, **3b** or **2b** PXRD patterns, while the peaks appearing at 14.4° and 20.4° 2θ in the **2b**, **3b** and **4b** PXRD patterns do not appear in the CUVHAC01 PXRD pattern. This CUVHAC01 structure consists of layers of stacked, antiparallel columns of CTV. Another clue for the answer to the first of these questions can be found in the VT-PXRD of **3**, when one compares the VT-PXRD patterns of **3** and **3b** (Fig. 3.41). These are found to be very similar, suggesting that the only change that has potentially occurred within the structure is the removal of the chloroform solvent molecules from between the layers of CTV columns and the subsequent decrease of the spaces between these layers of CTV columns.

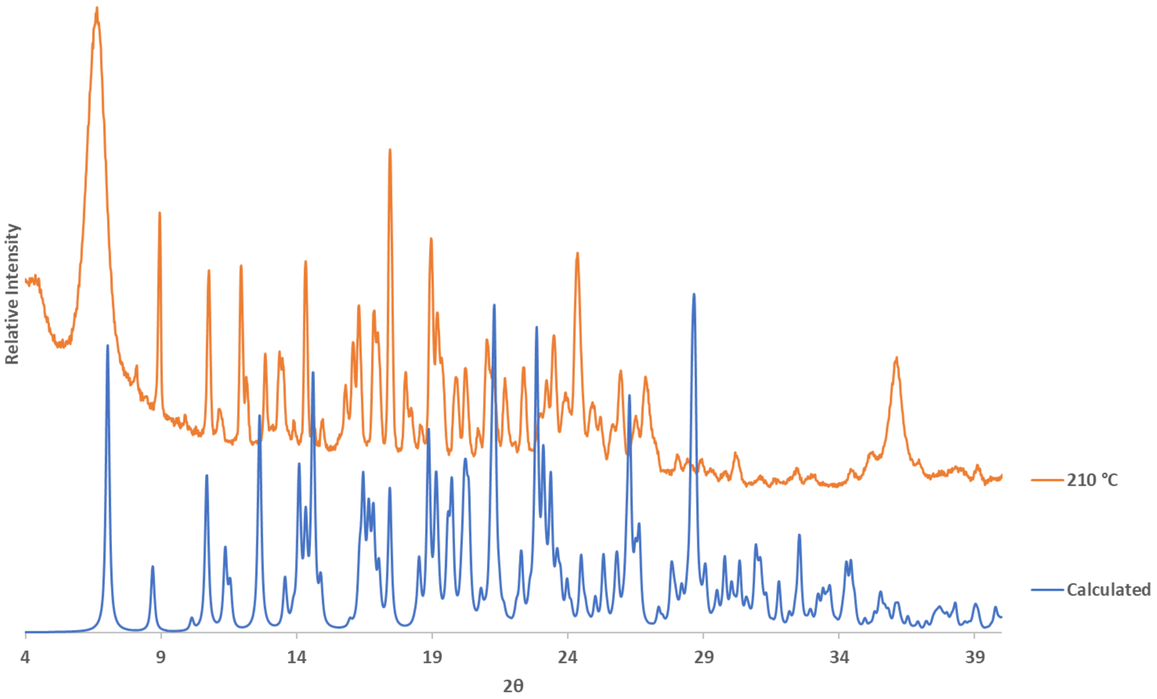

Figure 3.41: Comparison between calculated PXRD pattern obtained from single crystal structure of **3** (in blue) and the VT-PXRD powder pattern of **3b** at 210 °C (in orange).

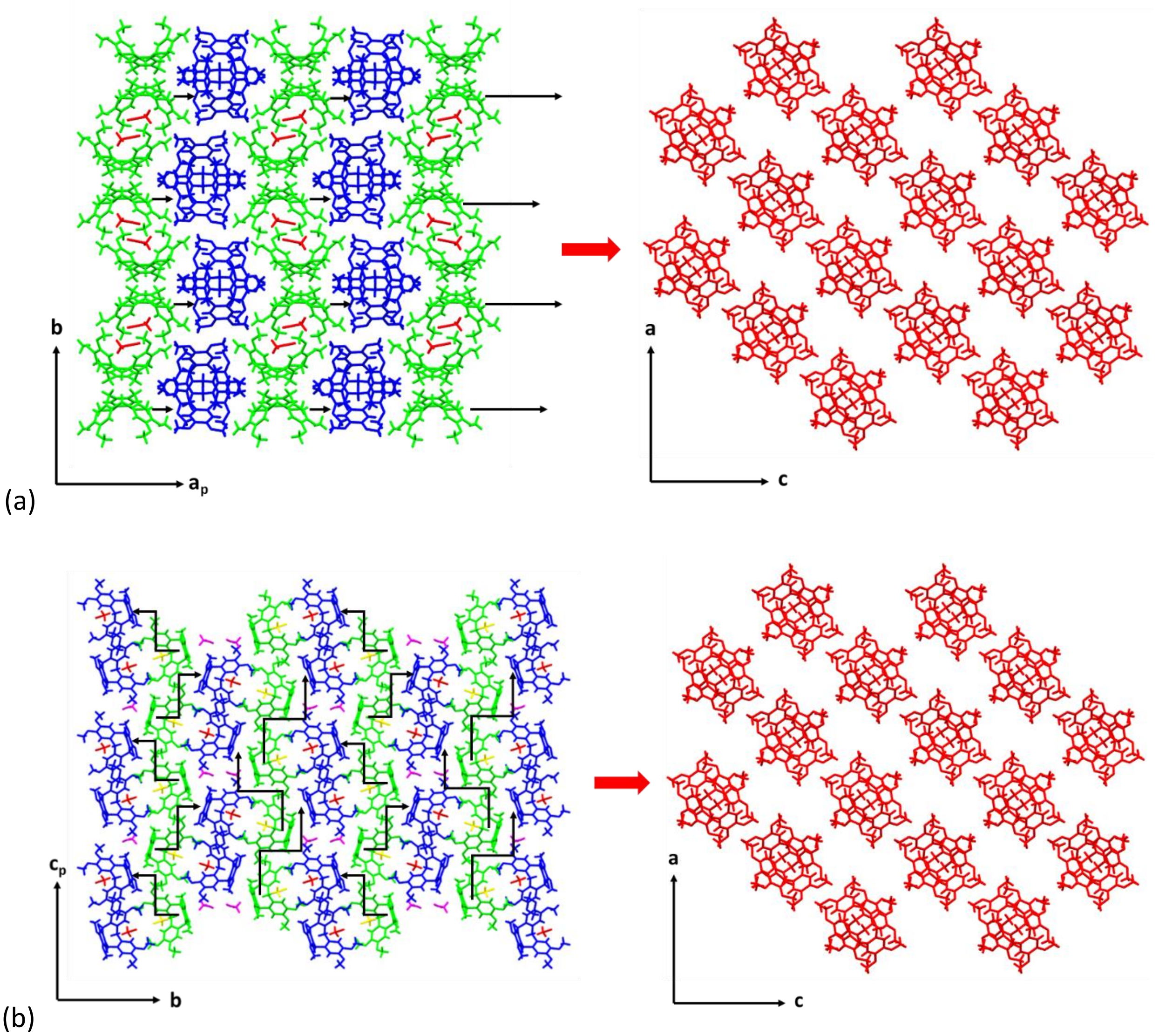

Figure 3.42: The proposed mechanism for the formation of stacked columns of CTV after solvent removal in (a) **1** and (b) **2**.

If this hypothesis is correct and the structure of **3b** consists of tightly-packed layers of antiparallel columns of CTV, then how do **1** and **4**, which also have dimeric capsules of CTV molecules within their respective structures, and **2**, which consists of semi-stacked antiparallel 'zippers' of CTV molecules, end up having the same desolvated structure? One hypothesis is that translational shifts and rotations of dimer CTV molecules result in the formation of columns which are antiparallel (Fig. 3.42). This may explain how these three different types of structures arrive at the same endpoint. Indeed, **1** and **4** already have alternating antiparallel columns for half of the structure.

3.4. Gas & Vapour Sorption

Table 3.18 displays the vapour pressure at 25 °C of the solvents used for vapour sorption. The desolvated compounds of **1**, **2**, **3** and **4** display the same PXRD pattern, and therefore are taken to be the same phase and therefore **1b** will be discussed as a representative example of the desolvated phases **b**. **2** could not be prepared in sufficient bulk and purity for gas sorption and hence gas sorption could not be performed on the **2b** phase of this compound.

Table 3.18: The vapour pressure at 25 °C of the solvents used for vapour sorption.

Solvent	Vapour Pressure at 25 °C (mm Hg)
Acetonitrile	91.4 [28]
Chloroform	196.8 [29]
2-butanone	90.6 [30]
Water	23.8 [31]

Table 3.19: Gas sorption maxima of all desolvated compounds of **1** for nitrogen (77 K), carbon dioxide (273 K), hydrogen (77 K) and water vapour (298 K).

Compound	Nitrogen (cm^3 (STP) g^{-1})	Carbon Dioxide (cm^3 (STP) g^{-1})	Hydrogen (cm^3 (STP) g^{-1})	Water (cm^3 (STP) g^{-1})
1a	5.53	9.47	16.48	32.47
1b	9.54	2.81	9.80	29.60

Form **1a**, the 'hollow' dimer structure which is not observed for **2**, **3** and **4**, and **1b**, the structure of which is unknown but is suggested to be a column structure closely related to **3**, were examined for their gas sorption capabilities for N_2, H_2 and CO_2. Nitrogen sorption at 77 K was negligible for both forms. Carbon dioxide sorption of **1a** was significant for the pressure (up to 783 mm Hg) and temperature (273 K) of analysis. The sorption of 9.47 cm^3 (STP) g^{-1} at 783 mm Hg for **1a** corresponds to ~0.38 CO_2 molecules per asymmetric unit. This sorption happens despite an obstructed route for CO_2 sorption (see Fig. 3.3b and 3.3c), which probably causes rotation of the methyl groups for sorption to be observed. This ability of CO_2 to frequently cause selective structural alterations in many structures without open channels has been accredited to its quadrupole moment.[32] The maximum sorption for **1b** is significantly lower at 2.81 cm^3 (STP) g^{-1} and 665 mm Hg. Another interesting occurrence was that for both **1a** and **1b** hysteresis was observed, showing that these materials are capable of holding on to CO_2 with decreasing pressure. Hydrogen sorption is also appreciable for the pressure and temperature (77 K) of analysis for both **1a** and **1b**. The hydrogen sorption of **1b** reached a maximum of 9.80 cm^3 (STP) g^{-1} at 816 mm Hg, corresponding to ~0.4 hydrogen molecules per asymmetric unit (or 0.088 wt. %). The hydrogen sorption of **1a** was greater, reaching a maximum of 16.48 cm^3 (STP) g^{-1} at 805 mm Hg, corresponding to ~0.6 hydrogen molecules per asymmetric unit (or 0.14 wt. %). Hysteresis was observed for the hydrogen desorption of both **1a** and **1b**. Water vapour sorption was similar for both **1a** and **1b** and was appreciable for the pressure and temperature (298 K) of analysis. Water vapour sorption for **1b** reached a maximum of 29.60 cm^3 (STP) g^{-1} at 18 mm Hg, corresponding to ~1.2 molecules of H_2O per asymmetric unit. Water vapour sorption for **1a** was found to be slightly higher, reaching a maximum of 32.47 cm^3 (STP) g^{-1} at 17 mm Hg, corresponding to ~1.3 molecules of H_2O per asymmetric unit.

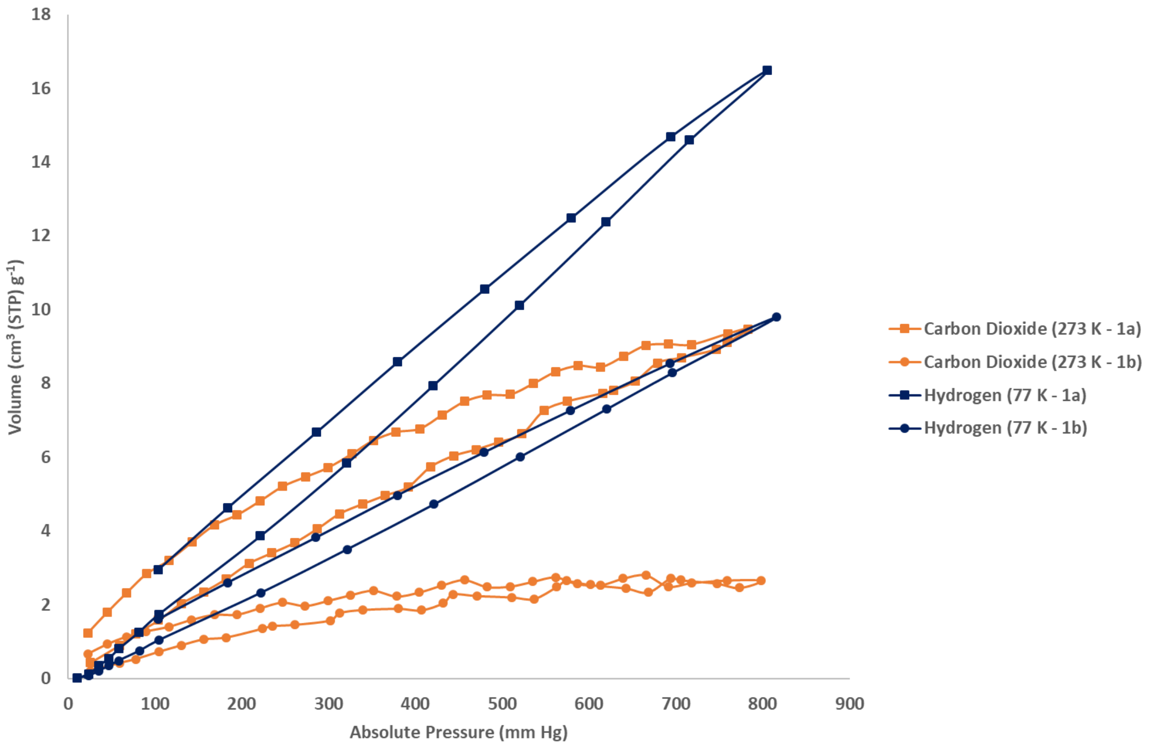

Figure 3.43: Carbon dioxide and hydrogen sorption isotherms of **1a** and **1b**.

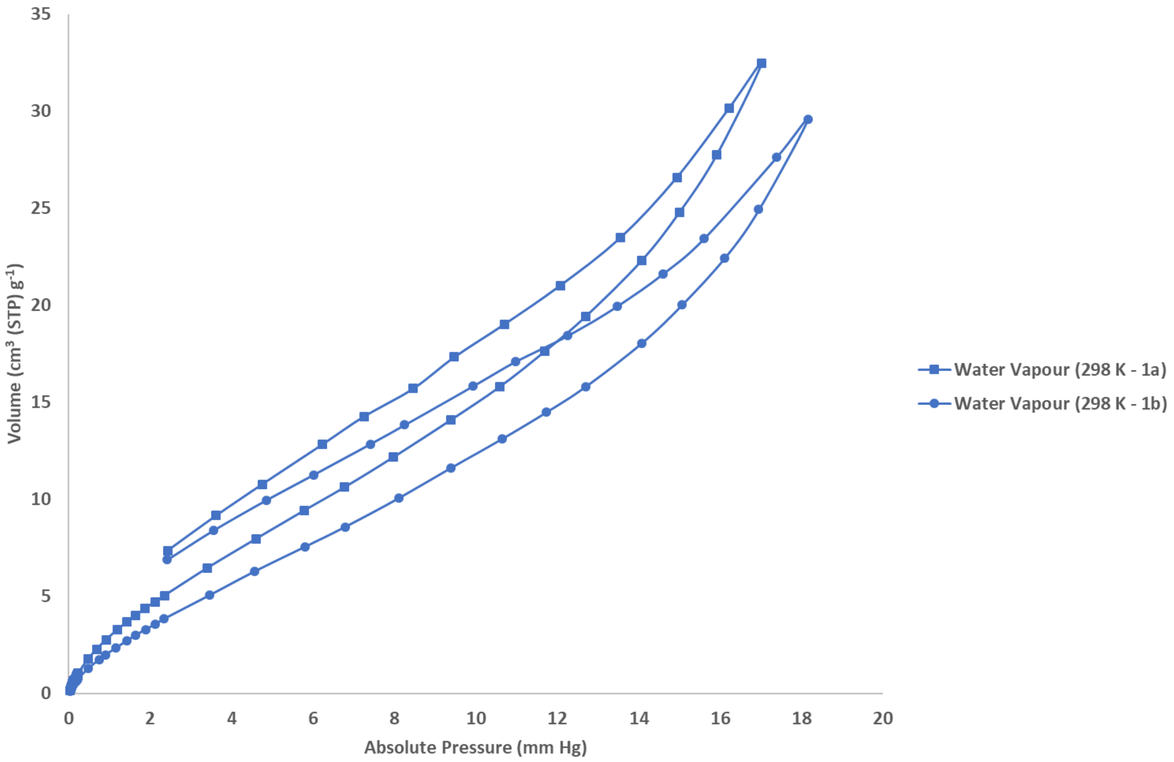

Figure 3.44: Water vapour sorption isotherms of **1a** and **1b**.

However, CO_2, H_2 and N_2 sorption were not as significant as hoped and therefore vapour sorption was attempted, where vapour generated from the original solvent of crystallization was used. Both **1a** and **1b** were subjected to acetonitrile vapour sorption on the gas sorption analyser. The acetonitrile vapour sorption for both phases was considerable for the pressure and temperature (298 K) of analysis (Fig. 3.45). The adsorption for **1b** shows a gradual increase with increasing pressure until an inflection point occurs at a pressure of 54 mm Hg and adsorption of 17.02 cm^3 (STP) g^{-1}, corresponding to ~0.7 molecules of acetonitrile per asymmetric unit. This indicates a structural change occurring, leading to a rapid increase in sorption. The adsorption is just beginning to plateau, which probably means the CTV host arrangement is now similar to that of **1**/**1a**, when the maximum sorption of 57.93 cm^3 (STP) g^{-1} at 71 mm Hg for **1b**, corresponding to ~2.3 acetonitrile molecules per asymmetric unit, is reached. Large hysteresis is observed upon decreasing pressure, showing the ability of this structure to trap the acetonitrile molecules within. This is consistent with TGA results showing that nearly 100 °C is required to desolvate **1**, which is in the absence of an external acetonitrile vapour pressure. The minimum sorption recorded upon desorption is 43.58 cm^3 (STP) g^{-1} at 9 mm Hg, corresponding to ~1.8 molecules of acetonitrile per asymmetric unit. The adsorption of acetonitrile vapour for **1a** is greater than **1b** across the pressure range, slowly increasing with increasing pressure, but no inflection point is observed, as opposed to the adsorption isotherm for **1b**. Instead, the slope of the adsorption isotherm initially gently increases with increasing pressure – however, there is a sharp increase in adsorption at higher pressures. This is expected, since the host arrangement within **1a** is relatively similar to that of **1**. The maximum sorption of 74.41 cm^3 (STP) g^{-1} at 67 mm Hg for **1a** corresponds to ~3.0 acetonitrile molecules per asymmetric unit. This is in comparison with the one per asymmetric unit observed in the single crystal X-ray structure of **1**, showing that the acetonitrile capacity of **1** is greater than originally observed. Once again, large hysteresis is observed upon decreasing pressure, with desorption occurring gradually but steadily until reaching a minimum of 58.27 cm^3 (STP) g^{-1} at 9 mm Hg. This corresponds with ~2.3 molecules of acetonitrile per asymmetric unit.

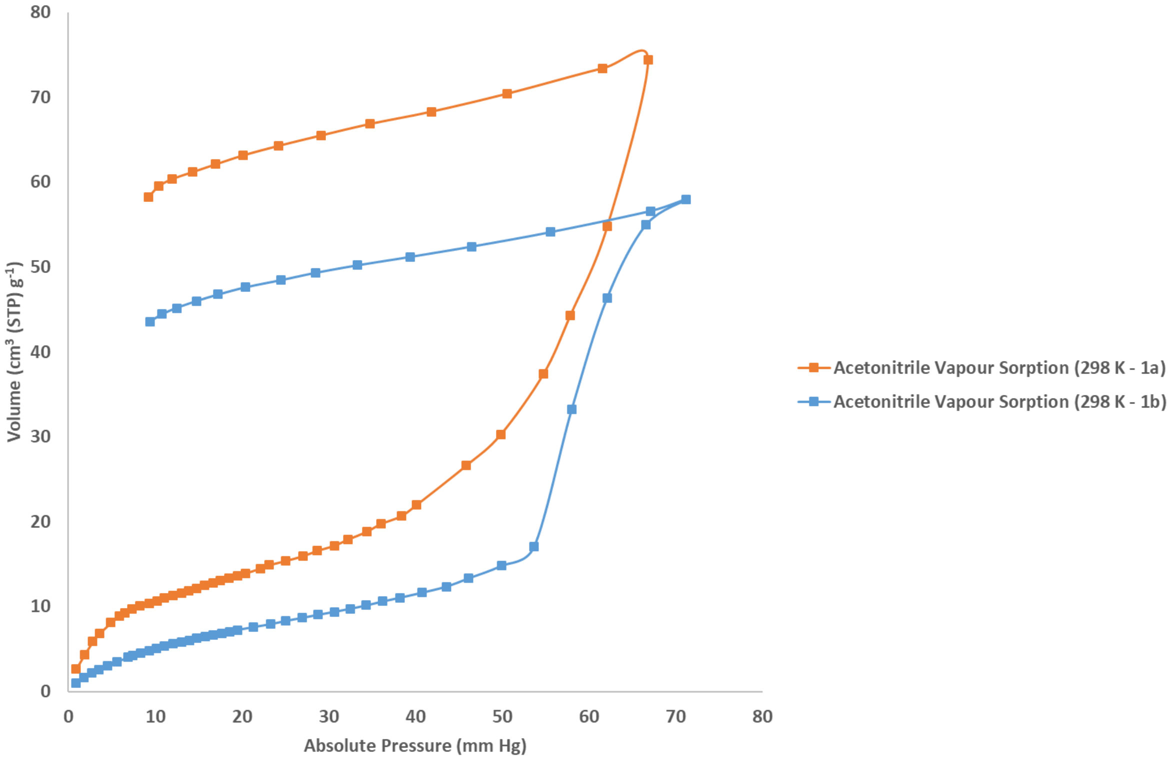

Figure 3.45: Acetonitrile vapour sorption isotherms of **1a** and **1b**.

PXRD experiments were done on both **1a** and **1b** after exposure to the acetonitrile vapour sorption experiment (Fig. 3.46). The structures of the two samples appear to have reverted to the structure of the initial solvated structure **1**. Both **1a** and **1b** show that they can accommodate a higher number of acetonitrile molecules per ASU than the original crystal structure. These are possibly accommodated between the dimer and column layers when **1a** and **1b** revert to **1** under acetonitrile pressure.

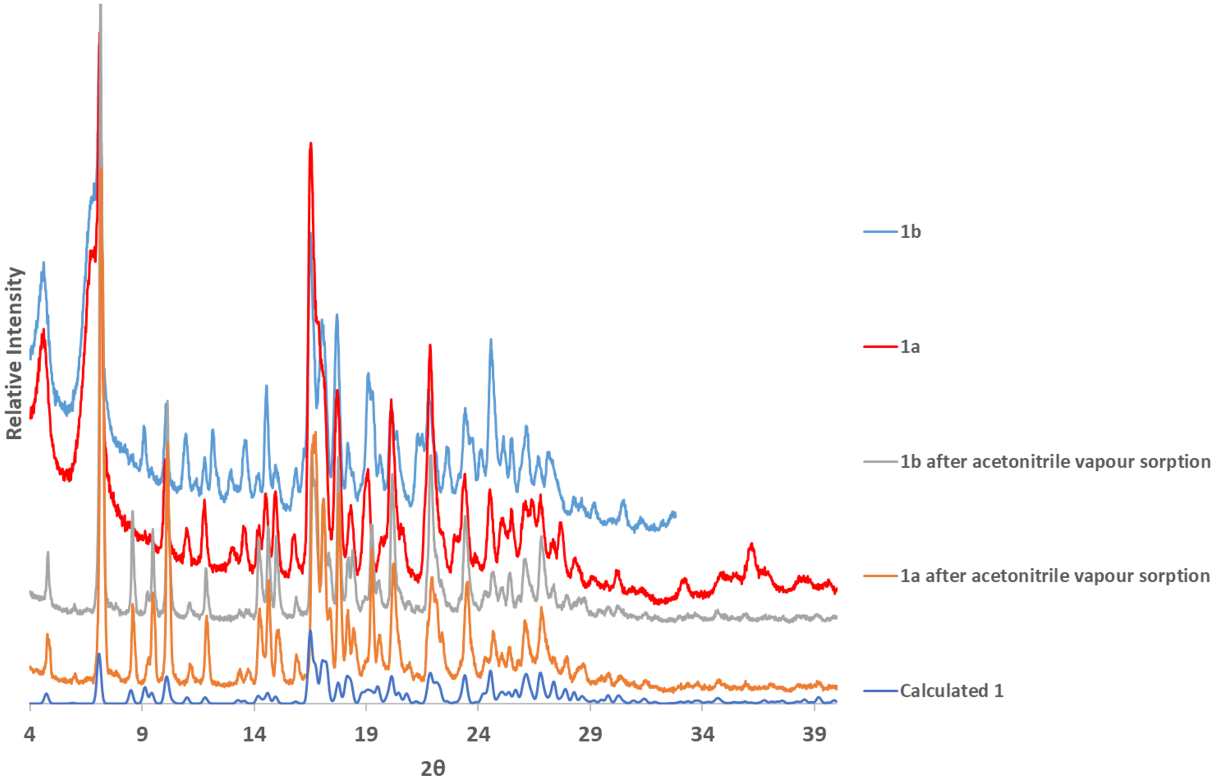

Figure 3.46: PXRD patterns of **1a** and **1b** after acetonitrile vapour sorption on the gas sorption analyser and comparison with the calculated PXRD pattern obtained from the structure of **1** and the PXRD patterns of **1a** and **1b**.

The chloroform sorption for **3b** is initially low, reaching only 3.08 cm^3 (STP) g^{-1} at a pressure of 33 mm Hg, corresponding to ~0.06 molecules of chloroform per asymmetric unit. At this point, an inflection point occurs, suggesting a critical pressure needs to be reached before a structural change occurs which facilitates sorption, as indicated by a substantial increase in chloroform vapour sorption observed from 3.08 cm^3 (STP) g^{-1} (33 mm Hg) to 105.36 cm^3 (STP) g^{-1} at 83 mm Hg. This corresponds to ~2.1 molecules of chloroform per asymmetric unit, similar to what is observed in the crystal structure. Subsequently, the sorption isotherm begins to plateau and increase more slowly, before reaching a maximum of 135.12 cm^3 (STP) g^{-1} at only ~162 mm Hg, corresponding to ~2.7 chloroform molecules per asymmetric unit, more than what is observed in the ASU of **3**, possibly suggesting a larger separation of the layers of 'stacked' CTV molecules, accommodating more chloroform molecules. Large hysteresis is observed upon decreasing pressure, indicating the structure is capable of trapping the chloroform molecules within. The minimum reached by the desorption isotherm is 104.09 cm^3 (STP) g^{-1} at 17 mm Hg, corresponding to ~2.1 molecules of chloroform per asymmetric unit, similar to what is observed within the crystal structure. A PXRD experiment was carried out on the sample after chloroform vapour sorption and comparison between the pattern obtained, the calculated pattern obtained from the crystal structure of **3** and the pattern of **3a** (Fig. 3.48) show that even though the sample has lost some crystallinity, probably due to solvent loss (TGA indicated solvent loss at low temperatures), the pattern is very similar to that of the desolvated state **3a**. Given the number of chloroform molecules per asymmetric unit calculated at the minimum of the desorption isotherm and the rapid solvent loss observed, it is reasonable to suspect that the material started as **3** upon removal from the gas sorption analyser and had already converted to **3a** by the time the PXRD was performed, despite attempting to do it as soon as possible after removal from the chloroform atmosphere.

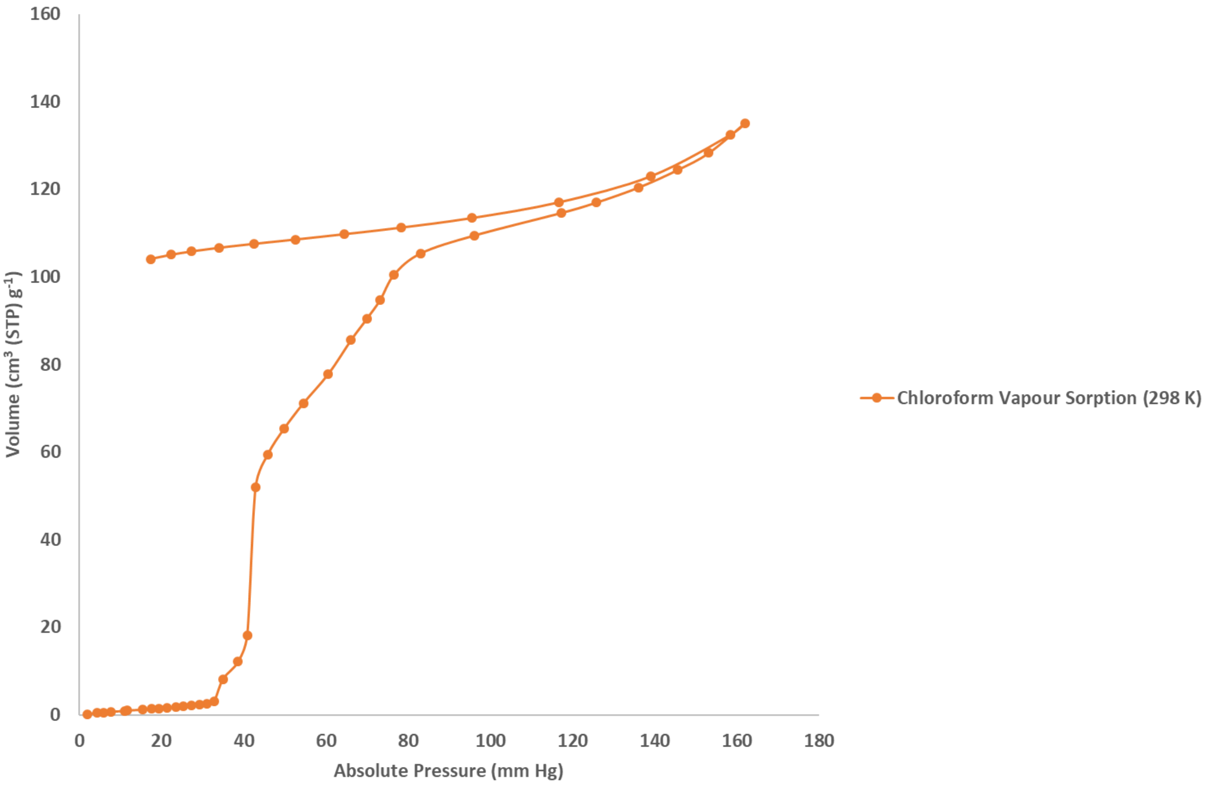

Figure 3.47: Chloroform vapour sorption isotherm of **3b**.

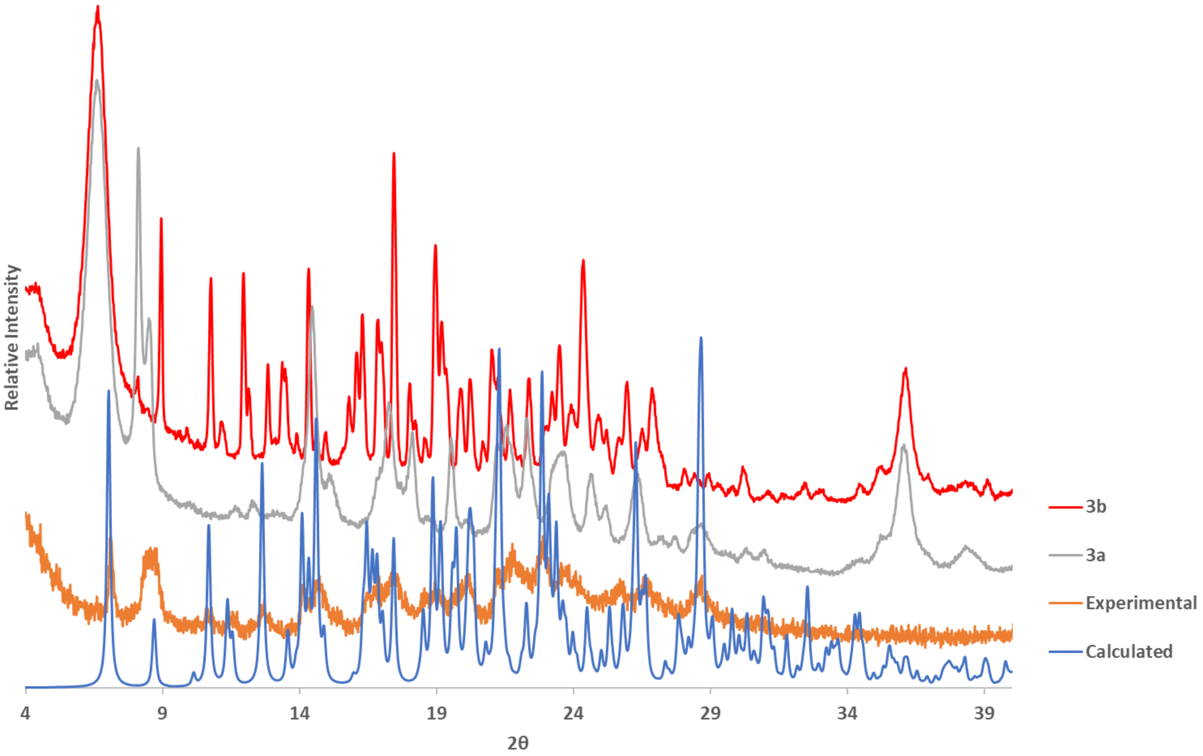

Figure 3.48: PXRD pattern of the **3b** sample after chloroform vapour sorption on the gas sorption analyser compared with the calculated pattern of **3** obtained from the crystal structure, along with the PXRD patterns of **3a** and **3b**.

The butanone sorption of **4b** is significant for the temperature (298 K) and pressure of analysis (up to 75 mm Hg). No inflection points are observed in the adsorption isotherm, suggesting any induced structural changes are gradual rather than sudden, supported by the gradual increase in butanone vapour sorption with increasing pressure. The maximum sorption of 35.27 cm^3 (STP) g^{-1} at only 75 mm Hg corresponds to ~1.4 butanone molecules per asymmetric unit, higher than what is observed in the ASU of **4**, 0.5 butanone molecules per ASU. Large hysteresis is observed upon decreasing the pressure, suggesting the structure is capable of trapping the 2-butanone molecules within. The minimum sorption reached on the desorption isotherm is 19.81 cm^3 (STP) g^{-1} at 10 mm Hg, corresponding to ~0.8 molecules of 2-butanone per asymmetric unit.

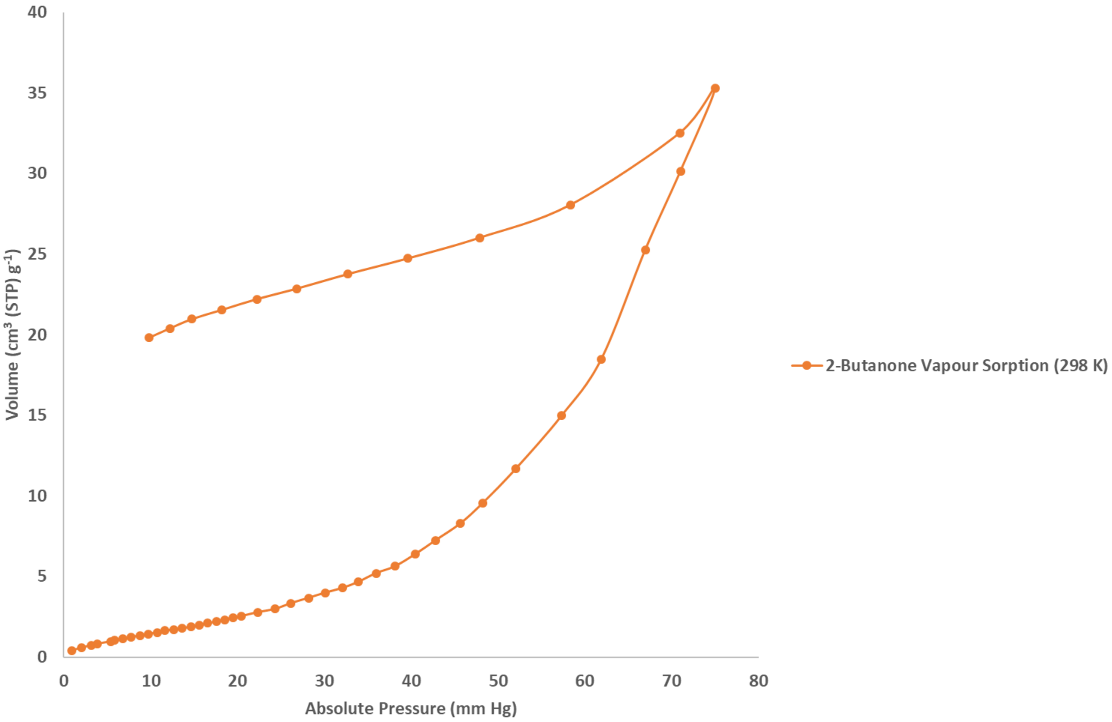

Figure 3.49: 2-butanone vapour sorption isotherm of **4b**.

The PXRD of **4b** after butanone vapour sorption on the gas sorption analyser is displayed (Fig. 3.50). While the sample displayed uptake of 2-butanone vapour, the PXRD pattern does not seem to have changed and is very similar to that of **4b**. Therefore, it can be suggested that the 2-butanone molecules have simply forced the layers of CTV columns apart within the proposed desolvated structure based on **3b** for sorption to occur, rather than the structure reverting to the structure of **4**.

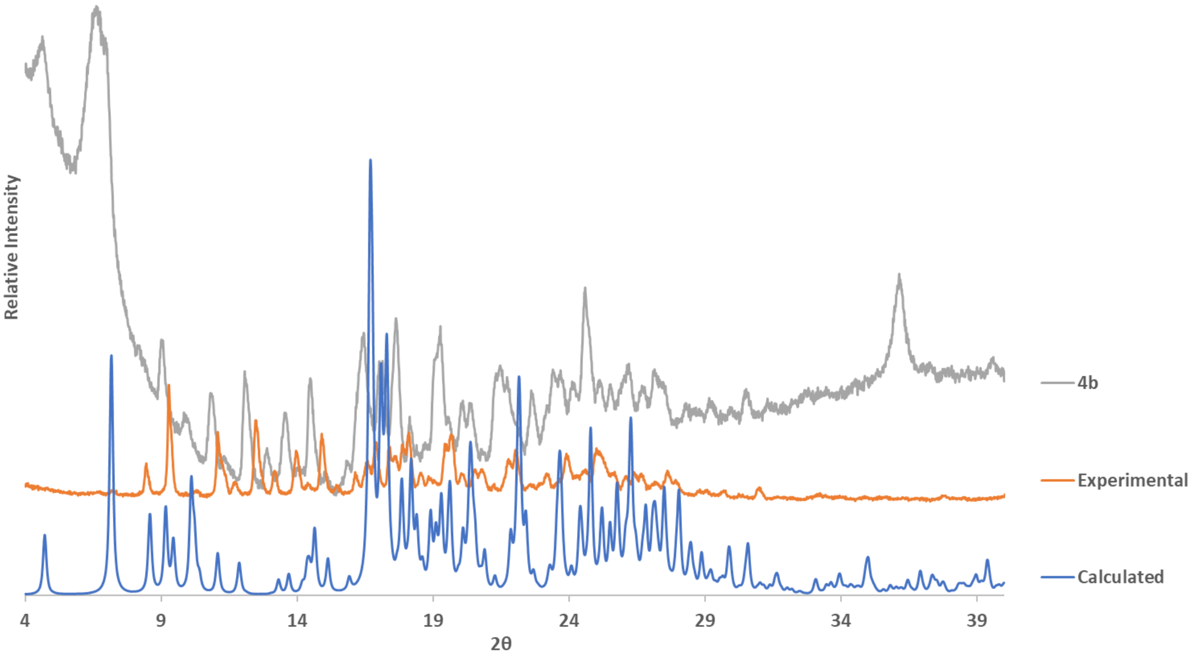

Figure 3.50: PXRD pattern of the **4b** sample after butanone vapour sorption on the gas sorption analyser (in orange) compared with the predicted pattern of **4** obtained from the crystal structure (in blue) and the PXRD pattern of **4b** before vapour sorption (in grey).

3.5. Summary

Several new CTV inclusion compounds have been isolated. These compounds are shown to crystallise from and include three different solvents – acetonitrile, chloroform and 2-butanone. In **1** and **4**, which are almost isostructural, the CTV molecules exist as dimeric capsules, which include acetonitrile (**1**) or 2-butanone (**4**), and as self-included CTV molecules which stack into columns. **2**, which also crystallises from and contains acetonitrile, is obtained from a saturated solution of CTV in acetonitrile and is most likely the kinetic product of the crystallization. It is therefore not very stable and loses solvent quickly upon heating. **3**, which crystallises from chloroform, has the CTV molecules packing in antiparallel columns. These columns form layers, and between these layers of CTV columns are layers of chloroform molecules. **1** could be desolvated into polymorphs **1a** and **1b**, with the transition to **1a** monitored by a single-crystal-to-single-crystal transformation. Even though **4** is isostructural with **1**, this phase is not observed (as indicated by VT-PXRD) – the only desolvated form of **4** that is observed, **4b**, has a PXRD pattern that matches the second desolvated form of **1**, **1b**, very closely. **2**, **3** and **4** lose their monocrystallinity immediately upon desolvation, therefore the structures of their desolvated forms, **2b**, **3b** and **4b**, are unknown. However, the PXRD pattern of **3b** is similar to that of the solvated form, **3**, so it is proposed that the packing of the host changes very little upon solvent removal, except that the layers of 'stacked' CTV molecules move closer together due to the absence of chloroform.

It has been shown that these four compounds all contain solvent which can be removed to obtain the same crystalline, potentially porous material which is suitable for gas sorption studies. The nitrogen gas sorption for all of these desolvated compounds is negligible. **1b** was taken as a representative example for **2b**, **3b** and **4b**. **1a** was also subjected to gas sorption as a hollow dimer form. Both **1a** and **1b** displayed CO_2, H_2 and H_2O vapour sorption. In each case, the sorption was higher for **1a** than for **1b**, although neither were very high. Thus, vapour sorption of the original solvents of crystallization was attempted. All compounds displayed significant vapour sorption upon exposure to the initial solvents which they were prepared from. In fact, **1a** and **1b** reverted to their original solvated form **1** upon exposure to acetonitrile vapour, while **3b** seemed to revert to **3** upon exposure to chloroform vapour with subsequent desolvation to **3a**, whilst **4b** seemed to display no transformation at all upon exposure to 2-butanone vapour.

These are significant rearrangements in the solid state by simply exposing these compounds to a vapour phase. The fact that essentially the same phase can trap these different solvents indicates its versatility as a trapping agent.

3.6. References

1. Hardie, M.J. *Chem. Soc. Rev.*, **2010**, *39*, 516-527.

2. A. Collet, J.-P. Dutasta, B. Lozach and J. Canciell, in *Supramolecular Chemistry I – Directed Synthesis and Molecular Recognition*, ed. E. Weber, Springer, Berlin, 1993, ch. 3, vol. 165, pp. 103–129.
3. Brotin, T.; Dutasta, J.-P. *Chem. Rev.*, **2009**, *109*, 88-130.
4. Lindsey, A.S. *Chem. Ind.*, **1963**, 823-824.
5. Ronson, T.K.; Fisher, J.; Harding, L.P.; Rizkallah, P.J.; Warren, J.E.; Hardie, M.J. *Nat. Chem.*, **2009**, *1*, 212-216.
6. Westcott, A.; Fisher, J.; Harding, L.P.; Rizkallah P.; Hardie, M.J. *J. Am. Chem. Soc.*, **2008**, *130*, 2950-2951.
7. Henkelis, J.J.; Ronson, T.K.; Harding, L.P.; Hardie, M.J. *Chem. Commun.*, **2011**, *47*, 6560-6562.
8. Steed, J.W.; Junk, P.C.; Atwood, J.L.; Barnes, M.J.; Raston, C.L.; Burkhalter, R.S. *J. Am. Chem. Soc.*, **1994**, *116*, 10346-10347.
9. Konarev, D.V.; Khasanov, S.S.; Vorontsov, I.I.; Saito, G.; Antipin, M.Y.; Otsuka, A.; Lyubovskaya, R.N. *Chem. Commun.*, **2002**, 2548-2549.
10. Rio, Y.; Nierengarten, J.F. *Tetrahedron Lett.*, **2002**, *43*, 4321-4324.
11. Zachary, R.O.; Dorjderem, N.; Richard, C.H.; Daniel, P.B. *Nanotechnology*, **2011**, *22*, 275611-275616.
12. Brotin, T.; Dutasta, J.-P. *Eur. J. Org. Chem.*, **2003**, 973-984.
13. Hardie, M.J.; Sumby, C.J. *Inorg. Chem.*, **2004**, *43*, 6872-6874.
14. Taratula, O.; Dmochowski, I.J. *Curr. Opin. Chem. Biol.*, **2010**, *14*, 97-104.
15. Collet, A. *Tetrahedron*, **1987**, *43*, 5725-5759.
16. Hardie, M.J.; Ahmad, R.; Sumby, C.J. *New J. Chem.*, **2005**, *29*, 1231-1240.
17. Hardie, M.J.; Raston, C.L. *Angew. Chem., Int. Ed.*, **2000**, *39*, 3835-3839.
18. Mough, S.T.; Goeltz, J.C.; Holman, K.T. *Angew. Chem., Int. Ed.*, **2004**, *43*, 5631-5635.
19. Arduini, A.; Calzavacca, F.; Demuru, D.; Pochini, A.; Secchi, A. *J. Org. Chem.*, **2004**, *69*, 1386-1388.
20. Sumby, C.J.; Fisher, J.; Prior, T.J.; Hardie, M.J. *Chem. – Eur. J.*, **2006**, *12*, 2945-2959.
21. Wytko, J.A.; Boudon, C.; Weiss, J.; Gross, M. *Inorg. Chem.*, **1996**, *35*, 4469-4477.

22. Holman, K.T.; Orr, G.W.; Atwood, J.L.; Steed, J.W. *Chem. Commun.*, **1998**, 2109-2110.
23. Staffilani, M.; Bonvicini, G.; Steed, J.W.; Holman, K.T.; Atwood, J.L.; Elsegood, M.R.J. *Organometallics*, **1998**, *17*, 1732-1740.
24. Ahmad, R.; Hardie, M.J. *Supramol. Chem.*, **2006**, *18*, 29-38.
25. Zhang, H.; Atwood, J.L. *J. Crystallogr. Spectrosc. Res.*, **1990**, *20*, 465-470.
26. Spek, A.L. *Acta Crystallographica Section D – Biological Crystallography*, **2009**, *65*, 148-155.
27. Macrae, C.F.; Bruno, I.J.; Chisholm, J.A.; Edgington, P.R.; McCabe, P.; Pidcock, E.; Rodriguez-Monge, L.; Taylor, R.; van de Streek, J.; Wood, P.A. *J. Appl. Cryst.*, **2008**, *41*, 466-470.
28. http://www.ddbst.com/en/EED/PCP/VAP_C3.php
29. http://www.ddbst.com/en/EED/PCP/VAP_C47.php
30. https://pubchem.ncbi.nlm.nih.gov/compound/2-Butanone#section=Vapor-Pressure
31. http://www.wiredchemist.com/chemistry/data/vapor-pressure
32. Hyun, S.-M.; Lee, J.H.; Jung, G.Y.; Kim, Y.K.; Kim, T.K.; Jeoung, S.; Kwak, S.K.; Moon, D.; Moon, H.R. *Inorg. Chem.*, **2016**, *55*, 1920-1925.

Chapter 4 – Preparation and Analysis of *C*-Methylcalix[4]resorcinarene Solvates

4.1. Introduction

Macromolecules found in nature can form sizeable supramolecular assemblies such as ribosomes, cellular membranes and viruses.[1-3] These complex structures are maintained by non-covalent interactions which are crucial to the functioning of these biological systems. Yet, large multi-component synthetic supramolecular assemblies ($n > 3$) consisting of small molecules, which encapsulate chemical space, are uncommon in supramolecular chemistry. The initial example of this was when six bowl-shaped host molecules of *C*-methylcalix[4]resorcinarene (CMCR) (Fig. 4.1) spontaneously assembled in a nitrobenzene solution to form a large, chiral assembly, with eight water molecules 'stitching' the CMCR molecules into this spherical assembly by O-H···O hydrogen bonds.[4] Since this discovery, a similar hexameric assembly of CMCR was reported, with six of the eight water molecules replaced by 2-ethylhexanol molecules.[5] Large hexameric assemblies have also been reported for the structurally similar pyrogallolarenes, which have three hydroxyl groups per aromatic ring and longer hydrocarbon chains replacing the methyl groups.[6-11] CMCR has also been shown to crystallise in two unique hexameric arrangements within the same crystal from 1-butanol.[12] These two hexameric assemblies were bound by a water molecule into a supra-heterodimer.

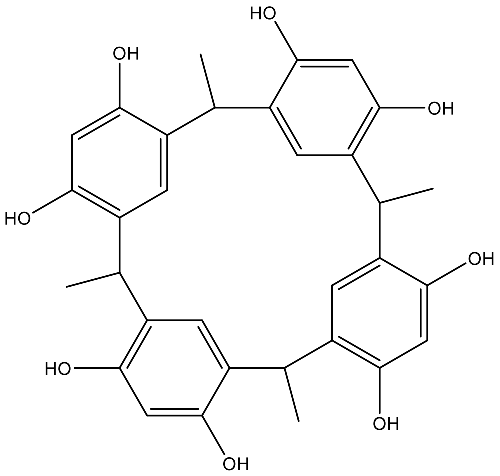

Figure 4.1: The structural formula of *C*-methylcalix[4]resorcinarene (CMCR).

Herein we present the synthesis of several CMCR-alcohol compounds, crystallised from methanol, ethanol, isopropanol, 1-propanol, 1-butanol and 1-pentanol, in order to examine the effect of the solvent chain length on the structure. These compounds have been characterized by X-ray diffraction and thermal analysis. After desolvation, all of the compounds were subjected to gas and/or vapour sorption studies.

4.2. Experimental

4.2.1. Materials

C-methylcalix[4]resorcinarene was purchased from Sigma Aldrich and used as received. All non-anhydrous solvents were purchased from KIMIX Chemical & Lab Supplies and used as received.

4.2.2. Preparation of crystal forms

4.2.2.1. CMCR-methanol (($C_{32}H_{32}O_8$) · (CH_4O)$_3$ · (H_2O)$_5$) (**5**)

CMCR (100 mg) was dissolved in methanol (3 mL) with heating and stirring. The remaining undissolved solid was removed by syringe filtration using a filter of 0.45 µm and the vial allowed to stand with the cap perforated. Slow evaporation resulted in the formation of clear, colourless needle-like crystals overnight, which, unfortunately, were not suitable for SCXRD analysis. However, other analyses such as PXRD and thermal analysis could be performed.

4.2.2.2. CMCR-ethanol (($C_{32}H_{32}O_8$) · (C_2H_6O)$_3$ · (H_2O)$_5$) (**6**)

CMCR (100 mg) was dissolved in ethanol (3 mL) with heating and stirring. The remaining undissolved solid was removed by syringe filtration and the vial allowed to stand with the cap perforated. Slow evaporation resulted in the formation of small, clear, white prismatic crystals after 1-2 days, which, unfortunately, were not suitable for SCXRD analysis. However, other analyses such as PXRD and thermal analysis could be performed.

4.2.2.3. CMCR-isopropanol (($C_{32}H_{32}O_8$) · (C_3H_8O)$_3$ · (H_2O)$_5$) (**7**)

CMCR (100 mg) was dissolved in isopropanol (3 mL) with stirring. The vial was then covered with perforated parafilm and allowed to stand. Slow evaporation resulted in the formation of clear, yellowish needle-like crystals after 5-10 days, which, unfortunately, were not suitable for SCXRD analysis. However, other analyses such as PXRD and thermal analysis could be performed.

4.2.2.4. CMCR-1-propanol (($C_{32}H_{32}O_8$) · (C_3H_8O)$_3$ · (H_2O)$_{1.67}$) (**8**)

CMCR (100 mg) was dissolved in 1-propanol (3 mL) with stirring. The vial was then covered with perforated parafilm and allowed to stand. Slow evaporation resulted in the formation of clear, brown, prismatic crystals after 7-10 days.

4.2.2.5. CMCR-1-butanol ($(C_{32}H_{32}O_8)_4 \cdot (C_4H_{10}O)_6 \cdot (H_2O)_{5.67}$) (**9**)

CMCR (100 mg) was dissolved in 1-butanol (3 mL) with stirring. The vial was then left uncapped and allowed to stand. Slow evaporation resulted in the formation of clear, brown prismatic crystals after 10-14 days.

4.2.2.6. CMCR-1-pentanol ($(C_{32}H_{32}O_8)_4 \cdot (C_5H_{12}O)_{5.33} \cdot (H_2O)_7$) (**10**)

CMCR (100 mg) was dissolved in 1-pentanol (3 mL) with stirring. The vial was then left uncapped and allowed to stand. Slow evaporation resulted in the formation of clear, brown prismatic crystals after 14-21 days.

4.2.3. Liquid-Assisted Grinding

Compounds **5**, **6**, **7** and **8** could also be prepared by liquid-assisted grinding in the presence of the appropriate solvent. The CMCR host was placed in a mortar and ground with a pestle after the addition of several drops of solvent to make a paste. Grinding proceeded for 10 – 60 minutes.

4.3. **Characterization Results & Discussion**

In this chapter, single crystal structures of **5** and **9** have been previously published by other authors.[20,12] In the case of **5**, the author of this thesis could unfortunately not produce suitable crystals for SCXRD analysis – however, characterization using PXRD and thermal analysis with gas and vapour sorption properties were also explored. The previous study of **5** only included a single crystal structure analysis as it was not the main thrust of the article. In the case of **9**, this author's SCXRD study reveals additional detail not evident in the published structure. In addition, **9** was subjected to VT-PXRD and vapour sorption studies.

4.3.1. Compound **5** (($C_{32}H_{32}O_8$) · (CH_4O)$_3$ · (H_2O)$_5$) (**5**), Compound **6** (($C_{32}H_{32}O_8$) · (C_2H_6O)$_3$ · (H_2O)$_5$) and Compound **7** (($C_{32}H_{32}O_8$) · (C_3H_8O)$_3$ · (H_2O)$_5$)

4.3.1.1. Single Crystal X-Ray Diffraction Analysis

This is a structure (**5**) published in the literature in 2006 (CSD refcode UCISUV).[20] The ASU of **5** is made up of half of a CMCR molecule, two methanol molecules and three water molecules. The CMCR molecules are not in a bowl conformation as is usually observed for these host molecules, but in a flattened 'boat' conformation (Fig. 4.2). The CMCR molecules pack in hydrogen-bonded chains along the *c*-axis, with channels containing both methanol and water found between these CMCR chains (Fig. 4.3).

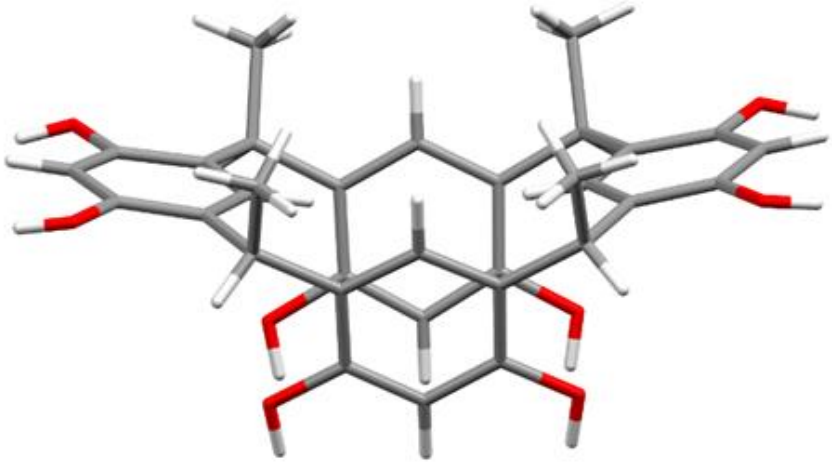

Figure 4.2: The conformation of CMCR in the crystal structure of **5**.

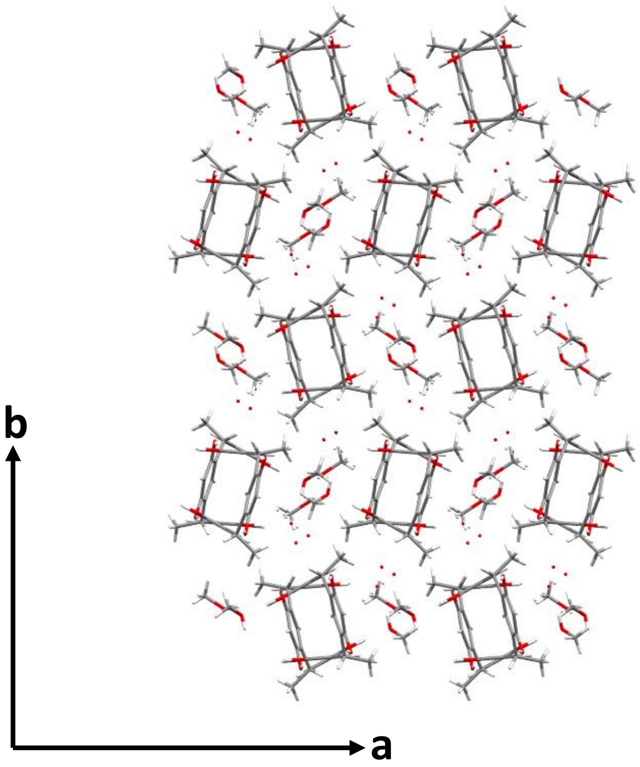

Figure 4.3: Packing diagram of **5** viewed along the *c*-axis.

Table 4.1: Unique hydrogen bonding parameters for **5**.*

Bonding atoms	D–H (Å)	H···A (Å)	D···A (Å)	D–H···A (°)	Symmetry operators
O4-H4···O25	0.84	1.96	2.774(3)	164	-x, 1-y, 1-z
O6-H6···O13	0.84	1.95	2.776(3)	169	-x, 1-y, 1-z
O13-H13···O52	0.84	1.87	2.688(4)	164	x, y, z
O25-H25···O50	0.84	1.87	2.700(4)	167	x, y, z
O50-H50···O52	0.84	1.92	2.745(4)	168	x, y, z
O51-H51G···O50	0.84	1.80	2.61(2)	163	x, y, z
O52···O54			2.738		x, y, z
O52···O53			2.751		½+x, 3/2-y, ½-z
O54···O6			2.952		½-x, -½+y, 1-z
C5-H5···O13	0.95	2.59	3.300(4)	131	-x, 1-y, 1-z
C29-H29C···O4	0.98	2.57	3.144(5)	117	x, y, z
C32-H32B···O6	0.98	2.58	3.153(4)	118	x, y, z

*This analysis is that of the author of this thesis.

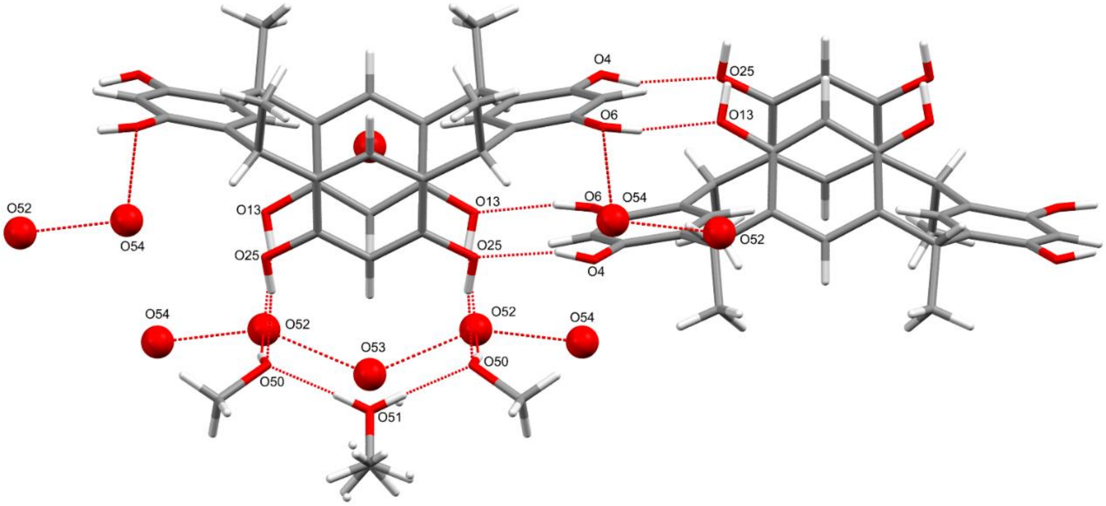

Figure 4.4: O-H···O hydrogen-bonding network between two CMCR molecules forming a chain along the *c*-axis, viewed along the *b*-axis.

There are nine unique conventional O–H···O hydrogen bonds present in the structure – one methanol···methanol, one CMCR···methanol, one methanol···water, two CMCR···water, two water···water and two CMCR···CMCR O–H···O hydrogen bonds. These hydrogen bonds seem to have an important role in linking the CMCR molecules together to form the chains which propagate along the *c*-axis (Fig. 4.4).[20]

Despite best efforts, suitable single crystals of **6** (CMCR-ethanol) and **7** (CMCR-isopropanol) for single crystal X-ray diffraction could not be obtained, however PXRD and thermal analysis could be performed on these samples.

4.3.1.2. Powder X-Ray Diffraction and Variable-Temperature Powder X-Ray Diffraction

5 has also been obtained by liquid-assisted grinding for 15 minutes in the presence of methanol, which likely contains water, as shown by close agreement of the PXRD patterns of **5** obtained by crystallization and LAG (Fig. 4.5). There are structures of CMCR in the literature which contain water and methanol (CSD refcode UCISUV),[20] methanol only (CSD refcode IFINAM)[21] or water only (CSD refcode MIGTUR).[22] However, comparison of the experimentally-obtained PXRD patterns of **5** with the three calculated patterns from these three crystal structures confirms that UCISUV is the most likely structure of **5**. The only difference between these patterns appears at around 13° 2θ, where one large peak is present in the calculated pattern of UCISUV (**5**), whereas no peak is evident in the experimentally-obtained LAG PXRD pattern.

It was found that the PXRD patterns obtained from ground crystals of **6** and **7** are almost identical to the experimental PXRD pattern of **5** (Fig. 4.6), indicating that **5**, **6** and **7** are isostructural or

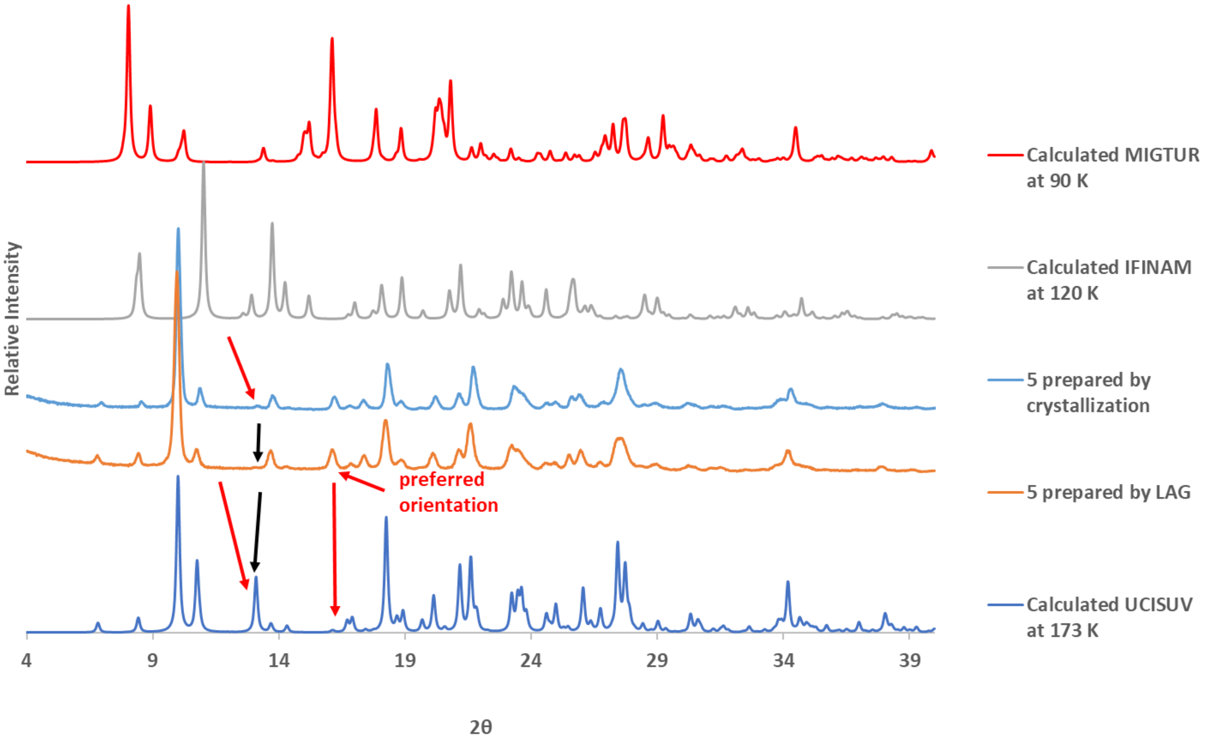

Figure 4.5: The experimentally-obtained PXRD pattern of **5** following 15 minutes of LAG in the presence of methanol (in orange) compared with the calculated PXRD pattern of **5** (UCISUV – CMCR, methanol and water) (in blue), the calculated PXRD pattern of IFINAM (CMCR and methanol) (in grey) and the calculated PXRD pattern of MIGTUR (CMCR and water) (in red). The unlabelled black arrow indicates the only small difference between the calculated **5** and experimentally-obtained **5**. The red arrows indicate different peak heights due to preferred orientation effects.

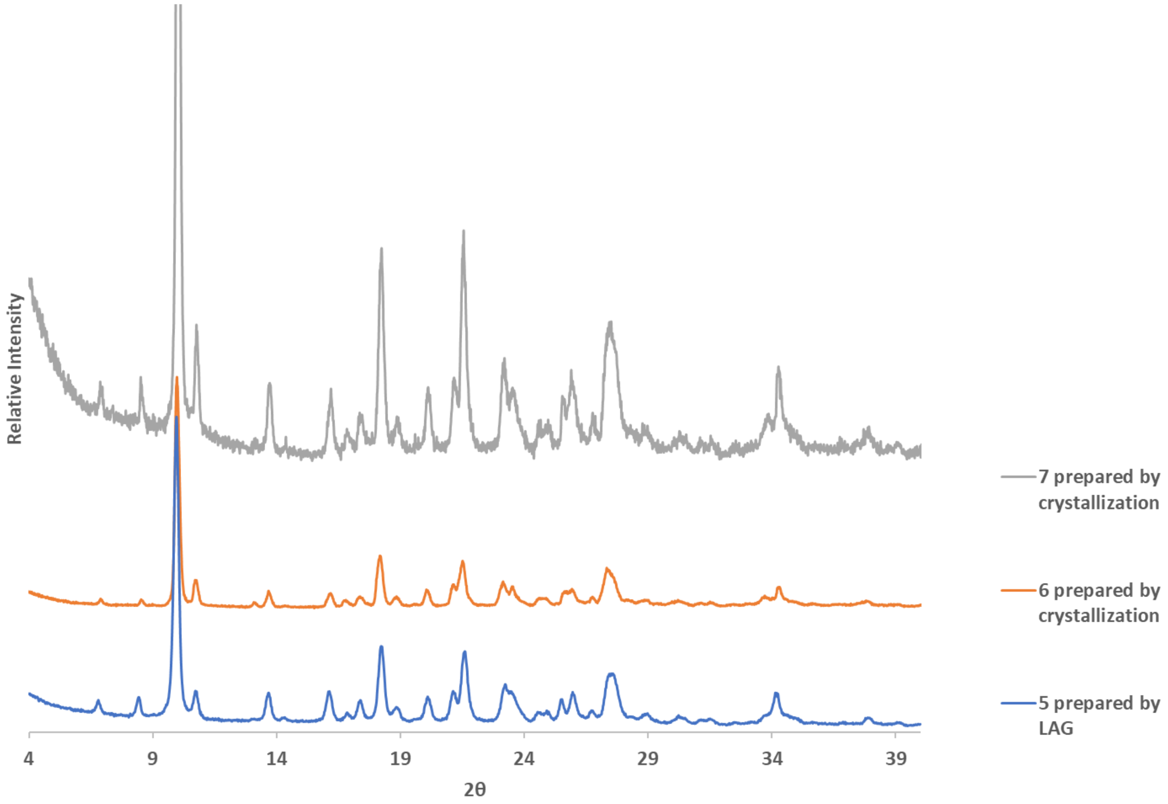

Figure 4.6: Experimental PXRD patterns of **6** (in orange) and **7** (in grey) compared with the experimental PXRD pattern obtained from **5** (in blue).

very close in the packing arrangement of their host molecules, despite differences in solvent content.

Variable-temperature PXRD experiments (VT-PXRD) performed on **5** over the temperature range 25–300 °C show that the sample is crystalline until 250 °C (Fig. 4.7). The 25 °C PXRD pattern agrees closely with the calculated PXRD pattern from the single crystal structure of **5**. The slight shifts in 2θ values are attributed to the different temperatures of analyses. At 50 °C, several changes are observed in the PXRD pattern (**5a**) (labelled with arrows in Fig. 4.7). A new peak has appeared at 12.2° 2θ, while the peaks at 18.0°, 21.4°, 23.0° and 27.3° 2θ have either decreased substantially or disappeared completely. The large peak at 9.8° 2θ has also decreased, and more so by 75 °C (PXRD pattern labelled as **5b**), while the peak that appeared at 12.2° 2θ has now disappeared and

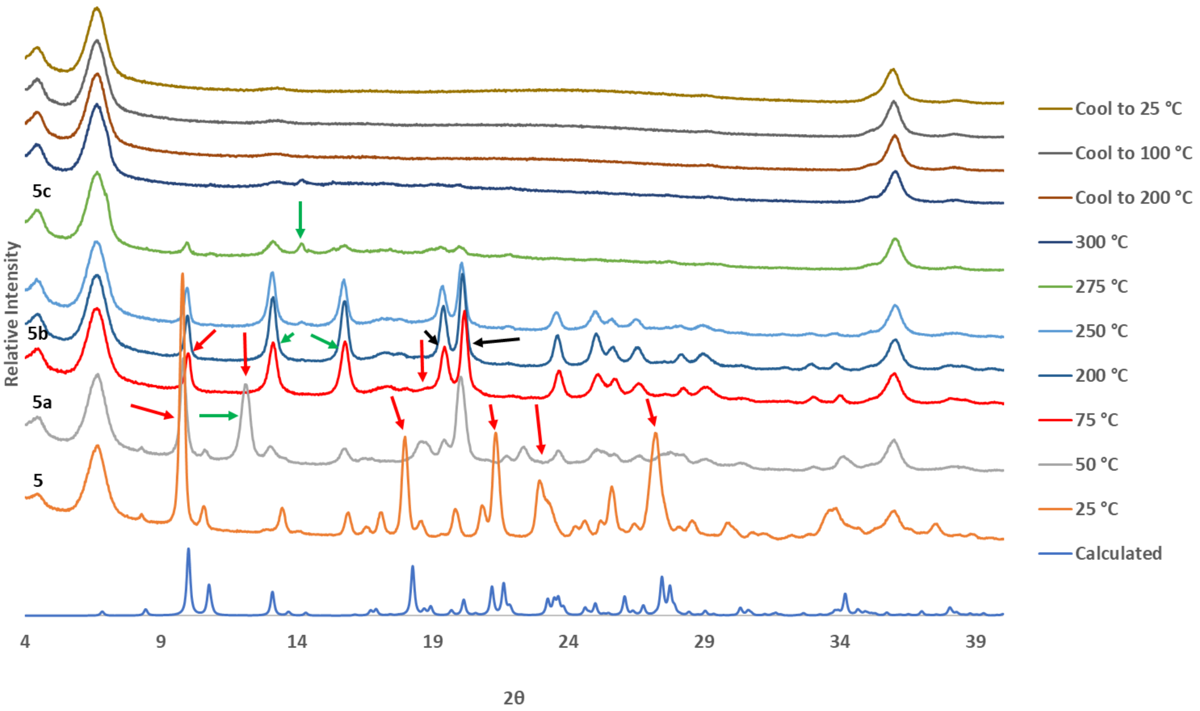

Figure 4.7: VT-PXRD patterns of **5** in the range 25-300 °C compared with the calculated PXRD pattern based on the crystal structure of **5**. Arrows indicate peaks referred to in the text (red – decreasing relative intensity, green – increasing relative intensity, black – increasing peak resolution).

the peaks at 13.2° and 15.9° 2θ have increased markedly at this temperature. The broad peak at around 18.8° 2θ seems to have disappeared, while the peaks at 19.5° and 20.2° 2θ are more resolved than in the 50 °C VT-PXRD pattern. This PXRD pattern (**5b**) remains virtually the same until 250 °C, when the sample begins to become amorphous at 275 °C but shows a peak appearing at 14.3° 2θ. This seems to be a new phase, **5c**. By 300 °C, it is almost completely amorphous and does not regain crystallinity upon cooling to 25 °C. It has likely decomposed (TGA indicates decomposition above 321.4 °C – this occurs at a lower temperature in the VT-PXRD experiment due to prolonged heating). Hence the temperature for desolvation of this compound, in preparation for gas or vapour sorption, should not exceed 250 °C.

Variable temperature-PXRD (VT-PXRD) experiments performed on **6** over the temperature range 25–300 °C (Fig. 4.8) reveal that the sample is crystalline throughout this temperature range, unlike **5**, which begins to lose crystallinity from 275 °C (Fig. 4.7). The 25 °C PXRD pattern agrees closely with the calculated PXRD pattern from the single crystal structure of **5**. The first transition is observed from **6** to **6a** from 25 – 50 °C, with a new peak appearing at 12.2° 2θ and the peaks at 17.9°, 21.2°, 22.9° and 27.2° 2θ have decreased. Another transition, from **6a** to **6b**, is observed upon heating to 75 °C, with the peaks at 8.4°, 9.8°, 10.6°, 12.2°, 17.9°, 20.1° and 21.2° 2θ either decreasing or disappearing, whilst the peaks at 13.2°, 15.9°, 19.5° and 20.3° 2θ are either appearing or increasing. The VT-PXRD patterns of **5b** between 75–250 °C seem to match the VT-PXRD patterns of **6b** between 75–100 °C, indicating that the structures in these temperature ranges are very similar. However, **5b** transitions briefly to **5c** at 275 °C and begins to lose crystallinity shortly thereafter, while **6b** maintains crystallinity and starts transitioning to a different form, **6c**, above 100 °C. This transition is complete at 175 °C. Examining this transition,

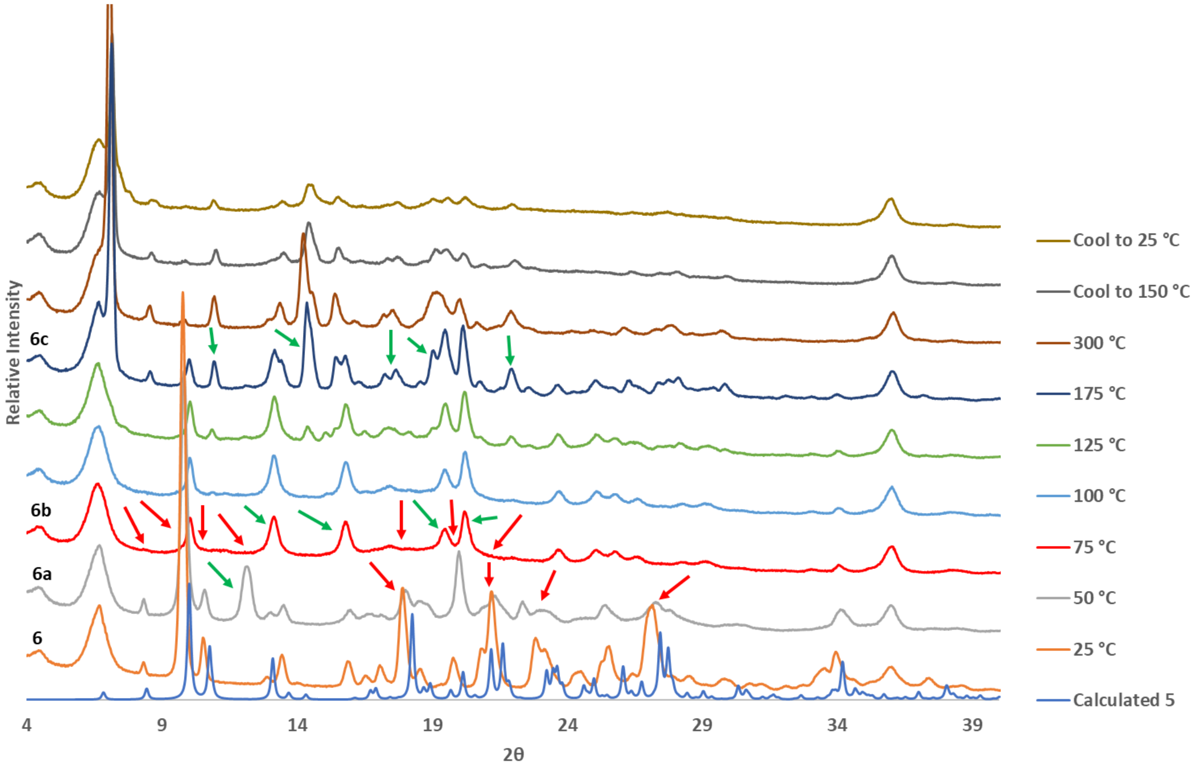

Figure 4.8: VT-PXRD patterns of **6** in the range 25-300 °C compared with the calculated PXRD pattern of **5**. Arrows indicate peaks referred to in the text (red – decreasing relative intensity, green – increasing relative intensity, black – increasing peak resolution).

peaks appear at 10.9°, 14.5°, 17.5°, 19.1° and 22.0° 2θ at 125 °C, increasing at 175 °C. **6c** is then observed to remain stable as the temperature increases to 300 °C and as the temperature returns to 25 °C thereafter.

VT-PXRD experiments were performed on **7** over the temperature range 25-275 °C (Fig. 4.9). **7** was not heated to 300 °C as TGA indicated that **7** begins to decompose at 315 °C and since events on the VT-PXRD occur at lower temperatures, it was decided not to heat the sample to 300 °C. The 25 °C pattern agrees closely with the calculated pattern from the single crystal structure of **5**. **7** seems to transition through two almost-amorphous phases, **7a** and **7b**, from 50 °C until 125 °C, when a second crystalline form, **7c**, appears. **7c** has a very similar PXRD pattern to **6c**, one of the desolvated forms of **6** (Fig. 4.10). This is not unexpected, as the PXRD patterns of **6** and **7** agree closely, suggesting isostructurality and therefore probably similar structural changes upon heating. The PXRD pattern of **5c** is also similar – however, the degree of crystallinity of **5c** has already started to decrease, indicating that decomposition may be underway at that point.

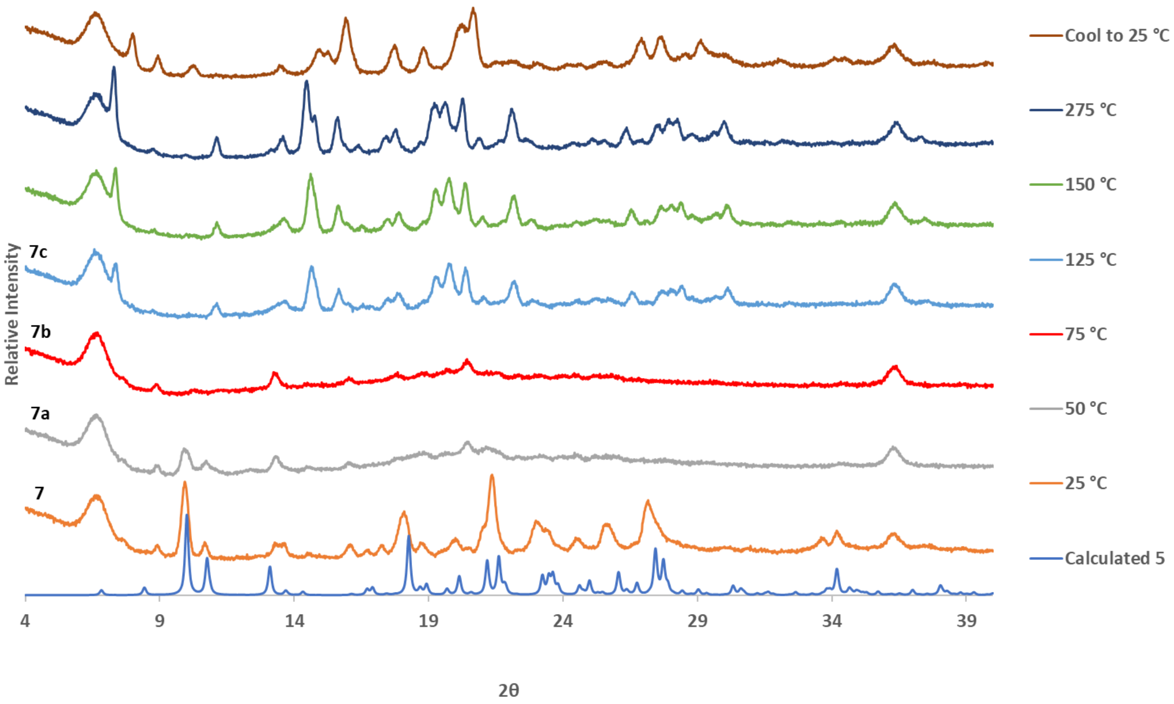

Figure 4.9: VT-PXRD patterns of **7** in the range 25-275 °C compared with the calculated pattern from the crystal structure of **5**.

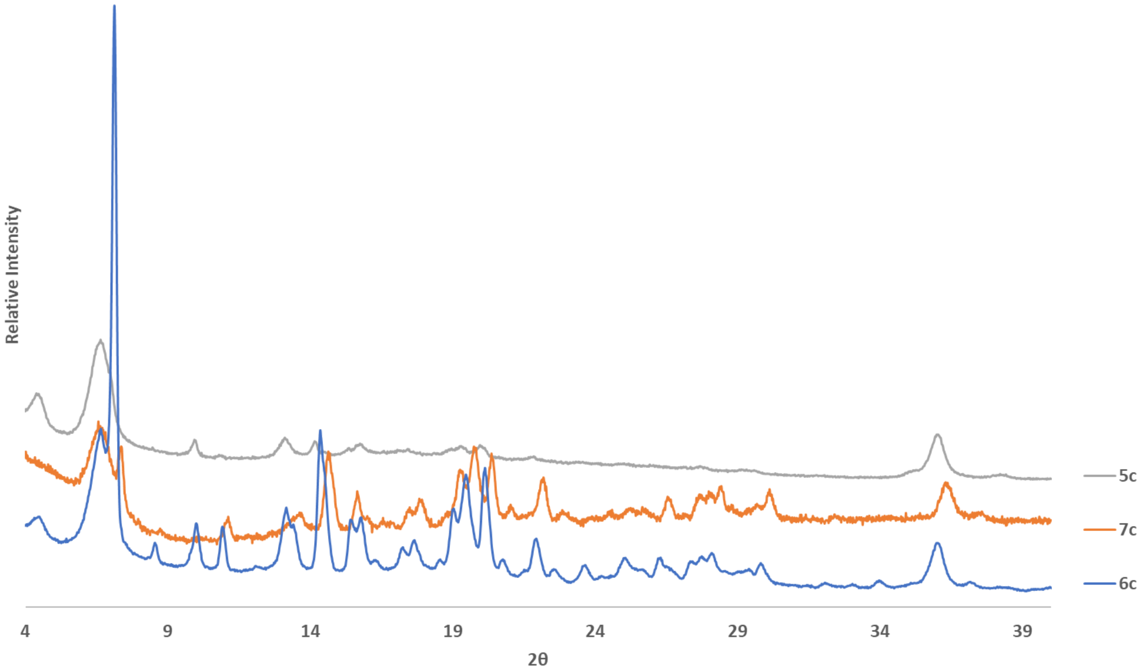

Figure 4.10: Comparison between VT-PXRD patterns of **5c**, **6c** and **7c**. The degree of crystallinity of **7c** is lower than that of **6c**, while the degree of crystallinity of **5c** is the lowest overall.

Comparison between the PXRD pattern of **5a**, **6a** and the calculated PXRD pattern of the CMCR and methanol-only structure from the literature (CSD refcode IFINAM)[21] reveals that there are similarities after the shift due to temperature difference is accounted for (Fig. 4.11). The conformation of the resorcinarene within the IFINAM[21] structure is described as a 'diamond' stereoisomer (Fig. 4.12), seemingly caught between the bowl conformation and the boat conformation of the macrocycle. Therefore, it seems possible that the CMCR host molecules adopt a similar conformation with the structure of **5a** en route to a bowl conformation that is probably present in **5c**, **6c** and **7c**.

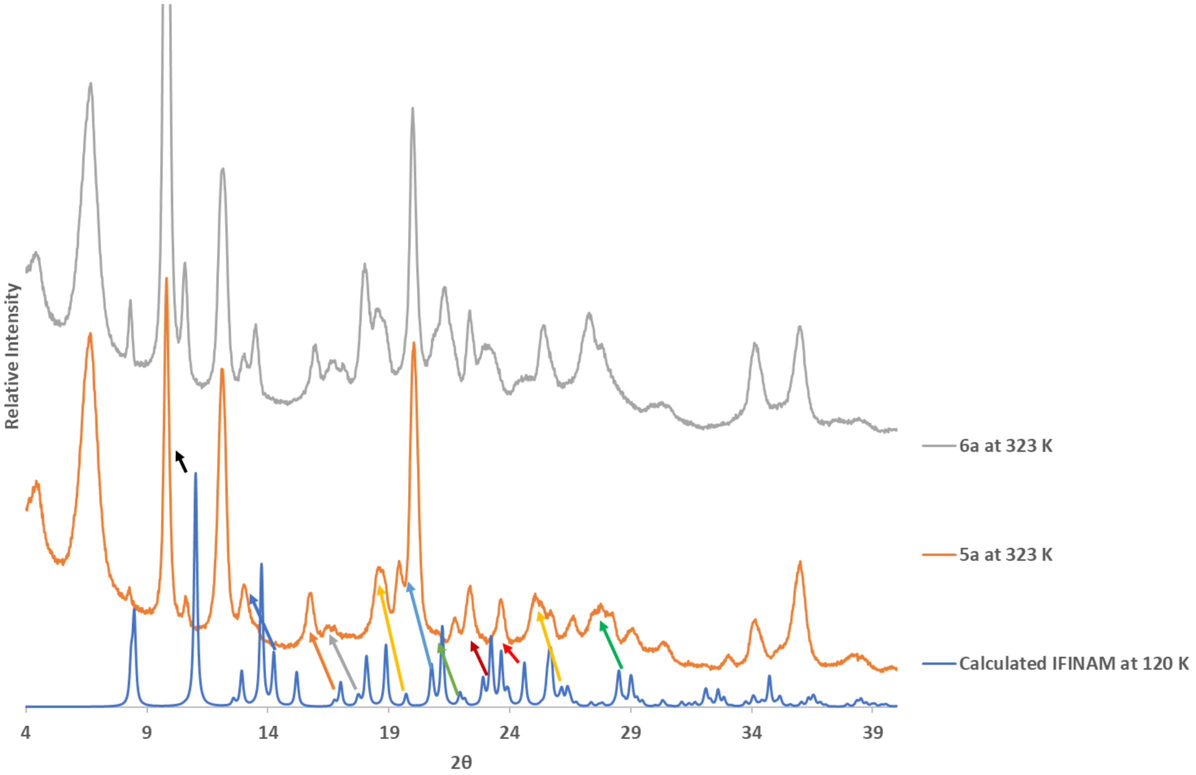

Figure 4.11: Comparison between the calculated PXRD pattern of IFINAM at 120 K (in blue), the PXRD pattern of **5a** at 50 °C (in orange) and the PXRD pattern of **6a** at 50 °C (in grey). The colour-coded arrows indicate corresponding peaks after the shift due to temperature difference is accounted for. **7a** is not included in comparison due to its amorphous character.

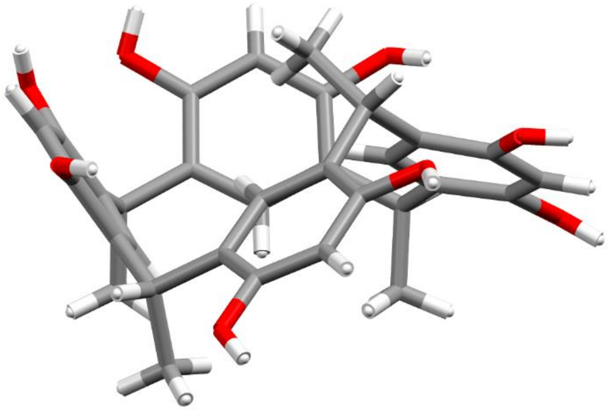

Figure 4.12: The 'diamond' conformation of the CMCR host molecule within the structure of IFINAM.[21]

4.3.1.3. Hot Stage Microscopy, Differential Scanning Calorimetry and Thermogravimetric Analysis

HSM photographs (Fig. 4.13) of crystals of **5** do not reveal any bubbling, even though mass loss was proved by TG analysis. The crystals begin to opacify at 70 °C, which is an indication of loss of monocrystallinity, which is probably due to desolvation. The crystals are completely opaque by 160 °C, subsequently decomposing at 331 °C, a process which is complete by 380 °C. TGA analysis displayed one mass loss event in the temperature range 21.2–132.1 °C before decomposition at 321.4 °C (Fig. 4.14). The mass loss event is 25.86 % (calculated 25.48 %), corresponding to 3 methanol molecules and 5 water molecules per CMCR molecule. DSC analysis reveals two thermal events, the first one occurring over the range 22.7–130.1 °C (with onset temp. 79.7 °C), corresponding to the loss of solvent on the TGA thermogram. The second thermal event is exothermic, probably a phase change from **5b** to the desolvated form **5c** (indicated by the VT-PXRD experiments), and occurs over the range 182.6–200.0 °C.

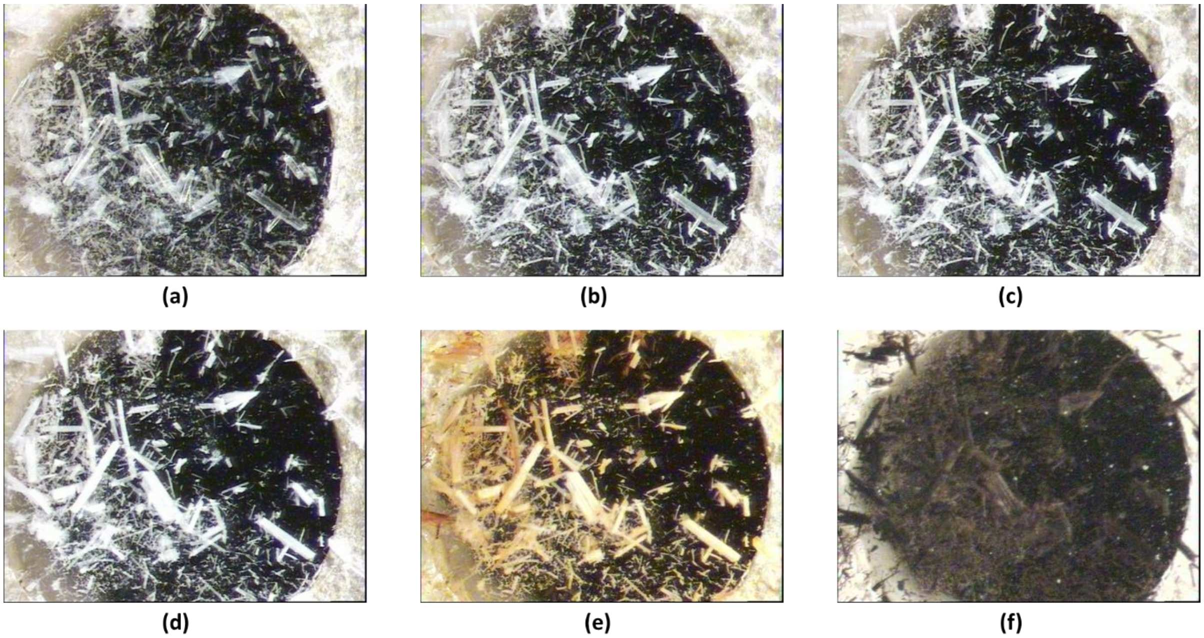

(a) (b) (c)

(d) (e) (f)

Figure 4.13: Hot stage microscope photographs of compound **5** under silicone oil at different temperatures: (a) 40 °C, (b) 70 °C, (c) 80 °C, (d) 160 °C, (e) 331 °C and (f) 380 °C.

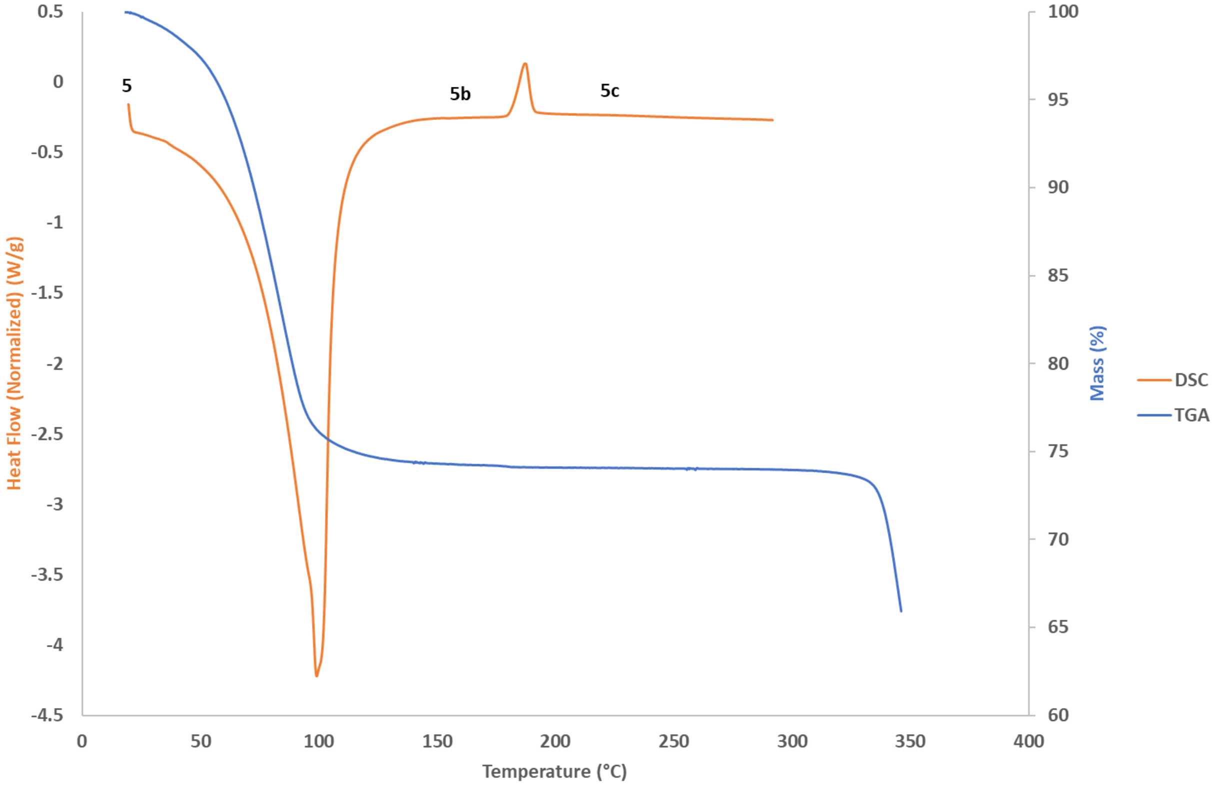

Figure 4.14: DSC and TGA thermograms of **5**.

Table 4.2: TGA analysis for compound **5**.

Thermal Event	Temperature Range (°C)	Mass Loss (%)
Mass loss	21.2–132.1	25.86 (calc. 25.48)
Decomposition	321.4–*	-

*not taken to full decomposition

Table 4.3: DSC analysis for compound **5**.

Thermal Event	Onset Temperature (°C)	Temperature Range (°C)	Peak Temperature (°C)	Enthalpy (J g^{-1})
Mass loss	79.7	79.7 – 130.1	100.3	616.04
Phase change	182.6	182.6 – 200.0	189.8	-11.37

HSM photographs of crystals of **6** (Fig. 4.15) display bubbles, indicating solvent loss, at 100 °C, while at 120 °C, more intense bubbling is occurs. Crystals which were clear turned opaque at the same temperature as bubbling commenced, indicating loss of monocrystallinity associated with solvent loss. Crystals begin to turn brown at 290 °C, with mild bubbling, indicating the onset of decomposition which is well underway by 340 °C and is complete by 390 °C. TGA displays two mass loss events in the temperature range 19.2–185.7 °C before decomposition starts at 321.6 °C (Fig. 4.16). The combined mass loss for these events is 27.79 %. Assuming isostructurality with **5** based on the closely-matching PXRD patterns with ethanol replacing methanol, this would give a calculated solvent mass loss of 29.54 %, slightly higher than what is observed. However, this could be due to immediate solvent loss upon removal from the mother liquor, as suggested by immediate solvent loss observed in the TGA thermogram. This suggests the presence of three ethanol molecules and five water molecules per CMCR host molecule in the structure. DSC analysis (Fig. 4.16) shows three thermal events before decomposition; the first two are endotherms which correspond to the two mass loss events observed in the TGA thermogram,

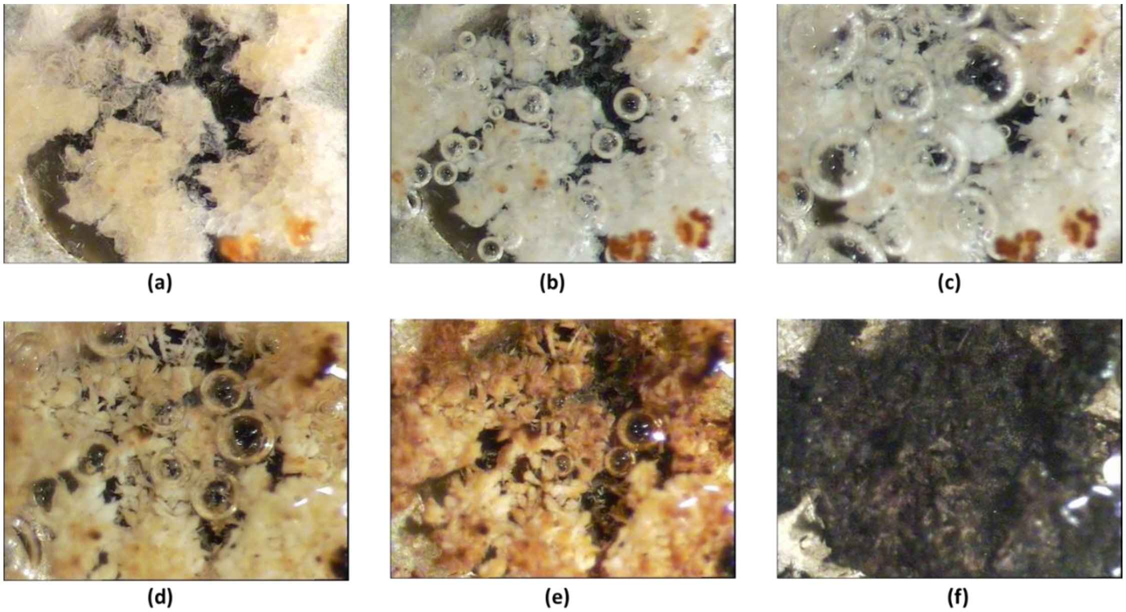

(a) (b) (c)

(d) (e) (f)

Figure 4.15: Hot stage microscope photographs of compound **6** under silicone oil at different temperatures: (a) 26 °C, (b) 100 °C, (c) 120 °C, (d) 290 °C, (e) 340 °C and (f) 390 °C (bubbling indicates solvent loss or decomposition).

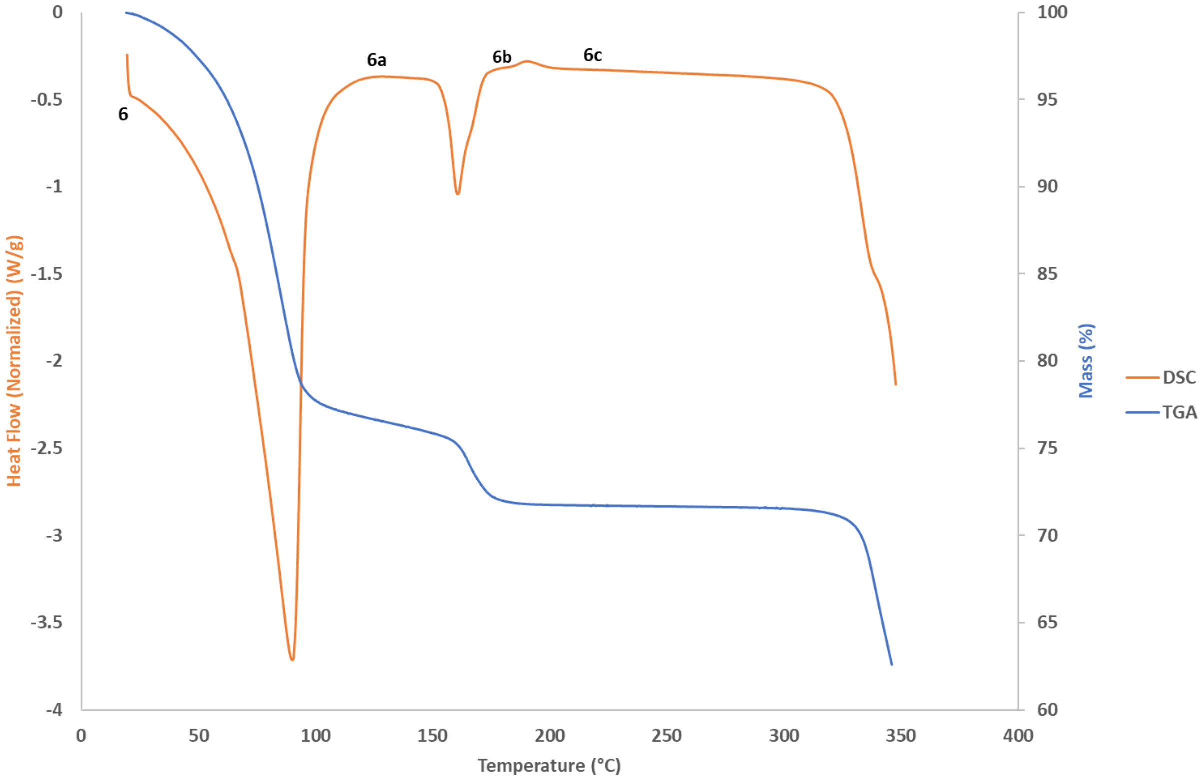

Figure 4.16: DSC and TGA thermograms of **6**, where **6a**, **6b** and **6c** correspond to structural changes observed during VT-PXRD analyses.

Table 4.4: TGA analysis for compound **6**.

Thermal Event	Temperature Range (°C)	Mass Loss (%)
Mass loss **1**	19.2–101.4	23.39
Mass loss **2**	157.2–185.7	4.40
Decomposition	321.6–*	-

*not taken to full decomposition

Table 4.5: DSC analysis for compound **6**.

Thermal Event	Onset Temperature (°C)	Temperature Range (°C)	Peak Temperature (°C)	Enthalpy (J g^{-1})
Mass loss **1**	77.9	77.9–115.2	93.0	523.42
Mass loss **2**	152.0	152.0–171.9	161.2	42.25
Thermal event **3**	155.1	155.1-204.0	190.2	41.87
Decomposition	338.7	338.7–*	-	-

*not taken to full decomposition

suggesting two desolvations representing the transitions **6-6a** (the **5-5a** transition was not observed in the TGA and DSC analysis of **5**) and **6a-6b**, respectively. These occur at higher temperatures than those observed in the VT-PXRD experiment, due to the prolonged heating at constant temperature required for each PXRD pattern in the VT-PXRD experiment. The third thermal event appears in the DSC thermogram as a small exotherm without a corresponding mass loss in the TGA thermogram, similar to that which is observed in the TGA thermogram of **5**. This third thermal event is assigned to the phase transition **6b-6c**.

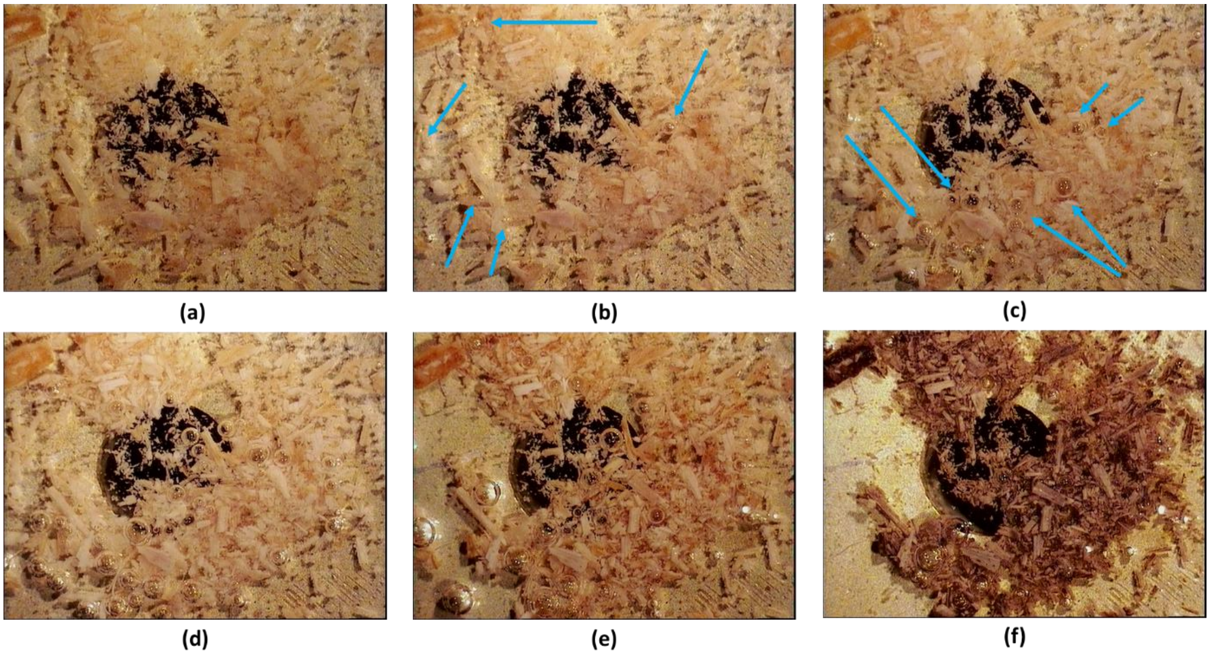

Figure 4.17: Hot stage microscope photographs of compound **7** under silicone oil at different temperatures: (a) 22 °C, (b) 70 °C, (c) 100 °C, (d) 150 °C, (e) 250 °C and (f) 320 °C (bubbling indicates solvent loss or decomposition – the light blue arrows in (b) indicate the first bubbles).

HSM photographs of **7** (Fig. 4.17) show the first bubble due to solvent loss appearing at 70 °C, while more rapid bubbling is observed at 100 °C. This rapid bubbling ceases, then resumes before 150 °C, after which decomposition begins at around 320 °C. DSC analysis (Fig. 4.18) displays two thermal events, the first with a shoulder indicated by a red arrow (Fig. 4.18), whilst the second event occurs at 134.0 °C. These thermal events correspond to mass loss observed in the TGA thermogram and have a combined total of 27.90 %. This is slightly less than the calculated value of 33.18 %, which assumes the isopropanol molecules have just replaced the methanol molecules in the structure of **5**. This could be explained by immediate solvent loss from the sample as soon as it is removed from the mother liquor, which is supported by the immediate mass loss observed in the TGA thermogram, or there are fewer solvent molecules present per CMCR molecule than in the case of **5**. The first thermal event is therefore the transition **7**-**7a**, with the second thermal event being the **7a**-**7b** transition. The thermal event representing the **7b**-**7c** transition (presumably an exotherm as for **5b-5c** and **6b-6c**) is not observed, possibly due to the relatively low enthalpy – however, this transition is evident in the VT-PXRD experiments (Fig. 4.9).

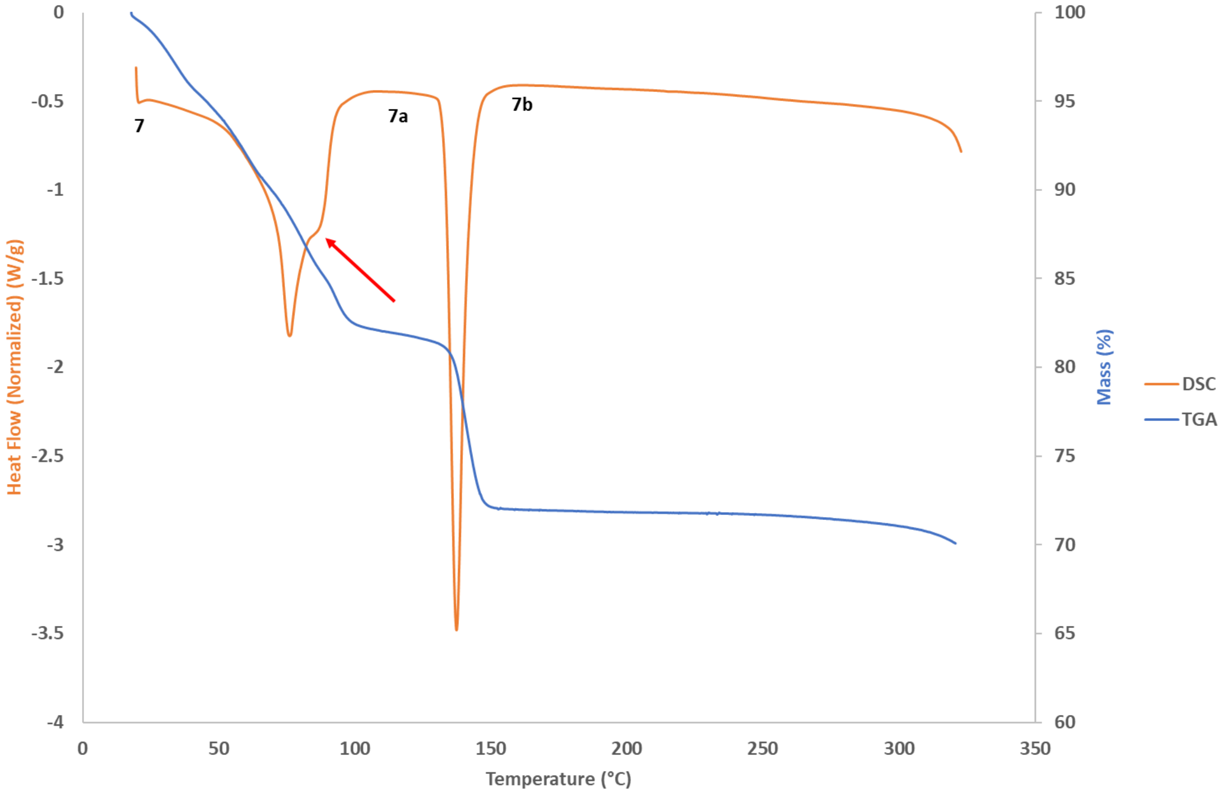

Figure 4.18: DSC and TGA thermograms of **7**, where **7a** and **7b** correspond to structural changes observed during VT-PXRD analyses. The red arrow indicates the shoulder endotherm corresponding to the **7**-**7a** transition.

Table 4.6: TG analysis for compound **7**.

Thermal Event	Temperature Range (°C)	Mass Loss (%)
Mass loss **1**	18.3–100.6	17.99
Mass loss **2**	131.6–149.9	9.91
Decomposition	315.5–*	-

*not taken to full decomposition

Table 4.7: DSC analysis for compound **7**.

Thermal Event	**Onset Temperature (°C)**	**Temperature Range (°C)**	**Peak Temperature (°C)**	**Enthalpy ($J\ g^{-1}$)**
Mass loss **1**	69.2	69.2–108.4	75.8	175.70
Mass loss **2**	134.0	134.0–155.3	137.2	108.19
Decomposition	318.1	318.1–*	-	-

*not taken to full decomposition

4.3.2. Compound **8** (($C_{32}H_{32}O_8$) · (C_3H_8O)$_3$ · (H_2O)$_{1.67}$)

4.3.2.1. Single Crystal X-Ray Diffraction Analysis

Structure solution and refinement showed that the ASU consists of one CMCR molecule, three propanol molecules, one of which is disordered over two positions with site occupancies of 0.44 (suffix B1) and 0.56 (suffix B2), two water molecules situated on a $\bar{3}$ axis with 1/3 site occupancy for each water molecule, plus an additional water molecule modelled in the cavity of the CMCR molecule (Fig. 4.19).

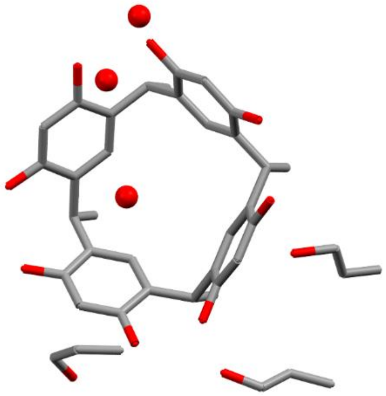

Figure 4.19: The asymmetric unit of **8**. Hydrogen atoms are omitted for clarity and the oxygen atoms of water molecules are shown as spheres.

Hydrogen atoms on water molecules were not modelled. Hydrogen atoms on hydroxyl groups were modelled using the SHELXL instruction AFIX 147 (pointing towards maximum electron density) or AFIX 83 (pointing towards nearest hydrogen-bond acceptor). Whether AFIX 147 or 83 were chosen depended on obtaining close-to-zero maximum shift/error values for these hydrogen atoms. Hydrogen bonding interactions involving hydroxyl groups or water molecules were based on donor-acceptor interactions identified by MERCURY[23] only (PLATON[24] was used to obtain the D···A distances) as X-ray diffraction cannot accurately determine hydrogen atom positions, especially for larger structures where data-to-parameter ratios are likely to be smaller.

Table 4.8: Crystal data and refinement parameters for **8**.

	8
Empirical formula	$(C_{32}H_{32}O_8) \cdot (C_3H_8O)_3 \cdot (H_2O)_{1.67}$
Formula weight	751.52
Temperature (K)	100(2)
Crystal system	Trigonal
Space group	$R\bar{3}$
***a* (Å)**	33.6175(18)
***b* (Å)**	33.6175(18)
***c* (Å)**	20.9185(13)
α (°)	90.00
β (°)	90.00
γ (°)	120.00
Volume (Å^3)	20 473(3)
Z	18
ρ_{calc} (g.cm^{-3})	1.097
μ (mm^{-1})	0.081
***F*(000)**	7 260.0
Crystal size (mm^3)	0.58 x 0.53 x 0.50
Radiation	MoKα (λ = 0.71073 Å)
2ϑ range for data collection (°)	2.398 – 61.248
Index ranges	$-44 \leq h \leq 20$, $-31 \leq k \leq 47$, $-29 \leq l \leq 29$
Reflections collected	34 346
Independent reflections	13 326 [R_{int} = 0.0553, R_{sigma} = 0.0870]
Data/restraints/parameters	13 326/205/533
Goodness-of-fit on F^2	1.187
Final *R* indices [$I \geq 2\sigma(I)$]	R_1 = 0.1211, wR_2 = 0.3313
Final *R* indices (all data)	R_1 = 0.2228, wR_2 = 0.4053
Largest diff. peak/hole (e.Å^{-3})	1.52/-0.68

The assembly consists of six CMCR molecules (Fig. 4.20), with opposing molecules in an eclipsed orientation leading to S_6 point group symmetry, resembling the Holman *et al* assembly. The Atwood *et al* and Oliver *et al* assemblies have opposing resorcinarenes rotated by ~45°. The geometry of the assembly can be compared to that of a cube where the resorcinarenes reside on the six faces of the cube and the solvent sites are the eight vertices of such a cube. In addition to the two water molecules on the surface of the assembly, the interior has eight water molecules, two of which are hydrogen-bonded to the water molecules on opposite sides of the assembly, and one in the cavity of each of the six resorcinarene host molecules. Interestingly, none of the cavity water molecules appear to be hydrogen-bonded to any other molecule, and are unlikely to be involved in O–H···π interactions due to large O···C_g distances,[25] which range from 3.991–4.297 Å. On the surface of the assembly six out of the eight 'surface' solvent sites have three 1-propanol molecules hydrogen bonded at these vertices of the assembly. The hydroxyl groups of these 1-propanol molecules are involved in hydrogen bonding, creating a seven-hydrogen bond motif with two CMCR molecules (Fig. 4.21). Two of these 1-propanol molecules have their aliphatic chains pointing towards the exterior of the assembly, whilst the third has its aliphatic chain pointing towards the interior (Fig. 4.21). The remaining two 'surface' solvent sites on the assembly are occupied by a single water molecule at opposite ends of the assembly, involved in O-H···O hydrogen bonding to three CMCR molecules and one interior water molecule.

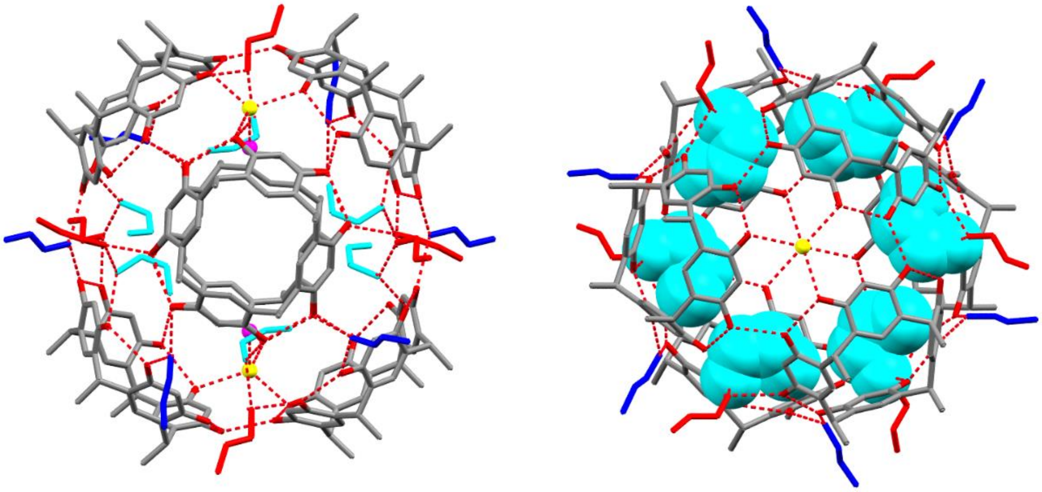
(a) (b)

Figure 4.20: Hexameric assembly **8** of CMCR host molecules, water (displayed as purple and yellow spheres) and 1-propanol (exterior-pointing – blue and red and interior-pointing – aqua) (a) showing eclipsed conformations of CMCR molecules on opposite sides of the assembly, with hydrogen bonds of the assembly indicated in red (b) viewed down the *c*-axis with interior 1-propanol guests depicted in space-filling style. Hydrogen atoms have been omitted for clarity.

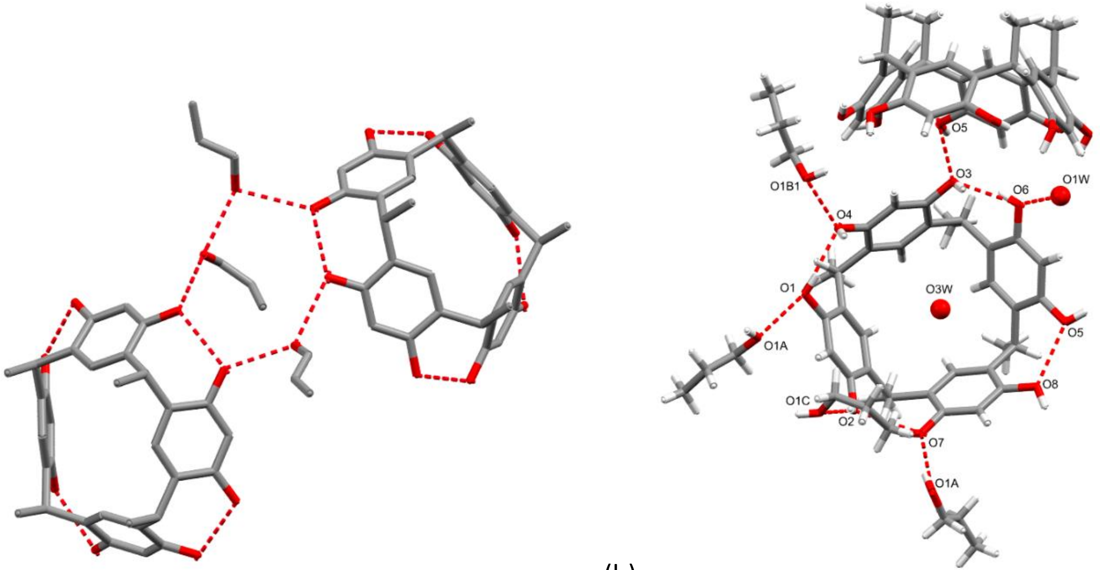

(a) (b)

Figure 4.21: Structure of **8** with CMCR host molecules, water (displayed as spheres) and 1-propanol (a) showing the insertion of three 1-propanol molecules at one assembly 'surface' solvent site and their hydrogen-bonding motif. Hydrogen atoms have been omitted for clarity (b) showing the hydrogen-bonding of one CMCR host molecule.

Each resorcinarene molecule has 6 unique hydrogen bonds within the assembly (Fig. 4.21) – 1 O-H···O hydrogen bond to a water molecule (O6···O1W), 4 O-H···O hydrogen bonds to 1-propanol molecules (O1···O1A, O7···O1A, O2···O1C, and O4···O1B1) and 1 O-H···O hydrogen bond to a neighbouring CMCR host molecule (O3···O5). In addition, each CMCR host molecule contains 4 intramolecular O-H···O hydrogen bonds (O1···O4, O2···O7, O3···O6 and O5···O8). Each assembly also contains 6 1-propanol···1-propanol O-H···O hydrogen bonds (O1B1···O1C) and 2 water···water O-H···O hydrogen bonds (O1W···O2W). These all add up to 68 hydrogen bonds – 24 CMCR intramolecular hydrogen bonds, 6 CMCR···water hydrogen bonds, 24 CMCR···1-propanol hydrogen bonds, 6 CMCR···CMCR hydrogen bonds, 6 1-propanol···1-propanol hydrogen bonds and 2 water···water hydrogen bonds. This is a comparable number of hydrogen bonds in comparison with the hexameric assemblies produced by Atwood *et al* (60), Holman *et al* (58), and Oliver *et al* (62 and 64 for assemblies denoted 'A' and 'B' in that structure).

Table 4.9: Unique hydrogen bonding parameters for **8**.

Bonding atoms	**D···A (Å)**	**Symmetry operators**
O1···O4	2.751(6)	x, y, z
O2···O7	2.671(6)	x, y, z
O3···O6	2.682(4)	x, y, z
O5···O8	2.666(5)	x, y, z
O1···O1A	2.782(6)	⅔+x-y, ⅓+x, ⅓-z
O2···O1C	2.684(9)	x, y, z
O3···O5	2.640(5)	1-y, 1+x-y, z
O4···O1B1	2.78(2)	1-y, 1+x-y, z
O6···O1W	2.726(3)	x, y, z
O7···O1A	2.599(6)	x, y, z
O1B1···O1C	2.577(18)	⅔+x-y, ⅓+x, ⅓-z
O1W···O2W	2.606(12)	x, y, z

Table 4.10: Unique C-H bonding parameters for **8**.

Bonding atoms	D–H (Å)	H···A (Å)	D···A (Å)	D–H···A (°)	Symmetry operators
C2-H2A···O1C	0.95	2.53	3.251(8)	132	x, y, z
C2-H2A···O1A	0.95	2.49	3.144(7)	126	⅔+x-y, ⅓+x, ⅓-z
C3C-H3CB···O1	0.98	2.55	3.285(19)	132	-⅓+y, ⅓-x+y, ⅓-z
C1B1-H1BB···Cg1[a]	0.99	2.79	3.75(3)	164	⅓+x-y, -⅓+x, ⅔-z
C24-H24B···Cg4[b]	0.98	2.77	3.618(4)	146	1-x, 1-y, 1-z

[a]Cg1 (C1/C2/C3/C4/C5/C6), [b]Cg4 (C25/C26/C27/C28/C29/C30)

Each CMCR host molecule also has 3 unique intermolecular, intra-assembly CMCR···1-propanol C-H···O hydrogen bonds (C2–H2A···O1C, C2–H2A···O1A and C3C–H3CB···O1) for an additional 18 hydrogen bonds per assembly (Fig. 4.22 and Table 4.10). Additionally, each CMCR host molecule is involved in 2 unique CMCR···CMCR C-H···π interactions (C24–H24B···Cg4 and C1B1–H1BB···Cg1), for a total of 12 C-H···π interactions per assembly. Both these unique C–H···π interactions are inter-assembly interactions.

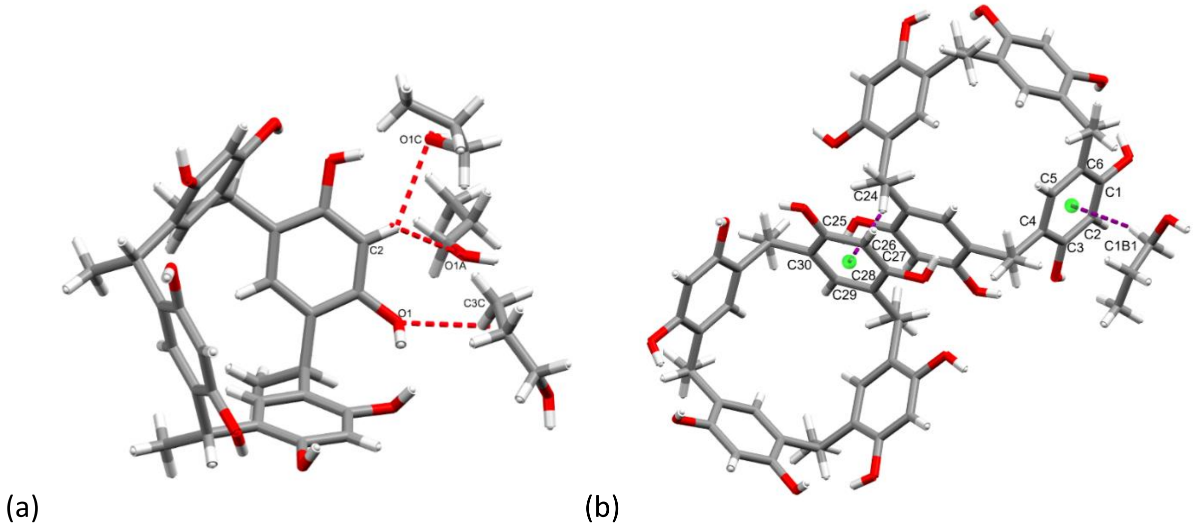

(a) (b)

Figure 4.22: (a) The unique intermolecular intra-assembly CMCR···1-propanol C-H···O interactions, displayed in red, to and from one CMCR molecule in the structure of **8** (b) The unique CMCR···CMCR C-H···π interactions displayed in purple, to one CMCR molecule in the structure of **8**. The centroids of the rings involved in these interactions are displayed in green.

Upon artificial removal of the interior 1-propanol and water molecules in order to be consistent with the interior void space calculations of earlier assemblies in the literature, where interior solvent molecules were not considered, the program MERCURY[23] calculated (using a probe radius of 1.2 Å) an interior volume of 1769 $Å^3$ (Fig. 4.23). To the best of this author's knowledge, this is the largest recorded interior volume of a calixarene-based purely-organic, supramolecular hexameric spherical assembly. The O···O distances of the water molecules on opposite sides of the assembly of **8** were assessed and compared with the Atwood *et al.* and Holman *et al.* hexameric assemblies from the literature (Fig. 4.24). This distance was found to be 17.5 Å in **8**, greater than in the Atwood (15.6 Å) and Holman (15.1 Å) assemblies.

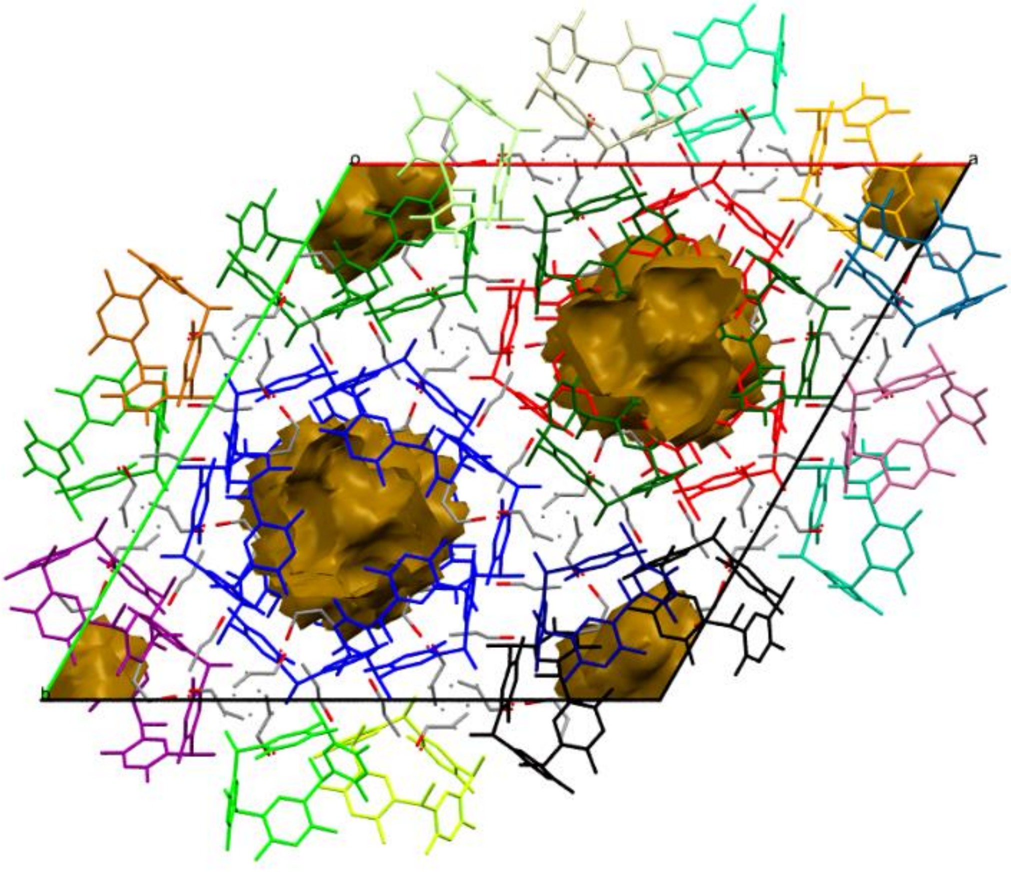

Figure 4.23: Packing diagram of the structure of **8** viewed along the *c*-axis. The only voids observed are those located inside the hexameric assemblies.

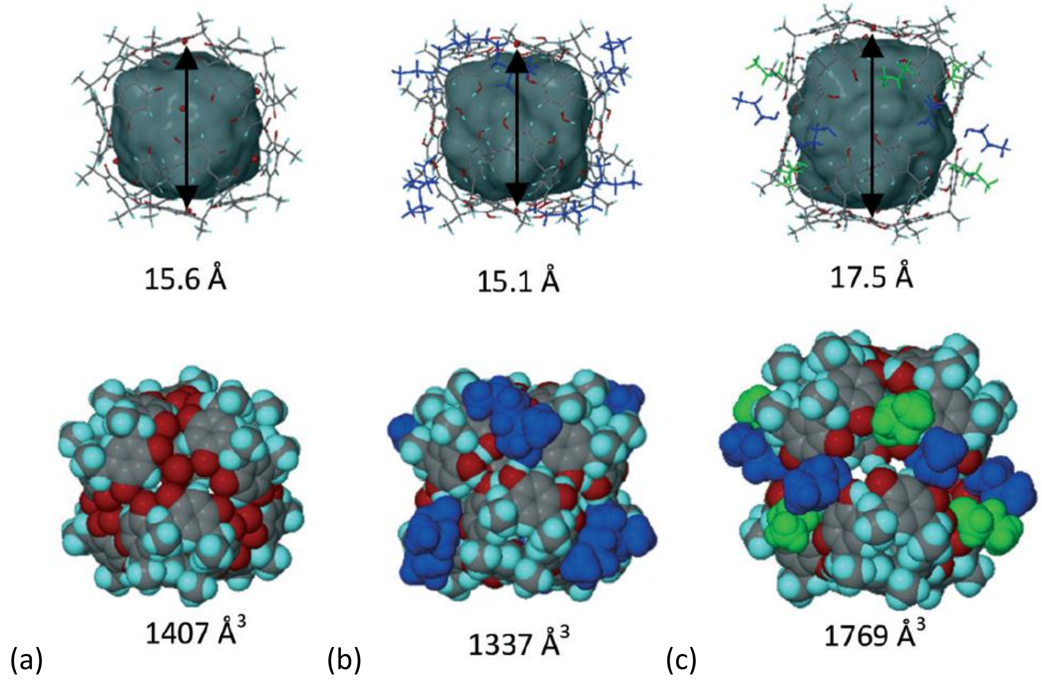

Figure 4.24: Wire-frame (including void spaces calculated by MSROLL) and space-filling depictions of hexameric spherical assemblies (a) Atwood *et al* (b) Holman *et al* and (c) **8**. The O···O distances between water molecules at opposite sides of the hexameric assemblies are displayed in the top depictions, whilst the interior volumes (a chosen probe radius of 1.55 Å was used based on the limitations of MSROLL requiring isolated voids) are shown in the bottom depictions. Symmetry-equivalent alcohol molecules are colour-coded.

4.3.2.2. Powder X-Ray Diffraction and Variable-Temperature Powder X-Ray Diffraction

Usually liquid-assisted grinding is only appropriate for preparing relatively simple structures, however, unusually for a complex spherical assembly, **8** can be prepared by liquid-assisted grinding in the presence of excess 1-propanol for 45-60 minutes (Fig. 4.25). Previously, dimeric capsules based on resorcin[4]arene which encapsulate C_{60} were prepared by ball-milling.[26] For a hexameric assembly, this has only been done for the first time in 2017 with a pyrogallol[4]arene, but, to the best of the author's knowledge, never before with a resorcinarene.[27] Additionally, the pyrogallol[4]arene hexamer was prepared using a ball mill and identified using NMR spectroscopy following dissolution in $CDCl_3$, not by PXRD and comparison with a calculated PXRD pattern from a single-crystal structure.

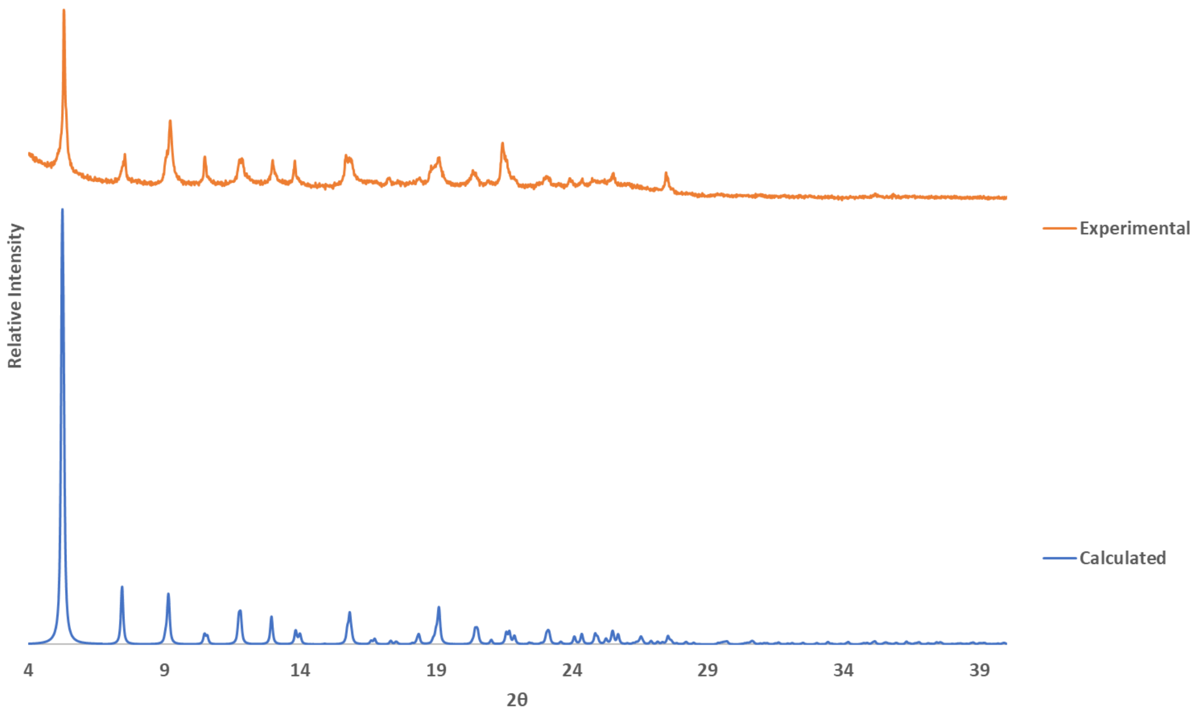

Figure 4.25: Comparison between the calculated PXRD pattern generated from the crystal structure of **8** (in blue) and the experimental powder pattern obtained after LAG in the presence of 1-propanol (in orange).

VT-PXRD experiments of **8** would represent the first such experiments, according to this author's knowledge, on a resorcinarene-based spherical assembly structure (Fig. 4.26) in order to examine the behaviour upon heating, determine the crystallinity upon desolvation and investigate how **8** should be prepared for gas or vapour sorption studies. The VT-PXRD pattern at 25 °C is very similar to the calculated PXRD pattern of **8**, confirming the purity of the bulk phase. At 75 °C, the severe decrease in peak intensities suggests the sample has become amorphous (**8a**), also observed at 100 °C. However, from 125-150 °C crystallinity is regained, however, with different peaks (relative to the 25 °C VT-PXRD pattern) thus showing that a different crystalline structure is in the process of being formed, referred to as **8b**. This pattern remains the same up to 225 °C. After cooling the sample to 30 °C, the VT-PXRD pattern at this temperature confirms that this

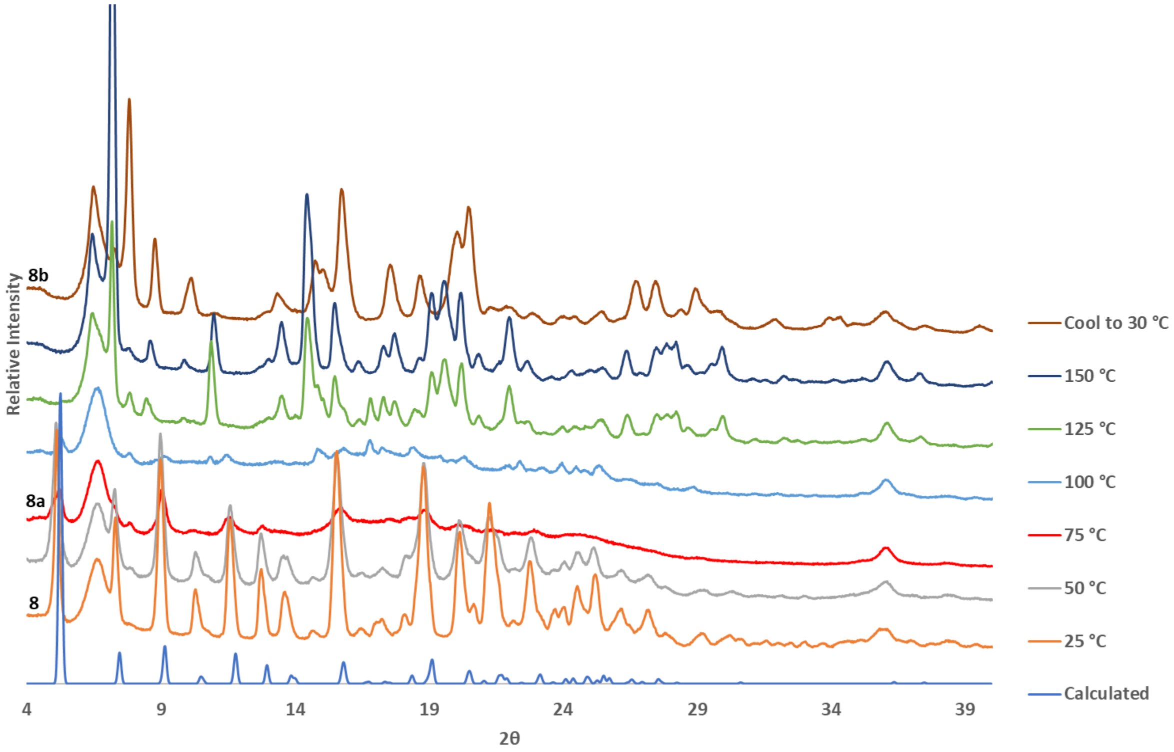

Figure 4.26: VT-PXRD patterns in the range 25-150 °C of **8**.

structure is basically the same as the 225 °C structure with slight shifting of peaks towards higher 2θ, presumably due to a smaller unit cell volume and thus smaller d-spacings at the lower temperature. A comparison between the PXRD trace of **8b** and the PXRD trace of a known structure (CSD code: MIGTUR[22]) (Fig. 4.27) showed that the patterns agree closely, suggesting that the structure of **8b** is a close match to the structure of MIGTUR,[22] which is a hydrate where CMCR molecules are arranged in a bilayer (Fig. 4.28). In fact, the only difference observed in the PXRD pattern of **8b** is the peak appearing at 7.3° 2θ, which does not appear in the calculated PXRD pattern of MIGTUR.[22]

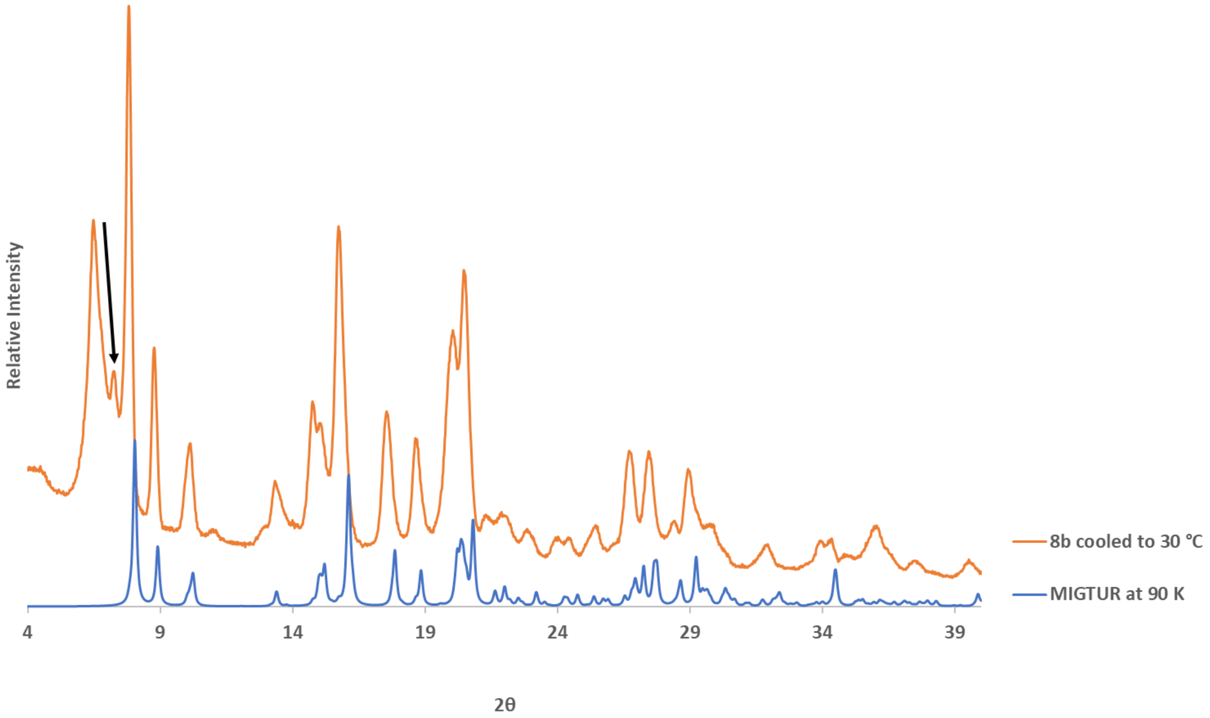

Figure 4.27: Comparison between calculated PXRD pattern of MIGTUR in blue and VT-PXRD 30 °C pattern of **8b** after heating in orange. Arrow indicates a peak in the PXRD pattern of **8b** that does not appear in the calculated PXRD pattern of MIGTUR.

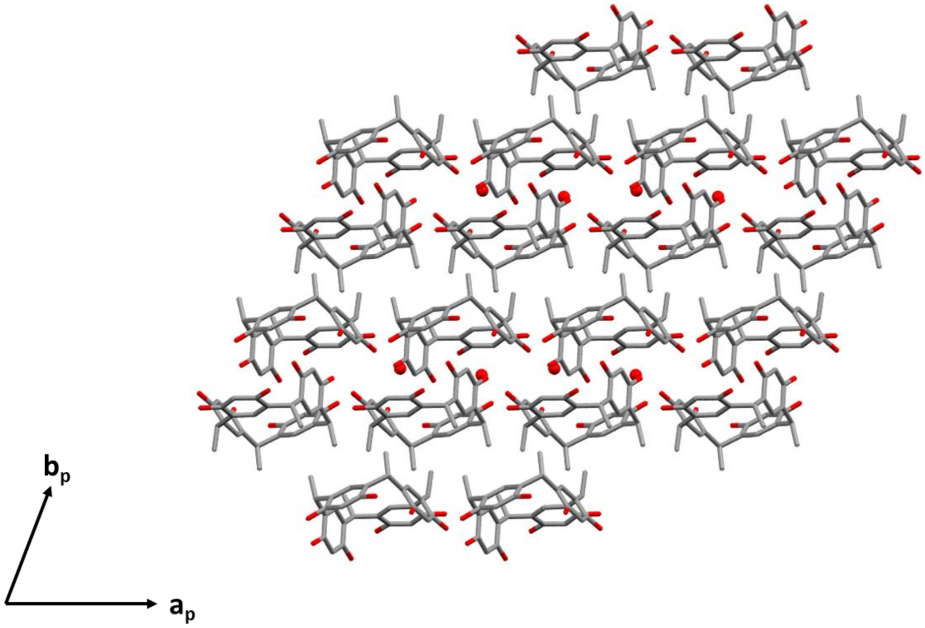

Figure 4.28: Packing diagram of MIGTUR viewed along the *c*-axis. Hydrogen atoms are omitted for clarity and water molecules are displayed as red spheres.

Surprisingly, **8** can be prepared by exposing **8b** to propanol vapour. An *in situ* PXRD for 1-propanol vapour sorption[28] was performed where **8b** was subjected to the maximum vapour pressure of 1-propanol at 25 °C (40 mm Hg) in an experiment where adjacent wells on a modified PXRD sample stage contained 1-propanol liquid (see Fig. 2.1 – Section 2.5.1). Each diffractogram was recorded over 45 minutes, with another 1.5 minutes taken for the start of the next run (Fig. 4.29). In the 46.5 min. PXRD trace, the peak at 6.7° 2θ has decreased drastically, while new peaks start appearing at 5.4°, 11.7° and 13.0° 2θ. Additionally, an increase in intensity is observed for the peaks at 19.0°, 21.6°, 23.0°, 24.3°, 24.8° and 25.4° 2θ. After 93 min., the peak at 6.7° 2θ has disappeared completely, while a new peak is appearing at 7.6° 2θ. The peak at 8.0° 2θ has continued decreasing, while the peaks at 9.2°, 11.8° and 12.9° 2θ have increased in intensity. The peaks at 15.0° and 17.9° 2θ have decreased in intensity, while the peaks at 19.0°, 21.5°, 23.0°, 24.3°, 24.8° and 25.4° 2θ have continued increasing in intensity. After 139 min., the peak at 8.0°

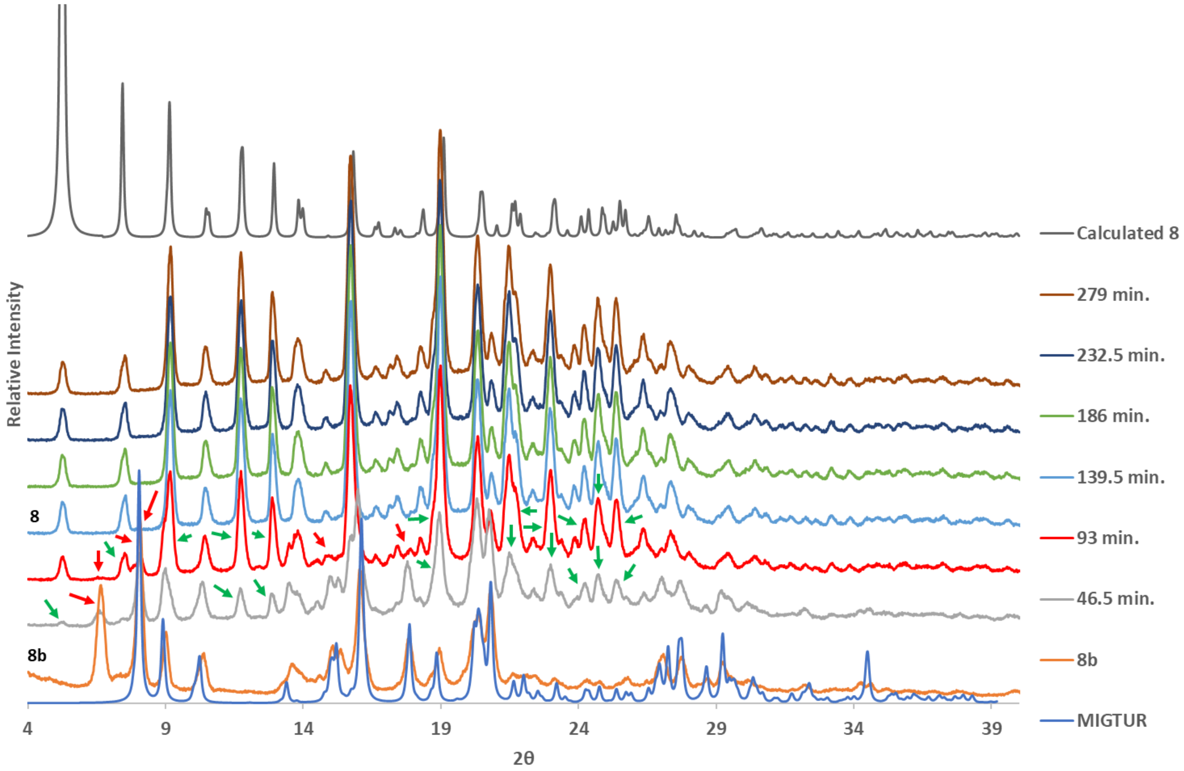

Figure 4.29: *In situ* propanol vapour sorption PXRD experiment, starting with **8b** (in orange) and transforming to **8** (in brown) over a period of ~4 hours. Arrows indicate peaks referred to in the text (red – decreasing relative intensity, green – increasing relative intensity).

2θ has disappeared completely and the original spherical hexameric structure of **8** was re-established (Fig. 4.29). This happens in the solid state, without any additional energy input, suggesting formation of the hexameric assembly **8** is highly favoured in the presence of 1-propanol, even if the 1-propanol is in the vapour phase. It should also be noted that water is a crucial part of the assembly and it is likely that the 1-propanol is wet, which may provide the water for the assembly, or the water is obtained from the atmosphere. The **8b-8a** resolvation does not go through an amorphous phase as in the case of desolvating **8** under heating where the route is **8-8a-8b**. Perhaps, this is not surprising as the conditions for the VT-PXRD experiment are not exactly reversed – for example, the temperature remained constant during the *in situ* PXRD vapour sorption experiment.

4.3.2.3. Hot Stage Microscopy, Differential Scanning Calorimetry and Thermogravimetric Analysis

HSM photographs (Fig. 4.30) of a crystal of **8** show bubbles due to solvent loss appearing at 70 °C, while at 100 °C, more vigorous bubbling is occurring, and the crystal is beginning to turn opaque, probably indicating loss of crystallinity as indicated by VT-PXRD experiments (Fig. 4.26). The crystal has turned completely opaque upon reaching 120 °C, but a second occurrence of bubbling begins at 200 °C and continues until approximately 280 °C. The crystal begins to turn brown at 320 °C, indicating the onset of decomposition which is probably near completion at 400 °C.

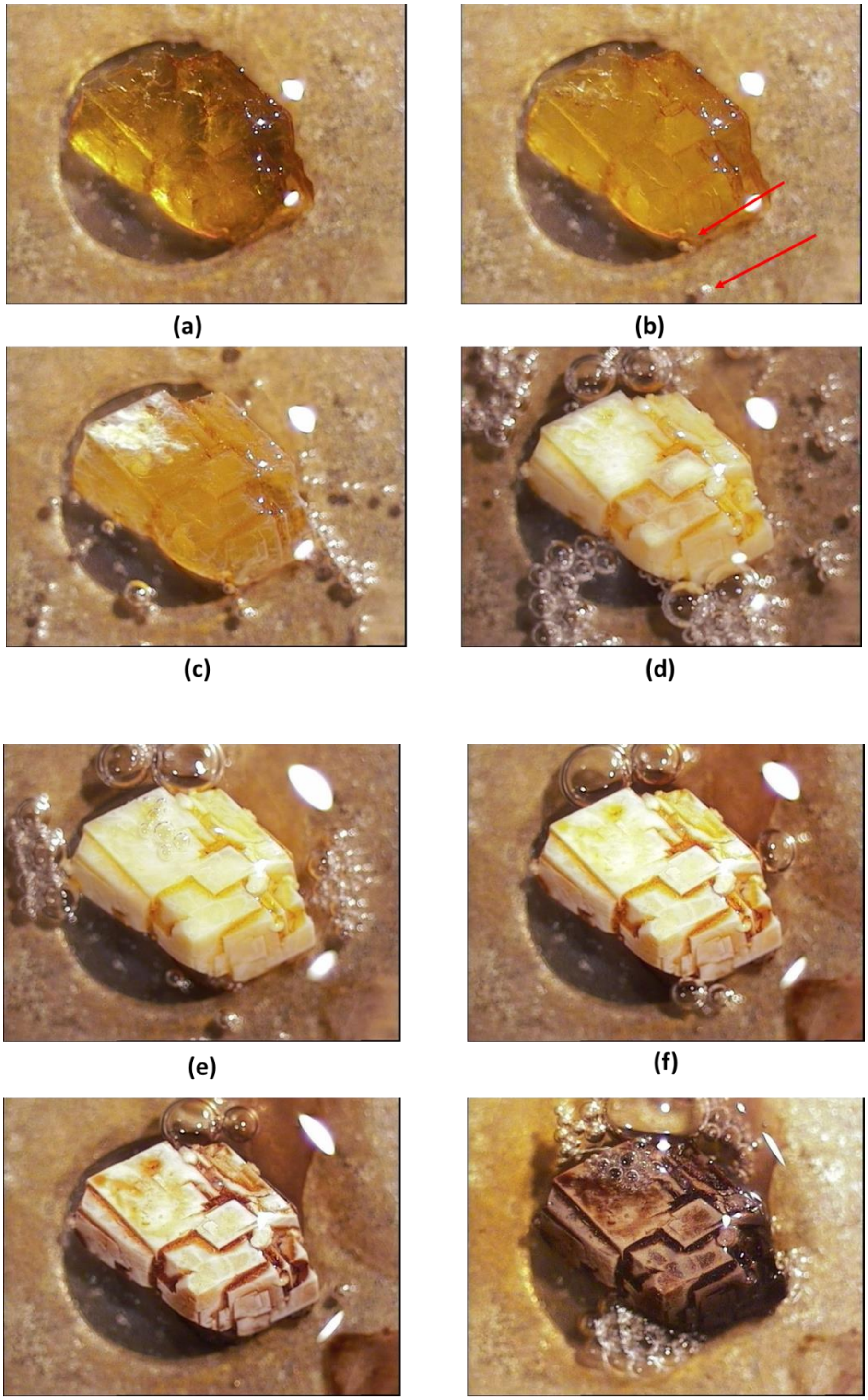

Figure 4.30: Hot stage microscope photographs of compound **8** under silicone oil at different temperatures: (a) 29 °C, (b) 70 °C, (c) 100 °C, (d) 120 °C, (e) 200 °C (f) 280 °C (g) 320 °C and (h) 400 °C (bubbles show the release of solvent or decomposition – the red arrows in (b) indicate the first bubbles).

TGA exhibited four mass loss events in the temperature range 30-220 °C before decomposition (Fig. 4.31). These four mass loss events have a combined total of 32.50 % (calc. 32.68 %) of the total mass, indicating that the crystallographic model does not account for all the solvent present in the structure. The initial mass loss of 25.87 % (calculated 26.00 %) from 26.9–123.3 °C (Table 4.11) accounts for all the solvent molecules present in the modelled structure (3 1-propanol molecules and 1.67 water molecules per CMCR molecule).

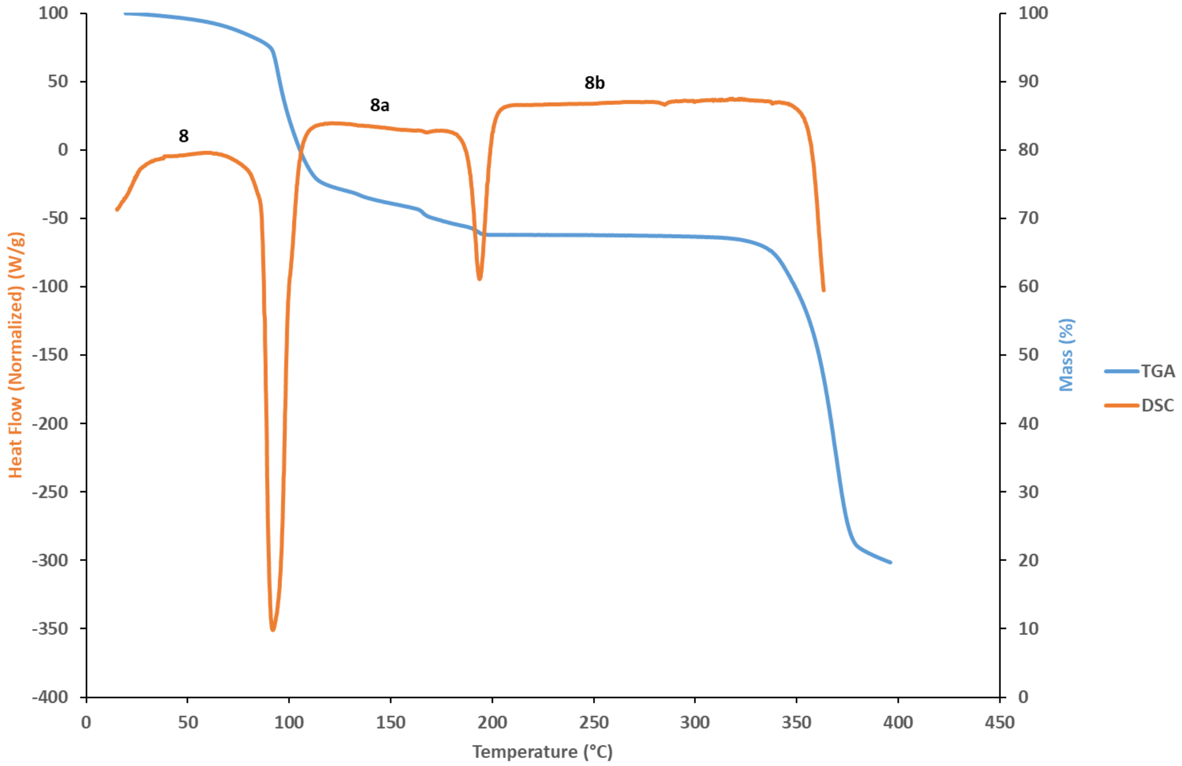

Figure 4.31: DSC and TGA thermograms of **8**.

Table 4.11: TG analysis for compound **8**.

Thermal Event	Temperature Range (°C)	Mass Loss (%)
Mass loss **1**	26.9–123.3	25.87 (calc. 26.00)
Mass loss **2**-**4**	124.6–195.1	6.64 (calc. 6.68)
Decomposition	322.7–379.18	-

Table 4.12: DSC analysis for compound **8**.

Thermal Event	Onset Temperature (°C)	Temperature Range (°C)	Peak Temperature (°C)	Enthalpy (J g^{-1})
Mass loss **1**	65.0	65.0-116.3	91.8	Not done
Mass loss **2**-**4**	180.3	180.3-207.8	193.8	Not done
Decomposition	347.0	347.0-*	-	-

*not taken to full decomposition

The subsequent three nearly-identical mass losses totalling 6.64 % (calculated 6.68 %) are assigned to the loss of 3 unmodelled water molecules per CMCR molecule. These water molecules are probably located within the assemblies as no void spaces were calculated by MERCURY[23] between assemblies (Fig. 4.23). The SQUEEZE routine in PLATON[24] calculated 28 residual electrons per ASU (no modelled solvent molecules were removed) which corresponds to ~2.8 water molecules (10 electrons in 1 water molecule) per CMCR molecule. Thus, the compound could also be formulated as $(C_{32}H_{32}O_8) \cdot (C_3H_8O)_3 \cdot (H_2O)_{4.47}$. Furthermore, the DSC analysis (Fig. 4.31) seems to indicate two thermal events, one in the temperature range 65.0–116.3 °C which corresponds to the bubbling in the HSM analysis, the solvent loss on the TGA thermogram and the VT-PXRD traces to form the amorphous **8a**, which is partially desolvated, with the second event from 180.3–207.8 °C indicating the transition to the fully desolvated phase, **8b**. While this happens at a much higher temperature than that observed in the VT-PXRD traces (**8b** is indicated by the 125 °C VT-PXRD trace), this can be explained by the different temperature programs used for the TGA/DSC and the VT-PXRD. The experiment was stopped at the onset of the third endotherm as TGA indicated that this was the onset of decomposition.

4.3.3. Compound **9** ($(C_{32}H_{32}O_8)_4 \cdot (C_4H_{10}O)_6 \cdot (H_2O)_{5.67}$) and Compound **10** ($(C_{32}H_{32}O_8)_4 \cdot (C_5H_{12}O)_{5.33} \cdot (H_2O)_7$)

4.3.3.1. Single Crystal X-Ray Diffraction Analysis

The structure of **9** has already been published in the literature in 2016.[12] However, structure solution and refinement presented in this thesis revealed additional structural information to the already-published structure. The structure of **9** consists of two unique hexameric assemblies (referred to as **9'** and **9"**, respectively, in this thesis), with the asymmetric unit made up of four CMCR molecules, nine water molecules (four with site occupancy equal to 1 and five positioned on a three-fold rotation axis, resulting in a total occupancy of [4 + (0.33 x 5) = 5.67] and six 1-butanol molecules. The F-labelled 1-butanol molecule was modelled as disordered over two positions with site occupancy factors of 0.58 and 0.42 for disordered components A and B, respectively. The published structure has the same number of water molecules but only four 1-butanol molecules. Hydrogen atoms on water molecules were not modelled. Hydrogen atoms on hydroxyl groups (for both **9** and **10**) were modelled using the SHELXL instruction AFIX 147 (pointing towards maximum density) or AFIX 83 (pointing towards nearest hydrogen-bond acceptor). Whether AFIX 147 or 83 were chosen depended on obtaining close-to-zero maximum shift/error values for these hydrogen atoms. Hydrogen bonding interactions involving hydroxyl groups or water molecules were based on donor-acceptor interactions identified by MERCURY[23] only (PLATON[24] was used to obtain the D···A distances – Tables 4.14 and 4.16 for **9** and **10**, respectively) as X-ray diffraction cannot accurately determine hydrogen atom positions, especially for larger structures where data-to-parameter ratios are likely to be smaller.

Similar to both the Atwood[4] and Holman[5] hexameric assemblies, both hexameric assemblies **9'** and **9"** comprise six CMCR molecules residing on the faces of a cube with water molecules residing on the vertices of such a cube, with a water molecule bonding three neighbouring CMCR molecules in a trigonal arrangement by water···CMCR O-H···O hydrogen bonding. In both **9'** and **9"** contain opposing resorcinarenes are rotated by ~45°, similar to the Atwood hexameric assembly. The point group symmetries of **9’** and **9”** are *C*3, and these assemblies are therefore chiral, as opposed to the Holman assembly that has S_6 point group symmetry and hence is achiral.

Table 4.13: Crystal data and refinement parameters for **9**.

	9
Empirical formula	$(C_{32}H_{32}O_8)_4 \cdot (C_4H_{10}O)_6 \cdot (H_2O)_{5.67}$
Formula weight	2 713.68
Temperature (K)	100(2)
Crystal system	Trigonal
Space group	*R*3*c*
***a* (Å)**	29.9039(7)
***b* (Å)**	29.9039(7)
***c* (Å)**	96.216(3)
***α* (°)**	90
***β* (°)**	90
***γ* (°)**	120
Volume (Å^3)	74 514(4)
Z	18
ρ_{calc} (g.cm^{-3})	1.089
μ (mm^{-1})	0.654
***F*(000)**	26 088.0
Crystal size (mm^3)	0.37 x 0.19 x 0.18
Radiation	Cu Kα (λ = 1.54178 Å)
2ϑ range for data collection (°)	3.874 – 150.618
Index ranges	$-37 \leq h \leq 37$, $-36 \leq k \leq 37$, $-120 \leq l \leq 120$
Reflections collected	384 821
Independent reflections	34 120 [R_{int} = 0.0635, R_{sigma} = 0.0347]
Data/restraints/parameters	34 120/484/1 833
Goodness-of-fit on F^2	1.426
Final *R* indices [$I \geq 2\sigma(I)$]	R_1 = 0.1076, wR_2 = 0.2816
Final *R* indices (all data)	R_1 = 0.1139, wR_2 = 0.3011
Largest diff. peak/hole (e.Å^{-3})	1.84/-0.51

9’ has eight water molecules at all eight vertices of the cube with **9”** having seven water molecules, the eighth one missing because of the closer arrangement of three CMCR molecules at this position (intersection of red molecules in Fig. 4.32b), and thus the three water···CMCR O-H···O hydrogen bonds are also absent at this point. Furthermore, three of these seven water molecules (indicated by red spheres in Fig. 4.32b) are hydrogen bonding with only two neighbouring CMCR molecules (and a 1-butanol molecule located at the same vertex) as opposed to hydrogen bonding to three neighbouring CMCR molecules as observed in **9'** (Fig. 4.32), which is also different from the structure published in the literature,[12] where water at these points is still hydrogen-bonded to three CMCR molecules.

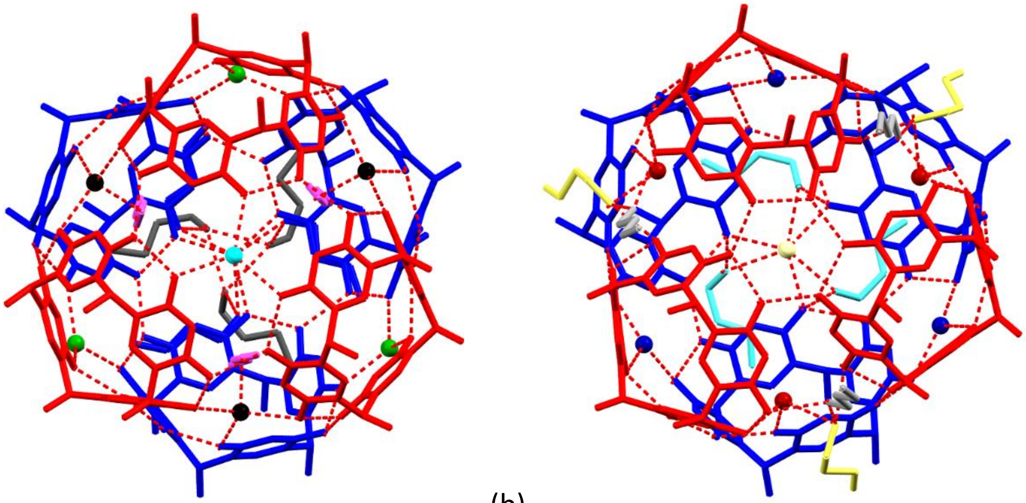

(a) (b)

Figure 4.32: Hexameric assemblies of CMCR, 1-butanol and water displaying the (a) regular hexameric assembly **9'** and the (b) distorted assembly **9"** with its interacting 1-butanol molecules and missing water molecule at the intersection of the red CMCR molecules (closest to the reader). Hydrogen atoms have been omitted for clarity. Water molecules are shown as spheres.

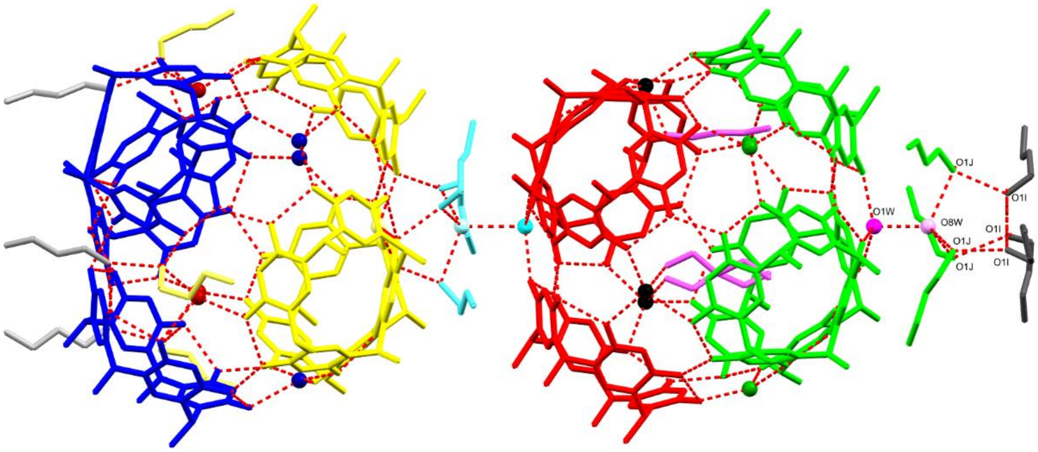

Figure 4.33: The dimer of hexameric assemblies formed by the two assemblies **9'** (right) and **9"** (left). Atoms are coloured according to symmetry equivalence. Hydrogen atoms have been omitted for clarity. Oxygen atoms involved in the 'double propeller' motif are labelled.

9’ and **9”** each contain two crystallographically unique CMCR molecules – A and B in **9’** and C and D in **9”**. Unique, strong hydrogen bonds involving CMCR within **9’** are indicated in Fig. 4.34. **9’** has 24 CMCR intramolecular hydrogen bonds (O2A···O28A, O4A···O10A, O12A···O18A, O20A···O26A, O2B···O28B, O4B···O10B, O12B···O18B and O20B···O26B) as each CMCR molecule has four intramolecular hydrogen bonds where one hydroxyl group forms a hydrogen bond with a hydroxyl group of the neighbouring resorcinol unit, 24 water···CMCR O-H···O hydrogen bonds (O4A···O3W, O12A···O4W, O20A···O1W, O28A···O4W, O2B···O4W, O10B···O3W, O18B···O2W and O26B···O3W) where each water molecule on the ‘surface’ of the assembly hydrogen bonds with three neighbouring CMCR molecules at eight such sites, and lastly 12 CMCR···CMCR intermolecular hydrogen bonds (O2A···O4B, O10A···O28B, O18A···O26A and O12B···O20B). Assembly **9’** contains 1 additional water···water O-H···O hydrogen bond, linking a ‘corner’ water molecule to a water molecule at one end of **9’** which forms part of a ‘double-propeller’ motif (not observed in the published structure) made up of 1-butanol molecules (O1W···O8W) (Fig. 4.33). There are also 3 hydrogen bonds between three 1-butanol molecules of the first ‘propeller’ and the central water molecule (O1J···O8W) and the 3 1-butanol···1-butanol hydrogen bonds between the first and second ‘propeller’ (O1I···O1J), which has no central water molecule. The 1-butanol molecules of the second ‘propeller’ are directly hydrogen-bonded to each other through 3 O-H···O hydrogen bonds (O1I···O1I). There are also the 3 1-butanol molecules inside the assembly which are hydrogen-bonded to ‘corner’ water molecules (O1G···O3W) (Fig. 4.42a). This forms a total of 73 hydrogen bonds for **9’**.

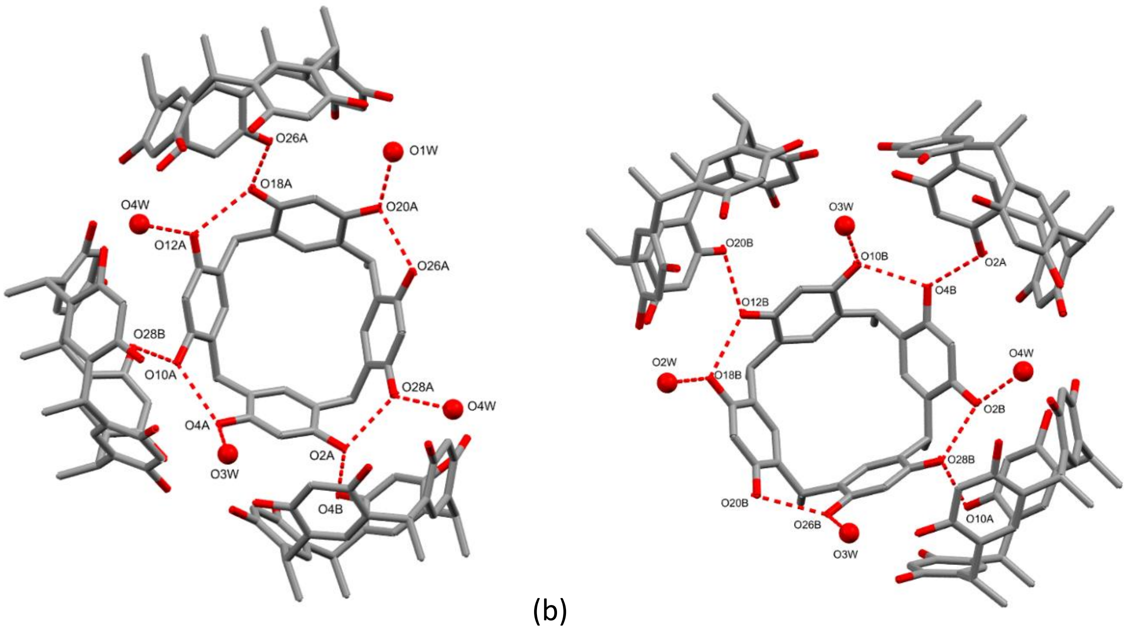

(a) (b)

Figure 4.34: (a) The unique O-H···O hydrogen bonds of the CMCR molecule A in **9'** (b) the unique O-H···O hydrogen bonds of the CMCR molecule B in **9'**. Water molecules are displayed as spheres and hydrogen atoms are omitted for clarity. Hydrogen bonds are displayed as dashed red lines.

Table 4.14: Unique hydrogen bonding parameters for **9**.

Bonding atoms	**D···A (Å)**	**Symmetry operators**
O2A···O28A	2.669(7)	x, y, z
O4A···O10A	2.698(6)	x, y, z
O12A···O18A	2.710(7)	x, y, z
O20A···O26A	2.629(7)	x, y, z
O2A···O4B	2.700(6)	-x+y, 1-x, z
O4A···O3W	2.798(7)	x, y, z
O10A···O28B	2.622(5)	x, y, z
O12A···O4W	2.795(9)	1-y, 1+x-y, z
O18A···O26A	2.630(8)	1-y, 1+x-y, z
O20A···O1W	2.677(4)	1-y, 1+x-y, z
O28A···O4W	2.765(10)	x, y, z
O2B···O28B	2.650(5)	x, y, z
O4B···O10B	2.679(6)	x, y, z
O12B···O18B	2.648(6)	x, y, z
O20B···O26B	2.706(7)	x, y, z
O2B···O4W	2.618(8)	1-y, 1+x-y, z
O10B···O3W	2.696(9)	1-y, 1+x-y, z
O12B···O20B	2.669(8)	1-y, 1+x-y, z

O18B···O2W	2.672(5)	x, y, z
O26B···O3W	2.688(7)	x, y, z
O1G···O3W	2.55(3)	x, y, z
O1I···O1I	2.77(5)	1-y, 1+x-y, z
O1I···O1J	2.84(5)	x, y, z
O1J···O8W	2.92(6)	x, y, z
O1W···O8W	2.587(17)	x, y, z
O2W···O9W	3.02(4)	x, y, z
O1H···O9W	2.93(5)	x, y, z
O2C···O28C	2.687(6)	x, y, z
O4C···O10C	2.707(6)	x, y, z
O12C···O18C	2.696(7)	x, y, z
O20C···O26C	2.641(7)	x, y, z
O2C···O5W	2.701(9)	x, y, z
O4C···O12C	2.666(9)	-x+y, 1-x, z
O10C···O7W	2.772(6)	x, y, z
O10C···O1H	2.58(4)	-x+y, 1-x, z
O18C···O5W	2.727(9)	1-y, 1+x-y, z
O20C···O26D	2.698(7)	1-y, 1+x-y, z
O26C···O6W	2.676(9)	x, y, z
O28C···O18D	2.653(6)	x, y, z
O2D···O28D	2.679(6)	x, y, z
O4D···O10D	2.690(8)	x, y, z
O12D···O18D	2.755(7)	x, y, z
O20D···O26D	2.769(7)	x, y, z
O2D···O1E	2.622(7)	x, y, z
O4D···O10D	2.684(7)	-x+y, 1-x, z
O12D···O1FA	2.671(15)	x, y, z
O20D···O5W	2.790(8)	x, y, z
O28D···O6W	2.811(9)	-x+y, 1-x, z
O1E···O1FA	2.771(13)	-x+y, 1-x, z
O1FA···O6W	2.987(13)	x, y, z

9” exhibits a more complicated hydrogen-bonding network (Fig. 4.33 and 4.35). Unique, strong hydrogen bonds involving CMCR are shown in Fig. 4.35. **9”** comprises 24 CMCR intramolecular hydrogen bonds (O2C···O28C, O4C···O10C, O12C···O18C, O20C···O26C, O2D···O28D, O4D···O10D, O12D···O18D and O20D···O26D), 18 water···CMCR O-H···O hydrogen bonds (O2C···O5W, O10C···O7W, O18C···O5W, O26C···O6W, O20D···O5W and O28D···O6W) and 12 CMCR···CMCR intermolecular hydrogen bonds (O4C···O12C, O20C···O26D, O28C···O18D and O4D···O10D), with the decrease in the number of water···CMCR hydrogen bonds caused by the distortion induced

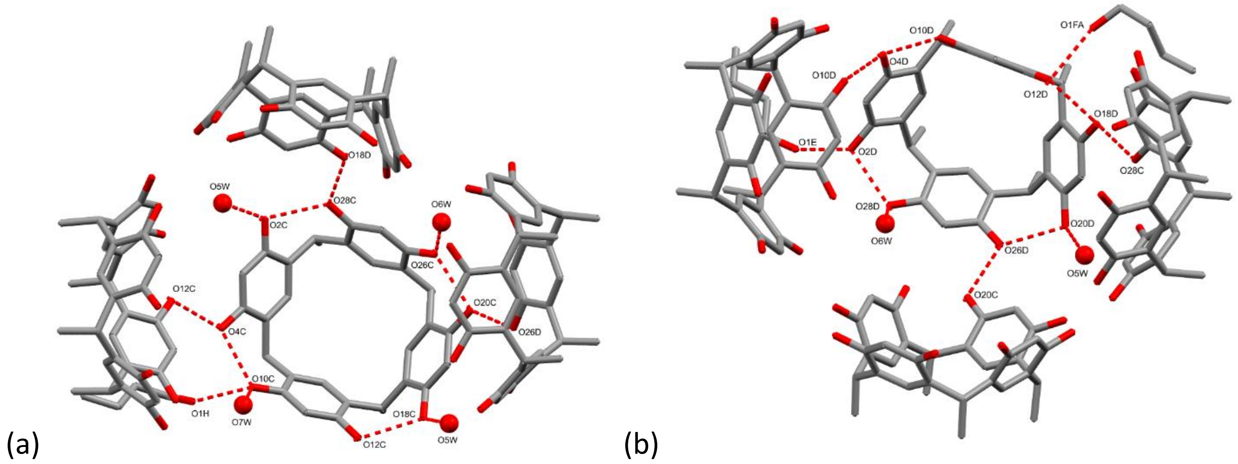

Figure 4.35: (a) The unique O-H···O hydrogen bonds of the CMCR molecule C in **9”** and (b) the unique O-H···O hydrogen bonds of the CMCR molecule D in **9”**. Water molecules are displayed as spheres and hydrogen atoms are omitted for clarity. Hydrogen bonds are displayed as dashed red lines.

by the 1-butanol molecules and the omission of the eighth water molecule. **9”** also has 6 CMCR···1-butanol hydrogen bonds (O2D···O1E and O12D···O1FA), 3 1-butanol···1-butanol (O1E···O1FA) and 3 1-butanol···water (O1FA···O6W) hydrogen bonds (displayed in Fig. 4.43), adding up to 66 hydrogen bonds. A heterodimer of hexameric assemblies is formed (Fig. 4.33) when taking account of the 3 hydrogen bonds that form between the three H-labelled 1-butanol molecules and the C-labelled CMCR molecules (O10C···O1H), the 3 hydrogen bonds that connect the H-labelled 1-butanol molecules to O9W to form the ‘propeller’ motif (O1H···O9W) – also shown in Fig. 4.40a – and the hydrogen bond between the O9W water molecule and the O2W water molecule of **9’** that connects it to the central ‘propeller’ (O2W···O9W). This adds up to a total of 146 hydrogen bonds making up the supra-heterodimer (Fig. 4.33) within the structure of **9**.

It should be noted that the three hydrogen bonds between the 1-butanol molecules of the central propeller and the CMCR molecules C of **9”** (O10C···O1H) were not observed in the published structure, and neither was the ‘double propeller’ motif made up of water and 1-butanol molecules adjacent to **9’**. Furthermore, the 1-butanol molecules modelled within **9’** were not shown to be involved in hydrogen bonding.

Structure solution and refinement of **10** revealed that the crystal structure is very similar to that of **9**. The ASU of **10** is made up of four unique CMCR molecules, six 1-pentanol molecules (one is disordered over three positions, resulting in a total occupancy of 5.33) and eleven water molecules (six are positioned on a three-fold rotation axis, resulting in a total occupancy of 7). Similar to **9**, **10** also consists of two unique spherical assemblies (Figs. 4.36 and 4.37), **10’** which encapsulates four water molecules (O10W and O11W) and three 1-pentanol molecules (pentanol molecule G – shown in green in Fig. 4.36), and the other, **10”**, which is apparently empty. The unit cells are also very similar, with the three axis lengths of **9** measuring approximately 29.9, 29.9 and 96.2 Å, while the three axis lengths of **10** measure approximately 30.1, 30.1 and 97.2 Å. Similar to **9’** and **9”**, both hexameric assemblies **10’** and **10”** comprise six CMCR molecules residing on the faces of a cube with water molecules residing on the vertices of such a cube, with a water molecule bonding three neighbouring CMCR molecules in a trigonal arrangement by water···CMCR O-H···O hydrogen bonding.

Table 4.15: Crystal data and refinement parameters for **10**.

	10
Empirical formula	$(C_{32}H_{32}O_8)_4 \cdot (C_5H_{12}O)_{5.33} \cdot (H_2O)_7$
Formula weight	2 760.40
Temperature (K)	100(2)
Crystal system	Trigonal
Space group	*R*3*c*
***a* (Å)**	30.121(2)
***b* (Å)**	30.121(2)
***c* (Å)**	97.168(7)
***α* (°)**	90
***β* (°)**	90
***γ* (°)**	120
Volume (Å^3)	76 348(12)
Z	18
ρ_{calc} (g.cm^{-3})	1.081
μ (mm^{-1})	0.649
***F*(000)**	26 544
Crystal size (mm^3)	0.52 x 0.40 x 0.27
Radiation	CuKα (λ = 1.54178 Å)
2ϑ range for data collection (°)	3.844 – 150.534
Index ranges	$-37 \le h \le 37$, $-36 \le k \le 37$, $-121 \le l \le 119$
Reflections collected	227 775
Independent reflections	34 426 [R_{int} = 0.0386, R_{sigma} = 0.0245]
Data/restraints/parameters	34 426/482/1 847
Goodness-of-fit on F^2	1.606
Final *R* indices [$I \ge 2\sigma(I)$]	R_1 = 0.1150, wR_2 = 0.3198
Final *R* indices (all data)	R_1 = 0.1181, wR_2 = 0.3315
Largest diff. peak/hole (e.Å^{-3})	1.44/-0.61

10’ has eight water molecules at all eight vertices of the cube with **10”** having seven water molecules, the eighth one missing because of the closer arrangement of three CMCR molecules at this position (intersection of red molecules in Fig. 4.36), and thus the three water···CMCR O-H···O hydrogen bonds are also absent at this point. Furthermore, three of these seven water molecules (indicated by red spheres in Fig. 4.36b) are hydrogen bonding with two neighbouring CMCR molecules (and a 1-pentanol molecule located at the same vertex) as opposed to hydrogen bonding to three neighbouring CMCR molecules as observed in **10’**. The opposing CMCR molecules of **10’** and **10”** are also rotated by ~45°. The point group symmetries of **10’** and **10”** are *C*3, and these assemblies are therefore also chiral, the same as **9’** and **9”**.

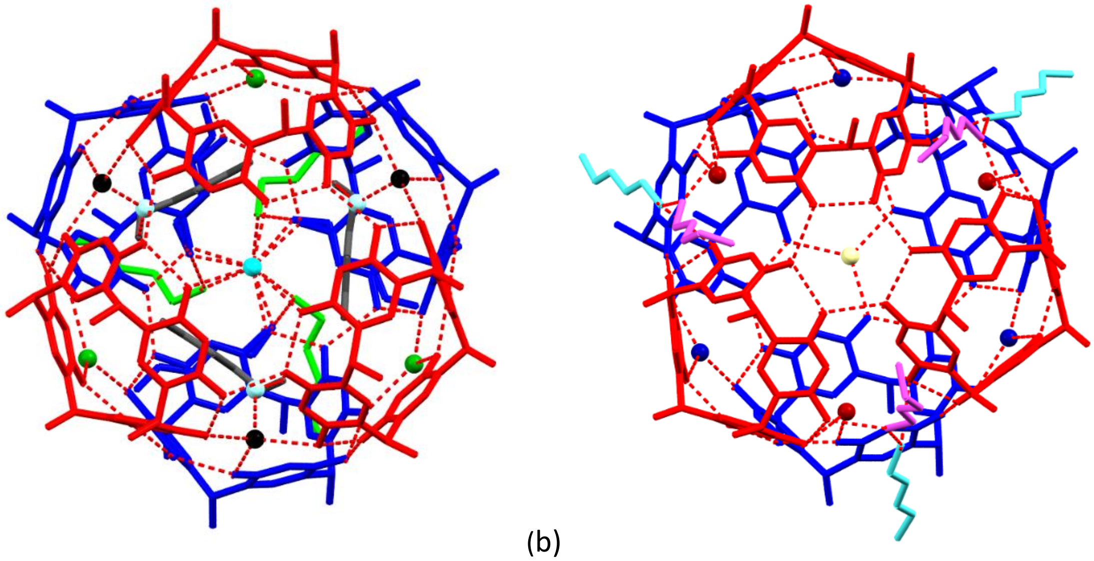
(a) (b)

Figure 4.36: Hexameric assemblies of CMCR, 1-pentanol and water displaying the (a) regular hexameric assembly **10’** and the (b) distorted assembly **10”**, showing the missing water molecule at the intersection of the red CMCR molecules. Both are displayed with their interacting 1-pentanol molecules. Hydrogen atoms have been omitted for clarity. Water molecules are shown as spheres.

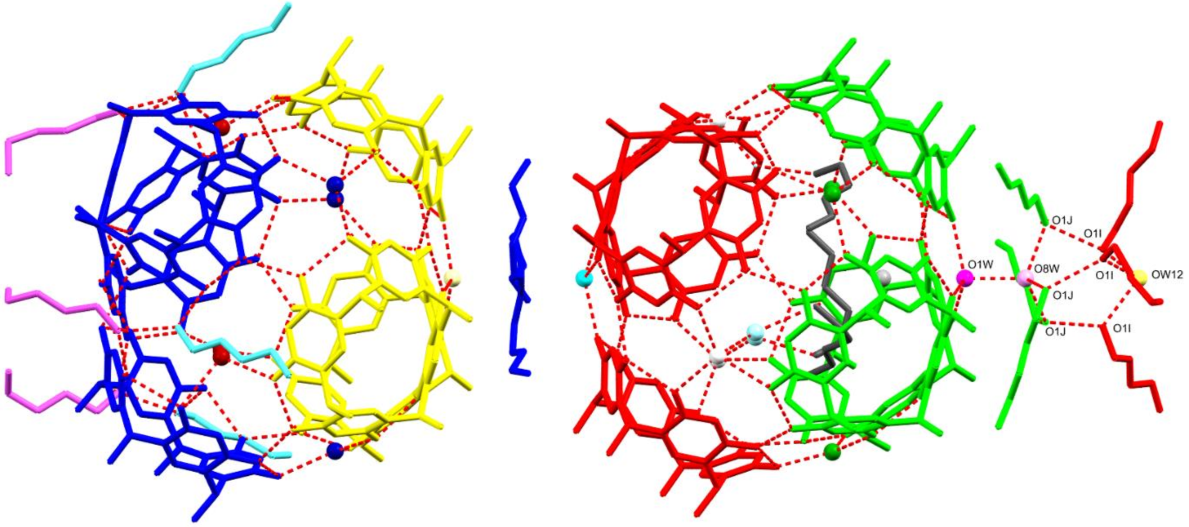

Figure 4.37: The neighbouring hexameric assemblies **10’** (right) and **10”** (left) in the crystal structure of **10**, which do not form a supra-heterodimer. Atoms are coloured according to symmetry equivalence. Hydrogen atoms have been omitted for clarity. Oxygen atoms involved in the ‘double propeller’ motif are labelled.

10’ and **10”** each contain two crystallographically unique CMCR molecules – A and B in **10’** and C and D in **10”**. Unique, strong hydrogen bonds involving CMCR within **10’** are shown in Fig. 4.38. **10’** has 24 CMCR intramolecular hydrogen bonds (O2A···O28A, O4A···O10A, O12A···O18A, O20A···O26A, O2B···O28B, O4B···O10B, O12B···O18B and O20B···O26B) as each CMCR molecule has four intramolecular hydrogen bonds where one hydroxyl group forms a hydrogen bond with a hydroxyl group of the neighbouring resorcinol unit, 12 CMCR···CMCR intermolecular hydrogen bonds (O2A···O4B, O10A···O28B, O18A···O26A and O12B···O20B) and 24 water···CMCR O–H···O hydrogen bonds (O4A···O3W, O12A···O4W, O20A···O1W, O28A···O4W, O2B···O4W, O10B···O3W, O18B···O2W and O26B···O3W), the same as in the case of **9’**, each water molecule hydrogen bonding with three CMCR molecules at eight such sites. However, **10’** also has 3 additional interior water···water O-H···O hydrogen bonds (O3W···O10W – shown in Fig. 4.42), 3 additional interior 1-pentanol···water hydrogen bonds (O1G···O10W – shown in Fig. 4.42) and an additional exterior water···water hydrogen bond (O1W···O8W) from a ‘surface’ water molecule to an exterior water molecule hydrogen bonded to three surrounding 1-pentanol molecules through 3 water···1-pentanol O-H···O hydrogen bonds (O1J···O8W). The three 1-pentanol molecules are further hydrogen bonded to a second group of three 1-pentanol molecules through 3 1-pentanol···1-pentanol O-H···O hydrogen bonds (O1I···O1J) to form a ‘double propeller’ motif. Lastly, the second group of 1-pentanol molecules are hydrogen bonded to a central water molecule through 3 1-pentanol···water hydrogen bonds (O1I···OW12). This makes a total of 76 hydrogen bonds making up the structure of **10’**.

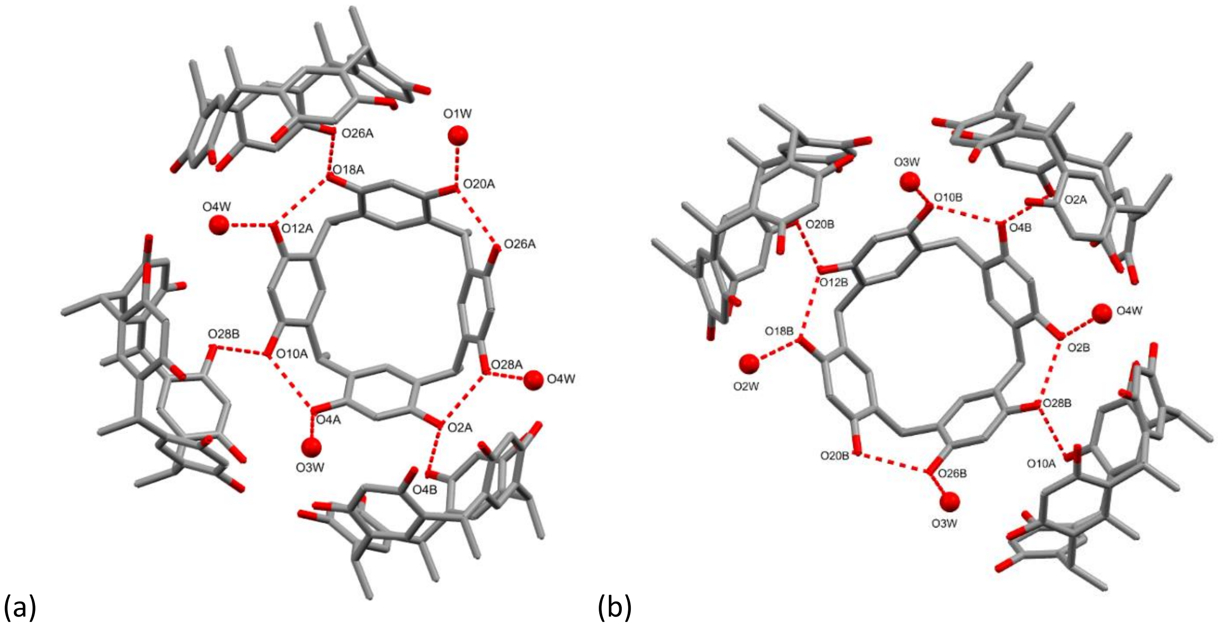

Figure 4.38: (a) The unique O-H···O hydrogen bonds of the CMCR molecule A in **10’** (b) the unique O-H···O hydrogen bonds of the CMCR molecule B in **10’**. Water molecules are displayed as spheres and hydrogen atoms are omitted for clarity. Hydrogen bonds are displayed as dashed red lines.

Table 4.16: Unique hydrogen bonding parameters for **10**.

Bonding atoms	D···A (Å)	Symmetry operators
O2A···O28A	2.674(7)	x, y, z
O4A···O10A	2.695(5)	x, y, z
O12A···O18A	2.726(7)	x, y, z
O20A···O26A	2.650(7)	x, y, z
O2A···O4B	2.697(6)	-x+y, 1-x, z
O4A···O3W	2.821(7)	x, y, z
O10A···O28B	2.632(5)	x, y, z
O12A···O4W	2.719(9)	1-y, 1+x-y, z
O18A···O26A	2.657(8)	1-y, 1+x-y, z
O20A···O1W	2.676(4)	x, y, z
O28A···O4W	2.808(9)	x, y, z
O2B···O28B	2.633(6)	x, y, z
O4B···O10B	2.684(7)	x, y, z
O12B···O18B	2.624(7)	x, y, z
O20B···O26B	2.720(8)	x, y, z
O2B···O4W	2.627(7)	1-y, 1+x-y, z
O10B···O3W	2.703(9)	1-y, 1+x-y, z
O12B···O20B	2.647(8)	1-y, 1+x-y, z

O18B···O2W	2.730(6)	x, y, z
O26B···O3W	2.688(7)	x, y, z
O1G···O10W	2.87(3)	x, y, z
O1I···OW12	2.61(5)	x, y, z
O1I···O1J	2.85(4)	x, y, z
O1J···O8W	2.66(3)	x, y, z
O1W···O8W	2.626(15)	x, y, z
O3W···O10W	2.57(3)	x, y, z
O2C···O28C	2.683(8)	x, y, z
O4C···O10C	2.659(6)	x, y, z
O12C···O18C	2.703(8)	x, y, z
O20C···O26C	2.622(7)	x, y, z
O2C···O5W	2.643(13)	x, y, z
O4C···O12C	2.667(9)	-x+y, 1-x, z
O10C···O7W	2.706(5)	x, y, z
O18C···O5W	2.712(13)	1-y, 1+x-y, z
O20C···O26D	2.680(7)	1-y, 1+x-y, z
O26C···O6W	2.635(11)	x, y, z
O28C···O18D	2.670(7)	x, y, z
O2D···O28D	2.695(10)	x, y, z
O4D···O10D	2.773(17)	x, y, z
O12D···O18D	2.758(12)	x, y, z
O20D···O26D	2.743(8)	x, y, z
O2D···O1E	2.52(3)	x, y, z
O4D···O10D	2.843(15)	-x+y, 1-x, z
O12D···O1F	2.99(3)	x, y, z
O20D···O5W	2.785(9)	x, y, z
O28D···O6W	2.822(12)	-x+y, 1-x, z
O1E···O1F	2.73(3)	-x+y, 1-x, z

Meanwhile, unique, strong hydrogen bonds involving CMCR within **10”** are shown in Fig. 4.39. **10”** has 24 CMCR intramolecular hydrogen bonds (O2C···O28C, O4C···O10C, O12C···O18C, O20C···O26C, O2D···O28D, O4D···O10D, O12D···O18D and O20D···O26D), 18 water···CMCR hydrogen bonds (O2C···O5W, O10C···O7W, O18C···O5W, O26C···O6W, O20D···O5W and O28D···O6W) and 12 CMCR···CMCR intermolecular O-H···O hydrogen bonds (O4C···O12C, O20C···O26D, O28C···O18D and O4D···O10D), the same as in the case of **9”**. In addition, there are 6 CMCR···1-pentanol hydrogen bonds (O2D···O1E and O12D···O1F) and 3 1-pentanol···1-pentanol hydrogen bonds (O1E···O1F – shown in Fig. 4.43). These add up to a total of 63 hydrogen bonds for **10”**.

The ‘faux propeller’ in between **10’** and **10”** is just one 1-pentanol molecule (labelled H) disordered over three positions with no central water molecule observed, and not three separate molecules hydrogen bonded to a central water molecule as observed within the structure of **9** (Fig. 4.40). The oxygen atoms of the three disordered positions for these H-labelled 1-pentanol molecule are 1.363 Å apart, forcing a disordered model to be adopted. The hydrogen atoms have not been placed on the water molecules within these structures, but the O2W water molecule is only 2.860 Å away from the O1H hydroxyl oxygen of this H-labelled 1-pentanol molecule. This is a reasonable D···A distance for a hydrogen bond but is not indicated as such by either PLATON[24] or MERCURY[23] and therefore has not been assigned as one. The O7W water molecule is not close enough to the hydroxyl oxygen of this 1-pentanol molecule (3.085 Å) to suggest the presence of a hydrogen bond linking this 1-pentanol molecule to **10’**. Thus, the absence of these hydrogen bonds means that a similar supra-heterodimer as in **9** is not observed in **10** (Fig. 4.37). The structures are still largely similar, however, this difference in the central ‘propellers’ is the first difference between the structures of **9** and **10**.

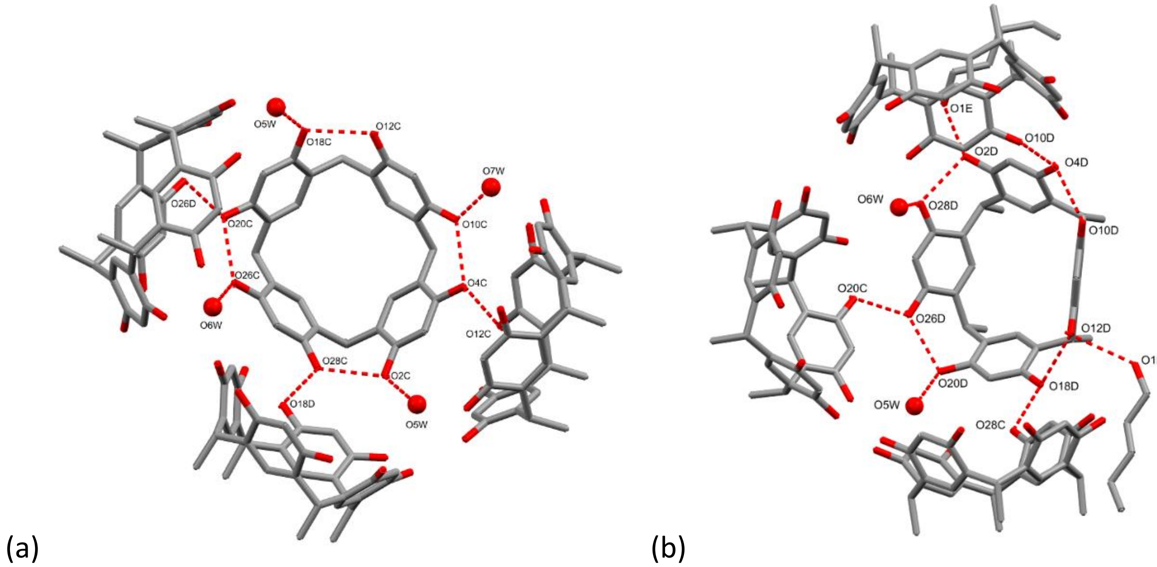

Figure 4.39: (a) The unique O-H···O hydrogen bonds of the CMCR molecule C in **10”** (b) the unique O-H···O hydrogen bonds of the CMCR molecule D in **10”**. Water molecules are displayed as spheres and hydrogen atoms are omitted for clarity. Hydrogen bonds are displayed as dashed red lines.

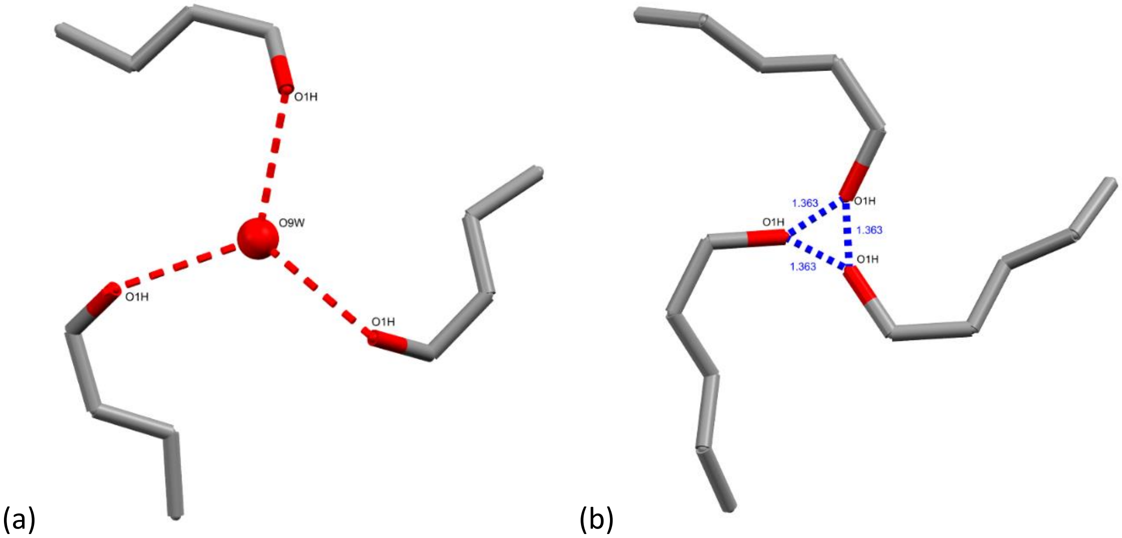

Figure 4.40: (a) The central 'propeller' within the structure of **9** and (b) the central 'faux propeller' within the structure of **10** (one 1-pentanol molecule is disordered over the three symmetry-related positions). Hydrogen atoms have been omitted for clarity and water molecules are displayed as spheres. Hydrogen bonds are represented as dashed red lines. Distances are represented as dashed blue lines and are labelled in angstroms.

The second observed difference is the two central water molecules apparent in the 'double propeller' motif of **10'**, in comparison with only one water molecule in the 'double propeller' motif of **9'** (Fig. 4.41). In **9'**, the second group of three 1-pentanol molecules are directly hydrogen bonded to one another (O1I···O1I).

The third apparent difference in the structures of **9** and **10** is the hydrogen bonding of the interior solvent molecules within the assemblies **9'** and **10'**, respectively (Fig. 4.42). The 1-butanol molecules within **9'** are hydrogen bonding directly to the surface water molecules O3W, while the 1-pentanol molecules within **10'** are hydrogen-bonded to bridging interior water molecules O10W, which in turn are hydrogen-bonded to the surface water molecules O3W.

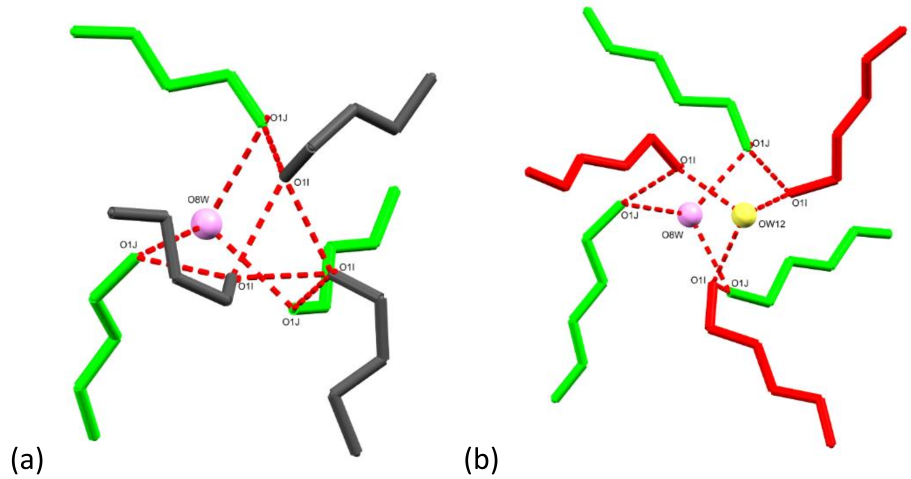

Figure 4.41: Frontal view of (a) 'double propeller' motif within **9** and (b) 'double propeller' motif within **10**. Hydrogen bonds are displayed as dashed red lines and water molecules as spheres. Molecules are colour-coded according to symmetry equivalence. Hydrogen atoms have been omitted for clarity.

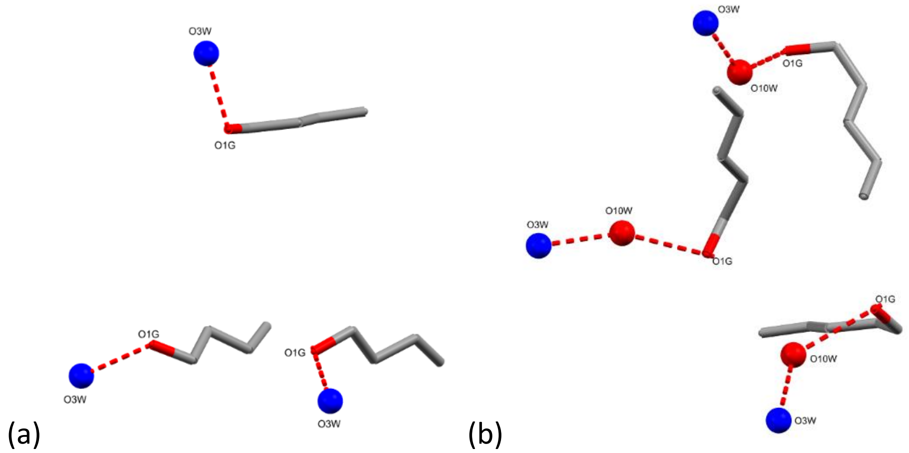

Figure 4.42: The hydrogen bonding of the interior solvent molecules within (a) **9'** and (b) **10'**. Hydrogen bonds are displayed as red dashed lines. Water molecules are shown as spheres. Hydrogen atoms have been omitted for clarity. Surface water molecules are coloured blue.

The fourth difference within the structures of **9** and **10** is the missing water···1-pentanol hydrogen bond at the site of 1-pentanol interaction with **10"** when compared with the hydrogen bonding network at the site of 1-butanol interaction with **9"** (Fig. 4.43). The FA 1-butanol molecule is engaged in a hydrogen bonding interaction with the O6W water molecule, forming a five-membered ring hydrogen bonding motif when interacting with **9"** (Fig. 4.43a), but the

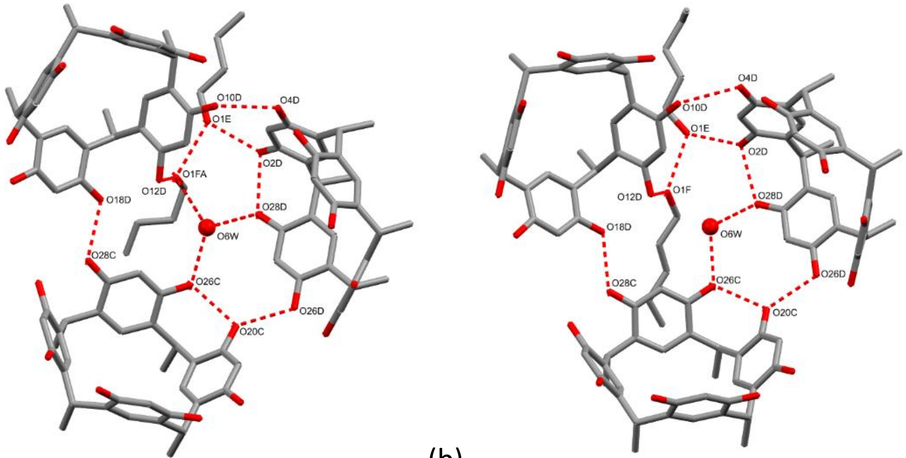

(a) (b)

Figure 4.43: (a) The hydrogen bonding network at the site of 1-butanol interaction with the assembly **9”** and (b) the hydrogen bonding network at the site of 1-pentanol interaction with the assembly **10”**. Hydrogen bonds are depicted as dashed red lines and water molecules as red spheres. Hydrogen atoms are omitted for clarity.

corresponding 1-pentanol molecule F is too far from the water molecule O6W when interaction with **10”** for a hydrogen bond to be possible (Fig. 4.43b).

Weaker hydrogen bonds are also present in the structures of **9** and **10**. In **9’**, CMCR molecule A (Fig. 4.44a) has one unique intermolecular inter-assembly CMCR···CMCR C-H···O hydrogen bond (C8A-H8AC···O4C), two unique intra-assembly CMCR···1-butanol C-H···π interactions with the included 1-butanol molecule (C4G-H4GA···Cg2^{b} and C4G-H4GB···Cg4^{d}), one other unique intra-assembly CMCR···1-butanol C-H···π interaction (C3J-H3JB···Cg3^{c}) and one unique intermolecular inter-assembly CMCR···CMCR C-H···π interaction (C32D-H32E···Cg2^{b}). In **10’**, the observed interactions are very similar, with CMCR molecule A (Fig. 4.44b) having two unique intra-assembly CMCR···1-pentanol C–H···π interactions with the included 1-pentanol molecule, but with adjacent aromatic rings as opposed to opposite aromatic rings in **9’** (C1G-H1GB···Cg1^{a} and C1G-H1GA···Cg4^{d}), one other unique intra-assembly CMCR···1-pentanol C-H···π interaction (C3J-H3JB···Cg3^{c}) and two unique intermolecular inter-assembly CMCR···CMCR C-H···π interactions involving one other CMCR molecule (C16A-H16C···Cg16^{p} and C32D-H32E···Cg2^{b}).

Table 4.17: Unique C-H bonding parameters for **9**.

Bonding atoms	D–H (Å)	H···A (Å)	D···A (Å)	D–H···A (°)	Symmetry operators
C8A-H8AC···O4C	0.98	2.57	3.428(7)	146	⅓+x, ⅔+x-y, ⅙+z
C1H-H1HA···O18B	0.99	2.57	3.53(2)	164	x, y, z
O1E-H1E···Cg14[n]	0.84	2.65	3.439(7)	156	-x+y, 1-x, z
C16A-H16C···Cg16[p]	0.98	2.57	3.428(6)	147	⅔+x, ⅓+y, ⅓+z
C4E-H4EB···Cg5[e]	0.98	2.83	3.496(10)	126	-⅔+x, -⅓+y, -⅓+z
C23D-H23D···Cg6[f]	1.00	2.92	3.860(5)	156	⅓-x+y, -⅔+y, -⅙+z
C4FA-H4FC···Cg12[l]	0.98	2.86	3.65(2)	139	x, y, z
C32D-H32E···Cg2[b]	0.98	2.68	3.528(7)	145	-⅔+x, -⅓+y, -⅓+z
C4G-H4GA···Cg2[b]	0.98	2.86	3.765(14)	154	x, y, z
C4G-H4GB···Cg4[d]	0.98	2.87	3.764(13)	152	x, y, z
C3J-H3JB···Cg3[c]	0.99	2.89	3.77(2)	148	x, y, z
C4FB-H4FE···Cg12[l]	0.98	2.74	3.67(4)	160	x, y, z

[b] Cg2 (C9A/C10A/C11A/C12A/C13A/C14A), [c] Cg3 (C17A/C18A/C19A/C20A/C21A/C22A), [d] Cg4 (C25A/C26A/C27A/C28A/C29A/C30A), [e] Cg5 (C1B/C2B/C3B/C4B/C5B/C6B), [f] Cg6 (C9B/C10B/C11B/C12B/C13B/C14B), [l] Cg12 (C25C/C26C/C27C/C28C/C29C/C30C), [n] Cg14 (C9D/C10D/C11D/C12D/C13D/C14D), [p] Cg16 (C25D/C26D/C27D/C28D/C29D/C30D)

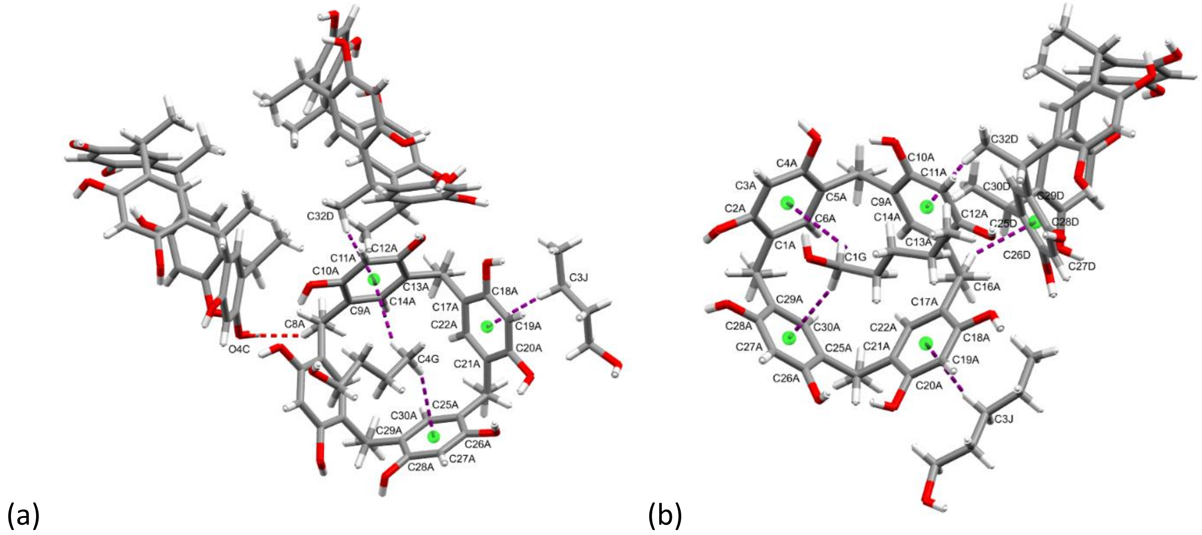

Figure 4.44: (a) The unique C-H···O hydrogen bonds (red) and C–H···π interactions (purple) of the CMCR molecule A in **9’** and (b) the unique C-H···O hydrogen bonds (red) and C-H···π interactions (purple) of the CMCR molecule A in **10’**. Centroids of aromatic rings involved in C-H···π interactions are displayed as green spheres.

The only other differences observed are that the C-H···O hydrogen bond (C8A-H8AC···O4C) appearing in **9'** does not appear in **10'** and the C16A-H16C···Cg16[p] bond appearing in **10'** does not appear in **9'**.

Table 4.18: Unique C-H bonding parameters for **10**.

Bonding atoms	D–H (Å)	H···A (Å)	D···A (Å)	D–H···A (°)	Symmetry operators
C27D-H27D···O20C	0.95	2.59	3.286(7)	131	-x+y, 1-x, z
C16A-H16C···Cg16[p]	0.98	2.63	3.507(7)	149	⅔+x, ⅓+y, ⅓+z
C4E-H4EA···Cg5[e]	0.99	2.92	3.60(2)	126	-⅔+x, -⅓+y, -⅓+z
C23D-H23D···Cg6[f]	1.00	2.92	3.855(6)	156	⅓-x+y, -⅔+y, -⅙+z
C4F-H4FA···Cg12[l]	0.99	2.79	3.70(2)	153	x, y, z
C32D-H32E···Cg2[b]	0.98	2.77	3.535(10)	136	-⅔+x, -⅓+y, -⅓+z
C1G-H1GA···Cg4[d]	0.99	2.72	3.682(17)	163	x, y, z
C1G-H1GB···Cg1[a]	0.99	2.90	3.643(18)	133	x, y, z
C3J-H3JB···Cg3[c]	0.99	2.96	3.75(3)	138	x, y, z
C4I-H4IB···Cg13[m]	0.99	2.73	3.60(2)	147	-x+y, y, ½+z
C4H-H4HA···Cg10[j]	0.99	2.72	3.70(3)	168	x, y, z

[a]Cg1 (C1A/C2A/C3A/C4A/C5A/C6A), [b]Cg2 (C9A/C10A/C11A/C12A/C13A/C14A), [c]Cg3 (C17A/C18A/C19A/C20A/C21A/C22A), [d]Cg4 (C25A/C26A/C27A/C28A/C29A/C30A), [e]Cg5 (C1B/C2B/C3B/C4B/C5B/C6B), [f]Cg6 (C9B/C10B/C11B/C12B/C13B/C14B), [j]Cg10 (C9C/C10C/C11C/C12C/C13C/C14C), [l]Cg12 (C25C/C26C/C27C/C28C/C29C/C30C), [m]Cg13 (C1D/C2D/C3D/C4D/C5D/C6D), [p]Cg16 (C25D/C26D/C27D/C28D/C29D/C30D)

CMCR molecule B in **9'** (Fig. 4.45a), meanwhile, has one unique CMCR···1-butanol C-H···O hydrogen bond from the central 1-butanol molecule of the supra-heterodimer (C1H-H1HA···O18B), one unique intermolecular inter-assembly CMCR···CMCR C-H···π interaction (C23D-H23D···Cg6[f]) and one unique inter-assembly CMCR···1-butanol C-H···π interaction (C4E-H4EB···Cg5[e]). CMCR molecule B in **10'** (Fig. 4.45b) has one unique intermolecular inter-assembly CMCR···CMCR C–H···π interaction (C23D-H23D···Cg6[f]) and one unique inter-assembly CMCR···1-pentanol C-H···π interaction (C4E-H4EA···Cg5[e]).

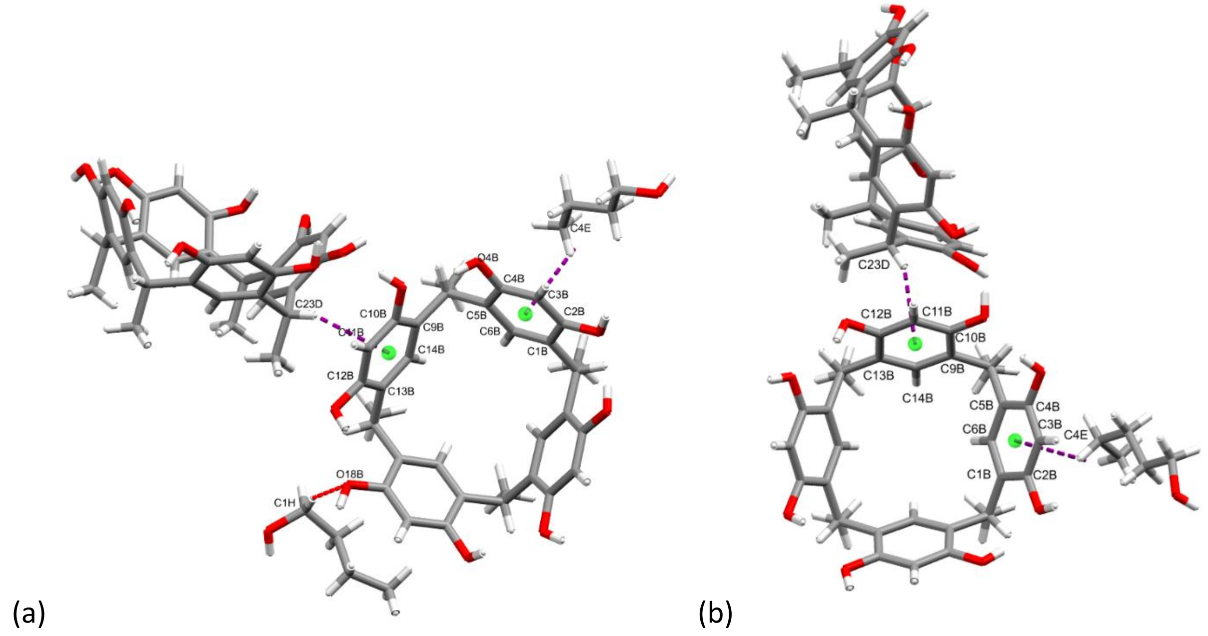

Figure 4.45: (a) The unique C-H···O hydrogen bonds (red) and C–H···π interactions (purple) of the CMCR molecule B in **9’** and (b) the unique C-H···π interactions (purple) of the CMCR molecule B in **10’**. Centroids of aromatic rings involved in C-H···π interactions are displayed as green spheres.

The only observed difference is the C1H-H1HA···O18B C-H···O hydrogen bond from the central 1-butanol molecule of the supra-heterodimer, which is observed for **9’** but not for **10’**.

CMCR molecule C in **9”** (Fig. 4.46a) has one unique intermolecular inter-assembly CMCR···CMCR C-H···O interaction (C8A-H8AC···O4C) and one unique intra-assembly CMCR···1-butanol C-H···π interaction (C4FA-H4FC···Cg12^{I} or C4FB-H4FE···Cg12^{I}, depending on which of the disordered 1-butanol molecules is present). CMCR molecule C in **10”** (Fig. 4.46b) has one unique intermolecular intra-assembly CMCR···CMCR C-H···O interaction (C27D-H27D···O20C), one unique 1-pentanol···CMCR intra-assembly C-H···π interaction (C4F-H4FA···Cg12^{I}) and one unique CMCR···1-pentanol C-H···π interaction involving the central 1-pentanol molecule located between **10’** and **10”** (C4H-H4HA···Cg10^{j}).

The main observed differences are the C8A-H8AC···O4C inter-assembly interaction observed for **9”** but not for **10”**, the C27D-H27D···O20C interaction observed for **10”** but not for **9”** and the differences in the way the CMCR molecule C interacts with the central ‘propeller’ solvent molecule(s): hydrogen bonding in **9** and a C-H···π interaction in **10**.

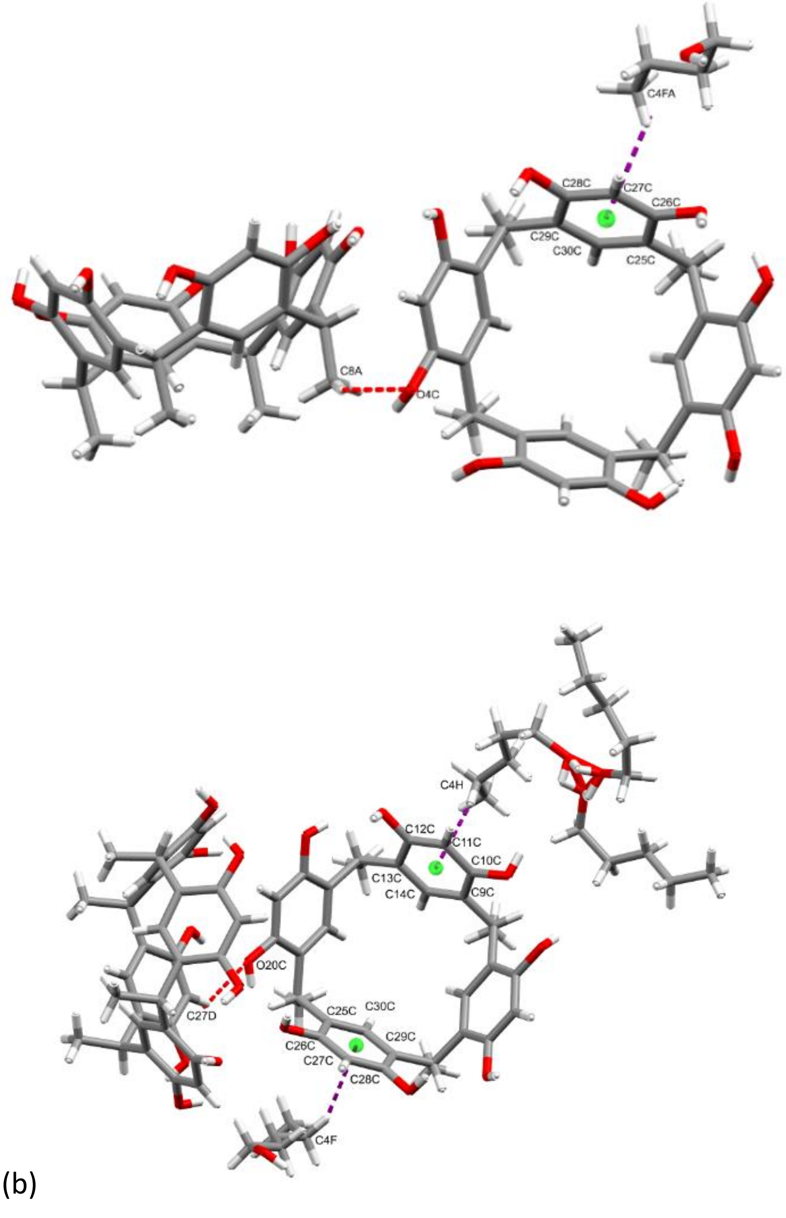

(a)

(b)

Figure 4.46: (a) The unique C-H···O hydrogen bonds (red) and C–H···π interactions (purple) of the CMCR molecule C in **9”** and (b) the unique C-H···O hydrogen bonds (red) and C-H···π interactions (purple) of the CMCR molecule C in **10”**. Centroids of aromatic rings involved in C-H···π interactions are displayed as green spheres.

CMCR molecule D in **9”** (Fig. 4.47a) has one unique intermolecular inter-assembly CMCR···CMCR C-H···π interaction (C16A-H16C···Cg16^{p}) and one unique intra-assembly 1-butanol···CMCR O-H···π interaction (O1E-H1E···Cg14^{n}), the only O-H···π bond in either **9** or **10**. CMCR molecule D in **10”** (Fig. 4.47b) has one unique intermolecular intra-assembly CMCR···CMCR C-H···O interaction (C27D-H27D···O20C), three unique intermolecular inter-assembly CMCR···CMCR C-H···π interactions (C23D-H23D···Cg6^{f}, C32D-H32E···Cg2^{b} and C16A-H16C···Cg16^{p}) and one unique inter-assembly 1-pentanol···CMCR C-H···π interaction involving the I-labelled ‘double-propeller’ 1-pentanol molecule (C4I-H4IB···Cg13^{m}).

The main differences observed are for the C-H···π interactions, where the CMCR molecule D in **10”** is involved in three inter-assembly interactions while the CMCR molecule D in **9”** is only involved in one inter-assembly interaction. The CMCR molecule D in **9”** is also involved in only an intra-assembly C-H···π interaction with 1-butanol, while the CMCR molecule D in **10”** is involved in a C-H···π interaction with the ‘double-propeller’ 1-pentanol molecule associated with another ‘pseudosupra-heterodimer’.

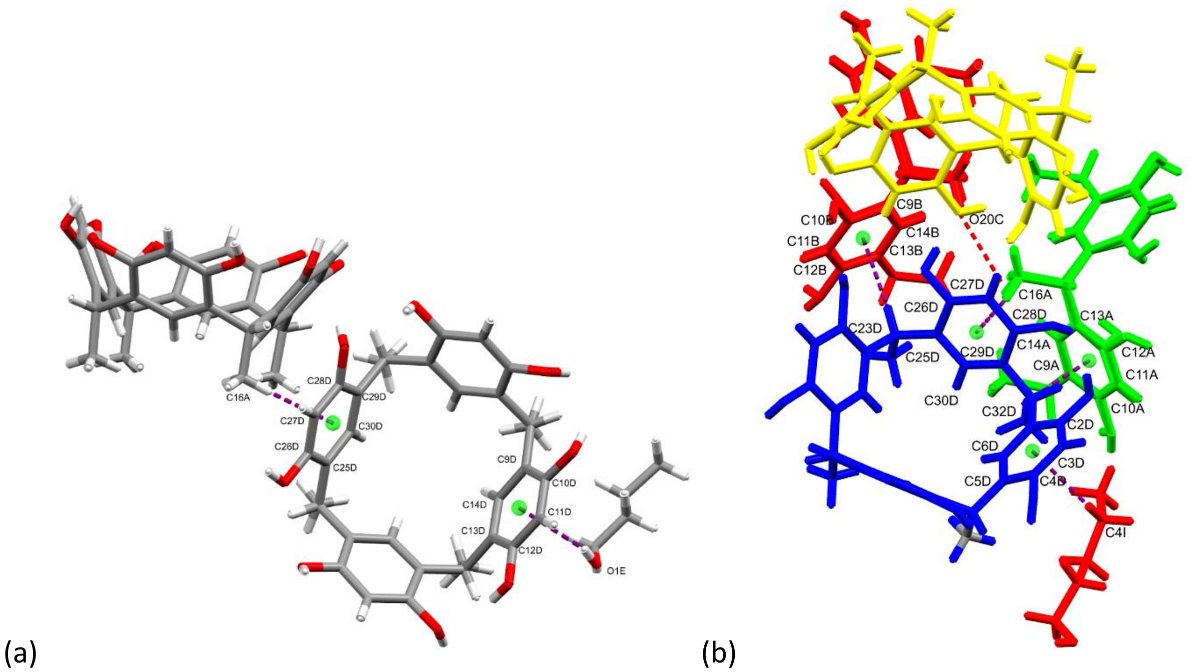

Figure 4.47: (a) The unique C–H···π interactions (purple) of the CMCR molecule D in **9”** and (b) the unique C-H···O hydrogen bonds (red) and C-H···π interactions (purple) of the CMCR molecule D in **10”** (molecules displayed in different colours for easier viewing). Centroids of aromatic rings involved in C-H···π interactions are displayed as green spheres.

However, a void space analysis after artificial removal of interior solvent molecules of both **9** (Fig. 4.48) and **10** (Fig. 4.49) in MSROLL, using a probe radius of 1.55 Å as MSROLL requires isolated voids, revealed that **9’** contains a total void space of 1 303 Å^3, with a cavity diameter of 16.6 Å. The same analysis on **10’** revealed a void volume per assembly of 1 330 Å^3, with the same cavity diameter as **9’**, 16.6 Å. Cavity diameter was determined by measuring the distance between water molecules on the 3-fold axis and opposite sides of the assembly in X-SEED. **9”** was found to encapsulate a void space of 1 181 Å^3, with a cavity diameter of 13.2 Å, while **10”** was shown to encapsulate a void space of 1 200 Å^3, with a cavity diameter of 13.6 Å. Therefore the distortion caused by the insertion of the alcohol molecules has resulted in a decrease in both the cavity diameters and interior volumes of the assemblies **9”** and **10”** relative to their respective counterparts **9’** and **10’**.

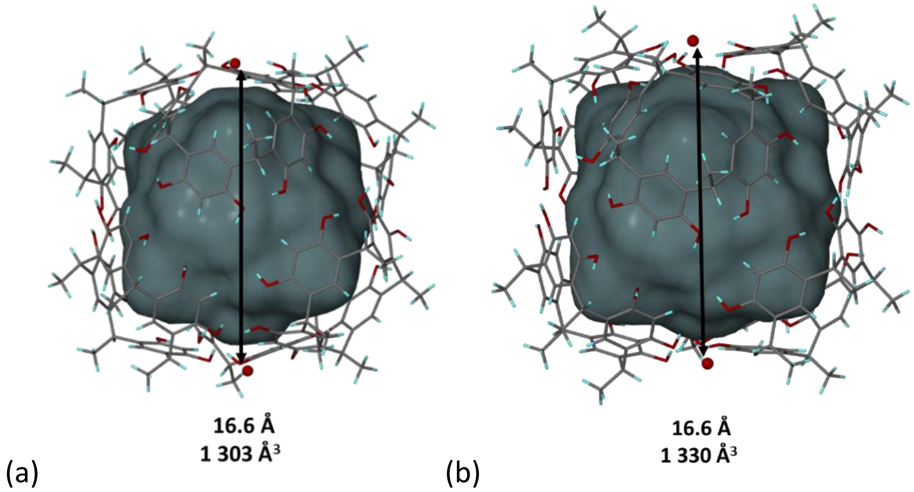

Figure 4.48: Wire-frame (including void spaces calculated by MSROLL) depictions of hexameric spherical assemblies (a) **9'** and (b) **10'**. The O···O distances between water molecules on the 3-fold axis and on opposite sides of the hexameric assemblies (shown as red spheres) are displayed in angstroms, whilst the interior volumes (a chosen probe radius of 1.55 Å was used based on the limitations of MSROLL requiring isolated voids) are shown in cubic angstroms.

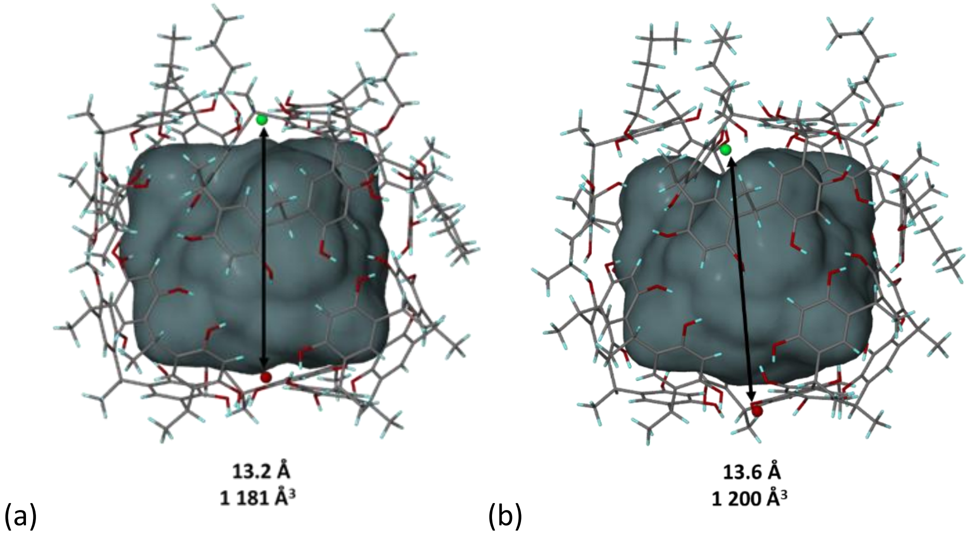

Figure 4.49: Wire-frame (including void spaces calculated by MSROLL) depictions of hexameric spherical assemblies (a) **9"** and (b) **10"**. The distances between water molecules on the 3-fold axis at one side of the hexameric assemblies (shown as red spheres) and the centroid of the hydroxyl oxygen atoms of the CMCR molecules at the vertex on the opposite side of the hexameric assemblies (shown as green spheres) were used in these cases, as the corresponding water molecule on the opposite side is missing. These distances are displayed in angstroms, whilst the interior volumes (a chosen probe radius of 1.55 Å was used based on the limitations of MSROLL requiring isolated voids) are shown in cubic angstroms.

Both **9** and **10** (with solvent molecules still present) were subjected to the SQUEEZE routine in PLATON,[24] which calculated 174 electrons per ASU for **9**, which correlates with ~4 unmodelled 1-butanol molecules, and 163 electrons per ASU for **10**, which correlates with ~3 unmodelled 1-pentanol molecules, if it is assumed that all unmodelled solvent is 1-butanol (in **9**) or 1-pentanol (in **10**). However, all of the void volume in both these structures appears to be contained within the hexameric assemblies (Figs. 4.50 and 4.51). This shows there may be disordered solvent molecules within the cavities of these hexameric assemblies. This is confirmed by the residual density found in the electron density maps – however, these densities could not be successfully modelled.

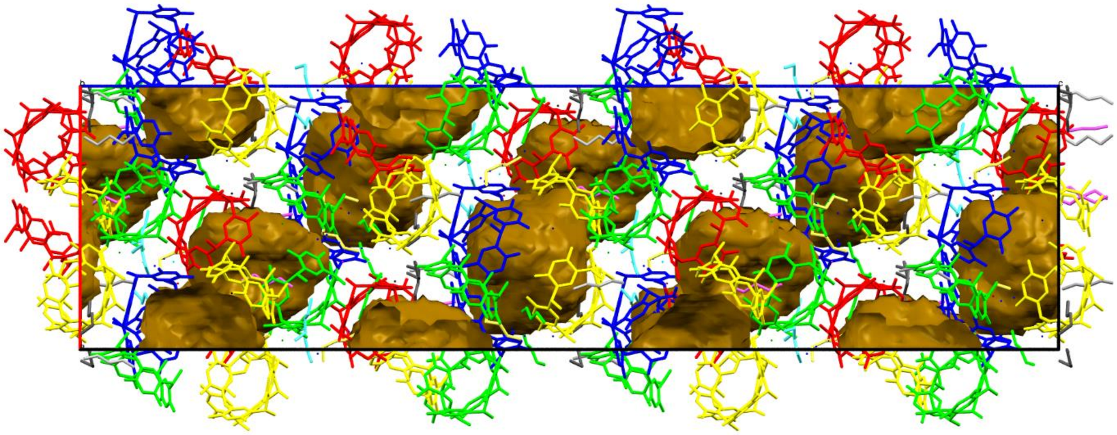

Figure 4.50: Packing diagram displaying hexamer interior cavities viewed along the *b*-axis. Hydrogen atoms have been omitted for clarity.

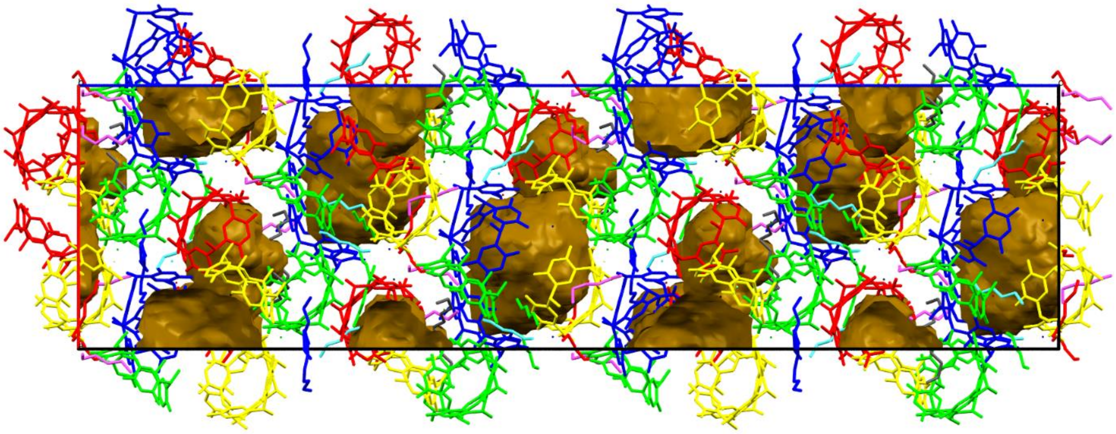

Figure 4.51: Packing diagram displaying hexamer interior spaces in the crystal structure of **10**. Hydrogen atoms have been omitted for clarity.

4.3.3.2. Powder X-Ray Diffraction and Variable-Temperature Powder X-Ray Diffraction

As is usually the case with these large spherical hexameric assemblies, **9** could not be obtained by liquid-assisted grinding but had to be obtained as crystals by slow evaporation. However, PXRD was still employed on ground crystals to establish the phase purity of the bulk sample (Fig. 4.52). VT-PXRD experiments in the temperature range 30-275 °C (Fig. 4.53) reveal that the sample initially agrees closely with the calculated PXRD pattern obtained from the crystal structure of **9** (the large peak at around 20° 2θ is a preferred orientation effect – a smaller peak is present in the calculated pattern). An amorphous phase, **9a**, is evident at 100 °C. However, at 125 °C, the sample appears to be en route to a second crystalline form. This phase is maintained until 275 °C, when a decrease in the peak at 10.2° 2θ is observed, as is a new peak appearing at 8.7° 2θ. After the sample has cooled to 30 °C, several changes are observed in the VT-PXRD pattern – the peaks at 7.2°, 11.0°, 14.4°, 15.5°, 19.0°, 19.5° and 22.0° 2θ have all either decreased or disappeared completely, while the peaks at 7.9°, 8.9°, 10.2°, 14.5°, 15.8° and 20.6° 2θ have all either appeared or increased. This new phase, **9b**, appears to match the MIGTUR[22] PXRD pattern, which also matches the desolvated forms **5c**, **6c**, **7c** and **8b**. This is remarkable, as even though the samples all contain the CMCR host, the solvated structure **9** is completely different from the surmised solvated structures **5**, **6**, and **7** (similar PXRD patterns to calculated PXRD pattern from the structure of **5**), although closer to **8**. This indicates that desolvation of these structures leads to the same, desolvated, dimeric phase.

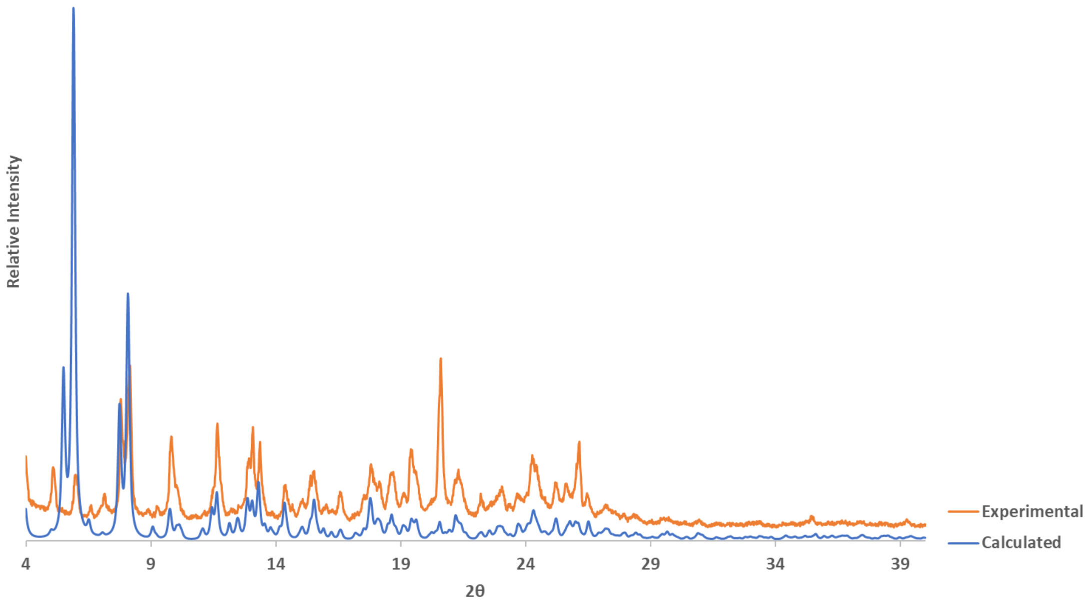

Figure 4.52: The PXRD pattern of ground crystals of **9** (in orange) and comparison with the calculated pattern from the single crystal structure of **9** (in blue).

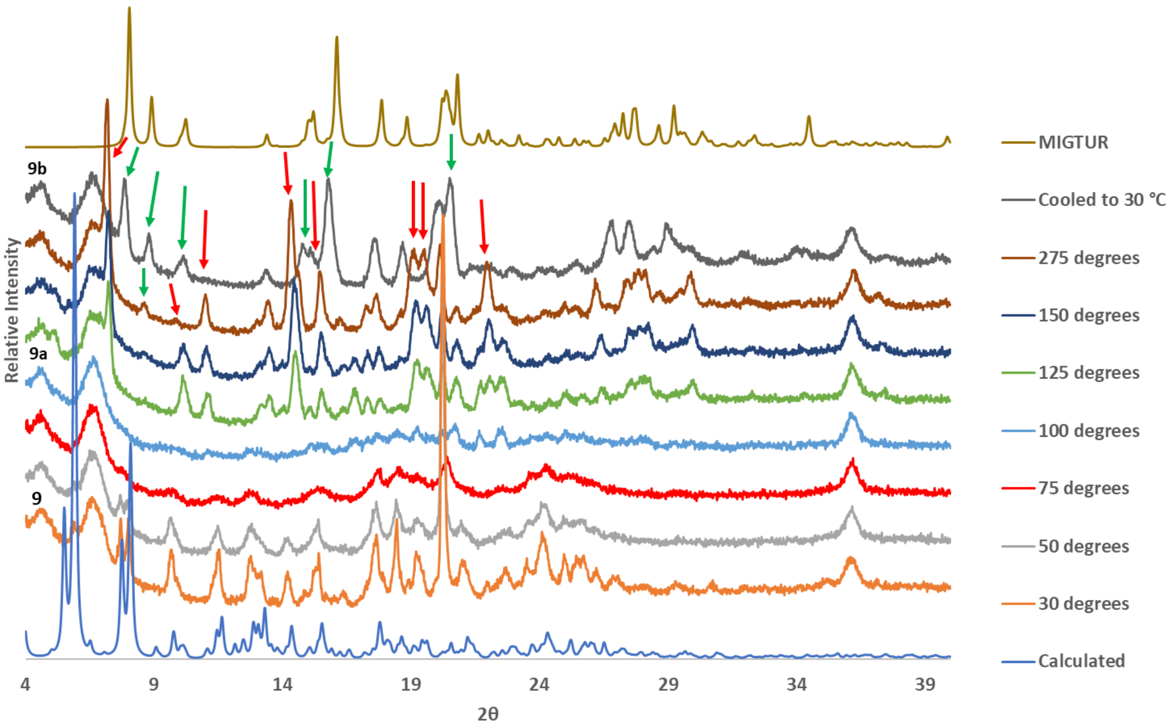

Figure 4.53: VT-PXRD patterns in the range 30-275 °C of **9**. Arrows indicate peaks referred to in the text (red – decreasing relative intensity, green – increasing relative intensity).

The predicted PXRD pattern of **10** is very similar to that of **9** (Fig. 4.54). This is unsurprising, as the structures are very similar, with only subtle differences. As is usually the case with hexameric spherical assemblies, **10** could not be prepared by liquid-assisted grinding, but only *via* crystallization by slow evaporation. However, purity of the bulk sample was ascertained by grinding crystals into powder form and comparing the obtained PXRD pattern against the calculated pattern obtained from the single crystal structure (Fig. 4.55).

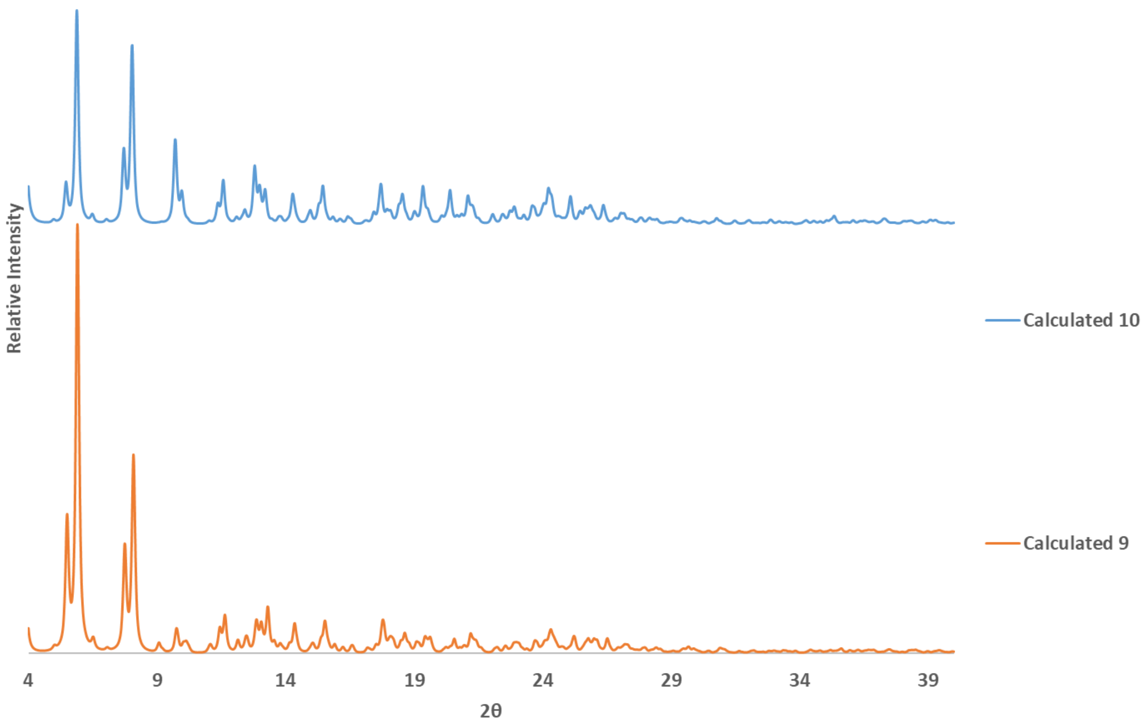

Figure 4.54: Comparison between the calculated PXRD pattern of **9** (in orange) and the calculated PXRD pattern of **10** (in blue).

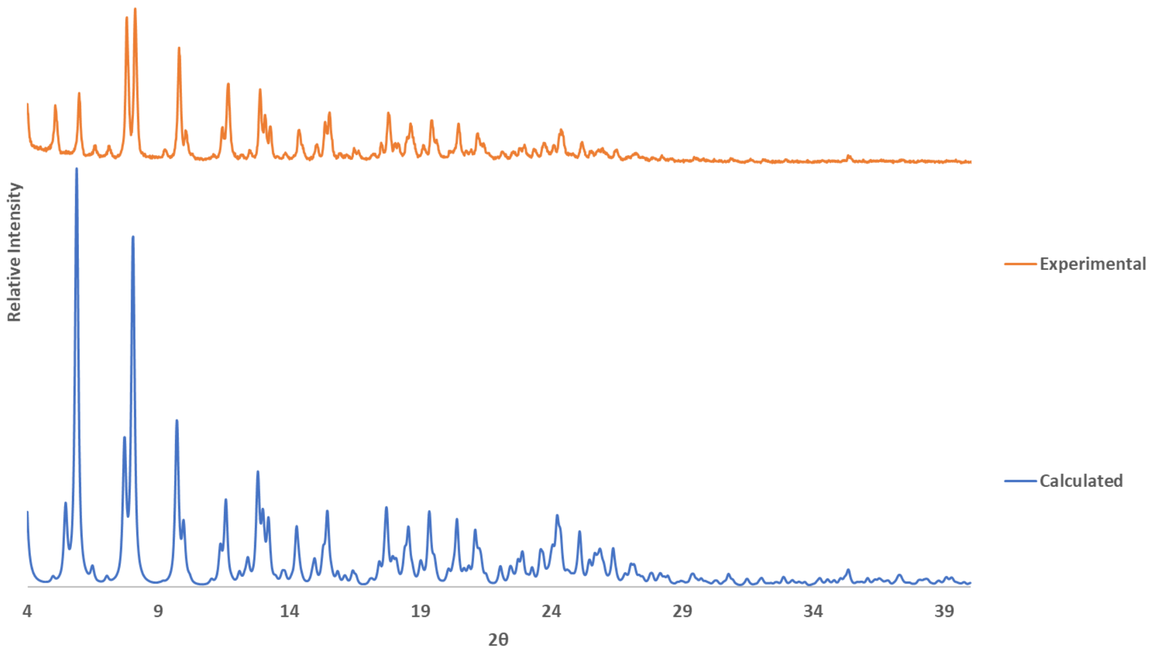

Figure 4.55: PXRD pattern obtained from gently ground crystals of **10** (in orange) and comparison with calculated PXRD pattern obtained from the single crystal structure of **10** (in blue).

VT-PXRD experiments in the temperature range 30-275 °C were performed (Fig. 4.56). The initial PXRD pattern at 30 °C compares favourably with the predicted pattern obtained from the structure of **10**. The sample appears to go through a less crystalline transition phase, **10a**, at 100 °C. At 125 °C, the sample again appears to be enroute to a new crystalline phase. This phase remains stable all the way up to 275 °C and cooling to 100 °C, but upon cooling to 30 °C, similar changes are observed to those observed for the transition to **9b** – the peaks at 7.4°, 11.2°, 14.7°, 15.7°, 19.4°, 19.9° and 22.3° 2θ have decreased or disappeared completely, while the peaks at 8.0°, 9.0°, 10.4°, 14.9°, 16.0° and 20.8° 2θ have increased or appeared. This phase, **10b**, also appears to match the MIGTUR[22] PXRD pattern, which also matches **9b**, **8b**, **7c**, **6c**, and **5c**, showing that desolvation leads to the same dimeric phase.

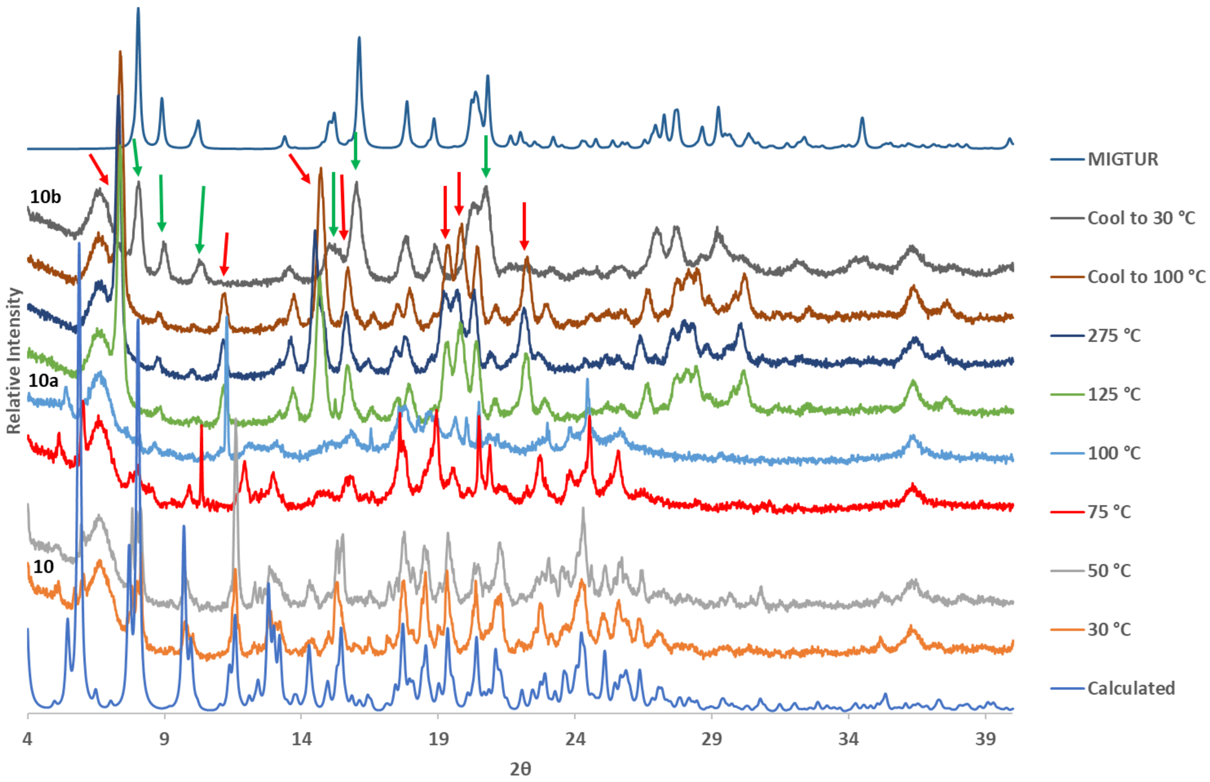

Figure 4.56: VT-PXRD patterns in the range 30-275 °C of **10**.

4.3.3.3. Hot Stage Microscopy, Differential Scanning Calorimetry and Thermogravimetric Analysis

HSM photographs (Fig. 4.57) of a crystal of **9** shows the crystal beginning to turn opaque at 40 °C, corresponding with the marginal loss of crystallinity observed in the 50 °C VT-PXRD trace, with the first bubbles appearing at 100 °C, by which point the VT-PXRD trace is already indicating an amorphous state for the sample. Vigorous bubbling increases at 120 °C and continues until approximately 250 °C. Decomposition then begins at 370 °C.

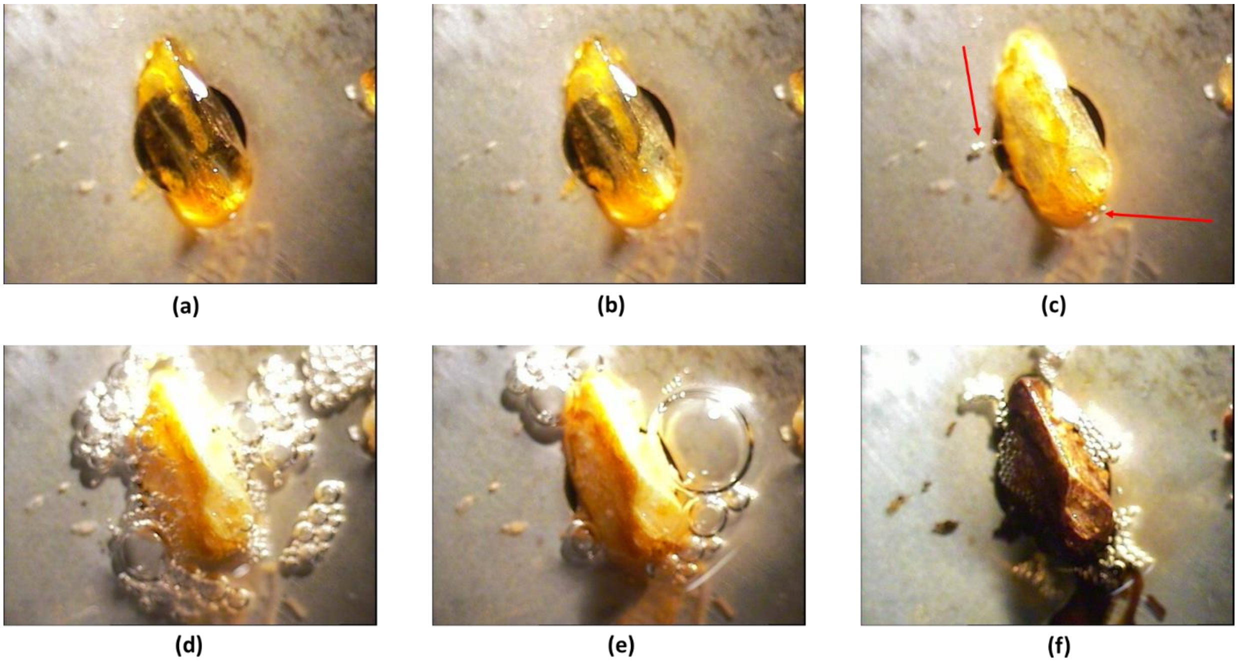
(a) (b) (c) (d) (e) (f)

Figure 4.57: Hot stage microscope photographs of compound **9** under silicone oil at different temperatures: (a) 23 °C, (b) 40 °C, (c) 100 °C, (d) 200 °C, (e) 250 °C and (f) 370 °C (bubbles show the release of solvent or decomposition – the red arrows in (c) indicate the first bubbles).

TGA analysis reveals three mass loss events totalling a combined mass loss of 27.79 % (Fig. 4.58), which is compares favourably with the calculated 27.91 % for the solvent in the ASU plus the additional unmodelled 4 1-butanol molecules per ASU indicated by the electron count of 174 obtained using the SQUEEZE routine in PLATON.[24] The first mass loss of 7.02 % could correspond to the loss of three ASU 1-butanol molecules (7.36 %), the second mass loss of 16.74 % to the loss of the other seven ASU 1-butanol molecules (17.17 %) and the third mass loss of 4.03 % to the loss of 5.67 ASU water molecules (3.38 %). DSC analysis (Fig. 4.58) reveals six thermal events – one beginning at 58.6 °C and finishing at 74.1 °C which corresponds to the first solvent loss on the TGA trace, the second starting at 84.2 °C and ending at 109.4 °C which corresponds to the second mass loss on the TGA thermogram, the third starting at 124.8 °C and finishing at 137.0 °C which also corresponds to the second solvent loss on the TGA trace, the fourth beginning at 138.3 °C and ending at 165.3 °C which corresponds to the third solvent loss on the TGA trace and the loss of crystallinity during the transition from **9** to **9a**, and the sixth starting at 318.9 °C which is decomposition. The fifth is indicated by the red arrow (Fig. 4.58) at approximately 198 °C, corresponding to a small, broad endotherm (enthalpy not measured). This is assigned to the **9a-9b** phase change. The differences in temperature in comparison with the VT-PXRD experiment could be due to the different temperature programmes used for the TGA/DSC and VT-PXRD experiments.

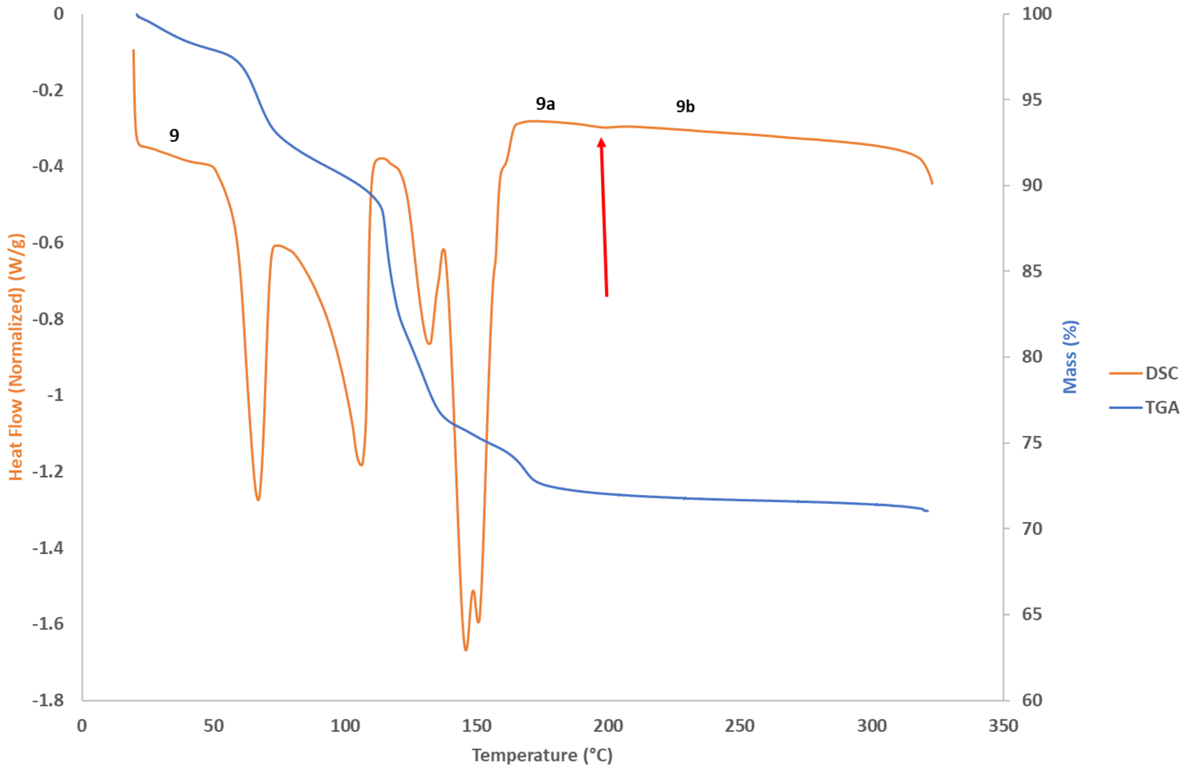

Figure 4.58: DSC and TGA thermograms of **9**.

Table 4.19: TG analysis for compound **9**.

Thermal Event	Temperature Range (°C)	Mass Loss (%)
Mass loss **1**	21.0–75.2	7.02 (calc. 7.36)
Mass loss **2**	76.1–141.1	16.74 (calc. 17.17)
Mass loss **3**	142.3–191.4	4.03 (calc. 3.38)
Decomposition	-	-

Table 4.20: DSC analysis for compound **9**.

Thermal Event	Onset Temperature (°C)	Temperature Range (°C)	Peak Temperature (°C)	Enthalpy (J g^{-1})
Mass loss **1**	58.6	58.6-74.1	65.5	32.737
Mass loss **2**	84.2	84.2-109.4	102.4	48.745
Mass loss **3**	124.8	124.8-137.0	131.2	8.266
Mass loss **4**	138.3	138.3-165.3	145.6	77.180
Decomposition	318.9	318.9-*	-	-

*not taken to full decomposition

HSM photographs of **10** under silicone oil (Fig. 4.59) show the crystals beginning to opacify at 40 °C. At 80 °C, the crystals have gone from their initial reddish orange colour to golden yellow. The first bubble appears at 90 °C, indicating the start of solvent loss, and the crystals opacify, indicating the loss of crystallinity observed during the VT-PXRD experiment after the phase change from **10** to **10a**. The bubbling and associated loss of monocrystallinity seems to continue until approximately 240 °C. Thereafter, decomposition begins at around 360 °C.

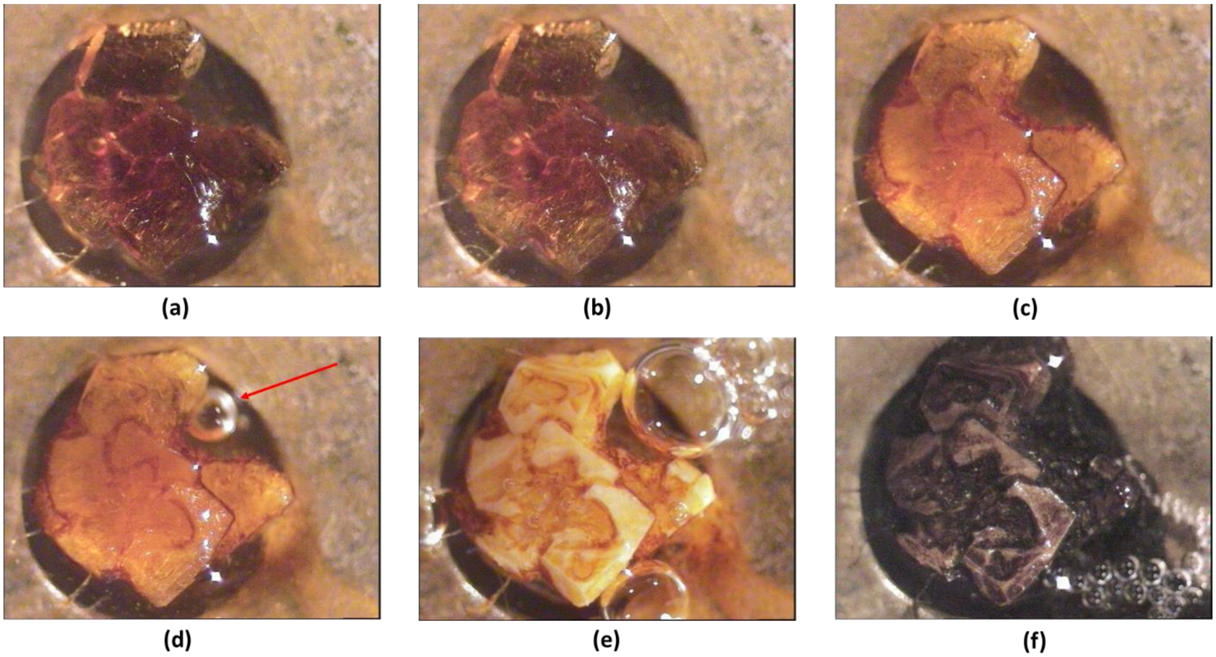

Figure 4.59: Hot stage microscope photographs of compound **10** under silicone oil at different temperatures: (a) 30 °C, (b) 40 °C, (c) 80 °C, (d) 90 °C, (e) 240 °C and (f) 360 °C (bubbles show the release of solvent or decomposition – the red arrow in (d) indicates the first bubble).

TGA analysis displays one mass loss event in the temperature range 127–146 °C before decomposition (Fig. 4.60). This mass loss event is measured to be 24.92 % of the total mass, which is less than the calculated mass loss from the ASU (including 3.3 unmodelled 1-pentanol molecules indicated by a SQUEEZE electron count of 163) of 29.01 %, and more than the 21.48 % calculated when only considering the solvent which has been modelled in the crystal structure. This suggests that there is indeed unmodelled solvent present in the structure, but SQUEEZE is perhaps overestimating the number of unmodelled solvent molecules present. It is also possible that there are both unmodelled 1-pentanol and water molecules – for example, one unmodelled 1-pentanol molecule and three unmodelled water molecules would give a mass loss of 24.56 %, which is reasonably close to the experimental value of 24.92 %. The DSC analysis seems to indicate three thermal events – one occurring in the range 88.5–109.3 °C which is probably the **10**–**10a** transition, with the second event corresponding to the solvent loss on the TGA thermogram (Fig. 4.60). The third event occurs in the range 166.7–189.0 °C, which is assigned to

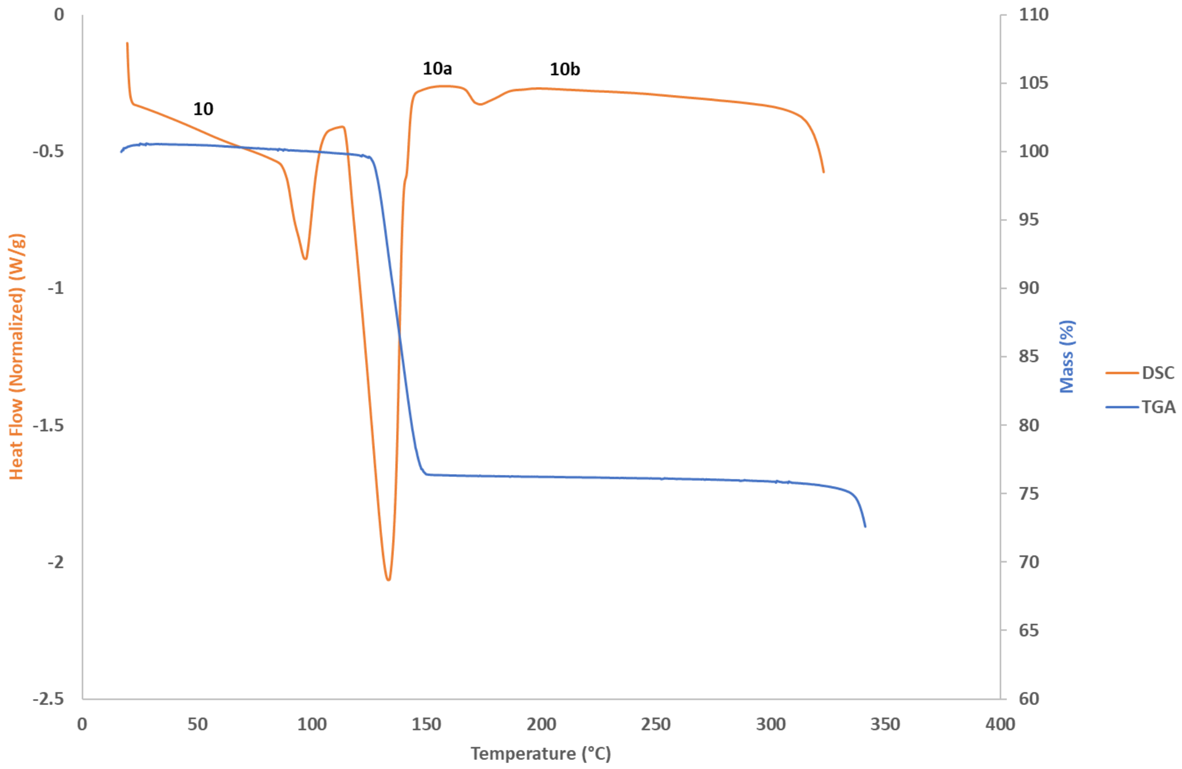

Figure 4.60: DSC and TGA thermograms of **10**.

the **10a**–**10b** phase change. As with the **9a-9b** transition, this occurs at a higher temperature than it does in the VT-PXRD experiment – this can again be explained by the different temperature programmes used for the TGA/DSC and VT-PXRD experiments.

Table 4.21: TG analysis for compound **10**.

Thermal Event	Temperature Range (°C)	Mass Loss (%)
Mass loss **1**	122.8–153.5	24.90 (calc. 29.01)
Decomposition	311.8-*	-

*not taken to full decomposition

Table 4.22: DSC analysis for compound **10**.

Thermal Event	**Onset Temperature (°C)**	**Temperature Range (°C)**	**Peak Temperature (°C)**	**Enthalpy ($J\ g^{-1}$)**
Thermal event **1**	88.5	88.5-109.3	97.2	22.82
Mass loss **1**	115.3	115.3-153.4	132.5	147.17
Thermal event **3**	166.7	166.7-189.0	176.4	4.55
Decomposition	317.9	317.9-*	-	-

*not taken to full decomposition

4.4. Gas & Vapour Sorption

The table below (Table 4.23) displays the vapour pressure at 25 °C of the solvents used for vapour sorption.

Table 4.23: The vapour pressure at 25 °C of the solvents used for vapour sorption.

Solvent	**Vapour Pressure at 25 °C (mm Hg)**
Methanol	127.0 [29]
Ethanol	60.8 [30]
Isopropanol	33.1 [31]
1-Propanol	21.0 [32]
1-Butanol	7.0 [33]
1-Pentanol	2.2 [34]
Water	23.8 [35]

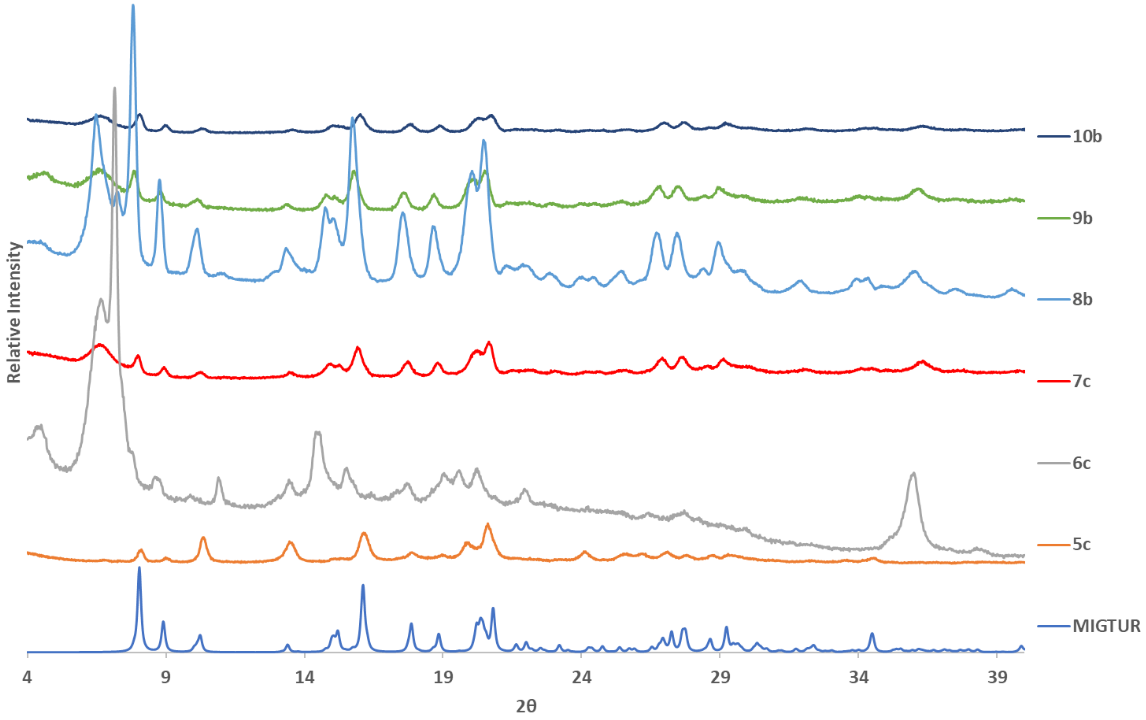

Figure 4.61: The PXRD patterns of all desolvated compounds **5**–**10**.

All desolvated compounds discussed in this chapter display the same PXRD pattern (Fig. 4.61). **6c** will be discussed as a representative example (Table 4.24). All numbers of molecules per ASU are based on the ASU of their original structures.

Table 4.24: Gas sorption maxima of desolvated compound **6c** for nitrogen (77 K), carbon dioxide (273 K), hydrogen (77 K) and water vapour (298 K).

Compound	Nitrogen (cm^3 (STP) g^{-1})	Carbon Dioxide (cm^3 (STP) g^{-1})	Hydrogen (cm^3 (STP) g^{-1})	Water (cm^3 (STP) g^{-1})
6c	12.66	3.99	20.29	80.37

6c was studied for gas sorption from vacuum to 700-800 mm Hg absolute pressure (Fig. 4.62 and 4.63). Nitrogen gas sorption at 77 K and CO_2 sorption at 273 K were found to be very low, with maxima of 12.66 cm^3 (STP) g^{-1} at 647 mm Hg corresponding to ~0.15 N_2 molecules per ASU and

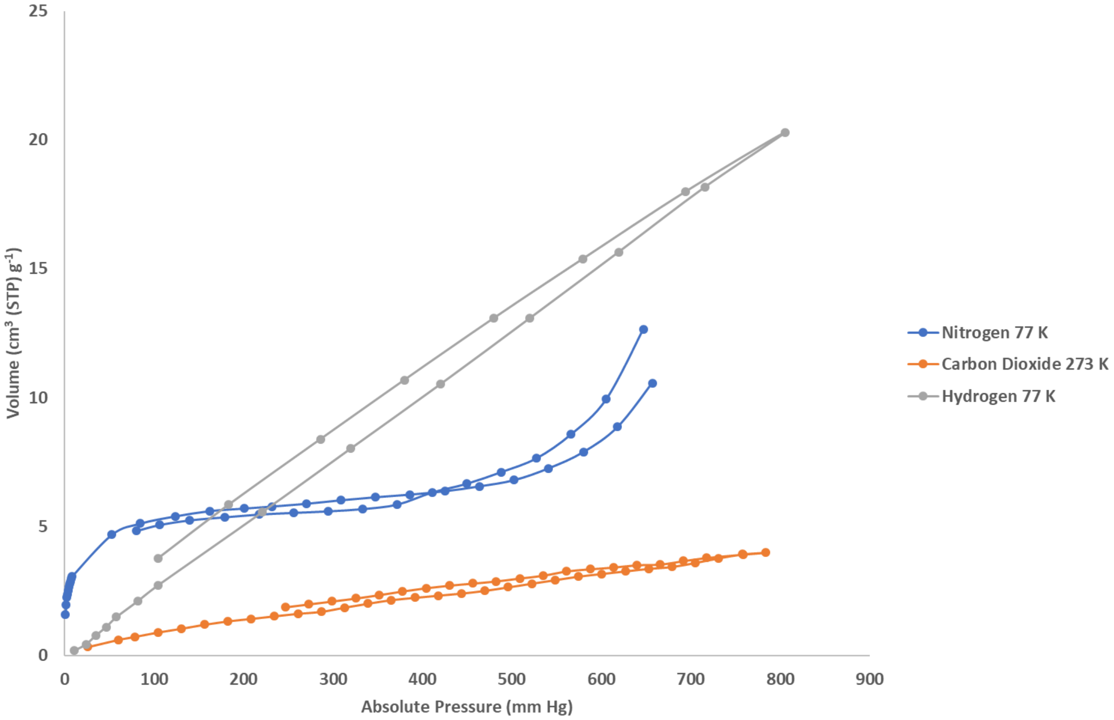

Figure 4.62: Nitrogen (77 K), carbon dioxide (273 K) and hydrogen (77 K) sorption isotherms of **6c**.

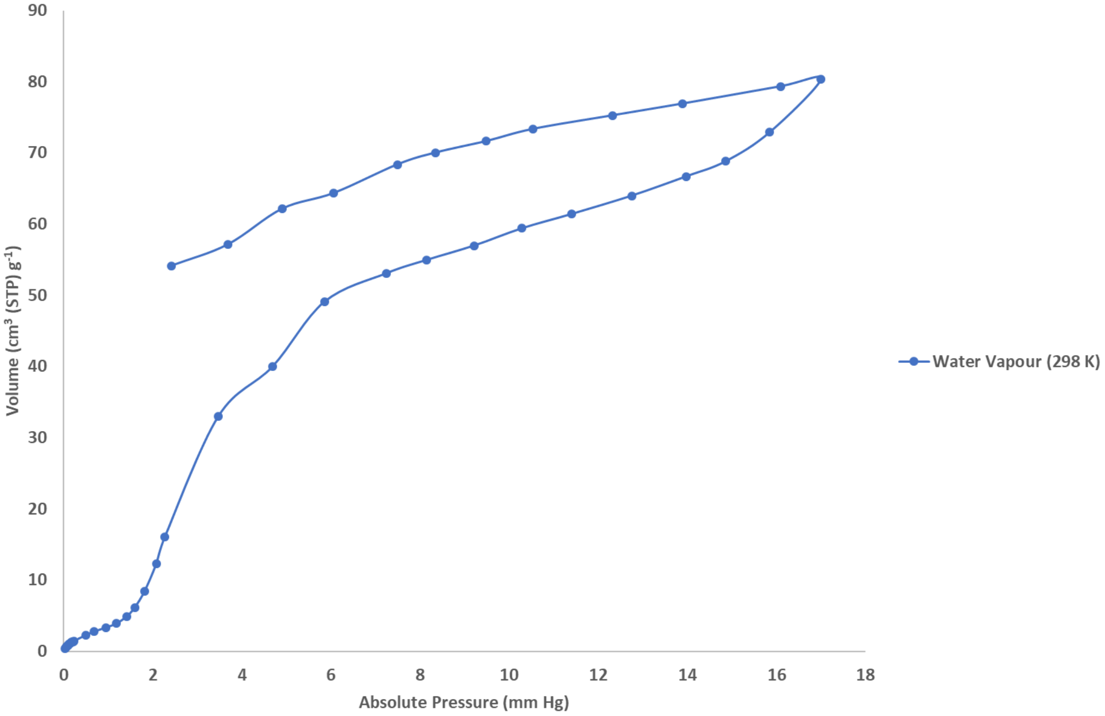

Figure 4.63: Water vapour sorption isotherm of **6c** at 298 K.

3.99 cm^3 (STP) g^{-1} at 784 mm Hg corresponding to ~0.05 CO_2 molecules per ASU, respectively. H_2 sorption at 77 K reached a maximum of 20.29 cm^3 (STP) g^{-1} at 806 mm Hg. This corresponds to ~0.25 H_2 molecules per asymmetric unit (or 0.18 wt. %). Hysteresis is observed for the hydrogen desorption. Water vapour sorption at 298 K begins gradually until an inflection point is reached at 4.86 cm^3 (STP) g^{-1} and a pressure of 1.4 mm Hg, corresponding to ~0.06 water molecules per asymmetric unit. Thereafter, a steep increase in adsorption is observed until around 49.07 cm^3 (STP) g^{-1} at 6 mm Hg, corresponding to ~0.6 water molecules per asymmetric unit. Subsequently, the water vapour sorption increased gradually until reaching a maximum of 80.37 cm^3 (STP) g^{-1} at 17 mm Hg. This corresponds to ~1.0 water molecule per ASU (i.e. 1 water molecule per half a CMCR molecule), which is double the amount for MIGTUR[22] (1 water molecule per CMCR molecule). Hysteresis is observed for the desorption isotherm, with sorption decreasing steadily with decreasing pressure, reaching a minimum of 54.15 cm^3 (STP) g^{-1} at 2.4 mm Hg, corresponding to ~0.7 water molecules per asymmetric unit.

However, CO_2, H_2 and N_2 sorption were not as significant as hoped and therefore vapour sorption was attempted on the desolvated phases of **5**, **6**, **7**, **8**, **9** and **10**, where vapour generated from the original solvent of crystallization was used. Methanol vapour sorption on **5c** (Fig. 4.64) initially showed gradual adsorption until the first inflection point occurred at 24.35 cm^3 (STP) g^{-1} at 32.5 mm Hg, corresponding to ~0.3 molecules of methanol per asymmetric unit. The adsorption isotherm then displays a slightly steeper increase until a second inflection point is reached at 67.00 cm^3 (STP) g^{-1} at a pressure of 49 mm Hg. This corresponds to ~0.8 molecules of methanol per asymmetric unit. After the second inflection point, a steep increase in adsorption is observed until approximately 219.58 cm^3 (STP) g^{-1} at 56 mm Hg, corresponding to ~2.7 molecules of methanol per asymmetric unit. Subsequent to this point, the adsorption isotherm started to level off but never plateaued, instead continuing to gradually increase until it reached a maximum of 263.94 cm^3 (STP) g^{-1} at ~97 mm Hg. This corresponds to ~3.2 molecules of methanol per asymmetric unit. Hysteresis is observed upon decreasing pressure, with almost no decline in the

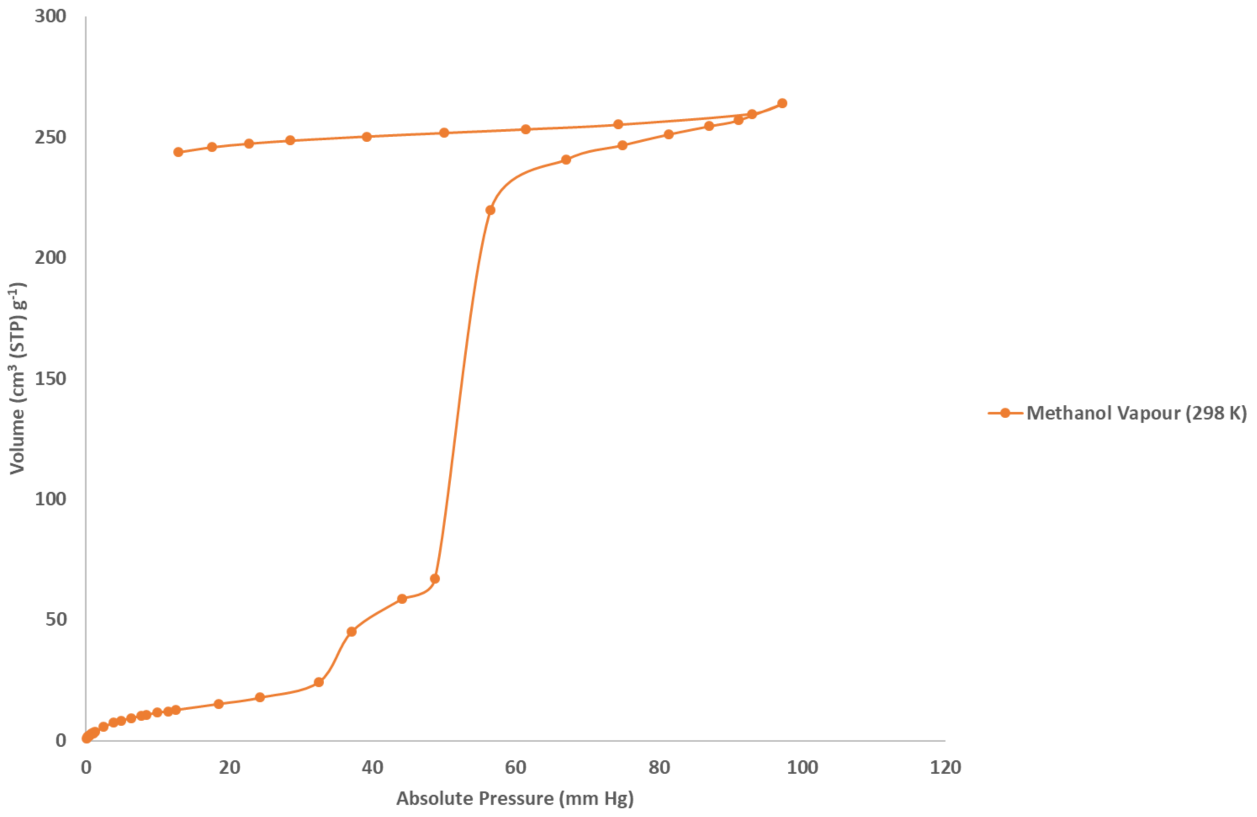

Figure 4.64: Methanol vapour sorption isotherm at 298 K of **5c**.

volume adsorbed. The desorption isotherm reached a minimum of 243.68 cm^3 (STP) g^{-1} at 13 mm Hg, corresponding to ~3.0 molecules of methanol per asymmetric unit. The amount adsorbed is double the 1.5 methanol molecules observed in the asymmetric unit in the crystal structure of **5**, suggesting that the capacity of **5** for methanol is greater than initially observed. It is also possible that the additional methanol molecules are accommodated in the locations of the water molecules in the original structure without changing the packing of the host molecules. A PXRD experiment was performed on **5c** after exposure to the methanol vapour sorption experiment (Fig. 4.65). The structure of the sample appears to have reverted to the structure of the initial solvated structure **5**.

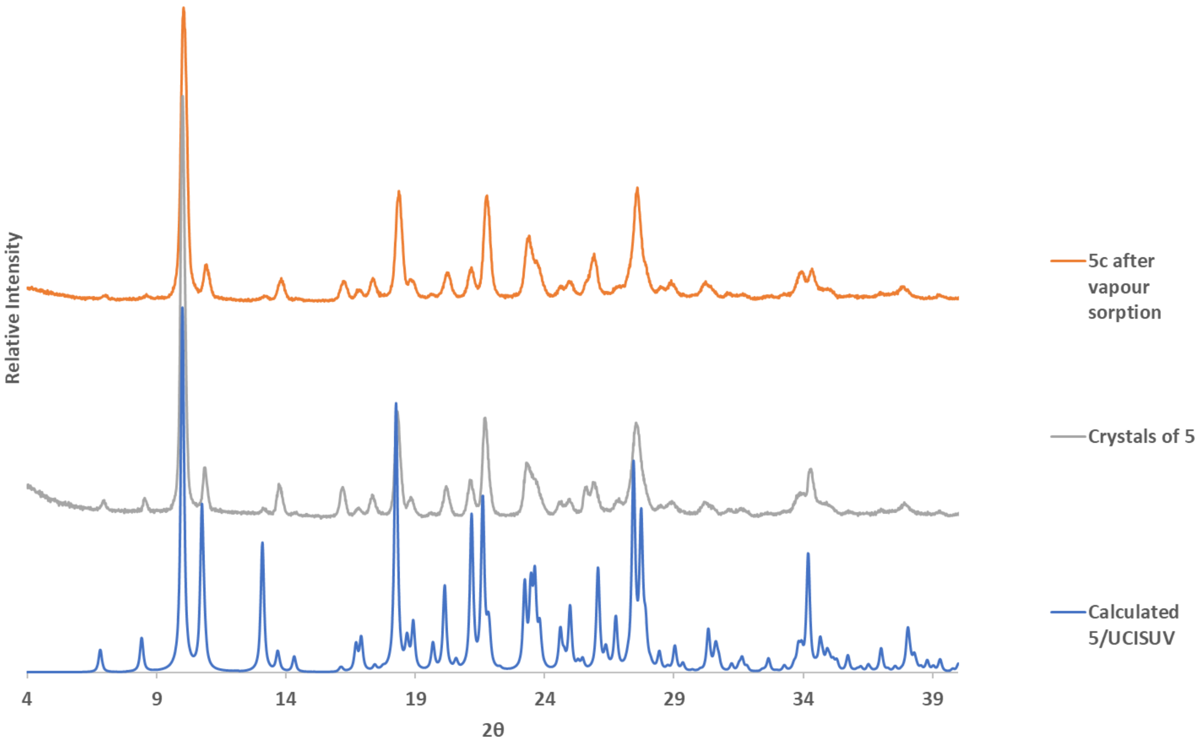

Figure 4.65: PXRD pattern of the **5c** sample obtained after methanol vapour sorption (in orange) compared with calculated pattern of **5** obtained from the literature single crystal X-ray structure UCISUV (in blue) and the PXRD pattern obtained from crystals of **5** (in grey). The differences in peak heights are attributed to preferred orientation effects.

Ethanol vapour sorption on **6c** (Fig. 4.66) increased gradually until an inflection point was reached at around 14.04 cm^3 (STP) g^{-1} at 12 mm Hg, corresponding to ~0.2 ethanol molecules per asymmetric unit. A steep increase in sorption was observed until around 43.91 cm^3 (STP) g^{-1} at 15 mm Hg, corresponding to ~0.5 ethanol molecules per asymmetric unit. Thereafter, the sorption increases gradually until a second inflection point is reached at around 60.17 cm^3 (STP) g^{-1} at 30 mm Hg, corresponding to ~0.7 ethanol molecules per asymmetric unit. After the second inflection point, a steep increase in sorption was observed, gradually becoming less steep as the maximum is reached – a maximum of 113.93 cm^3 (STP) g^{-1} at 46.6 mm Hg. This corresponds to ~1.4 molecules of ethanol per asymmetric unit. Hysteresis is observed upon decreasing pressure. A low degree of desorption is observed. The desorption isotherm reaches a

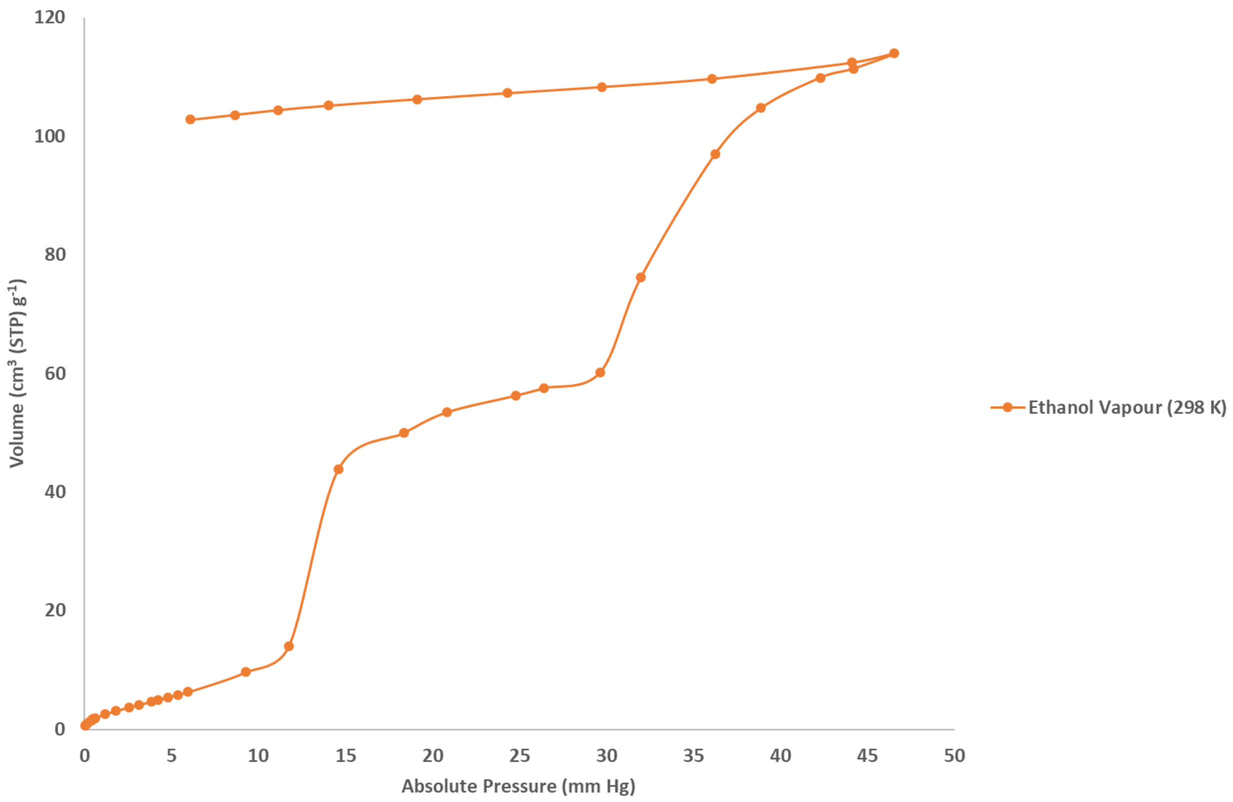

Figure 4.66: Ethanol vapour (298 K) sorption isotherm of **6c**.

minimum of 102.76 cm^3 (STP) g^{-1} at 6 mm Hg, corresponding to ~1.2 ethanol molecules per asymmetric unit. A PXRD experiment was performed on **6c** after exposure to the ethanol vapour sorption experiment (Fig. 4.67). The structure of the sample appears to have resolvated to the structure of **6**, although the sample is still quite amorphous at 2θ values above approximately 15°. The PXRD pattern of the sample below 15° 2θ is very similar to **6**, with the main difference being the large peak at 9.2° 2θ, which is observed within the PXRD pattern of **6** at 10.0° 2θ (indicated by the black arrows in Fig. 4.67).

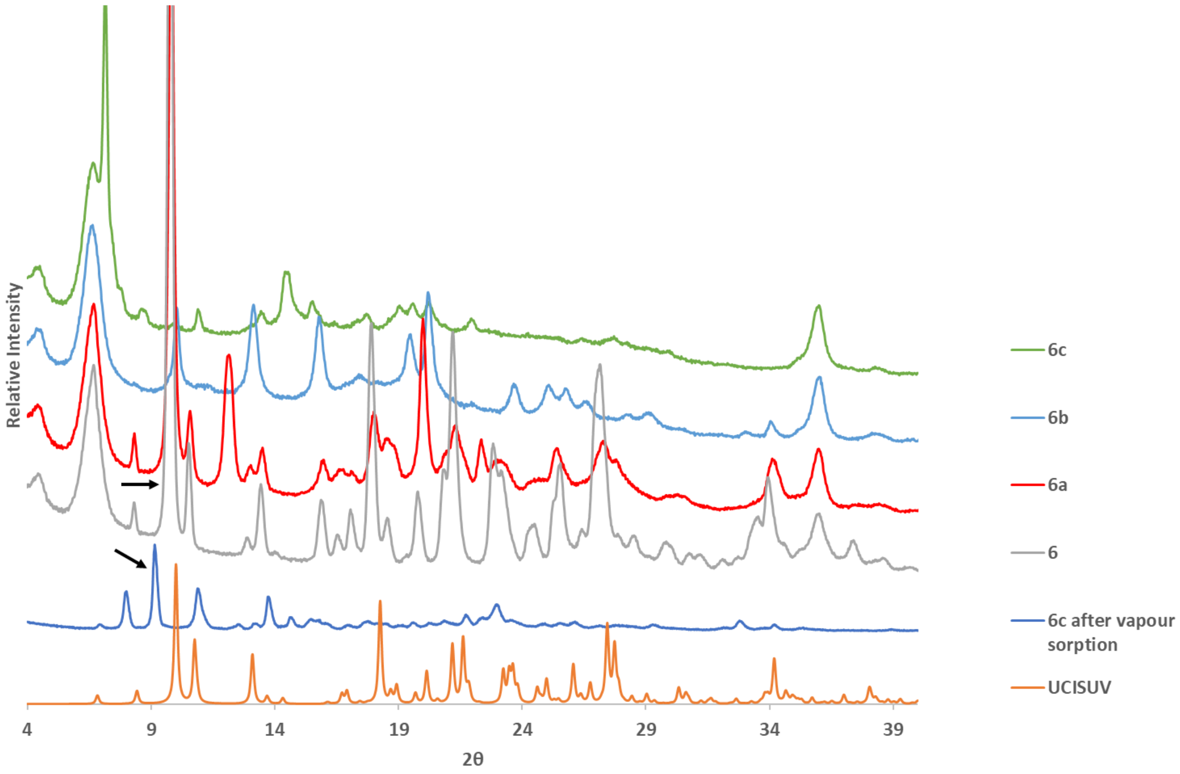

Figure 4.67: PXRD pattern of **6c** obtained after ethanol vapour sorption (in blue) compared with calculated pattern of **5** (UCISUV) obtained from the literature structure (in orange), and the PXRD patterns of **6** (in grey), **6a** (in red), **6b** (in light blue) and **6c** (in green). The black arrows indicate the main difference between **6c** after vapour sorption and **6**.

Isopropanol vapour sorption on **7c** (Fig. 4.68) slowly increases until reaching a maximum of 155.89 cm^3 (STP) g^{-1} at 22 mm Hg. This corresponds to ~1.9 isopropanol molecules per ASU. Immediate hysteresis is observed upon decreasing pressure, to the extent that a polymorphic transition is suspected. A slight decrease in pressure to 22 mm Hg resulted in a sharp desorption to 100.68 cm^3 (STP) g^{-1}, corresponding to ~1.2 molecules of isopropanol per asymmetric unit. Only a slight decrease occurs from this point, with a minimum of 91.98 cm^3 (STP) g^{-1} reached at only 4 mm Hg, corresponding to ~1.1 molecules of isopropanol per asymmetric unit. This sorption isotherm was shown to be reproducible.

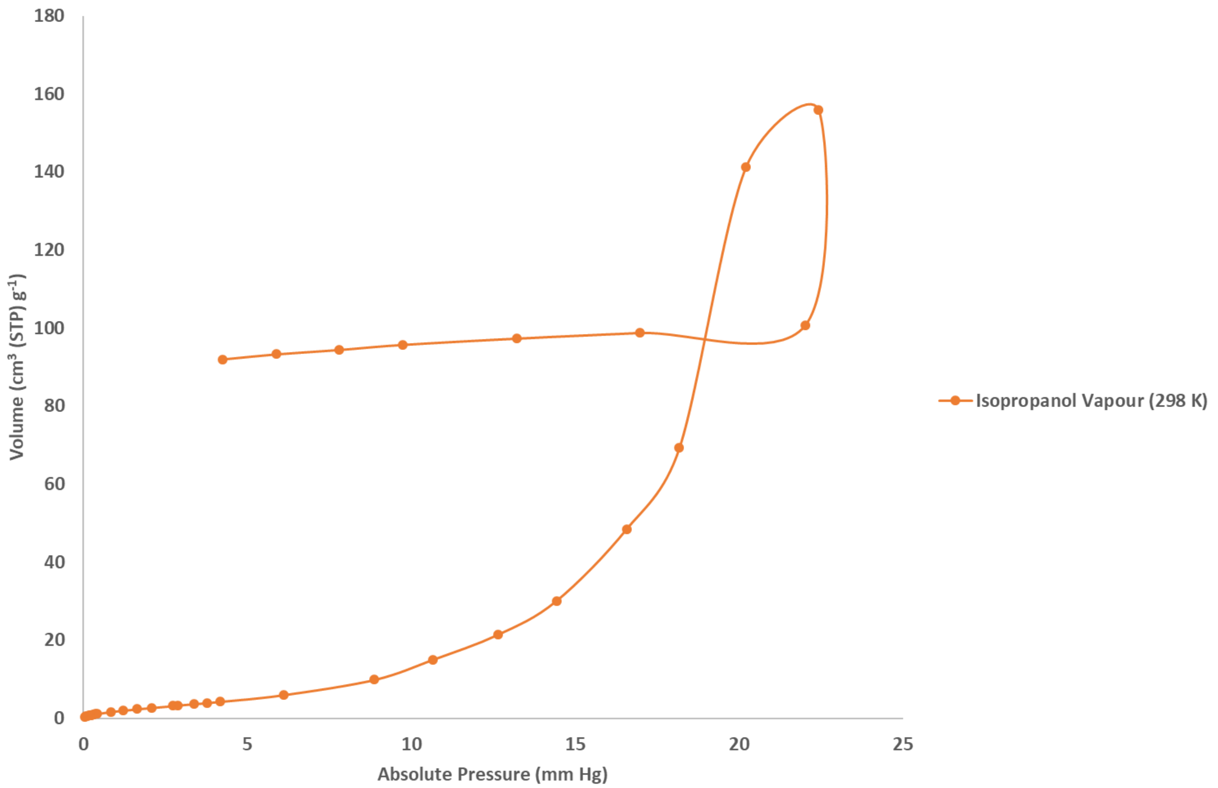

Figure 4.68: Isopropanol vapour sorption isotherm at 298 K of **7c**.

A PXRD experiment was performed on **7c** after exposure to the isopropanol vapour (Fig. 4.69). The structure of the sample appears to have formed a new phase which does not match **7**, **7a**, **7b** or **7c**.

The PXRD pattern of this polymorph obtained after isopropanol vapour sorption performed on **7c** does not match any of the VT-PXRD patterns of **7** (or **5** or **6**) and therefore this is not an intermediate phase which can be obtained when heating **5**, **6** or **7**.

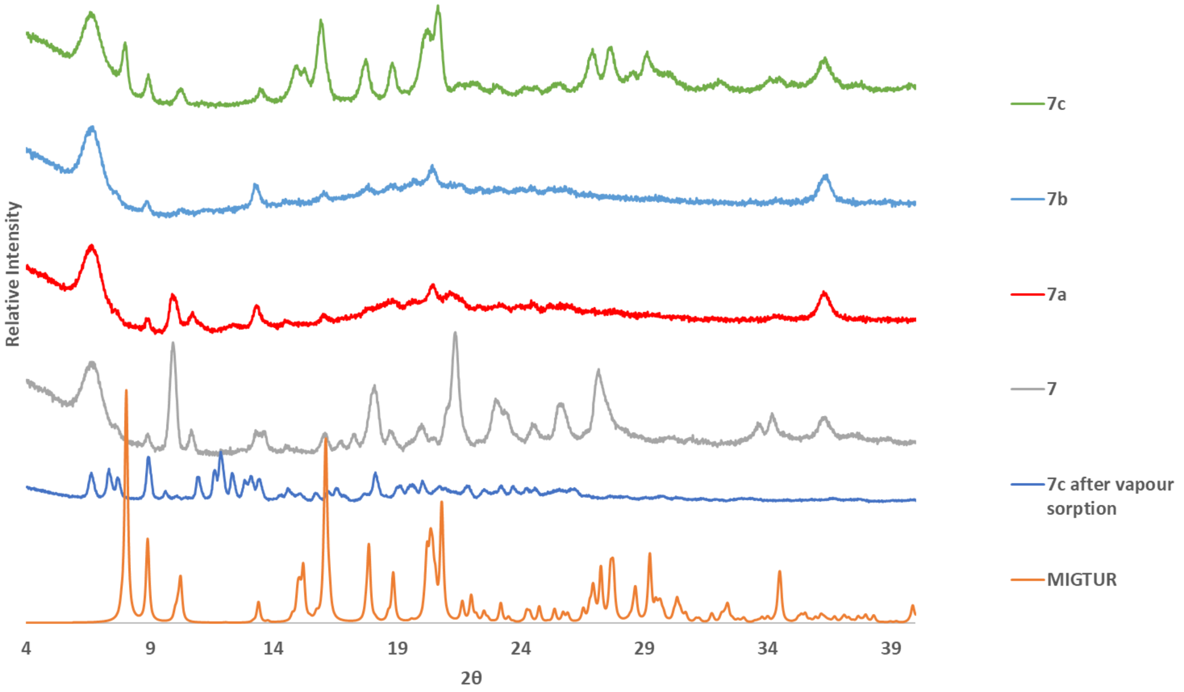

Figure 4.69: PXRD pattern of **7c** obtained after isopropanol vapour sorption (in blue) compared with calculated pattern of MIGTUR obtained from the literature structure (in orange), and the PXRD patterns of **7** (in grey), **7a** (in red), **7b** (in light blue) and **7c** (in green).

It has been shown that **8** could also be prepared by exposing desolvated form **8b** to 1-propanol vapour. This was performed by *in situ* PXRD vapour sorption over 4 hours. However, sorption was also achieved on a gas sorption analyser at 20 °C on **8b** (Fig. 4.70). Due to the long equilibration times between each incremental increase in the 1-propanol vapour pressure, this took 8 days to complete.

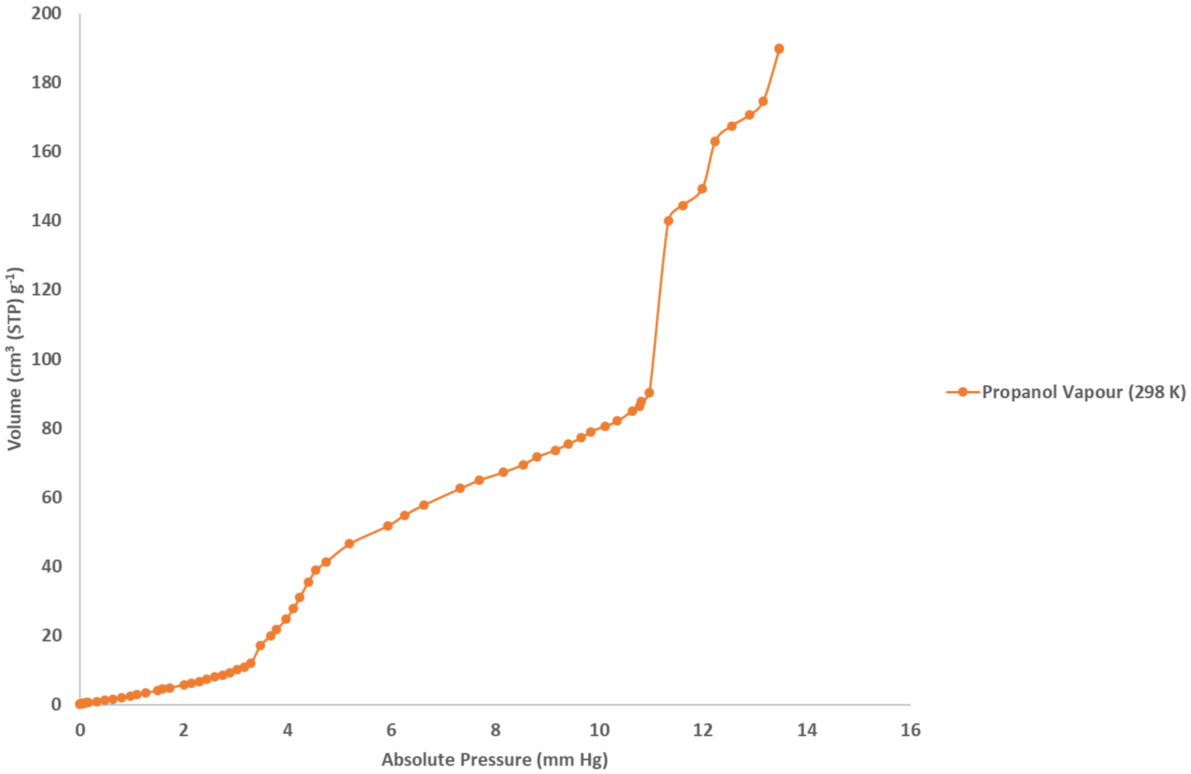

Figure 4.70: 1-propanol vapour sorption isotherm of **8b** at 298 K.

The inflection points in the isotherms reveal structural transformations occurring as **8b** absorbed 1-propanol, confirmed by subsequent PXRD analysis after the experiment which found that the original hexameric structure **8** was re-established (Fig. 4.71). The first inflection point occurred at 11.91 cm^3 (STP) g^{-1} and a pressure of 3.29 mm Hg, corresponding to ~0.3 1-propanol molecules per asymmetric unit. The increase in sorption became steeper until 38.92 cm^3 (STP) g^{-1} at 4.55 mm Hg, corresponding to ~0.9 1-propanol molecules per asymmetric unit. Subsequently, the increase in sorption became more gradual until another inflection point at 90.37 cm^3 (STP) g^{-1} and a pressure of 10.97 mm Hg, corresponding with ~2.2 1-propanol molecules per asymmetric unit. The steep increase following this inflection point continues until 140.06 cm^3 (STP) g^{-1} at 11.33 mm Hg, corresponding with ~3.4 1-propanol molecules per asymmetric unit. There was then a more gradual sorption increase until 149.39 cm^3 (STP) g^{-1} at 11.99 mm Hg, corresponding with ~3.6 1-propanol molecules per asymmetric unit. Thereafter, there is another steep sorption

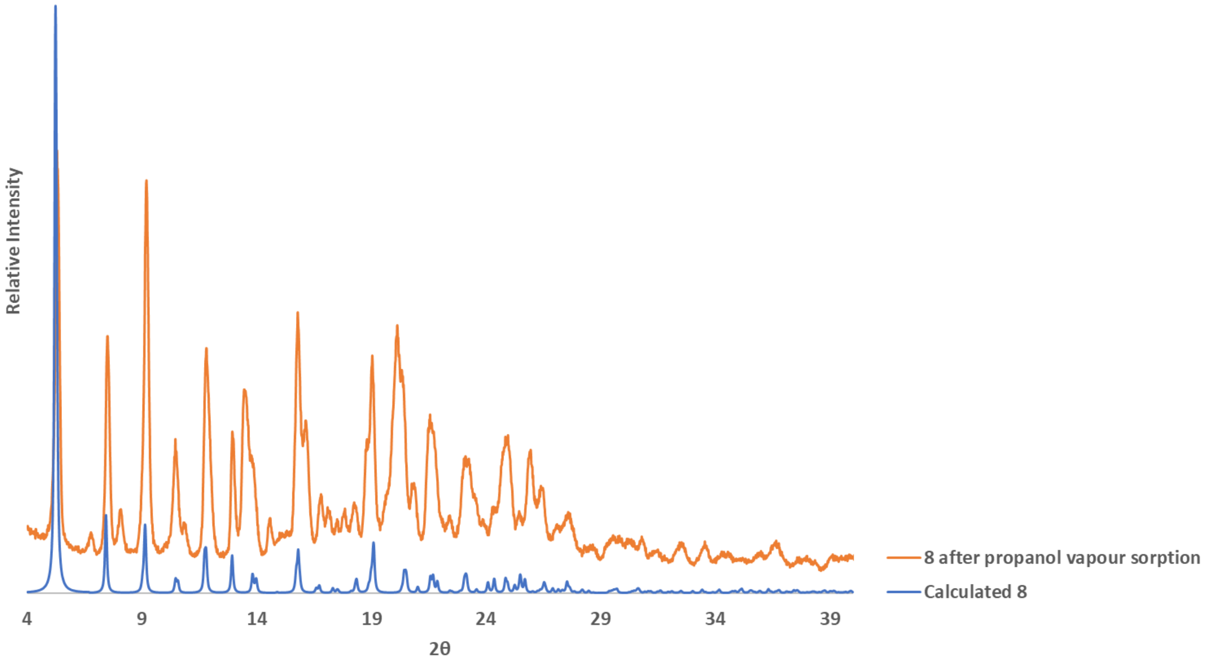

Figure 4.71: PXRD pattern of **8** obtained after 1-propanol vapour sorption on the gas sorption analyser and comparison with predicted pattern of **8** obtained from the single crystal X-ray structure.

increase until 163.03 cm^3 (STP) g^{-1} at a pressure of 12.24 mm Hg, corresponding with ~4.0 1-propanol molecules per asymmetric unit. Thereafter follows another more gradual increase in sorption until 174.64 cm^3 (STP) g^{-1} at a pressure of 13.16 mm Hg, corresponding with ~4.2 1-propanol molecules per asymmetric unit. Subsequently, there is another steep increase in sorption until 189.75 cm^3 (STP) g^{-1} at 13.47 mm Hg, corresponding with ~4.6 1-propanol molecules per asymmetric unit. The maximum sorption is finally reached at 190.03 cm^3 (STP) g^{-1} at 13.48 mm Hg, corresponding to ~4.6 1-propanol molecules per asymmetric unit. In the single crystal X-ray structure of **8**, there are only three 1-propanol molecules per asymmetric unit. However, this could be due to the water present in the 'wet' 1-propanol, which is required for the formation of **8**, not being accounted for in these calculations.

Sorption of 1-butanol vapour at 298 K and 1-pentanol vapour at 298 K on **9b** and **10b** respectively was not successful due to the low vapour pressures of 1-butanol (7.0 mm Hg)[31] and 1-pentanol (2.2 mm Hg)[32] at this temperature.

4.5. Summary

A series of CMCR-alcohol compounds has been studied and their thermal behaviour has been determined. Compounds **6** and **7**, prepared with ethanol and isopropanol respectively, have PXRD patterns which are very similar to a known compound, **5**, prepared with methanol. A new CMCR-propanol compound, **8**, has been isolated, obtained from a solution of 1-propanol. The CMCR molecules, 1-propanol and water molecules are found to form a hexameric spherical assembly, which includes 1-propanol, therefore having potential to include other small molecules, and to the best of our knowledge, possesses the largest interior cavity of any calixarene- or resorcinarene-based hexameric spherical assembly currently known. Remarkably, **8** can also be prepared by liquid-assisted grinding of the CMCR host with 1-propanol. Another novel compound, **10**, formed with 1-pentanol, also contains hexameric spherical assemblies and is very similar to a known structure, **9**, formed from 1-butanol. **10** also contains two different types of hexameric spherical assemblies, albeit in this structure, the supra-heterodimers of spherical assemblies are not observed as they are in **9**. Attempts to desolvate **8** led to the loss of crystallinity, followed by the appearance of a second crystalline form, the structure of which displays a similar powder pattern to that of a known structure (CSD code: MIGTUR).[22] This desolvated form, **8b**, has shown the ability to transform back to **8** upon exposure to 1-propanol vapour. 1-butanol and 1-pentanol vapour sorption failed on compounds **9b** and **10b**, respectively, but methanol vapour sorption on compound **5c**, ethanol vapour sorption on compound **6c** and isopropanol vapour sorption on compound **7c** all proved successful. Furthermore, in the cases of **5c**, the original compound **5** was successfully regenerated.

4.6. References

1. Ariga, K.; Hill, J.P.; Lee, M.V.; Vinu, A.; Charvet, R.; Acharya, S. *Sci. Technol. Adv. Mater.*, **2008**, *9*, 014109.
2. Liu, Z.; Qiao, J.; Niu, Z.; Wang, Q. *Chem. Soc. Rev.*, **2012**, *41*, 6178-6194.
3. Uhlenheuer, D.A.; Petkau, K.; Brunsveld, L. *Chem. Soc. Rev.*, **2010**, *39*, 2817-2826.
4. MacGillivray, L.R.; Atwood, J.L. *Nature*, **1997**, *389*, 469-472.
5. Ugono, O.; Holman, K.T. *Chem. Commun.*, **2006**, 2144-2146.
6. Gerkensmeier, T.; Iwanek, W.; Agena, C.; Frohlich, R.; Kotila, S.; Nather, C.; Mattay, J. *Eur. J. Org. Chem.*, **1999**, 2257-2262.
7. Atwood, J.L.; Barbour, L.J.; Jerga, A. *Chem. Commun.*, **2001**, 2376-2377.
8. Avram, L.; Cohen, Y. *J. Am. Chem. Soc.*, **2003**, *125*, 16180-16181.
9. Cave, G.W.V.; Antesberger, J.; Barbour, L.J.; McKinlay, R.M.; Atwood, J.L. *Angew. Chem., Int. Ed.*, **2004**, *43*, 5263-5266.
10. Zhang, Q.; Adams, R.D.; Fenske, D. *J. Inclusion Phenom. Macrocyclic Chem.*, **2005**, *53*, 275-279.
11. Dalgarno, S.J.; Power, N.P.; Antesberger, J.; McKinlay, R.M.; Atwood, J.L. *Chem. Commun.*, **2006**, 3803-3805.
12. Oliver, C.L.; Báthori, N.B.; Jackson, G.E.; Kuter, D.; Cruickshank, D.L. *CrystEngComm*, **2016**, *18*, 3015-3018.
13. Atwood, J.L.; Barbour, L.J.; Jerga, A. *Proc. Nat. Acad. Sci. USA*, **2002**, *99*, 4837-4841.
14. Kulikov, O.; Li, R.; Gokel, G.W. *Angew. Chem., Int. Ed.*, **2009**, *48*, 375-377.
15. Kulikov, O.; Rath, N.P.; Zhou, D.; Carasel, I.A.; Gokel, G.W. *New J. Chem.*, **2009**, *33*, 1563-1569.
16. Martin, A.D.; Boulos, R.A.; Iyer, K.S.; Sobolev, A.N.; Bond, C.S.; Atwood, J.L.; Dalgarno, S.J.; Raston, C.L. *Chem. Commun.*, **2011**, *47*, 9882-9884.
17. Atwood, J.L.; Barbour, L.J.; Jerga, A. *J. Supramol. Chem.*, **2001**, *1*, 131-134.
18. Cave, G.W.V.; Dalgarno, S.J.; Antesberger, J.; Ferrarelli, M.C.; McKinlay, R.M.; Atwood, J.L. *Supramol. Chem.*, **2008**, *20*, 157-160.

19. Dalgarno, S.J.; Antesberger, J.; McKinlay, R.M.; Atwood, J.L. *Chem. – Eur. J.*, **2007**, *13*, 8248-8255.
20. Åhman, A.; Nissinen, M. *Chem. Commun.*, **2006**, 1209-1211.
21. He, M.; Johnson, R.J.; Escobedo, J.O.; Beck, P.A.; Kim, K.K.; St. Luce, N.N.; Davis, C.J.; Lewis, P.T.; Fronczek, F.R.; Melancon, B.J.; Mrse, A.A.; Treleaven, W.D.; Strongin, R.M. *J. Am. Chem. Soc.*, **2002**, *124*, 5000-5009.
22. Ma, B.-Q.; Coppens, P. *Chem. Commun.*, **2002**, 424-425.
23. Macrae, C.F.; Bruno, I.J.; Chisholm, J.A.; Edgington, P.R.; McCabe, P.; Pidcock, E.; Rodriguez-Monge, L.; Taylor, R.; van de Streek, J.; Wood, P.A. *J. Appl. Cryst.*, **2008**, *41*, 466-470.
24. Spek, A.L. *Acta Crystallographica Section D – Biological Crystallography*, **2009**, *65*, 148-155.
25. Fucke, K.; Anderson, K.M.; Filby, M.H.; Henry, M.; Wright, J.; Mason, S.A.; Gutmann, M.J.; Barbour, L.J.; Oliver, C.; Coleman, A.W.; Atwood, J.L.; Howard, J.A.K.; Steed, J.W. *Chem. Eur. J.*, **2011**, *17*, 10259-10271.
26. Szymański, M.; Wierzbicki, M.; Gilski, M.; Jędrzejewska, H.; Sztylko, M.; Cmoch, P.; Shkurenko, A.; Jaskólski, M.; Szumna, A. *Chem. Eur. J.*, **2016**, *22*, 3148-3155.
27. Journey, S.N.; Teppang, K.L.; Garcia, C.A.; Brim, S.A.; Onofrei, D.; Addison, J.B.; Holland, G.P.; Purse, B.W. *Chem. Sci.*, **2017**, *8*, 7737-7745.
28. Sykes, N.M.; Su, H.; Weber, E.; Bourne, S.A.; Nassimbeni, L.R. *CrystEngComm*, **2017**, *19*, 5892-5896.
29. https://pubchem.ncbi.nlm.nih.gov/compound/methanol#section=Vapor-Pressure
30. https://www.chem.purdue.edu/gchelp/liquids/vpress.html
31. http://msdssearch.dow.com/PublishedLiteratureDOWCOM/dh_08ac/0901b803808aca73.pdf
32. https://pubchem.ncbi.nlm.nih.gov/compound/1-propanol#section=Vapor-Pressure
33. https://pubchem.ncbi.nlm.nih.gov/compound/1-butanol#section=Vapor-Pressure
34. https://pubchem.ncbi.nlm.nih.gov/compound/1-Pentanol#section=Vapor-Pressure
35. http://www.wiredchemist.com/chemistry/data/vapor-pressure

Chapter 5 – Conclusion & Future Work

5.1. Conclusion

Several novel structures containing CTV or CMCR hosts have been prepared, and structural analyses of these compounds have been performed. Also included are two known structures containing CMCR, in order to do a complete analysis of how the length of the alkyl chain effects the crystal structure obtained. It has been found that the shorter alkyl chain alcohols methanol (**5**), ethanol (**6**) and isopropanol (**7**) favour the formation of channel-type structures with the CMCR molecule in a 'boat' conformation, while the longer chain alcohols 1-propanol (**8**), 1-butanol (**9**) and 1-pentanol (**10**) favour the formation of hexameric spherical assembly structures with the CMCR molecule in the 'bowl' conformation. As for the CTV compounds, **1** and **4** crystallise from acetonitrile and 2-butanone, respectively, and are almost isostructural, forming layers of dimeric capsules which encapsulate the solvent molecules separated by layers of antiparallel stacked columns. **2** crystallises from a saturated solution of acetonitrile and forms a zipper-like motif. **3** crystallises from chloroform and does not form the dimeric capsules which are observed in the structures of **1** and **4**, but forms layers of antiparallel stacked columns of CTV molecules separated by layers of chloroform molecules.

A new CTV inclusion compound containing acetonitrile, **1**, was isolated. **1** could be desolvated upon heating to **1a** and **1b**, with the transition to **1a** occurring as a single-crystal-to-single-crystal transformation. The methyl groups seem to act as 'gates' in order to let the acetonitrile escape and, indeed, to return.

All compounds have been subjected to thermal analysis and were found to maintain crystallinity upon heating and desolvation – however, a few transitioned through an amorphous phase. The desolvated CTV compounds **1b**, **2b**, **3b** and **4b** all display the same PXRD pattern and are therefore taken to be the same desolvated phase. This is also confirmed by similar onset of melting temperatures. The PXRD pattern of the desolvated **3b** is very similar to that of the solvated **3**, suggesting that the layers of antiparallel columns of CTV molecules have simply move closer together after chloroform removal. This is therefore also the proposed structure for the desolvated **1b**, **2b** and **4b**.

A novel CMCR hexameric spherical assembly has been prepared, **8**, containing 1-propanol as the solvent. **8** has a 25 % larger interior volume than any previous organic, supramolecular hexameric assembly due to the insertion of additional solvent molecules between molecules of CMCR, forcing them further apart, and can remarkably be prepared by liquid-assisted grinding.

The structure of **9** has already been published in the literature. However, SCXRD studies for this work revealed additional structural information not represented in the literature structure. The structure of **10** was shown to be very similar to the structure of **9**, with certain specific differences.

Desolvation of the CMCR compounds **5**–**10** resulted in the formation of desolvated phases **5c**, **6c**, **7c**, **8b**, **9b** and **10b**. These phases are all a very close match to MIGTUR, a bilayer structure already in the Cambridge Structural Database which contains CMCR and water. This phase was eventually obtained after desolvation despite vastly different channel-type structures for **5**, **6** and **7** compared with the spherical hexameric assemblies of **8**, **9** and **10**.

All activated compounds have been subjected to gas sorption analysis. Some of these compounds have been shown to resolvate back to their original structures merely upon exposure of the desolvated powders to the solvent vapours, including the hexameric spherical assembly **8** upon exposure to 1-propanol vapour. These transitions occur in the solid state, at 298 K, with almost zero energy input required – the only requirement is sufficient vapour pressure of the appropriate solvent. These compounds are therefore potentially useful as separating and/or storage agents, or as detection agents, for these solvent vapours.

5.2. Future Work

Efficiency Testing

The compounds which have been shown to resolvate upon exposure to solvent vapour should be tested for efficiency – how many times can these compounds be desolvated and resolvated before they start to lose crystallinity and/or uptake efficiency?

Solvent Exchange

Another aspect of these compounds that can be investigated is whether the solvent can be replaced by immersing crystals obtained from one solvent in a different solvent. Further, can this be done in the vapour phase? Additionally, after heating and desolvation, it can be studied if the compounds can then absorb different solvent vapour to the initial solvent.

Competition Experiments

It can also be investigated if the respective hosts prefer one solvent or another in a 1:1 mixture of solvents or upon exposure to a 1:1 mixture of solvent vapour.

Different Desolvation Methods

Modified heating approaches can be attempted in order to desolvate the interior of hexameric assemblies, such as mild heating under vacuum, or ‘flushing’ out with supercritical CO_2.

Vapour Sorption of **9** and **10**

Vapour sorption should be attempted again on compounds **9** (with 1-butanol vapour) and **10** (with 1-pentanol vapour) at temperatures higher than 298 K, which should increase the probability of successful sorption with these two vapours.

5.3. Final Remarks

The synthesis and analysis of the host-guest compounds presented in this thesis reaffirms the importance of detailed structural studies in rationalizing their thermal, gas and vapour sorption properties. The resolvation of most of the host-guest compounds to their original structures also shows that dynamic structural changes are possible in the solid state with very little input energy, showing that the desolvated materials have potential applications in sensing, storage or separation of vapours. The ‘future work’ discussed under the previous heading proposes that the further investigation of these type of supramolecular systems is warranted.